



HAL
open science

Novel nanosecond and millielectronvolt spectroscopies in the electron microscope and their applications to nano-optics

Yves Auad

► To cite this version:

Yves Auad. Novel nanosecond and millielectronvolt spectroscopies in the electron microscope and their applications to nano-optics. Soft Condensed Matter [cond-mat.soft]. Université Paris-Saclay, 2022. English. NNT: 2022UPASP061 . tel-03990400

HAL Id: tel-03990400

<https://theses.hal.science/tel-03990400v1>

Submitted on 15 Feb 2023

HAL is a multi-disciplinary open access archive for the deposit and dissemination of scientific research documents, whether they are published or not. The documents may come from teaching and research institutions in France or abroad, or from public or private research centers.

L'archive ouverte pluridisciplinaire **HAL**, est destinée au dépôt et à la diffusion de documents scientifiques de niveau recherche, publiés ou non, émanant des établissements d'enseignement et de recherche français ou étrangers, des laboratoires publics ou privés.

Novel nanosecond and millielectronvolt
spectroscopies in the electron microscope
and their applications to nano-optics
*Nouvelles spectroscopies nanosecondes et milliélectronvolts
au microscope électronique et leurs applications à la
nano-optique*

Thèse de doctorat de l'Université Paris-Saclay

École doctorale n° 572 : ondes et matière (EDOM)

Spécialité de doctorat : Physique

Graduate School : Physique, Référent : Faculté des sciences d'Orsay

Thèse préparée dans l'unité de recherche LPS Laboratoire de Physique des Solides (Université Paris-Saclay, CNRS), sous la direction de **Mathieu KOCIAK**, directeur de recherche et la co-direction de **Luiz TIZEI**, chargé de recherche.

Thèse soutenue à Paris-Saclay, le 1 juillet 2022, par

Yves AUAD

Composition du jury

Emmanuelle DELEPORTE

Professeure des Universités, École normale supérieure Paris-Saclay, France

Présidente

Pieter KRUIT

Professeur des Universités, Delft University of Technology, The Netherlands

Rapporteur & Examineur

Yannick DUMEIGE

Professeur des Universités, Université Rennes-I, France

Rapporteur & Examineur

Jo VERBEECK

Professeur des Universités, University of Antwerp, Belgium

Examineur

Mathieu KOCIAK

Directeur de recherche, Centre national de la recherche scientifique (CNRS), France

Directeur de thèse

Acknowledgements

To begin with, I would like to thank Mathieu and Luiz, my research advisor and co-advisor, for their support, care, and invaluable feedback during the three years of my thesis. To them, I express my most profound appreciation for helping me pave my scientific career, a dream of mine that has finally begun. I would also like to thank Marcel, responsible for sparking much of my desire and love to work with scientific instrumentation. I cannot thank you three enough.

I would also like to thank my thesis jury: Emmanuelle Deleporte, Pieter Kruit, Yannick Dumeige, and Jo Verbeeck. They have helped to create this unique moment in a Ph.D. student's life, with many exciting and positive critiques of my work.

I am also grateful to the entire STEM group, of whom I have spent a good bunch of my time during my thesis — meeting many people, having uncountable discussions, telling jokes, and sharing good food and coffee. I would like to give a special thanks to Jean-Dennis and Xiaoyan for enabling all the STEM group experiments to happen, including mine, by maintaining the microscopes alive. I also gratefully acknowledge the assistance of the laboratory staff, always ready to help the students.

I want to thank all my friends, the many I made while living in Brazil, and the new ones I made on my journey abroad. I am also very grateful to my partner Rachel for the support and care throughout these years. Finally, I would like to thank all the supportive members of my family, with special thanks to my brother and his spouse, Yan and Manuela, my mother Sonia, and my father, Reynaldo.

Résumé

Dans cette thèse, j'ai exploré un ensemble d'interactions entre électron, matière, et lumière dans un microscope électronique en transmission à balayage (STEM, *scanning transmission electron microscope*). J'ai ainsi combiné des spectroscopies électroniques traditionnelles, telles que la spectroscopie de perte d'énergie d'électrons (EELS, *electron energy-loss spectroscopy*) et la cathodoluminescence (CL) avec de nouvelles techniques, telles que la spectroscopie de gain d'énergie d'électrons (EEGS, *electron energy-gain spectroscopy*) et la spectroscopie d'excitation de cathodoluminescence (CLE, *cathodoluminescence excitation spectroscopy*). Mon travail a consisté à une contribution importante au développement de ces deux dernières spectroscopies. En particulier, l'étude de résonances à bande étroite d'un micro-résonateur à modes de galerie (WGMR, *whispering-gallery mode resonators*) optique a motivé le développement de l'EEGS. Il s'agit d'une technique prometteuse qui pourrait combiner la résolution spectrale des sources laser avec la résolution spatiale des microscopes électroniques modernes. En outre, l'échelle des temps de vie des résonances, de l'ordre de la nanoseconde, a déclenché le développement de l'instrumentation de déflecteurs et de détecteurs rapides à résolution temporelle, tels que la Timepix3 (TPX3).

La microscopie électronique en champ proche induite par des photons (PINEM, *photon-induced near-field electron microscopy*) est une technique actuellement bien établie, utilisée dans les microscopes électroniques ultrarapides (UEMs, *ultra-fast electron microscopes*). La PINEM permet d'observer l'interaction des électrons et des photons lorsqu'un échantillon est exposé à un champ optique intense. Dans les microscopes à canon à électrons continus, l'EEGS est plus facilement réalisé en utilisant un laser pulsé ainsi qu'un déflecteur de faisceau à résolution temporelle, qui permet de synchroniser l'impulsion laser et les électrons détectés. La résolution temporelle de l'impulsion laser et du déflecteur étant de l'ordre de la nanoseconde, l'EEGS est observée dans le spectre EELS par une ou plusieurs résonances à gauche du pic de perte nulle (ZLP, *zero-loss peak*). Celles-ci sont associées à un gain d'énergie de l'électron détecté. Contrairement aux microscopes électroniques

pulsés utilisant des sources laser femtosecondes, dans lesquels des centaines de résonances de gain d'énergie peuvent être observées en même temps, les expériences de EEGS dans un microscope à canon à électrons continu peuvent être très difficiles, notamment en raison de l'importance et de la difficulté de l'alignement du système d'injection de lumière. Dans le premier chapitre, j'ai essayé de faire de l'EEGS une technique spectroscopique de routine dans les microscopes électroniques disponibles, similaire au EELS et à la CL. Pour cela, nous avons réalisé l'importance de contrôler le microscope électronique pour développer et essayer de nouvelles idées, ce qui a été fait efficacement dans un microscope VG HB501¹. Le contrôle des éléments du microscope, c'est-à-dire l'unité de balayage, les détecteurs, les lentilles magnétiques, les diafragmes, la platine de déplacement de l'échantillon, etc. a été écrit en Python3 et contrôlé graphiquement par l'utilisateur à l'aide du logiciel d'imagerie Nionswift. Ce contrôle a permis de développer une procédure d'alignement laser par fibre, dans laquelle le spot lumineux est centré à moins de $< 1 \mu\text{m}$ de l'axe optique du microscope. L'expérience a été transférée avec succès sur ChromaTEM, un microscope qui peut atteindre une résolution spectrale de $\sim 5 \text{ meV}$, et dans lequel des expériences préliminaires de EEGS ont été démontrées dans ce travail. Malheureusement, la longue fibre optique monomode utilisée a induit de forts processus de diffusion Raman stimulée, ce qui a nuit à des mesures spectroscopiques plus significatives. Afin d'explorer d'autres options d'expériences EEGS dans un canon à électrons continu, des mesures sans le déflecteur, utilisant uniquement le monochromateur d'électrons, ont été démontrées pour des sources lumineuses picosecondes, qui présentent un potentiel pour de futures applications spectroscopiques résolues dans le temps. De plus, l'expérience est également démontrée en n'utilisant ni le monochromateur d'électrons ni le déflecteur de faisceau, mais plutôt une nouvelle génération de détecteurs à résolution temporelle et basée sur les événements, appelée Timepix3.

Les micro-résonateurs qui ont motivé le développement initial du EEGS sont examinés dans le chapitre 02. En raison de la symétrie sphérique des WGMR, le couplage de la lumière à partir du champ lointain peut être difficile, et plusieurs mesures ont donc été effectuées en utilisant uniquement l'EELS et la CL sur le ChromaTEM. Des résonateurs de 1.5 à $2.0 \mu\text{m}$ de rayon ont présenté plus de 80 modes de Mie, avec des facteurs de qualité allant jusqu'à 200, entre 1.5 eV et 7.0 eV grâce au degré remarquable de monochromaticité du faisceau d'électrons. Pour étudier ces modes à l'aide de l'EEGS, une nanoparticule métallique est placée au bord du résonateur, ce qui pourrait interfacer le champ lointain et les modes de galerie. Les mesures d'EELS et de CL dans le système couplé ont révélé que le couplage faible entre le système se produit dans les modes qui ont un moment dipolaire net plus élevé, tels que les modes dipolaires et de coin distal du cube. En étudiant les variations spatiales du signal associé au mode dipolaire, on a également observé que la polarisation du mode galerie excitée suit le moment dipolaire net induit par la sonde électronique, ce qui présente un potentiel d'application

¹Fabriqués par l'entreprise Vacuum Generators.

dans la détection optique et la manipulation de la lumière. Les micro-résonateurs sphériques plus grands de $\sim 4 \mu\text{m}$ de rayon n'ont pas pu être étudiés par EELS et CL en raison de la résolution énergétique limitée du faisceau d'électrons. Dans ce cas, l'EELS a été utilisée pour dévoiler d'autres informations spectrales de l'échantillon, notamment le intervalle spectral libre de $\sim 34 \text{ meV}$, qui était impossible à résoudre dans les spectres EELS. Les facteurs de qualité mesurés dans l'EELS étaient de ~ 120 , incompatibles avec la théorie de Mie et signifiant ainsi que la nanoparticule métallique limite le facteur de qualité atteignable. Enfin, des cristaux à bande interdite photonique ont également été étudiés. Bien que des défauts ponctuels à très haut Q n'aient pas été observés, un défaut unique (trou manquant) dans la structure périodique diélectrique a été détecté et cartographié spatialement avec une résolution spectrale de 15 meV , ce qui ouvre la voie à de futures études sur de tels dispositifs.

Le TPX3 est le premier détecteur direct d'électrons basé sur les événements disponible commercialement. Au-delà de la résolution temporelle de l'ordre de la nanoseconde, le TPX3 offre également une lecture pratiquement sans bruit grâce au système de seuil à pixel unique et une fonction d'étalement du point améliorée grâce à sa détection directe des électrons. Ces propriétés remarquables ont déclenché le développement de ce que nous avons appelé l'EELS hyperspectral basé sur l'événement (event-based EELS), dans lequel les ensembles de données 3D, contenant 2 coordonnées spatiales et 1 coordonnée spectrale, sont reconstruits électron par électron aussi rapidement que le temps du pixel de l'unité de balayage. Ceci est différent des acquisitions hyperspectrales plus traditionnelles basées sur des frames, dans lesquelles le temps de balayage de la position de la sonde électronique est limité par le temps de lecture de la caméra, généralement une caméra CCD (*charged-coupled device*) ou CMOS (*Complementary metal-oxide-semiconductor*). J'ai développé un logiciel d'acquisition en Rust avec les performances nécessaires pour effectuer le traitement des données en direct. Naturellement, des bibliothèques de post-traitement ont également été développées pour étendre les fonctionnalités du détecteur au-delà de l'acquisition en direct. Grâce à celles-ci, le event-based EELS hyperspectral a été démontrée dans la décomposition de la calcite (CaCO_3) en oxyde de calcium (CaO) et en dioxyde de carbone (CO_2), déclenché par l'irradiation électronique. Des données hyperspectrales à résolution temporelle arbitraire ont été démontrées, tant que l'intervalle de la tranche de temps est un multiple du temps d'une seule acquisition de frame. La structure fine des plasmons de la calcite est mesurée dans le temps, ce qui permet de suivre sa transformation en oxyde de calcium. Les spectres de perte *core-loss* montrent le fractionnement du champ cristallin du bord L du calcium et, en outre, le signal du bord K du carbone disparaît avec le temps, conséquence de la forme gazeuse du sous-produit CO_2 . Grâce à ce travail, nous pensons que les données EELS hyperspectrales résolues à l'échelle de la nanoseconde vont être de plus en plus disponibles, en particulier dans les échantillons sensibles, où l'irradiation électronique modifie les propriétés de l'échantillon.

La résolution temporelle nanoseconde de la TPX3 a également déclenché le développement d'une nouvelle technique spectroscopique à l'intérieur d'un microscope électronique à transmission, appelée CLE de par son analogie avec la spectroscopie d'excitation de photoluminescence (PLE, photoluminescence excitation spectroscopy). Dans la PLE, la longueur d'onde d'excitation d'une source laser est balayée tandis que l'émission de photons dans une fenêtre d'énergie sélectionnée est collectée, ce qui permet d'étudier le processus d'absorption dépendant de la longueur d'onde et donc de dévoiler les voies de décroissance de l'émission de photons à partir de l'énergie d'émission souhaitée. Cependant, étant limitée par la diffraction, la méthode PLE ne convient pas aux études à l'échelle nanométrique. Jusqu'à présent, la CLE n'a pas été réalisée dans un STEM car les électrons rapides excitent une large gamme d'énergie. Pour l'EELS, il s'agit d'une propriété généralement souhaitée, car le spectre d'absorption peut être étudié depuis des dizaines de meV jusqu'aux rayons X mous. Cependant, comment relier les spectres d'émission, s'il y en a, en CL avec l'électron détecté? En d'autres termes, comment savoir quels électrons, et leur énergie correspondante, ont déclenché l'émission d'un photon? C'est précisément ce que peut faire CLE. À ce titre, la STEM-CLE peut être considérée comme une contrepartie à l'échelle nanométrique de la PLE. Dans ce contexte, la CLE a été utilisée pour étudier les processus d'émission de photons émis en phase par rapport à la source d'excitation, comme le rayonnement de transition et les plasmons de surface, dans des nanosphères d'or à coquille de silice, ainsi que les processus d'émission de photons sans relation de phase, comme les défauts dans les échantillons de semi-conducteurs. Dans ce dernier cas, des flakes de h-BN et leur émission de défauts à 4.3 eV ont été étudiées. Il a été démontré que les plasmons de volume sont responsables de la plupart des photons émis. De plus, l'efficacité quantique relative dépendante de l'énergie augmente linéairement après la bande interdite du h-BN jusqu'à la gamme d'énergie des rayons X mous, ce qui suggère que les électrons uniques créent des paires électrons-trous multiples, qui peuvent ainsi se recombiner radiativement.

Resumo

Nesta tese, uma miríade de interações elétron/matéria/luz foram exploradas em um microscópio eletrônico de varredura por transmissão (STEM, do inglês *scanning transmission electron microscope*) com uma combinação de técnicas tradicionais de espectroscopia de elétrons, tais como a espectroscopia de perda de energia de elétrons (EELS, do inglês *electron energy-loss spectroscopy*) e cathodoluminescência (CL), com técnicas inovadoras, tais como a espectroscopia de ganho de energia de elétrons (EEGS, do inglês *electron energy-gain spectroscopy*) e espectroscopia de excitação de elétrons (CLE, do inglês *cathodoluminescence excitation spectroscopy*), nas quais este trabalho contribuiu para desenvolvê-las. Em particular, as ressonâncias de banda estreita de um micro-ressonador óptico motivaram o desenvolvimento da implementação de um sistema automatizado de aquisição EEGS, uma técnica promissora que visa combinar a resolução espectral de fontes laser com a resolução espacial de microscópios eletrônicos modernos. Além disso, a escala de tempo das ressonâncias desejadas, na faixa de nanosegundos, desencadeou o desenvolvimento de instrumentação de defletores e detectores rápidos com resolução temporal, como a Timepix3 (TPX3).

A microscopia eletrônica de campo próximo induzida por fótons (PINEM, do inglês *photon-induced near-field electron microscopy*) é uma técnica atualmente bem estabelecida utilizada em microscópios eletrônicos ultra-rápidos (UEMs, do inglês *ultra-fast electron microscopes*). PINEM é capaz de observar a interação de elétrons e fótons ao irradiar uma amostra com uma intensa luz laser. Nos microscópios de canhão de elétrons contínuos, o EEGS é mais facilmente realizado usando um feixe de laser pulsado juntamente com um deflector rápido de elétrons resolvido no tempo, o qual permite sincronizar o pulso do laser e os elétrons detectados. Como o pulso laser e a resolução temporal do deflector estão na escala de tempo do nanosegundo, o EEGS é observado no espectro EELS por uma ou poucas ressonâncias à esquerda do pico de perda de energia nula (ZLP, do inglês *zero-loss peak*), associado a um ganho de energia do elétron detectado. Diferente dos microscópios de elétrons pulsados que utilizam fontes laser com pulsos na or-

dem de femtosegundos, nos quais centenas de ressonâncias de ganho de energia podem ser observadas simultaneamente, as experiências com um microscópio de canhão de elétrons contínuo podem ser muito desafiadoras, especialmente devido à dificuldade e à importância do alinhamento do sistema de injeção de luz. No primeiro capítulo, tentei estabelecer o EEGS como uma técnica espectroscópica de rotina nos microscópios eletrônicos disponíveis, semelhante ao que já acontece com o EELS e a CL. Para isto, percebemos a importância de controlar integralmente o microscópio eletrônico para desenvolver e experimentar novas ideias, o que foi efetivamente feito em um antigo microscópio VG² HB501. O controle dos elementos do microscópio, ou seja, a unidade de varredura, os detectores, as lentes magnéticas, os diafragmas, o estágio de movimentação da amostra, *etc* foi programado em Python3 e controlado pelo usuário graficamente a partir do software Nionswift. Este controle permitiu o desenvolvimento de um procedimento de alinhamento do sistema de injeção de luz, no qual utiliza uma fibra ótica, em que o feixe central é alinhado a menos de $< 1 \mu\text{m}$ do eixo óptico do microscópio. O experimento foi transferido com sucesso para o ChromaTEM, um microscópio que pode alcançar resolução espectral de $\sim 5 \text{ meV}$, e no qual experimentos preliminares de EEGS foram demonstrados neste trabalho. Infelizmente, as longas fibras óticas mono-modo utilizadas induziram processos de espalhamento Raman estimulado, o que prejudicou as medições espectroscópicas mais significativas. Para explorar mais opções de experimentos de EEGS em um canhão de elétrons contínuo, foram demonstradas medições sem o deflector do feixe usando o monocromador de elétrons para fontes de luz picosegundo, que possuem potencial para futuras aplicações espectroscópicas resolvidas no tempo. Além disso, o experimento também foi demonstrado sem usar nem o monocromador nem o deflector de elétrons, mas sim uma nova geração de detectores baseada na detecção de eventos individuais de elétrons e resolvida no tempo chamada Timepix3.

Os micro-ressonadores que motivaram o desenvolvimento inicial do EEGS são examinados no capítulo 02. Devido à simetria esférica dos micro-ressonadores ópticos, o acoplamento de luz a partir do campo distante pode ser um desafio, e assim várias medições foram realizadas usando apenas o EELS e a CL no ChromaTEM. Ressonadores de $1.5\text{-}2.0 \mu\text{m}$ de raio exibiram mais de 80 modos de Mie, com fatores de qualidade de até 200, entre 1.5 eV e 7.0 eV graças ao notável grau de monocromaticidade do feixe de elétrons. Para estudar estes modos usando o EEGS, uma nanopartícula metálica é colocada na borda do ressonador, usada para interfacear o campo distante e os modos de galeria dos micro-ressonadores. As medições no sistema revelaram que existe um acoplamento fraco entre a nanopartícula metálica e o ressonador nos modos que têm um momento de dipolo resultante significativo, como no modo dipolar e o modo de canto distal do cubo. Ao estudar o modo dipolar espacialmente, também foi observado que a polarização excitada do modo de galeria segue o momento dipolo da rede induzido pela sonda de elétrons, o que sugere um potencial para aplicações em sensoriamento óptico e para a manipu-

²Produzido pela empresa *Vacuum Generators*.

lação da luz. Micro-ressonadores esféricos maiores de $\sim 4 \mu\text{m}$ de raio não puderam ser estudados por EELS e CL devido à resolução limitada de energia do feixe de elétrons. Neste caso, o EEGS foi usado para revelar mais informações espectrais da amostra, especialmente a distância espectral entre ressonâncias consecutivas de $\sim 34 \text{ meV}$, muito difícil de resolver nos espectros do EELS. Os fatores de qualidade medidos em EEGS foram de ~ 120 , incompatíveis com a teoria de Mie e, portanto, sugerindo que o baixo fator de qualidade das nanopartículas metálicas está limitando o fator de qualidade do sistema acoplado. Finalmente, cristais fotônicos também foram estudados. Embora defeitos pontuais com ultra-alto fator de qualidade não tenham sido observados, um defeito único na estrutura dielétrica periódica foi detectado e mapeado espacialmente com resolução espectral de $\sim 15 \text{ meV}$, o que abre o caminho para futuros estudos em tais dispositivos.

O TPX3 é o primeiro detector direto de elétrons baseado na detecção de eventos individuais disponível comercialmente. Além da resolução temporal na faixa de nanosegundos, o TPX3 também oferece uma leitura praticamente sem ruído devido ao sistema de *threshold* e de uma melhor função de espalhamento pontual (PSF, do inglês *point-spread function*) graças a sua detecção direta de elétrons. Estas características impressionantes desencadearam o desenvolvimento do que chamamos de reconstrução hiperspectral do EELS baseada em eventos, no qual conjuntos de dados 3D, contendo 2 coordenadas espaciais e 1 coordenada espectral, são reconstruídos elétron por elétron tão rapidamente quanto o tempo do pixel da unidade de varredura. Isto é diferente das mais tradicionais aquisições hiperspectrais baseadas em imagens, nas quais o tempo de varredura da posição da sonda de elétrons é limitado pelo tempo de leitura da câmera, geralmente uma CCD (do inglês *charged-coupled device*) ou de uma CMOS (do inglês *Complementary metal-oxide-semiconductor*). Eu desenvolvi um software de aquisição em Rust com a performance necessária para realizar o tratamento de dados ao vivo, no qual, naturalmente, bibliotecas de pós-processamento também foram programadas para estender as funcionalidades do detector para além da aquisição ao vivo. Com isso, o EELS hiperspectral foi demonstrado ao estudar a decomposição da calcita (CaCO_3) em óxido de cálcio (CaO) e dióxido de carbono (CO_2), reação causada pela exposição do material ao feixe de elétrons. Foram demonstrados dados hiperspectrais resolvidos no tempo arbitrariamente, desde que o intervalo de tempo da amostragem temporal seja um múltiplo do tempo de uma única varredura completa do feixe de elétrons na região de interesse. A estrutura fina do plásmom de volume da calcita é medida ao longo do tempo, o que permite acompanhar sua transformação em óxido de cálcio. Os espectros de EELS na faixa de energia do *core-loss* mostram a divisão do campo do cristal da borda L de cálcio e, adicionalmente, o sinal da borda K de carbono desaparece com o tempo, uma consequência do estado gasoso do subproduto CO_2 . Com este trabalho, esperamos que os dados de EELS hiperspectral resolvidos em nanosegundos estejam cada vez mais disponíveis, especialmente importantes em amostras sensíveis à irradiação ao feixe de elétrons.

A resolução temporal de nanosegundos da Timepix3 também permitiu o desenvolvimento de uma nova técnica espectroscópica dentro de um microscópio eletrônico de transmissão, chamado CLE graças à sua analogia com a espectroscopia de excitação com fótons (PLE, do inglês *photoluminescence excitation spectroscopy*). Na PLE, o comprimento de onda de excitação de uma fonte laser é escaneado enquanto a emissão de fótons em uma janela de energia selecionada é coletada, o que permite estudar o processo de absorção dependente do comprimento de onda de excitação e, portanto, revela as vias de decaimento da emissão de fótons. Entretanto, por ser limitada pela difração, a PLE não é adequada para estudos na nano escala. Até agora, a CLE não foi realizada em um microscópio eletrônico de varredura por transmissão porque os elétrons rápidos excitam uma faixa larga de energia. Para EELS, esta é uma propriedade geralmente desejada, pois o espectro de absorção pode ser estudado desde dezenas de meV até os raios-X moles. No entanto, como relacionar os fótons nos espectros de emissão, se houver, com o elétron excitante? Em outras palavras, como saber quais elétrons, e suas energias correspondentes, desencadearam a emissão de um fóton? Isto é precisamente o que o CLE pode fazer. A STEM-CLE, por esse motivo, provou ser uma contraparte em escala nanométrica da PLE. Neste contexto, a CLE foi usada para estudar os processos de emissão de fótons em fase com relação a fonte de elétrons excitante, como a radiação de transição e os plásmons de superfície localizados, em nano esferas de ouro envoltas por uma camada de óxido de silício, bem como os processos de emissão de fótons sem relação de fase, como defeitos em amostras semicondutoras. Para estes últimos, foram estudados *flakes* finos de nitreto de boro hexagonal (h -BN) e sua emissão de defeitos 4.3 eV. Foi demonstrado que os plásmons de volume são o caminho de decaimento responsáveis pela maioria dos fótons emitidos. Além disso, a eficiência quântica relativa dependente da energia do elétrons aumenta linearmente após o bandgap h -BN bandgap até a faixa de energia dos raios X moles, sugerindo que os elétrons criam múltiplos pares elétrons-buraco, que podem assim decair de forma radiativa.

Summary

In this thesis, a myriad of electron/matter/light interactions have been explored in a scanning transmission electron microscope (STEM) combining traditional electron spectroscopies, such as electron energy-loss spectroscopy (EELS) and cathodoluminescence (CL) with novel techniques, such as electron energy-gain spectroscopy (EEGS) and cathodoluminescence excitation spectroscopy (CLE), in which this work has contributed to developing. In particular, the narrow-band resonances of an optical whispering-gallery mode resonator (WGMR) have motivated the development of EEGS, a promising technique that could combine the spectral resolution of laser sources with the spatial resolution of modern electron microscopes. Besides, the time-scale of the desired resonances, in the nanosecond range, has triggered instrumentation developments of time-resolved fast deflectors and detectors, such as Timepix3 (TPX3).

Photon-induced near-field electron microscopy (PINEM) is a currently well-established technique used in ultrafast electron microscopes (UEMs). PINEM is capable of observing the interaction of electrons and photons upon shining a sample with an intense optical field. In continuous electron gun microscopes, EEGS is most easily performed by using a pulsed laser along with a time-resolved beam blanker, which allows synchronizing the laser pulse and the detected electrons. Because the laser pulse and the blanker temporal resolution are in the nanosecond time scale, EEGS is observed in the EELS spectrum by one or few resonances at the left of the zero-loss peak (ZLP), associated with an energy-gain of the incoming electron. Different from pulsed electron microscopes employing femtosecond laser sources, in which hundreds of energy-gain resonances can be observed at once, EEGS experiments in a continuous electron gun microscope can be very challenging, especially due to the importance and difficulty of the light injection system alignment. In the first chapter, I have tried to place EEGS as a routine spectroscopic technique in the available electron microscopes, similar to EELS and CL. For this, we have realized the importance of controlling the electron micro-

scope to develop and try new ideas, which was effectively done in a 40-year-old Vacuum Generators (VG) HB501 microscope. The control of the microscope elements, i.e. the scanning unit, the detectors, the magnetic lenses, the apertures, the stage, *etc* was written in Python3 within the Nionswift imaging software. This control has allowed the development of a fiber-based laser alignment procedure, in which the light spot is centered within $< 1 \mu\text{m}$ from the microscope optical axis. The experiment has been successfully transferred to ChromaTEM, a microscope that can achieve $\sim 5 \text{ meV}$ spectral resolution, and in which preliminary EEGS experiments were demonstrated in this work. Unfortunately, the long single-mode optical fiber used induced strong stimulated Raman scattering processes, which have undermined more meaningful spectroscopic measurements. To explore further options of EEGS experiments in a continuous electron gun, measurements without the beam blanker using the electron monochromator have been demonstrated for picosecond light sources, which hold potential for future time-resolved spectroscopic applications. Further, the experiment is also demonstrated using neither an electron monochromator nor a beam blanker, but rather a new generation of event-based and time-resolved hybrid-pixel detector (HPD) called TPX3.

The microresonators that have motivated the initial development of EEGS are scrutinized in chapter 02. Due to the spherical symmetry of WGMR, the far-field light coupling can be challenging, and thus several measurements were performed using only EELS and CL at ChromaTEM. Bare resonators of $1.5\text{-}2.0 \mu\text{m}$ radius have displayed more than 80 Mie modes, with quality factors up to 200, between 1.5 eV and 7.0 eV thanks to the remarkable degree of monochromaticity of the electron beam. To study these modes using EEGS, a metallic nanoparticle (MNP) is placed at the edge of the resonator, which could interface the far-field and the bounded modes of the WGMR. EELS and CL measurements in the coupled system have revealed that the weak-coupling between the MNP-WGMR system happens in the modes that have a higher net-dipole moment, such as the dipolar and the cube distal corner modes. By studying the dipolar mode spatially, it was also observed that the excited gallery-mode polarization follows the net dipole moment induced by the electron probe, which holds potential for application in optical sensing and light manipulation. Larger spherical microresonators of $\sim 4 \mu\text{m}$ radius could not be studied by EELS and CL because of the limited energy resolution of the electron beam. In this case, EEGS has been used to unveil further spectral information of the sample, especially the $\sim 34 \text{ meV}$ free spectral range, which was impossible to resolve in the convoluted EELS spectra. The measured quality factors in EEGS was ~ 120 , incompatible with the Mie theory and thus meaning that the lossy MNP is limiting the attainable quality factor. Finally, photonic bandgap crystals have also been studied. Although ultrahigh-Q point defects have not been observed, a single missing hole defect in the periodic dielectric structure has been detected and spatially mapped with $\sim 15 \text{ meV}$ spectral resolution, which paves the way for future studies in such devices.

The TPX3 is the first commercially available event-based direct electron detector. Beyond the temporal resolution in the nanosecond range, TPX3 also offers a practically noiseless readout due to the single-pixel threshold system and an improved point-spread function thanks to its direct electron detection. These remarkable properties have triggered the development of what we have called event-based hyperspectral EELS, in which 3D datasets, containing 2 spatial coordinates and 1 spectral coordinate, are reconstructed electron-by-electron as fast as the scanning unit dwell time. This is different from the more traditional frame-based hyperspectral acquisitions, in which the electron probe position scanning time is limited by the readout time of the camera, usually a charged-coupled device (CCD) or a complementary metal–oxide–semiconductor (CMOS). I have developed an acquisition software in Rust with the necessary performance to perform live data treatment, in which, naturally, post-processing libraries have also been developed to extend the detector functionalities beyond live acquisition. With these, the hyperspectral EELS has been demonstrated in the decomposition of calcite (CaCO_3) into calcium oxide (CaO) and carbon dioxide (CO_2), which is caused by the electron irradiation. Arbitrary time-resolved hyperspectral data has been demonstrated, as long as the time slice interval is a multiple of the time of a single annular dark-field (ADF) frame acquisition. The calcite bulk plasmon fine structure is measured over time, which allows to track its transformation into calcium oxide. The core-loss spectra show the crystal-field splitting of the calcium L edge, and, additionally, the carbon K edge signal vanishes over time, a consequence of the gaseous form of the sub-product CO_2 . With this work, we expect that nanosecond-resolved hyperspectral EELS data are going to be more and more available, especially in sensitive samples, where electron irradiation modifies the sample properties.

The nanosecond temporal resolution of TPX3 has also triggered the development of a novel spectroscopic technique inside a transmission electron microscope, called CLE thanks to its analogy with photoluminescence excitation spectroscopy (PLE). In PLE, the excitation wavelength of a laser source is rastered while the photon emission in a selected energy window is collected, which allows to study of the wavelength-dependent absorption process and hence unveils the photon emission decay pathways from the desired emission energy. However, being diffraction-limited, PLE is not suitable for studies in the nanoscale range. Up until now, CLE has not been performed in a STEM because fast electrons excite a broadband energy range. For EELS, this is a generally desired property, as the absorption spectrum can be studied from tens of meV up to the soft X-rays. However, how to relate the emission spectra, if any, in CL with the incoming electron? In other words, how to know which electrons, and their corresponding energy, have triggered a photon emission? This is precisely what CLE can do. STEM-CLE, on that account, has proven to be a nanometer-scale counterpart of PLE. In this context, CLE has been used to study the photon emission processes phase-locked relative to the exciting source, such as transition radiation and surface plasmons,

in silica-shelled gold nanospheres, as well as non-phase-locked photon emission processes, such as defects in semiconductor samples. For the latter, thin h -BN flakes and their 4.3 eV defect emission has been studied. It is shown that the bulk plasmons are responsible for most of the emitted photons. Additionally, the energy-dependent relative quantum efficiency is shown to linearly increase after the h -BN bandgap up to the soft X-rays energy range, suggesting that single electrons create multiple electrons-hole pairs, which can thus decay radiatively.

Contents

Introduction	18
1 Concepts and mathematical Tools	23
1.1 Introduction	23
1.2 Foundations of Nano Optics	23
1.2.1 Maxwell's equations and Green's functions	23
1.2.2 The classical dipole radiation	29
1.2.3 The basics of Quantum Electrodynamics	33
1.3 Scanning Transmission Electron Microscope	39
1.3.1 Electron sources	41
1.3.2 The basics of electron optics	43
1.4 Electron Spectroscopy	45
1.4.1 Electron Energy Loss Spectroscopy	45
1.4.2 Cathodoluminescence	47
1.4.3 Electron Energy Gain Spectroscopy	48
1.5 The microscopes	50
1.6 Numerical Methods	52
2 EEGS with a monochromated and continuous electron beam	54
2.1 Introduction	54
2.2 Instrumental developments	60
2.2.1 Controlling the electron microscope	61
2.2.2 EEGS experiment	62
2.3 Methods and results	67
2.3.1 Alignment	67
2.3.2 Preliminary experiments	68
2.3.3 Gain without the fast blanker	74
2.4 Conclusions & prospects	78

3	Optical microcavities & electron beams	81
3.1	Introduction	81
3.1.1	Whispering-gallery mode resonators	85
3.1.2	Whispering-gallery mode resonators & metallic nanoparticles	88
3.1.3	Photonic crystals	89
3.2	Results	91
3.2.1	Bare microspheres	91
3.2.2	Coupled microspheres	93
3.2.3	Photonic bandgap crystals	102
3.3	Conclusions & prospects	104
4	Event-based EELS: developments & applications in the nanosecond scale	106
4.1	Introduction	106
4.1.1	The Timepix3 and the CheeTah solution	108
4.2	Event-based hyperspectral EELS implementation	111
4.3	The calcite decomposition	115
4.3.1	Cluster correction	116
4.3.2	Results & discussion	118
4.4	Conclusions & prospects	120
5	Cathodoluminescence excitation spectroscopy	122
5.1	Introduction	122
5.1.1	Light emission mechanisms	124
5.1.2	Correlation algorithm	126
5.2	Results & Discussion	127
5.3	Conclusions & prospects	133
6	General conclusions & prospects	135
7	Appendix	138
7.1	Concepts and Mathematical Tools	138
7.2	EEGS in monochromated continuous electron gun	145
7.3	Optical microcavities & electron beams	148
7.4	Event-based EELS: developments & applications in the nanosecond scale	153
	Bibliography	158
	List of publications	180
	Glossary	182

Introduction

From the colored stained glass in old churches and cathedrals to modern television screens, nano-optics, or nanophotonics, is ubiquitous. The number of different ways to study the light-matter interaction in the nanoscale is way too large to be discussed here. One of them, however, is the core of this thesis: the electron microscope. The fast electrons, traveling at approximately 55% of the speed of light for a typical acceleration voltage of 100 keV, focused in a sub-nanometric beam are capable of probing the optical properties of materials at the nanoscale range, placing electron microscopes as one of the most thriving instruments for nano-optics.

In this work, confined optical modes and electron/matter/light interaction have been explored in a scanning transmission electron microscope (STEM), thanks to a variety of novel spatially resolved spectroscopies, some of which this work has contributed to developing. In particular, optical cavities with long-lived excitations and sharp linewidths were studied, which led to contributions to the development of electron energy-gain spectroscopy (EEGS), a promising technique combining the spectral resolution of modern laser sources with the spatial resolution of electron microscopes. Besides, the time-scale of the desired resonances, in the nanosecond range, has triggered instrumentation developments of time-resolved fast deflectors and detectors, as shall be seen later below. As expected, these developments were used along with more traditional spectroscopies in a STEM, such as electron energy-loss spectroscopy (EELS) and cathodoluminescence (CL) (schematized in Figure 1), all of them spatially resolved at the nanoscale range.

The idea of reversing the process of energy loss upon using an external light field has its first appearance in a small paragraph of a seminar given by Archie Howie [1, 2] and it is the main subject of **chapter 01**. In 2008, the feasibility of this technique, baptized as EEGS, was studied in depth [3]. In 2009, the first measurement was performed by Barwick *et. al* [4] in the context of ultrafast electron microscopy. This has triggered a variety of works [5–7], all of them using pulsed electron guns, until the work of Das *et. al* [8] in 2019, in which the

the first continuous-gun EEGS measurement was performed. The motivation to perform EEGS with a continuous electron gun is that nanosecond laser sources can be used, differently from the typical femtosecond laser sources in ultrafast electron microscopy, and hence, by Heisenberg's uncertainty principle, narrower laser linewidth can be obtained ($\sim 1 \mu\text{eV}$ in nanosecond sources against $\sim 10 \text{ meV}$ in picosecond sources). Additionally, performing EEGS with a continuous electron gun allows using the higher-brightness cold field-emission gun (cFEG) instead of the usual thermionic gun in pulsed microscopes and, consequently, to explore all the recent technologies in modern STEMs, such as aberration correctors and electron monochromators. Finally, as the synchronization is done by modifying the detection scheme instead of the electron gun, switching between EEGS to more conventional microscopy techniques (i.e. EELS, CL, diffraction *etc*) is trivial, which could provide supplementary information from the sample. With this, one of the main goals of this thesis can be stated: to perform EEGS in the ChromaTEM microscope, an ultrahigh energy-resolved STEM containing all the aforementioned technologies. This system was first designed to be tested on high quality factors (Q factors) cavities, such as whispering-gallery resonators or photonic bandgap crystals. Alternatively, a more complete study of EELS, CL, and EEGS with measurements performed in the same highly-monochromated electron microscope was also aimed, which could experimentally validate many

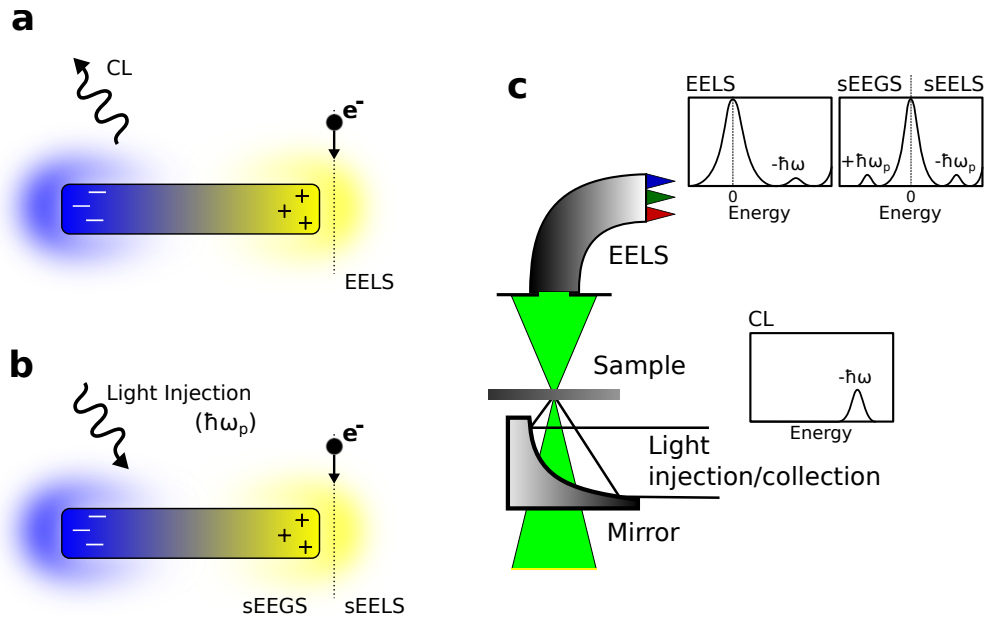


Figure 1: Scheme of the experimental variations performed during this thesis. (a) An incoming electron loses energy (EELS) upon interaction with the sample, which could trigger a photon emission (CL). (b) Upon light injection, the electron can interact with the induced fields and has a probability of being accelerated (EEGS, or energy-gain) or decelerate (sEELS, or energy-loss). (c) The experimental scheme and how the mentioned techniques in (a) and (b) are measured in a scanning transmission electron microscope.

theoretical aspects of these spectroscopies. As shall be seen in the manuscript, the development of such experiments in a demanding machine was a motivation to program from scratch an electron microscope, including the control of the EELS spectrometer, the magnetic lenses, the laser, *etc.* This robust microscope control has allowed the development of a precise alignment procedure that systematizes gain experiments, and a multi-microscope-compatible platform: the instrumental developments were performed in a dedicated machine and the experiment was immediately ready to be performed on ChromaTEM. These two projects, the microscope control and the laser module, are open-source and are available to the community under MIT licensing [9, 10].

The potential three orders of magnitude spectral resolution increase in EEGS with respect to EELS paves the way for studying high Q factor optical devices in an electron microscope, as shall be seen in **chapter 02**. A whispering-gallery mode resonator (WGMR) is a good candidate, as it hosts multiple trapped narrowband circulating optical resonances. Unfortunately, the microscope in which EEGS was performed could only work at a maximum of 100 kV and thus the necessary phase-matching condition could not be achieved. Besides, the spherical symmetry and low field leakage of dielectric microspheres make it difficult to probe their high-quality optical modes using far-field radiation [11, 12], which has prevented performing gain experiments in bare resonators. To circumvent this problem, EEGS was performed in a coupled system of WGMR and a metallic nanoparticle (MNP), in which the latter was used to interface the optical far-field and the bounded cavity modes. In this context, however, it was soon realized that ChromaTEM spectral resolution was able to unveil this coupled system. It is important to mention that similar bare spheres ($> 1 \mu\text{m}$ radius, $Q \sim 50\text{-}100$) have been studied using energy-gain with a pulsed laser, and a few resonant modes have been identified by a chirped light beam [13]. Additionally, Hyun *et. al.* has seen whispering-gallery resonances directly on EELS, although in the far-ultraviolet and in much smaller spheres of ~ 140 nm radius, which limits the achieved Q factor [14]. These works, however, could not resolve a large number of modes. Besides, the bare resonators did not offer much to be spatially explored due to their spherical symmetry. In this work, I studied, using EELS and CL, bare and coupled whispering-gallery resonators. By modifying the electron velocity, one can couple more or less to the gallery resonators due to the phase-matching condition and thus the influence of a sole silver nanocube at the edge of the resonator could be explored. With the remarkable spectral resolution of ChromaTEM, it was also possible to study how each mode of the silver nanocube, usually divided between corner (C), edge (E), and face (F) modes, interacts with the resonator, including the influence of the well-known mode splitting into proximal and distal modes due to a substrate presence [15]. These measurements lead to a publication [16], in which it is expected not only to path future works on high-Q cavities in STEM using EELS and CL but also to contribute to the microresonators community, especially the ones working with sensing, as single-particle identification

using whispering-gallery resonators is a major research field [17, 18].

During the development of EEGS in the Vacuum Generators model HB 501 (VG), an instrumentation-dedicated microscope, Timepix3 (TPX3), a hybrid-pixel detector (HPD), has arrived in the group. It was motivated by the already successful Medipix3, another HPD, in the older generation UltraSTEM microscope, and by the ideas of electron-photon coincidence detection that have been developing among some of the researchers in the laboratory. TPX3 shares all the improvements of Medipix3 for EELS, most notably the reduced point spread function (PSF) from the scintillator layer removal and the practically noiseless readout scheme due to a pixel-wise threshold system. TPX3, however, provides more when compared to Medipix3. It is event-based and thus is capable of discriminating single electron detection with nanosecond temporal resolution, represented by the time of arrival (ToA) and time over threshold (ToT) of the incident electron. The detector solution used is produced by Amsterdam Scientific Instruments (ASI), which also provides two time-to-digital converters (TDCs) as input lines. These allow producing timestamps of TTL-based signals along with the same data flow of electrons, meaning any external signal can be temporally related to the electron events.

The first application of this system, discussed in **chapter 04**, was to create what we have called event-based hyperspectral EELS, in which the scanning unit of the microscope sends periodical signals to the TPX3, every beginning of a new scan line, and a hyperspectral image can be performed at the same speed as standard imaging systems i.e. annular dark-field (ADF) and bright-field (BF) detectors. This is almost a six orders of magnitude speed increase, as single spectra can be reconstructed limited by the pixel time of the scanning unit (~ 40 nanoseconds in the present case) instead of the readout of the detector (typically ~ 1 ms for a charged-coupled device (CCD)). An acquisition software was developed [19] in Rust with the necessary performance to perform live data treatment. Naturally, the library is used to extend the camera functionalities beyond live acquisitions, being able to fast post-process data within more control parameters. The results of this work is already published and can be found in ref. [20].

The second interesting application of TPX3 was the development of cathodoluminescence excitation spectroscopy (CLE) in **chapter 05**, which was inspired by its powerful analog in optics: photoluminescence excitation spectroscopy (PLE). In PLE, the exciting laser wavelength is rastered and the associated emission spectra are collected. With it, the decay pathways from the selected energy range can be unveiled [21]. However, being diffraction-limited, PLE is not suitable for studies in the nanoscale range. One of the interesting properties of EELS is that the fast electron can be seen as a source of “white-light”, and hence the loss spectra contain information from a broadband energy range. In the context of a possible CLE, however, this is a very poor property: how to relate the emission spectra, if any, in CL with the incoming electron? In other words, how to know which electron, and its corresponding energy loss, has triggered a photon emission? This

is precisely what CLE can do. STEM-CLE, on that account, has proven to be a nanometer-scale counterpart of PLE. This work is currently under revision and its preprint version can be found in ref. [22].

Concepts and mathematical Tools

1.1 Introduction

The spectroscopic techniques used in this thesis are extensively documented in the literature. Instead of mathematically proving these, it was rather chosen to try to give a more intuitive sense to them by using fundamental electrodynamics concepts. It will be seen, for example, that electron energy-loss spectroscopy (EELS) has a very well-known relation with the Green's tensor. This physical quantity, however, is also straightforwardly defined within the classical dipole radiation frame, which helps connecting the Green's tensor with EELS. The dipole radiation is not only allegedly easier to grasp, but also brings to scope new useful concepts, such as spontaneous decay and radiation damping. In the next section, most of the fundamental physics concepts that will be used throughout this work are defined and discussed with the required depth. The following section is mostly based on Jackson's, Notovny's, and Stratton's books [23–25].

1.2 Foundations of Nano Optics

1.2.1 Maxwell's equations and Green's functions

The generalized macroscopic Maxwell's equations describe the behavior of static and dynamic electric and magnetic fields. In this frame, bounded charges and currents are incorporated in the displacement field \mathbf{D} and the magnetizing field \mathbf{H} , and the equations below only depend on free charges and currents:

$$\left. \begin{aligned} \nabla \cdot \mathbf{D}(\mathbf{r}, t) &= \rho(\mathbf{r}, t), \\ \nabla \times \mathbf{H}(\mathbf{r}, t) &= \mathbf{J}(\mathbf{r}, t) + \frac{\partial \mathbf{D}(\mathbf{r}, t)}{\partial t}, \\ \nabla \cdot \mathbf{B}(\mathbf{r}, t) &= 0, \\ \nabla \times \mathbf{E}(\mathbf{r}, t) &= -\frac{\partial \mathbf{B}(\mathbf{r}, t)}{\partial t}, \end{aligned} \right\} \quad (1.1)$$

where ρ and \mathbf{J} are the free charges and the free current density, respectively, and \mathbf{E} and \mathbf{B} denote the electric and magnetic fields, respectively. From top to bottom, the set of four equations is called Gauss's law, Ampère's law, Gauss's law for magnetism, and Faraday's law.

If one applies the gradient in the rotational of the magnetizing field and notices they are orthogonal ($\nabla \cdot \nabla \times \mathbf{H} = 0$), the charge-conservation equation is obtained

$$\nabla \cdot \mathbf{J}(\mathbf{r}, t) + \frac{\partial \rho(\mathbf{r}, t)}{\partial t} = 0. \quad (1.2)$$

The displacement field and the magnetizing field are related to the macroscopic polarization \mathbf{P} and magnetization \mathbf{M} by

$$\left. \begin{aligned} \mathbf{D}(\mathbf{r}, t) &= \varepsilon_0 \mathbf{E}(\mathbf{r}, t) + \mathbf{P}(\mathbf{r}, t), \\ \mathbf{M}(\mathbf{r}, t) &= \mu_0^{-1} \mathbf{B}(\mathbf{r}, t) - \mathbf{H}(\mathbf{r}, t). \end{aligned} \right\} \quad (1.3)$$

The displacement and the magnetizing fields can be expressed in terms of the applied electric and magnetic fields. This is done by introducing the complex response functions $\varepsilon(\mathbf{r}, t)$ and $\mu(\mathbf{r}, t)$ called, respectively, the electric permittivity and magnetic permeability. Alternatively, one can express the polarization and magnetization as a function of the applied fields. In this case, the response functions are written as $\chi_e(\mathbf{r}, t)$ and $\chi_m(\mathbf{r}, t)$ and are called electric and magnetic susceptibility, respectively. These equations can be resumed as

$$\left. \begin{aligned} \mathbf{D}(\mathbf{r}, t) &= \varepsilon_0 \varepsilon(\mathbf{r}, t) \mathbf{E}(\mathbf{r}, t), \\ \mathbf{H}(\mathbf{r}, t) &= [\mu_0 \mu(\mathbf{r}, t)]^{-1} \mathbf{B}(\mathbf{r}, t), \\ \mathbf{P}(\mathbf{r}, t) &= \varepsilon_0 \chi_e \mathbf{E}(\mathbf{r}, t), \\ \mathbf{M}(\mathbf{r}, t) &= \chi_m \mathbf{H}(\mathbf{r}, t). \end{aligned} \right\} \quad (1.4)$$

They can be substituted in equations 1.1 to obtain the wave equation for \mathbf{E} :

$$\nabla \times \nabla \times \mathbf{E} + \varepsilon_0 \mu_0 \frac{\partial^2 \mathbf{E}}{\partial t^2} = -\mu_0 \frac{\partial}{\partial t} \left(\mathbf{J} + \frac{\partial \mathbf{P}}{\partial t} + \nabla \times \mathbf{M} \right) = -\mu_0 \frac{\partial \mathbf{J}_T}{\partial t}, \quad (1.5)$$

where \mathbf{J}_T is the total current density. The wave propagation velocity is $c = (\varepsilon_0 \mu_0)^{-1/2}$ and is known as the light of speed in vacuum. The bounded current density, thus, is $\partial \mathbf{P} / \partial t + \nabla \times \mathbf{M}$.

The spectral representation of the fields is much more suitable for spectroscopy. The Fourier transform from time to frequency domain is

$$\mathbf{E}(\omega, t) = \frac{1}{2\pi} \int_{-\infty}^{+\infty} \mathbf{E}(\mathbf{r}, t) e^{i\omega t} dt, \quad (1.6)$$

and, applying it to the set of equations 1.1, we have:

$$\left. \begin{aligned} \nabla \cdot \mathbf{D}(\mathbf{r}, \omega) &= \rho(\mathbf{r}, \omega), \\ \nabla \times \mathbf{H}(\mathbf{r}, \omega) &= \mathbf{J}(\mathbf{r}, \omega) - i\omega \mathbf{D}(\mathbf{r}, \omega), \\ \nabla \cdot \mathbf{B}(\mathbf{r}, \omega) &= 0, \\ \nabla \times \mathbf{E}(\mathbf{r}, \omega) &= i\omega \mathbf{B}(\mathbf{r}, \omega). \end{aligned} \right\} \quad (1.7)$$

For a plane wave, the resulting electric field is

$$\mathbf{E}(\mathbf{r}, t) = \Re\{\mathbf{E}(\mathbf{r})e^{-i\omega t}\} = 1/2[E(\mathbf{r})e^{-i\omega t} + E^*(\mathbf{r})e^{i\omega t}], \quad (1.8)$$

where the symbol \Re denotes the real part of the expression in the curly brackets. With this in hand, we can write a third set of Maxwell's equations, valid for harmonic fields, as

$$\left. \begin{aligned} \nabla \cdot \mathbf{D}(\mathbf{r}) &= \rho(\mathbf{r}), \\ \nabla \times \mathbf{H}(\mathbf{r}) &= \mathbf{J}(\mathbf{r}) - i\omega \mathbf{D}(\mathbf{r}), \\ \nabla \cdot \mathbf{B}(\mathbf{r}) &= 0, \\ \nabla \times \mathbf{E}(\mathbf{r}) &= i\omega \mathbf{B}(\mathbf{r}), \end{aligned} \right\} \quad (1.9)$$

which are equivalent of a set of equations 1.7 for arbitrary time-dependent fields but can now assume complex values.

Poynting's Theorem

Another important generalized result of Maxwell's equations is the Poynting theorem, which is an energy-conservation law. For a charge q under the influence of an electric and magnetic field \mathbf{E} and \mathbf{B} , the Lorentz force \mathbf{F} acting on it is

$$\mathbf{F} = q(\mathbf{E} + \mathbf{v} \times \mathbf{B}), \quad (1.10)$$

where \mathbf{v} is the charge velocity. As the charge propagation is perpendicular to the applied force, the magnetic field does not perform work and thus the work per unit of time is $q\mathbf{v} \cdot \mathbf{E} = \mathbf{J} \cdot \mathbf{E}$. For an arbitrary distribution of charge in an arbitrary given volume V , one can reach [23]

$$\int_V (\mathbf{J} \cdot \mathbf{E}) d^3x = - \int_V \left[\nabla \cdot (\mathbf{E} \times \mathbf{H}) + \frac{\partial u}{\partial t} \right] d^3x, \quad (1.11)$$

where u is the energy density, defined as

$$u = \frac{1}{2}(\mathbf{E} \cdot \mathbf{D} + \mathbf{B} \cdot \mathbf{H}). \quad (1.12)$$

As the integration volume is arbitrary and the same on both sides, this relation can be written in its differential form

$$\frac{\partial u}{\partial t} + \nabla \cdot \mathbf{S} = -\mathbf{J} \cdot \mathbf{E}, \quad (1.13)$$

in which the vector \mathbf{S} is

$$\mathbf{S}(\mathbf{r}, t) = \mathbf{E}(\mathbf{r}, t) \times \mathbf{H}(\mathbf{r}, t), \quad (1.14)$$

and is called the Poynting vector. The rate of change of electromagnetic energy inside the volume V plus the energy flow through the volume boundary is equal to the energy dissipation inside V .

As said before, harmonic fields are particularly useful and can be used to obtain the time average of the Poynting vector ($\bar{\mathbf{S}}$). From the set of equations 1.8,

$$\mathbf{J}(\mathbf{r}, t) \cdot \mathbf{E}(\mathbf{r}, t) = \frac{1}{2}\Re[\mathbf{J}^*(\mathbf{r}) \cdot \mathbf{E}(\mathbf{r})] + \frac{1}{2}\Re[\mathbf{J}(\mathbf{r}) \cdot \mathbf{E}(\mathbf{r})e^{-2i\omega t}], \quad (1.15)$$

and thus it is possible to reach the time-averaged Poynting vector

$$\bar{\mathbf{S}}(\mathbf{r}) = \frac{1}{2}\Re[\mathbf{E}(\mathbf{r}) \times \mathbf{H}^*(\mathbf{r})]. \quad (1.16)$$

By following similar steps for the time-dependent fields, the analogous of equation 1.11 can be written as

$$\int_V \frac{1}{2}\Re[\mathbf{J}^* \cdot \mathbf{E}]d^3x + \oint_{\partial V} (\bar{\mathbf{S}} \cdot \mathbf{n})da = 0, \quad (1.17)$$

where the second integral is calculated in the surface area of the arbitrarily defined volume V . Equation 1.17 provides a convenient interpretation of the Poynting vector as the surface integral on the second term is the net energy flow of the system. The Poynting vector, thus, is a vectorial quantity that represents the direction of propagation of the electromagnetic energy.

Vector and scalar potentials and the Lorentz gauge

The set of Maxwell's equations shown so far are represented by four coupled first-order differential equations. It is usually more convenient to reduce them to a set of two uncoupled second-order differential equations by using a vector (\mathbf{A}) and a scalar (Φ) potentials, which is achieved by applying a mathematical procedure known as gauge fixing. From equations 1.1, $\nabla \cdot \mathbf{B} = 0$ and $\nabla \cdot \nabla \times \mathbf{A} = 0$, and hence

$$\mathbf{B} = \nabla \times \mathbf{A}. \quad (1.18)$$

Using Faraday's law,

$$\nabla \times \left(\mathbf{E} + \frac{\partial \mathbf{A}}{\partial t} \right) = 0, \quad (1.19)$$

and as $\nabla \times (\nabla \Phi) = 0$, the scalar potential can be defined as

$$\mathbf{E} + \frac{\partial \mathbf{A}}{\partial t} = -\nabla \Phi. \quad (1.20)$$

Finally, by exhausting Maxwell's equations (Gauss and Ampère's laws),

$$\left. \begin{aligned} \nabla^2 \Phi + \frac{\partial}{\partial t} (\nabla \cdot \mathbf{A}) &= -\rho / (\varepsilon_0 \varepsilon), \\ \nabla^2 - \frac{1}{c^2} \frac{\partial^2 \mathbf{A}}{\partial t^2} - \nabla (\nabla \cdot \mathbf{A} + \frac{1}{c^2} \frac{\partial \Phi}{\partial t}) &= -(\mu_0 \mu) \mathbf{J}, \end{aligned} \right\} \quad (1.21)$$

in which an even more complicated coupled second-order differential equations are left. The problem is simplified by recognizing the absolute arbitrariness of the chosen \mathbf{A} and Φ to notice an invariant transformation

$$\left. \begin{aligned} \mathbf{A} &\rightarrow \mathbf{A} + \nabla \Gamma, \\ \Phi &\rightarrow \Phi - \frac{\partial \Gamma}{\partial t}, \end{aligned} \right\} \quad (1.22)$$

which is equivalent to say that \mathbf{A} and Φ must satisfy the so-called Lorentz Condition [26]:

$$\nabla \cdot \mathbf{A} + \frac{1}{c^2} \frac{\partial \Phi}{\partial t} = 0, \quad (1.23)$$

and which finally allows uncoupling the set of equations 1.22 into

$$\left. \begin{aligned} \nabla^2 \Phi - \frac{1}{c^2} \frac{\partial^2 \Phi}{\partial t^2} &= -\rho / (\varepsilon_0 \varepsilon), \\ \nabla^2 \mathbf{A} - \frac{1}{c^2} \frac{\partial^2 \mathbf{A}}{\partial t^2} &= -\mu_0 \mu \mathbf{J}. \end{aligned} \right\} \quad (1.24)$$

Equations 1.24 are equivalent to Maxwell's equations but now only one vector and one scalar must be solved. Gauge fixing is very common for reducing the number of degrees of freedom of coupled differential equations and is systematically used in the following sections.

Green's functions

In its most general description, a Green's function $\mathbf{G}(\mathbf{r}, \mathbf{r}')$ is the impulse response function of the linear differential operator L such that it is any solution of [27]

$$L\mathbf{G}(\mathbf{r}, \mathbf{r}') = \delta(\mathbf{r} - \mathbf{r}'), \quad (1.25)$$

where $\delta(\mathbf{r}, \mathbf{r}')$ is the Dirac delta function. If the linear operator L acts on the vector field $\Psi(\mathbf{r})$ with the source term $f(\mathbf{r})$ such as $L\Psi(\mathbf{r}) = f(\mathbf{r})$, the vector field solution is

$$\Psi(\mathbf{r}) = \int_V G(\mathbf{r}, \mathbf{r}') f(\mathbf{r}') dV'. \quad (1.26)$$

Similarly to what has been done to the spectral representation of Maxwell's equations, the Fourier transform of the set 1.24 become

$$\left. \begin{aligned} (\nabla^2 + k^2)\Phi(\mathbf{r}, \omega) &= -\rho/(\varepsilon_0\varepsilon), \\ (\nabla^2 + k^2)\mathbf{A}(\mathbf{r}, \omega) &= -\mu_0\mu\mathbf{J}, \end{aligned} \right\} \quad (1.27)$$

where $k = \omega/c$ is the scalar wavevector. To solve both Φ and \mathbf{A} , it is only necessary to know the scalar Green's function associated with the operator $\nabla^2 + k^2$. For such, one must solve

$$(\nabla^2 + k^2)G_0(\mathbf{r}, \mathbf{r}') = -\delta(\mathbf{r} - \mathbf{r}'). \quad (1.28)$$

The solution of this problem in the free space is [23]

$$G_0(\mathbf{r}, \mathbf{r}') = \frac{e^{\pm ik|\mathbf{r}-\mathbf{r}'|}}{4\pi|\mathbf{r} - \mathbf{r}'|}, \quad (1.29)$$

where the (+) solution represents a spherical wave propagating outwards the origin, while the (−) solution represents a spherical wave that converges towards the center. Equation 1.29 allows to determine the vector and scalar potential by directly applying 1.26.

For the electric and the magnetic field, the linear operator is slightly different because, from the Maxwell's equations 1.7,

$$\nabla \times \nabla \times \mathbf{E}(\mathbf{r}) - k^2\varepsilon(\mathbf{r})\mathbf{E}(\mathbf{r}) = i\omega\mu_0\mu\mathbf{J}(\mathbf{r}). \quad (1.30)$$

It must be found the corresponding Green's function that satisfies the tensorial expression

$$\nabla \times \nabla \times \vec{\mathbf{G}}(\mathbf{r}) - k^2\varepsilon(\mathbf{r})\vec{\mathbf{G}}(\mathbf{r}) = \vec{\mathbf{I}}\delta(\mathbf{r} - \mathbf{r}'), \quad (1.31)$$

where $\vec{\mathbf{G}}(\mathbf{r}, \mathbf{r}')$ is called the dyadic Green's function and $\vec{\mathbf{I}}$ is the unit dyad [28, 29]. To determine an expression for the dyadic Green's function, one can use the vector field \mathbf{A} definition in equation 1.27 along equation 1.29 to reach [23]

$$\vec{\mathbf{G}}(\mathbf{r}, \mathbf{r}') = \left[\vec{\mathbf{I}} + \frac{1}{k^2\varepsilon(\mathbf{r})}\nabla^2 \right] G_0(\mathbf{r}, \mathbf{r}'). \quad (1.32)$$

Finally, it is possible to express the electric and magnetic fields in any point of the space outside an arbitrary volume V as

$$\mathbf{E}(\mathbf{r}) = \mathbf{E}_0(\mathbf{r}) + i\omega\mu_0\mu \int_V \vec{\mathbf{G}}(\mathbf{r}, \mathbf{r}')\mathbf{J}(\mathbf{r}')dV', \quad (1.33)$$

and

$$\mathbf{H}(\mathbf{r}) = \mathbf{H}_0(\mathbf{r}) + \int_V \left[\nabla \times \vec{\mathbf{G}}(\mathbf{r}, \mathbf{r}') \right] \mathbf{J}(\mathbf{r}') dV'. \quad (1.34)$$

These two equations are sometimes denoted as volume integral equations, which permits to describe both fields as a function of the Green's tensor ¹.

1.2.2 The classical dipole radiation

In this section, the fields are written for a set of discrete charges q_n . The charge and the current density are

$$\left. \begin{aligned} \rho(\mathbf{r}) &= \sum_n q_n \delta(\mathbf{r} - \mathbf{r}'), \\ \mathbf{J}(\mathbf{r}) &= \sum_n q_n \frac{\partial \mathbf{r}}{\partial t} \delta(\mathbf{r} - \mathbf{r}'). \end{aligned} \right\} \quad (1.35)$$

One common approximation of the current density is to expand it in a Taylor series around the point \mathbf{r}_0 , here taken at the center of the charge distribution. In a first-order approximation [24],

$$\mathbf{J}(\mathbf{r}, t) = \frac{d\mathbf{p}(t)}{dt} \delta(\mathbf{r} - \mathbf{r}_0), \quad (1.36)$$

where \mathbf{p} is the net dipole moment, given by $\mathbf{p}(t) = \sum_n q_n (\mathbf{r}_n(t) - \mathbf{r}_0)$. For harmonic fields, the current density can be written as

$$\mathbf{J}(\mathbf{r}) = -i\omega \mathbf{p} \delta(\mathbf{r} - \mathbf{r}_0). \quad (1.37)$$

Substituting equations 1.33 and 1.34 in the obtained current density 1.37 leads to

$$\mathbf{E}(\mathbf{r}) = \omega^2 \mu_0 \mu \vec{\mathbf{G}}(\mathbf{r}, \mathbf{r}_0) \mathbf{p}, \quad (1.38)$$

and

$$\mathbf{H}(\mathbf{r}) = -i\omega \left[\nabla \times \vec{\mathbf{G}}(\mathbf{r}, \mathbf{r}_0) \right] \mathbf{p}. \quad (1.39)$$

To calculate the total energy radiated by the dipole, one can use equation 1.17 and write

$$\bar{P}_{loss} = \frac{dW}{dt} = -\frac{1}{2} \int_{V'} \Re\{\mathbf{J}^* \cdot \mathbf{E}\} dV', \quad (1.40)$$

where W is the work done by both electric and magnetic fields and thus defines the time-averaged power loss of the system. The integral result only depends on

¹Note that these are sometimes written with negative signs due to different time-dependency conventions, by either using $e^{-i\omega t}$ or $e^{i\omega t}$. Also, a 4π term can be encountered when written in Gaussian's units.

the electric field measured at the position \mathbf{r}_0 because of the Dirac delta at equation 1.37. Thus, from equations 1.37 and 1.38, this relation becomes

$$\bar{P}_{loss} = \frac{\omega^3 p^2}{2c^2 \epsilon_0 \epsilon} \Im \left\{ \mathbf{n}_p \cdot \vec{\mathbf{G}}(\mathbf{r}_0, \mathbf{r}_0, \omega) \cdot \mathbf{n}_p \right\}, \quad (1.41)$$

in which the Green's tensor is taken at the direction of the net dipole momentum \mathbf{p} . The Green's tensor, therefore, contains the entire energy balance information of a system of point charges. It must be noted that the net energy, in this case, is in the form of emitted radiation into the far-field. As long as non-point systems are considered, ohmic losses can also play a role.

Radiation damping

As seen in the previous section, the energy loss of a point classical oscillating dipole is translated into radiated electromagnetic radiation. This radiation, however, does not only dissipate the energy of the oscillator but also acts back on the charge and influences its motion. This effect is known as radiation reaction or radiation damping. To better grasp the system dynamics, one can model the charge motion as a forced harmonic oscillator,

$$m \frac{d^2 \mathbf{r}}{dt^2} + \omega_0^2 m \mathbf{r} = \mathbf{R}, \quad (1.42)$$

where \mathbf{R} is the radiation reaction force. By simple energy conservation in a sufficiently high time interval $[0, t']$ [24]

$$\int_0^{t'} \left[\bar{P}_{loss} + \mathbf{R} \cdot \frac{d\mathbf{r}}{dt} \right] dt' = 0, \quad (1.43)$$

integration by parts led to [24]:

$$\mathbf{R} = \frac{q^2}{6\pi\epsilon_0 c^3} \frac{d^3 \mathbf{r}}{dt^3}, \quad (1.44)$$

where q is the dipole charge. For an oscillatory solution, $\frac{d^3 \mathbf{r}}{dt^3} = -\omega_0^2 \frac{d\mathbf{r}}{dt}$ and thus

$$\frac{d^2 \mathbf{r}}{dt^2} + \gamma_0 \frac{d\mathbf{r}}{dt} + \omega_0^2 \mathbf{r} = 0, \quad \gamma_0 = \frac{1}{4\pi\epsilon_0} \frac{2q^2 \omega_0^2}{3c^3 m}. \quad (1.45)$$

Hence, equation 1.45 shows that the effect of the emitted radiation acting back on the oscillating dipole is to create a mathematically equivalent damped undriven harmonic oscillator, in which the resonance frequency is ω_0 and the linewidth is γ_0 . In general, the equation of motion is written in terms of the dipole moment $\mathbf{p}(t)$ instead of the charge position:

$$\frac{d^2 \mathbf{p}}{dt^2} + \gamma_0 \frac{d\mathbf{p}}{dt} + \omega_0^2 \mathbf{p} = 0, \quad (1.46)$$

which has a solution for \mathbf{p} as

$$\mathbf{p} = \Re\{p_0 e^{-i\omega_0 t} \sqrt{1 - (\gamma_0^2/4\omega_0^2)} e^{\gamma_0 t/2}\}. \quad (1.47)$$

The damping term γ_0 enters in both the amplitude and the oscillatory terms of the solution, meaning it affects not only the dipole strength but also the resonance frequency. The characteristic time of the oscillator is defined as the time in which the amplitude decreases as a factor of e^{-1} from its maximum value. In such a case,

$$\tau_0^{-1} = \gamma_0 = \frac{1}{4\pi\epsilon_0} \frac{2q^2\omega_0^2}{3c^3m}, \quad (1.48)$$

which is known as the decay rate of the classical dipole in a vacuum, and as shall see later on using quantum electrodynamics, it is the classical analog of the quantum spontaneous decay for a two-level system.

Dipole's interaction with the environment

Up until now, the presented mathematical formalism only considers a set of isolated charges in free space. Although important for introducing concepts, this is not always the case. Most of the time, the system solution comprises a non-homogeneous environment with multiple dipoles. In this section, the canonical macroscopic charge example is studied: it includes an arbitrary number N of point charges and a macroscopic body, considered as a continuous presence of dipoles. The excited field, instead of the resulting electric field, is obtained, considering the influence of the individual point charges and the macroscopic body, both described by their respective Green's tensor, as shown in Figure 1.1. This mathematical approach is sometimes referred to as the self-consistent dipole or the coupled-dipole method and the excited field is usually called self-field (\mathbf{E}_{sf}). The Green's tensor is first split in two contributions: the direct dipole field $\vec{\mathbf{G}}_0$ and the scattered field $\vec{\mathbf{G}}_s$ due to inhomogeneities on the system such that $\vec{\mathbf{G}} = \vec{\mathbf{G}}_0 + \vec{\mathbf{G}}_s$. Under an external exciting field \mathbf{E}_0 , the self-field is given by [24]

$$\begin{aligned} \mathbf{E}_{sf}(\mathbf{r}_k) = & \mathbf{E}_0(\mathbf{r}_k) + \omega^2 \mu_0 \mu \vec{\mathbf{G}}_s(\mathbf{r}_k, \mathbf{r}_k) \mathbf{p}_k \\ & + \omega^2 \mu_0 \mu \sum_{n=1}^N \vec{\mathbf{G}}(\mathbf{r}_k, \mathbf{r}_n) \mathbf{p}_n, \quad n \neq k, \quad k \in [1, N]. \end{aligned} \quad (1.49)$$

One particular solution of equation 1.49 is the analytical solution of the self-fields for a single dipole interacting with a non-homogeneous environment. Its dipole moment and the polarizability tensor $\vec{\alpha}(\omega)$ is related to the local self-field as

$$\mathbf{p} = \vec{\alpha}(\omega) \mathbf{E}_{sf}, \quad (1.50)$$

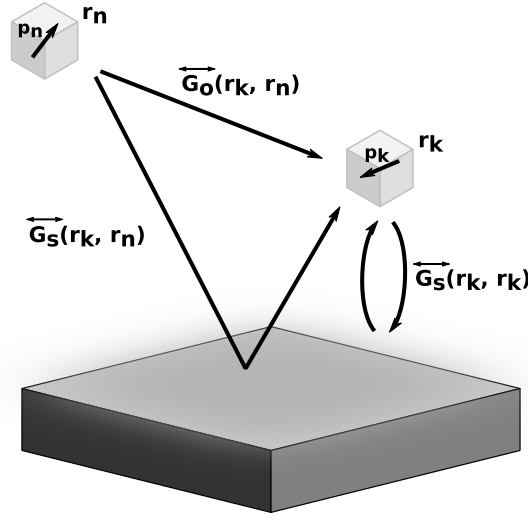


Figure 1.1: Coupled dipole or the self-consistent dipole method. The volume k (at \mathbf{r}_k) is under an external exciting field \mathbf{E}_0 and the self-field at this position is given by equation 1.49.

and equation 1.49, in this case, writes as

$$\mathbf{E}_{sf}(\mathbf{r}_0) = \mathbf{E}_0(\mathbf{r}_0) + \omega^2 \mu_0 \mu \vec{\mathbf{G}}_s(\mathbf{r}_0, \mathbf{r}_0) \mathbf{p}. \quad (1.51)$$

The self-consistent dipole moment is thus determined by both the scattering part of the Green's function and by the particle polarizability $\vec{\alpha}(\omega)$. The dipole moment can be written as a function of an effective polarizability and the exciting field \mathbf{E}_0 such

$$\mathbf{p} = \vec{\alpha}_{eff}(\omega) \mathbf{E}_0, \quad (1.52)$$

and the reflected fields can be accounted due to the non-homogeneous environment after correcting the particle polarizability:

$$\vec{\alpha}_{eff}(\omega) = \frac{\vec{\alpha}(\omega)}{1 - \omega^2 \vec{\alpha}(\omega) \vec{\mathbf{G}}_s(\mathbf{r}_0, \mathbf{r}_0)} = \frac{1}{\vec{\alpha}(\omega)^{-1} - \omega^2 \vec{\mathbf{G}}_s(\mathbf{r}_0, \mathbf{r}_0)}, \quad (1.53)$$

which is equivalent to state that the presence of a scattering object transforms the polarizability of the dipole from $\vec{\alpha}$ to $\vec{\alpha}_{eff}$.

To further understand the coupled system, one can use the dipole motion equation 1.46 derived for the damping radiation. The scattered field enters in the dynamics of the dipole moment through a driving term in the harmonic oscillator,

$$\frac{d^2 \mathbf{p}}{dt^2} + \gamma_0 \frac{d\mathbf{p}}{dt} + \omega_0^2 \mathbf{p} = \frac{q^2}{m} \mathbf{E}_s, \quad (1.54)$$

in which the trivial solution is suggested to have an oscillatory term with a different resonant frequency than the natural frequency ω_0 . The amplitude envelope also changes from γ_0 to γ and the solution can be written as

$$\left. \begin{aligned} \mathbf{p}(t) &= \Re\{\mathbf{p}_0 e^{-i\omega t} e^{-\gamma t/2}\}, \\ \mathbf{E}_s(t) &= \Re\{\mathbf{E}_0 e^{-i\omega t} e^{-\gamma t/2}\}, \end{aligned} \right\} \quad (1.55)$$

which can be solved in the motion equation and afterwards compared to equation 1.48 to obtain the relationship [30]

$$\frac{\gamma}{\gamma_0} = 1 + \frac{6\pi\epsilon_0}{|\mathbf{p}_0|^2 k^3} \Im\{\mathbf{p}_0^* \cdot \mathbf{E}_s(\mathbf{r}_0)\}, \quad (1.56)$$

which measures the linewidth change in a simple inhomogeneous media. This result has successfully explained the behavior of spontaneous emission of single molecules over planar [31, 32] and complex [33] substrates. Additionally, relation 1.56 also explains the fluorescence quenching of molecules near planar interfaces [34, 35] with remarkable accuracy.

1.2.3 The basics of Quantum Electrodynamics

This section introduces the basics of quantum electrodynamics (QED) to provide further insights into the discussed concepts. Besides, new physical quantities can be defined within the QED frame, as it is more suitable to explain a myriad of cavity-related problems. Examples include the Purcell effect, which is the enhancement of the spontaneous decay in plasmonics systems due to its surroundings [36]; the role of cavities in the decay rate of molecules or atoms [37–41] and the characterization of the different atom-cavity coupling regimes. The central physical quantity that can describe all the aforementioned physical phenomena is the local electromagnetic density of states (EMLDOS). As shall be seen in later sections, EMLDOS is also the core concept of electron-based spectroscopy.

The single-particle Hamiltonian under an electromagnetic field

Before deriving a fully-quantized model, a semiclassical one is obtained by introducing quantum-mechanical operators for the atomic state, but using classical field quantities. In this frame, the light-dipole, or light-atom, interaction is expressed by perturbation theory by the interaction Hamiltonian. For an isolated particle of mass m under the potential \hat{V} , the Hamiltonian is

$$\hat{H}_0 = \frac{\hat{\mathbf{p}}^2}{2m} + \hat{V}(\mathbf{r}). \quad (1.57)$$

If the particle is under the Lorentz force (equation 1.10), it can be shown that its effect is completely described by replacing the particle's momentum as [42, 43]

$$\mathbf{p} \rightarrow \mathbf{p} - q\mathbf{A}, \quad (1.58)$$

which leads to the new Hamiltonian

$$\hat{H} = \frac{(\hat{\mathbf{p}} - q\mathbf{A})^2}{2m} + V(\mathbf{r}) = \hat{H}_0 + \hat{H}_{int}, \quad (1.59)$$

and thus the particle-field interaction Hamiltonian can be written by substituting $\mathbf{p} = -i\hbar\nabla$ and considering weak perturbations fields, and hence dropping the quadratic terms of \mathbf{A} :

$$\hat{H}_{int} = \frac{i\hbar q}{2m}(\nabla \cdot \mathbf{A} + \mathbf{A} \cdot \nabla). \quad (1.60)$$

In the Coulomb gauge, the invariant transformation of equation 1.22 is gauge fixed by the condition $\nabla \cdot \mathbf{A} = 0$. In this frame, the perturbed Hamiltonian is

$$\hat{H}_{int} = \frac{i\hbar q}{m} \mathbf{A} \cdot \nabla = -\frac{q}{m} \mathbf{A} \cdot \hat{\mathbf{p}}, \quad (1.61)$$

which is the generalized expression for the interaction Hamiltonian. Under the so-called dipole approximation, one considers $e^{i\mathbf{k}\cdot\mathbf{r}} \rightarrow 1$, meaning the radiated wavelength is much smaller than the atomic/molecule structure. It is possible to show that, with the Hamiltonian commutation relation $[\hat{\mathbf{x}}, \hat{H}_0] = i\hbar\hat{\mathbf{p}}/m$, the well-known interaction potential for a dipole in a field [44] expression can be written

$$\hat{H}_{int} = -\hat{\boldsymbol{\mu}} \cdot \mathbf{E}, \quad (1.62)$$

where $\hat{\boldsymbol{\mu}}$ is the total electric dipole moment operator of the atom and it is written as $\hat{\boldsymbol{\mu}}$ instead of $\hat{\mathbf{p}}$ to follow most books conventions. It is given by

$$\hat{\boldsymbol{\mu}} = q \sum_{i=1}^Z \hat{\mathbf{r}}_i. \quad (1.63)$$

These are the fundamental aspects of the semiclassical light-dipole interaction. In the next section, the derived semiclassical Hamiltonian is used to introduce the quantization of the electromagnetic fields, leading to a fully quantized model.

Fock states and the quantization of the electromagnetic field

The most common approach into the electromagnetic field quantization is the replacement of the potential vector into the potential operator ($\mathbf{A} \rightarrow \hat{\mathbf{A}}$). To do so, the classical field is compared to the quantum harmonic oscillator [45–47], in which it is assumed the reader is familiar with. The vector potential must be expanded in terms of the wavevector \mathbf{k} (k_x , k_y and k_z) and from the two transverse polarizations (λ_1 and λ_2), generating the orthonormal basis $\mathbf{e}_{\mathbf{k},\lambda}$. Similarly to the harmonic oscillator, the destruction ($\hat{a}_{\mathbf{k},\lambda}$) and the creator ($\hat{a}_{\mathbf{k},\lambda}^\dagger$) operators destroy and create one photon of energy ω_k in the mode $\mathbf{k}\lambda$. The eigenvalues of these states, $n_{k,\lambda}$, designates the number of photons in the cavity, as can be seen in the set of equations below. The complete derivation of this section can be found in the appendix.

$$\left. \begin{aligned} \hat{a}_{\mathbf{k},\lambda} |n_{\mathbf{k},\lambda}\rangle &= \sqrt{n_{\mathbf{k},\lambda}} |n_{\mathbf{k},\lambda} - 1\rangle, \\ \hat{a}_{\mathbf{k},\lambda}^\dagger |n_{\mathbf{k},\lambda}\rangle &= \sqrt{n_{\mathbf{k},\lambda} + 1} |n_{\mathbf{k},\lambda} + 1\rangle, \\ \hat{n}_{\mathbf{k},\lambda} &= \hat{a}_{\mathbf{k},\lambda}^\dagger \hat{a}_{\mathbf{k},\lambda}, \\ \hat{n}_{\mathbf{k},\lambda} |n_{\mathbf{k},\lambda}\rangle &= n_{\mathbf{k},\lambda} |n_{\mathbf{k},\lambda}\rangle. \end{aligned} \right\} \quad (1.64)$$

These quantum eigenstates of light are more usually known as photon-number states or Fock states of the electromagnetic field. The Hamiltonian of the radiation field can be obtained by the analogy with the 1D harmonic oscillator as

$$\hat{H}_R = \sum_{\mathbf{k}} \sum_{\lambda} \hat{H}_{\mathbf{k},\lambda}, \quad (1.65)$$

where

$$\hat{H}_{\mathbf{k},\lambda} = \frac{\hbar\omega_{\mathbf{k}}}{2} (\hat{a}_{\mathbf{k},\lambda} \hat{a}_{\mathbf{k},\lambda}^\dagger + \hat{a}_{\mathbf{k},\lambda}^\dagger \hat{a}_{\mathbf{k},\lambda}), \quad (1.66)$$

in which the subscript R stands for the radiation Hamiltonian. The analogy also allows to obtain the electromagnetic field operators $\hat{\mathbf{A}}(\mathbf{r}, t)$, $\hat{\mathbf{B}}(\mathbf{r}, t)$, and $\hat{\mathbf{E}}(\mathbf{r}, t)$. For the electric field,

$$\hat{\mathbf{E}}(\mathbf{r}, t) = \sum_{\mathbf{k}} \sum_{\lambda=1,2} \mathbf{e}_{\mathbf{k},\lambda} \hat{E}_{\mathbf{k},\lambda}(\mathbf{r}, t), \quad (1.67)$$

in which

$$\hat{E}_{\mathbf{k},\lambda}(\mathbf{r}, t) = i\omega_{\mathbf{k}} \sqrt{\frac{\hbar}{2\varepsilon_0 V \omega_{\mathbf{k}}}} \left[\hat{a}_{\mathbf{k},\lambda} e^{-i\omega_{\mathbf{k}} t + i\mathbf{k} \cdot \mathbf{r}} - \hat{a}_{\mathbf{k},\lambda}^\dagger e^{i\omega_{\mathbf{k}} t - i\mathbf{k} \cdot \mathbf{r}} \right]. \quad (1.68)$$

For convenience, the electric field operator is split into $\hat{\mathbf{E}} = \hat{\mathbf{E}}^+ + \hat{\mathbf{E}}^-$ to reach

$$\left. \begin{aligned} \hat{\mathbf{E}}^+(\mathbf{r}, t) &= \sum_{\mathbf{k}} \sum_{\lambda=1,2} \mathbf{e}_{\mathbf{k},\lambda} i \sqrt{\frac{\hbar\omega_{\mathbf{k}}}{2\varepsilon_0 V}} \hat{a}_{\mathbf{k},\lambda} e^{-i\omega_{\mathbf{k}} t + i\mathbf{k} \cdot \mathbf{r}}, \\ \hat{\mathbf{E}}^-(\mathbf{r}, t) &= - \sum_{\mathbf{k}} \sum_{\lambda=1,2} \mathbf{e}_{\mathbf{k},\lambda} i \sqrt{\frac{\hbar\omega_{\mathbf{k}}}{2\varepsilon_0 V}} \hat{a}_{\mathbf{k},\lambda}^\dagger e^{i\omega_{\mathbf{k}} t - i\mathbf{k} \cdot \mathbf{r}}, \end{aligned} \right\} \quad (1.69)$$

in which the operators $\hat{\mathbf{E}}^+$ and $\hat{\mathbf{E}}^-$ are complex conjugates and are responsible for destroying (absorbing) or creating (emitting) one photon in the cavity, respectively.

Second quantization of the atomic state

The eigenstates, or Fock states, were described in terms of the ladder operators for the electromagnetic field, following a similar mathematical formalism of the quantum 1D harmonic oscillator. It is possible to introduce the creation and the annihilation operators for the atomic state as well, which means the Hamiltonian can be entirely described in terms of these two sets of ladder operators. This is known as the second quantization of the atomic Hamiltonian, which can be

done by writing the dipole operator in terms of any complete basis of an energy eigenstate such as [47]

$$\hat{\boldsymbol{\mu}} = \sum_i |i\rangle \langle i| \hat{\boldsymbol{\mu}} \sum_j |j\rangle \langle j| = \sum_{i,j} \boldsymbol{\mu}_{i,j} |i\rangle \langle j|, \quad (1.70)$$

where

$$\boldsymbol{\mu}_{i,j} = \langle i| \hat{\boldsymbol{\mu}} |j\rangle, \quad (1.71)$$

and the sum is over any complete basis of unmixed states. As the dipole operator acts in the atomic state, $\boldsymbol{\mu}_{i,j} = 0$ for $i = j$, i.e. there is no atomic transition when the states are equal. For the two-level atom system consisting of the ground $|1\rangle$ and the excited states $|2\rangle$ and with a transition frequency of $\omega_0 = \omega_2 - \omega_1$, one can define the operators

$$\left. \begin{aligned} \hat{\pi} &= |1\rangle \langle 2|, \\ \hat{\pi}^\dagger &= |2\rangle \langle 1|, \end{aligned} \right\} \quad (1.72)$$

and the atomic level transitions are defined by

$$\left. \begin{aligned} \hat{\pi}^\dagger |1\rangle &= |2\rangle & \text{and} & & \hat{\pi}^\dagger |2\rangle &= 0, \\ \hat{\pi} |1\rangle &= 0 & \text{and} & & \hat{\pi} |2\rangle &= |1\rangle, \end{aligned} \right\} \quad (1.73)$$

Clearly $\hat{\pi}$ and $\hat{\pi}^\dagger$ behave as the annihilation and creation operators for the atomic state, respectively. If the dipole operators have real eigenvalues for the eigenstates $|1\rangle$ and $|2\rangle$, equation 1.70 can be re-written as

$$\hat{\boldsymbol{\mu}} = \boldsymbol{\mu}_{1,2} (\hat{\pi} + \hat{\pi}^\dagger), \quad (1.74)$$

and thus equation 1.62 becomes

$$\hat{H}_{int} = i \sum_k \sum_\lambda g_{\mathbf{k},\lambda} (\hat{a}_{\mathbf{k},\lambda} e^{i\mathbf{k}\cdot\mathbf{r}} - \hat{a}_{\mathbf{k},\lambda}^\dagger e^{-i\mathbf{k}\cdot\mathbf{r}}) (\hat{\pi} + \hat{\pi}^\dagger), \quad (1.75)$$

in which equation 1.67 was used for the electric field and

$$g_{\mathbf{k},\lambda} = \sqrt{\frac{\hbar\omega_k}{2\varepsilon_0 V}} \mathbf{e}_{\mathbf{k},\lambda} \cdot \boldsymbol{\mu}_{1,2}. \quad (1.76)$$

Equation 1.75 explicit the four combinations between the photon population (\hat{a} and \hat{a}^\dagger) and the current atomic state ($\hat{\pi}$ and $\hat{\pi}^\dagger$) by using two sets of ladders operators. As can be seen in Figure 1.2, however, not all of these transitions are allowed because changing the atomic state necessarily means absorbing or losing the appropriate energy amount. In other words photon emission must be accompanied by a relaxation to the ground state, while photon absorption must excite the electron to the excited state of the two-level system.

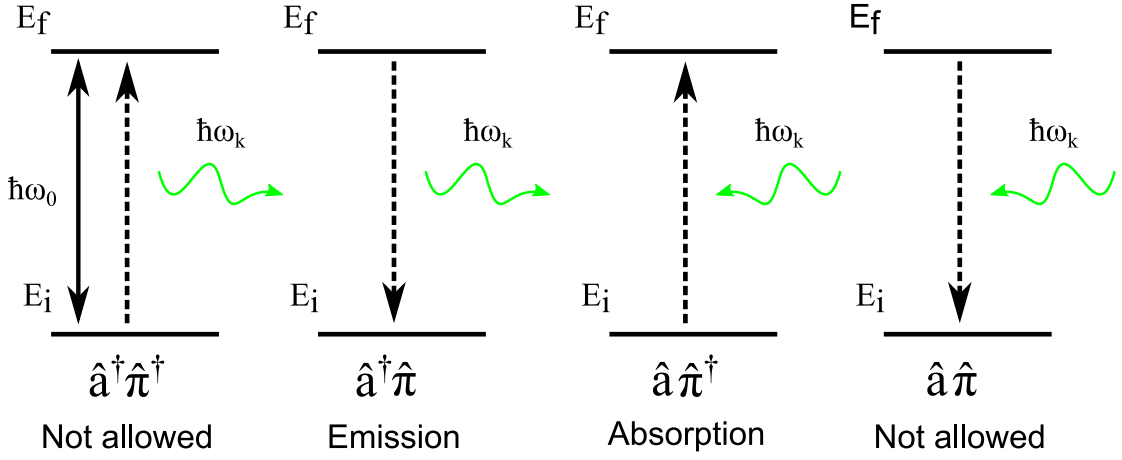


Figure 1.2: The four combinations of the ladder operators for the electromagnetic field (\hat{a} and \hat{a}^\dagger) and for the atomic state ($\hat{\pi}$ and $\hat{\pi}^\dagger$). The energy between atomic levels is $E_f - E_i = \hbar(\omega_2 - \omega_1) = \hbar\omega_0$ and the photon energy is $\hbar\omega_k$.

Excluding the forbidden transitions, the effective interaction Hamiltonian becomes

$$\hat{H}_{int} = i \sum_k \sum_\lambda g_{\mathbf{k},\lambda} (\hat{a}_{\mathbf{k},\lambda} \hat{\pi}^\dagger e^{i\mathbf{k}\cdot\mathbf{r}} - \hat{a}_{\mathbf{k},\lambda}^\dagger \hat{\pi} e^{-i\mathbf{k}\cdot\mathbf{r}}), \quad (1.77)$$

and its matrix elements are

$$\left. \begin{aligned} \langle n_{\mathbf{k},\lambda} - 1, 2 | \hat{H}_{int} | n_{\mathbf{k},\lambda}, 1 \rangle &= ig_{\mathbf{k},\lambda} e^{i(\omega_0 - \omega_k)t + i\mathbf{k}\cdot\mathbf{r}} \sqrt{n_{\mathbf{k},\lambda}}, \\ \langle n_{\mathbf{k},\lambda} + 1, 1 | \hat{H}_{int} | n_{\mathbf{k},\lambda}, 2 \rangle &= -ig_{\mathbf{k},\lambda} e^{-i(\omega_0 - \omega_k)t - i\mathbf{k}\cdot\mathbf{r}} \sqrt{n_{\mathbf{k},\lambda} + 1}. \end{aligned} \right\} \quad (1.78)$$

The top equation means the atomic level starts at the ground state and ends up in the excited state accompanied by a photon lost in the cavity (absorption). The bottom equation is the opposite, as it decays to the ground state upon an emitted photon (emission). As it shall be seen soon, the probability of transition per unit time is given by Fermi's Golden Rule, which depends on the square modulus of the matrix elements. They can be written as

$$\left. \begin{aligned} \left| \langle n_{\mathbf{k},\lambda} - 1, 2 | \hat{H}_{int} | n_{\mathbf{k},\lambda}, 1 \rangle \right|^2 &= n_{\mathbf{k},\lambda} g_{\mathbf{k},\lambda}^2, \\ \left| \langle n_{\mathbf{k},\lambda} + 1, 1 | \hat{H}_{int} | n_{\mathbf{k},\lambda}, 2 \rangle \right|^2 &= (n_{\mathbf{k},\lambda} + 1) g_{\mathbf{k},\lambda}^2. \end{aligned} \right\} \quad (1.79)$$

The photon absorption probability is proportional to the photon population $\propto n_{\mathbf{k},\lambda}$, while the photon emission probability is $\propto (n_{\mathbf{k},\lambda} + 1)$. The term independent of $n_{\mathbf{k},\lambda}$ is the spontaneous decay, as the transition from the excited to the ground state can happen even in the absence of photons. The component that depends on photon population and is identical to the photon absorption rate probability is called stimulated emission, which is proved here using the QED formalism. The sum of both phenomena naturally translates into the total photon emission probability.

The decay rate and the partial local density of states

In this section, Fermi's golden rule is used to quantify the transition rate from these different eigenstates under the weak-perturbation frame [45]:

$$\gamma = \frac{2\pi}{\hbar^2} \sum_f \left| \langle f | \hat{H}_{int} | i \rangle \right|^2 \delta(\omega_i - \omega_f). \quad (1.80)$$

As discussed, spontaneous decay is associated with the term independent of $n_{\mathbf{k},\lambda}$ so its transition rate probability γ_{sp} can be written as

$$\gamma_{sp} = \frac{2\pi}{\hbar^2} \sum_{\mathbf{k}} \sum_{\lambda} g_{\mathbf{k},\lambda}^2 \delta(\omega_{\mathbf{k}} - \omega_0), \quad (1.81)$$

and, using the definition of $g_{\mathbf{k},\lambda}$ (equation 1.76),

$$\gamma_{sp} = \frac{\pi\omega_{\mathbf{k}} |\boldsymbol{\mu}_{1,2}|^2}{\hbar\epsilon_0} \frac{1}{V} \sum_{\mathbf{k}} \sum_{\lambda} \mathbf{n}_{\mu} \cdot |\mathbf{e}_{\mathbf{k},\lambda}|^2 \mathbf{n}_{\mu} \delta(\omega_{\mathbf{k}} - \omega_0), \quad (1.82)$$

where \mathbf{n}_{μ} is a unit vector taken in the direction of the dipole momentum. The right part of this equation is called a projection in the $\boldsymbol{\mu}$ direction of the EMLDOS. This can be written as

$$\rho_{e,\mu}(\mathbf{r}, \omega_0) = \frac{1}{V} \sum_{\mathbf{k}} \sum_{\lambda} \mathbf{n}_{\mu} \cdot |\mathbf{e}_{\mathbf{k},\lambda}|^2 \mathbf{n}_{\mu} \delta(\omega_{\mathbf{k}} - \omega_0). \quad (1.83)$$

Hence, the spontaneous decay time can be re-written as

$$\gamma_{sp} = \frac{\pi\omega_{\mathbf{k}} |\boldsymbol{\mu}_{1,2}|^2}{\hbar\epsilon_0} \rho_{e,\mu}(\mathbf{r}, \omega_0). \quad (1.84)$$

To trace the correspondence with the classical result, the EMLDOS must be defined in terms of Green's function, in which the complete derivation can be found in the appendix:

$$\rho_{e,\mu}(\mathbf{r}, \omega) = \frac{2\omega}{\pi c^2 V} \left[\mathbf{n}_{\mu} \cdot \Im \{ \vec{\mathbf{G}}(\mathbf{r}, \mathbf{r}', \omega) \} \mathbf{n}_{\mu} \right]. \quad (1.85)$$

In Cartesian coordinates, the entire density of states instead of its projection in a given axis can be obtained by summing up in the canonical basis \mathbf{n}_x , \mathbf{n}_y , and \mathbf{n}_z such that

$$\rho_e(\mathbf{r}, \omega) = \sum_{\mathbf{u}=\mathbf{n}_x, \mathbf{n}_y, \mathbf{n}_z} \frac{2\omega}{\pi c^2 V} \left[\mathbf{u} \cdot \Im \{ \vec{\mathbf{G}}(\mathbf{r}, \mathbf{r}', \omega) \} \mathbf{u} \right]. \quad (1.86)$$

By using quantum formalism, the EMLDOS, intimately linked to spontaneous decay, is introduced. Additionally, this quantity was related to the projection of the imaginary part of the Green's tensor along the net dipole direction. As shall be seen, EELS can be qualitatively associated with the classical dipole power loss and,

thus, with the imaginary Green's tensor and the ELMDOS. Cathodoluminescence (CL) processes that are phase-locked with the exciting fast electron, on the other hand, measures the energy transferred to the far-field, and so is better related to the Poynting vector. CL can also be linked to the QED formalism of spontaneous decay, as an electron can excite atomic states and light emission can happen even in the absence of external optical fields. Electron energy-gain spectroscopy (EEGS), a less usual electron spectroscopic technique, also can be explained by the light-matter interaction Hamiltonian developed in the QED frame.

1.3 Scanning Transmission Electron Microscope

The scanning transmission electron microscope (STEM), in an utterly simple description, uses relativistic free electrons generated in an electron gun and a set of electron lenses, also called magnetic round lenses, to form a small electron beam onto a thin sample. The transmitted electrons are used to obtain images, diffraction patterns, or spectroscopic information of the sample. The magnetic lens used to form the probe in the sample is called an objective lens, while lenses before it are normally called condenser lenses. The small probe is rastered on the sample by using a set of scanning coils. For every rastered pixel, a variety of signals can be simultaneously collected e.g. annular dark-field (ADF), bright-field (BF), and electron energy-loss spectra. EELS is a multi-channel signal, meaning a spectrum is acquired per probe position, while ADF and BF signals are both single-channel imaging detectors. BF is usually an electron scintillator coupled to a photomultiplier tube (PMT) placed in the optical axis of the electron microscope up to ~ 15 mrad for typical values. The ADF is also a scintillator-PMT system, although placed at higher angles and containing a central hole in which the low-angle electrons can pass through and do not contribute to the imaging contrast.

To perform EELS experiments, an electron prism, a set of magnetic quadrupoles (Q_4), and an electron detector are required. Additionally, in modern microscopes, sextupoles (Q_6) can also be included to correct for chromatic aberration, also called C_c correction. Due to the large energy range detected by EELS, from the far-infrared regime to the soft X-rays, the spectrum is generally divided between low-loss, from tens of meV excitations up to ~ 100 eV, and core-loss, from ~ 100 eV and beyond. Figure 1.3 displays a simplified scheme of a STEM column along with the basic aspects of EELS experiments. In the low-loss region, the unscattered or the elastically scattered electrons produce the most intense spectral feature, also called the zero-loss peak (ZLP), while the other losses come from electron inelastic scattering with outer-shell electrons of the sample. Inner-shell excitations are studied in the core-loss part of the spectrum. At the bottom of Figure 1.3b, the ionization threshold for the carbon K edge and the calcium L edges are displayed. More details of EELS are provided in the following sections.

Many interesting aspects of electron microscopy come from the wave nature of the electron beam. The electron wavelength is related to its momentum by the

Planck constant as

$$\lambda = \frac{h}{p}. \quad (1.87)$$

The wave nature of the electron beam explains the origin of the contrast of both typical imaging systems. While low-angle scattered electrons are known to have a strong contribution from phase-contrast, typically associated with the BF, higher-angle scattered electrons form an incoherent form of imaging, meaning the

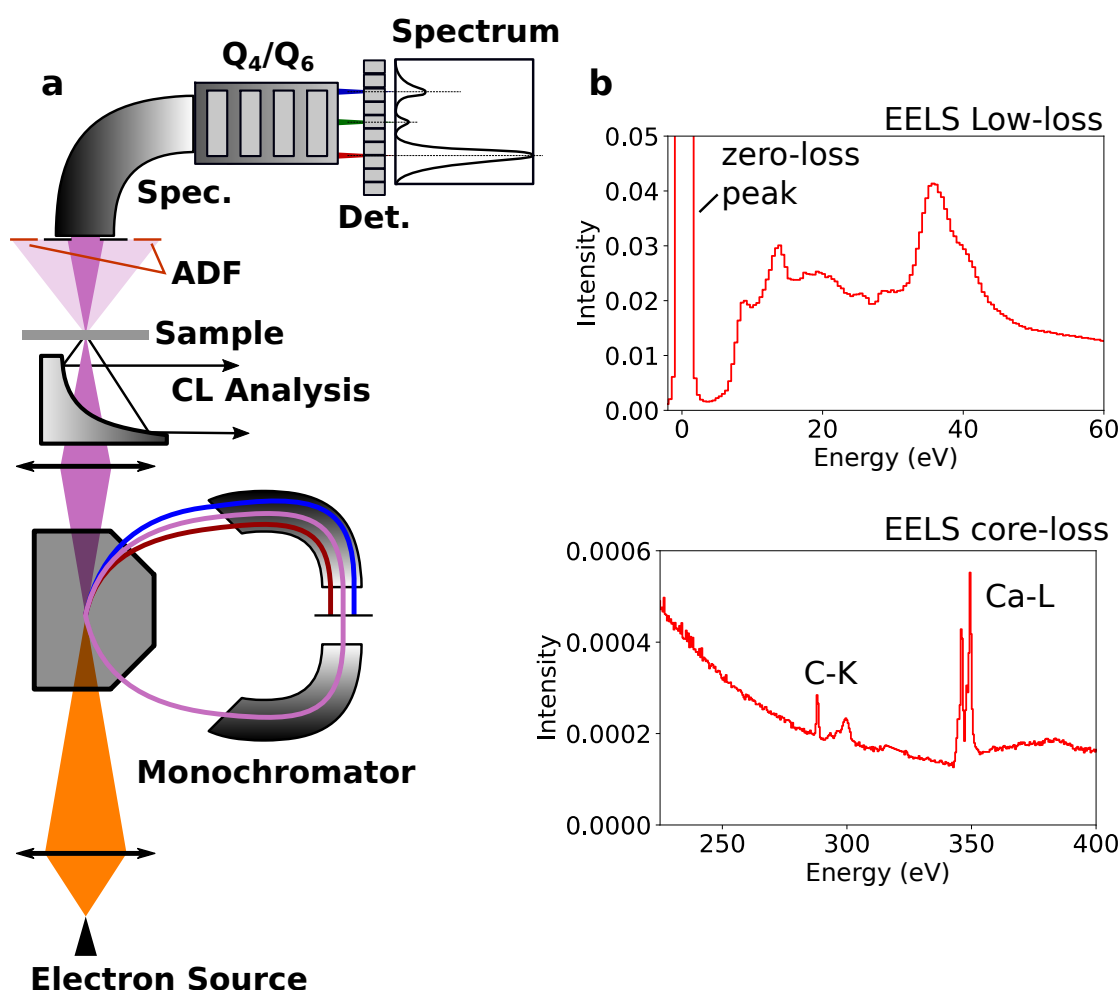


Figure 1.3: Scheme of the electron microscope and an acquired EELS spectrum. (a) Simplified version of a STEM column. Electrons are generated in the source and pass through a monochromator. A parabolic mirror allows to perform light emission or light injection experiments. Scattered electrons in higher angles form the ADF contrast, while lower angles go through the EELS spectrometer. A set of quadrupoles (Q₄) permit to set the proper experiment dispersion to reach the electron detector. Additionally, in modern EELS systems, sextupoles (Q₆) are used to correct chromatic aberrations. (b) Examples of low-loss and core-loss EELS spectra, in which the intensity is normalized relative to the ZLP.

interference effects of the phase-contrast are mostly washed out, typically associated with the ADF [48, 49]. In the scattering theory, a strong atomic number contrast is also perceived in high-angle scattered electrons, making the ADF an important chemically sensitive imaging system [50, 51]. Because ADF has a central hole in which the inelastically scattered beam can pass through, ADF is a particularly important imaging system for STEMs performing EELS because they can be acquired simultaneously. There are many other well-known techniques available in a STEM that are not used in this work e.g. nano diffraction [52, 53], an important tool in material's science, and energy-dispersive X-ray spectroscopy (EDX) a widely used technique capable of performing atomic-resolved chemical mapping by collecting the emitted X-rays from the sample upon interaction with the fast electron [54, 55].

Many available resources discuss these fundamental aspects of electron microscopy. The reader can find excellent discussions in the references [48, 49, 56, 57]. Nonetheless, a very brief discussion will be done for the distinct available electron sources, the EELS spectrometer, and modern electron monochromator designs, in special the one used in this work. These elements are displayed in the sketch of Figure 1.3a.

1.3.1 Electron sources

In most textbook discussions on electron microscopy, one physical quantity reigns when the objective is to gauge the electron microscope performance: the brightness B . It is defined in terms of the current I passing through a surface of area A within a solid angle Ω . Electron acceleration voltage (V), however, changes the gun brightness thanks to the change in the convergence angle [57]. More appropriately, a reduced brightness can be defined as

$$B = \frac{I}{A\Omega V}. \quad (1.88)$$

Few things in an electron microscope disrupt the principle of brightness conservation. One is the Boersch effect, a stochastic Coulomb interaction between electrons [58] especially important in a focused probe, and that increases the energy spread of electrons. The second is electron energy-filters, or electron monochromators, which reduce the intrinsic energy spread of the beam. Energy-filtering decreases beam current without changing area or the solid angle and thus also decreases the beam brightness. This sometimes leads to alternate definitions of brightness, such as including the energy spread in the denominator of equation 1.88.

Brightness and energy spread, despite the possibility of manipulating them in the electron column, are intrinsic properties of the electron gun. They are also related to a more complex physical quantity: electron coherence. If two points in the beam are coherent, it means that there is a well-defined phase relationship between them. The temporal coherence length is how much distance in the column

this spatial coherence is sustained [57]. Temporal coherence length, therefore, is related to the electron beam energy spread. Monochromated electron sources, for example, have high temporal coherence because electrons travel at similar speeds between each other. Coherence is an important concept in a microscope thanks to its relation to a constant electron phase and, consequently, the ability to form a strong phase-contrast and diffraction patterns. Temporal coherence length is also important because magnetic lenses focus strength depends on the electron energy and thus sharper images are formed within a beam with smaller energy spread (smaller chromatic aberration).

There are several types of electron guns. They are generally divided into thermionic sources, Schottky field-emission guns (Schottky FEGs), and cold field-emission guns (cFEGs). Thermionic guns (usually made of tungsten (W) or Lanthanum hexaboride (LaB_6) filaments) can be simply explained by the temperature-dependent Fermi-Dirac distribution. As the temperature of the filament rises, states with energies above the Fermi-level are occupied. The fermions that are in energy states beyond the work function ϕ of the source material ($\phi = 4.5$ eV for Tungsten and $\phi = 2.4$ for LaB_6) are unbounded and hence can be extracted. The available current density, in units of A/m^2 , for the source is expressed by Richardson's law:

$$j_{th} = aT^2 e^{\frac{-\phi}{\kappa T}}, \quad (1.89)$$

where a is the emission constant, or Richardson's constant, of the emitter, κ is the Boltzmann's constant and T is the emitter temperature. Usually, high temperatures are required to achieve reasonable gun brightness, which in turn spread out the Fermi-Dirac distribution too much in the energy axis, creating a poor gun spectral resolution, in the order of 3.0 eV and 1.5 eV for W and LaB_6 , respectively.

Schottky FEGs are usually described similarly to thermionic sources, using Richardson's law, but with an appropriate correction due to the reduced work function, thanks to an external field applied to the surface of the emitter. Schottky FEGs achieve a spectral resolution around 0.5 - 0.8 eV and brightness in the order of 5×10^7 A/(m² sr V) [59, 60].

CFEGs, on the other hand, works not at "cold" temperatures, but rather at room temperature. The free electrons are obtained by quantum tunneling in the presence of a strong electrostatic field. Field emission was successfully described by Ralph Fowler and Lothar Nordheim and the equation that describes the current density is called the Fowler-Nordheim's equation expressed as

$$j_{fe} = a\beta^2 \frac{U^2}{\phi} \exp^{-b \frac{\phi^{3/2}}{\beta U}}, \quad (1.90)$$

where β is the field-enhancement factor, $a \sim 1.54 \times 10^{-6}$ and $b \sim 6.83 \times 10^9$ are constants and U is the extraction voltage.

The energy distribution of the field-emission process was analytically solved 30 years after the theoretical developments of Fowler and Nordheim [61]. Today a generally accepted value for the inherent spectral resolution of cFEGs is approximately ~ 0.3 eV, while brightness can be as high as 4×10^8 A/m² sr V. Systematic efforts have been put into the microscope community to find higher-brightness electron sources. One of the most successful attempts was done by using carbon nanotubes as electron sources [62, 63] thanks to its very chemically inert surface when compared to tungsten tips. The brightness from carbon nanotubes is virtually infinity due to the single-atom electron emission. However, these tips are still far from being practical; tip changing involves fib-milling, micro-manipulation, and complicated welding processes. Efforts are still being put to turn such sources viable [64]. As a second and interesting example, LaB₆ nanowires have been recently proved to be extremely stable emissions guns. Higher brightness and a smaller spectral resolution when compared to tungsten tips have been observed, including the first atomic-resolved imaging [65, 66]. However, similarly from the carbon nanotubes, LaB₆ nanowires as cFEGs are still very dependent on intricate fabrication methods.

1.3.2 The basics of electron optics

Aberration correction

The ultimate goal of a scanning transmission electron microscope is the acquisition of atomic-resolved images along with its spectroscopic information with the best possible spectral resolution. It is rather obvious that correcting the aberrations from the electron probe benefits the microscope's spatial resolution. Aberration correction, however, also plays a significant role in electron spectrometers and electron monochromators. Decades of trying to produce aberration correctors are probably responsible for a lot of recent developments in electron microscopy. It is therefore impossible to discuss electron spectrometers and monochromators without correctors.

Aberration correction in electron microscopy is almost as old as electron microscopy itself. In 1931 Ruska demonstrated that a magnetic coil acts as an electron lens, similar to how an optical lens acts in a photon. In 1936, Otto Scherzer proved that these coils always have inherent chromatic and spherical aberrations associated. His finding, the Scherzer theorem, has stimulated decades of work from a generation of physicists around the world [67–69]. Third-order spherical aberration, also known as C_s , is known to be one of the most limiting aberrations to achieve atomic-resolved images. Efforts to correct C_s are countless. They include a pair of sextupoles and a telescopic pair of electron round lenses [70], and the quadrupole-octupole corrector, initially performed in a scanning electron microscope [71] and later in a STEM [72–74].

The goal of correctors is, therefore, to compensate induced aberrations from imperative optical elements, such as the microscope objective lens, with other

non-imperative optical elements. In practice, one can understand it as wavefront correctors. Similar to what happens in optics, in which spatially coherent beams can be focused in a small light probe, electron probes achieve smaller probes when these wavefronts are flat.

The magnetic prism

The magnetic prism is the central element in EELS. Its principle is rather easy to understand: fast electrons travelling at a speed v along the main microscope column axis are deflected by an electromagnet in which a magnetic field \mathbf{B} is present and it is orthogonal to the electron propagation direction. The electron is submitted to the Lorentz's force, given by $\mathbf{F} = -e(\mathbf{E} + \mathbf{v} \times \mathbf{B})$. In the absence of electric field \mathbf{E} , the electrons travel in a circular trajectory in which the radius is given by [75]

$$R = \frac{\gamma m_0}{eB} v, \quad (1.91)$$

where $\gamma = \frac{1}{\sqrt{(1-\frac{v}{c})^2}}$ is the Lorentz factor and m_0 is the electron rest mass.

As it is clear from Equation 1.91, the electrons perform a circular trajectory with a distinct radius for different electron energies thanks to the energy dependency on the electron velocity. The magnetic prism is designed in such a way that the electrons exit the section at around $\pi/2$ angle relative to its entrance, explaining the very characteristic shape of electron microscopes having electron spectrometers, as sketched in Figure 1.3a. In a standard magnetic prism, radial focusing is achieved to first-order, meaning that, for a point beam at the entrance of the microscope, the microscope focuses the beam in the dispersive direction [76]. The magnetic prism, therefore, produces electron bending, dispersion, and focusing.

The dispersion of these elements is rather small, approximately 1-2 $\mu\text{m}/\text{eV}$, meaning that small slits were required when detection is made immediately after the electron spectrometer, as it was performed with single-channel detectors like PMTs. With a parallel detector, such as a charged-coupled device (CCD), a set of quadrupoles are used between the section exit and the detector plane to chose the appropriate dispersion conditions for the experiment (see Figure 1.3). Like any other electron optics, electron spectrometers produce aberrations in the electron beam so correctors must be placed to reduce them [77]. Additionally, the careful design of the section angle of the spectrometer can also be used to reduce the induced aberrations [75].

Electron monochromators

Similar to aberration correctors, the design of energy-filtering devices began very early on. However, differently, these systems had experienced great early success, pushing the limits of energy-filtered imaging and energy spectroscopy since the 60s.

The dispersive properties of the magnetic section have allowed the development of the first energy-selecting electron filter, called Henry-Castaing filter, or Prism-Mirror filter [78, 79]. The Wien's filter, developed in 1898 for a positive-ion beam, uses simultaneously an electric and magnetic field, perpendicular to each other and to the electron propagation direction. The fields obey the relation $E = v_e B$, meaning that electrons traveling through the filter axis with speed v_e have their trajectory unperturbed, while others perform a helical path, creating an energy-dependent focus along the electron direction. Wiens's filters have achieved the very impressive spectral resolution of ~ 5 meV using 25-40 keV electrons back in the 60s, being capable of detecting phonons [80] (only seen in STEM with good spatial resolution in 2014 by Krivanek *et. al.* [81]) and temperature-dependent electron energy-gain at ~ 42 meV [82] from the ZLP. Despite all these impressive works, the spatial resolution was limited to ~ 100 μm .

Among all the other possible filter designs, Krivanek *et. al.* have developed an electron monochromator, right after the electron gun, employing several magnetic prisms whose energy-filtering is effectively done by a mid-path slit, as shown in Figure 1.3a. The first prism is responsible for deflecting the beam right into the second prism, which disperses the beam into the slit. The monochromated beam passes through a third prism, which regroups the dispersed beam into the first prism. The symmetry of these systems, also called α -filters for their similarity with the Greek letter, make the electron beam trajectory direction unchanged [83, 84]. The last magnetic section in the microscope, at the EELS spectrometer, has the same current passing through the electron monochromator. Careful design of these two parts of the system results in an EELS spectrometer without energy shifts even in the presence of small current variations [85]. Additionally, the slit is capable of measuring the incident current at both halves, which is used in a control system for the high-voltage system to keep the beam centered at the slit. Finally, a set of quadrupoles and sextupoles are used to correct first and second-order aberrations, creating the smallest probe possible at the slit plane.

As shall be explained in a later section, one of the microscopes used in this thesis employs the described α -filter. The microscope has also an aberration corrector up to the fifth-order, systematically achieving atomic-resolved images under ~ 15 meV spectral resolution.

1.4 Electron Spectroscopy

1.4.1 Electron Energy Loss Spectroscopy

EELS, as it should be clear at this point, measures the energy lost by an electron upon interaction with a sample. The origin of the EELS signal is usually explained in terms of the work done by the induced electric field \mathbf{E}^{ind} acting back on the electron [86, 87] as

$$\Delta E = e \int \mathbf{v} \cdot \mathbf{E}^{ind}(\mathbf{r}, t) dt = \int_0^{+\infty} \hbar\omega \Gamma_{EELS}(\omega) d\omega, \quad (1.92)$$

where \mathbf{v} is the electron velocity and Γ_{EELS} is the electron energy loss probability, given in units of the inverse of energy (usually eV⁻¹). This equation can be rewritten as

$$\Gamma_{EELS}(\omega) = \frac{e}{\hbar\pi\omega} \int \Re\{e^{-i\omega t} \mathbf{v} \cdot \mathbf{E}^{ind}(\mathbf{r}, t)\} dt. \quad (1.93)$$

The general form of 1.93 is rather instructive. If one determines the induced electric field due to the fast-moving charge in the frequency domain, loss probability can be retrieved.

Only a few problems in EELS have analytical solutions, especially for symmetrical structures such as spheres and cylinders or for simple objects such as planar structures. These analytical problems can be solved by three forms: (i) by the so-called quasi-static approach, in which the problem dynamics is considered to be instantaneous; (ii) by solving all the fields using Maxwell's equations, which includes retardation effects; (iii) by using a quantized model. All of the required concepts in this thesis can be sufficiently explained by the complete solution of the fields using Maxwell's equations. In this picture, the current density is $\mathbf{J} = \mathbf{v}\rho$, where ρ is the electron charge density. One can thus use the volume integral equation for the electric field in equation 1.33 into equation 1.93 for an electron propagating in the z direction to reach [87]

$$\Gamma_{EELS}(\mathbf{r}, \omega) = \frac{4e^2}{\hbar} \int \int \cos\left[\frac{\omega(z-z')}{v}\right] \times \Im\{-\mathbf{z} \cdot \vec{\mathbf{G}}(z, z', \omega) \cdot \mathbf{z}\} dz dz', \quad (1.94)$$

where \mathbf{r} in this context is the electron impact parameter, which lies in a perpendicular plane relative to the electron propagation.

To give a more concrete meaning for Γ_{EELS} , note how the integrand on equation 1.94 is similar to the power loss obtained for the classical dipole radiation in equation 1.41 through the imaginary part of the Green's tensor. It is important to note that EELS is capable of measuring this power loss along the electron propagation, meaning that only the component of the dipole moment along this direction contributes to the measured spectrum. In other words, a fast electron can induce a dipole momentum onto a sample, including directions that lie outside the traveling path, but EELS is only capable of measuring the work done by the z -component of these induced fields, partially depicting the total power loss from the induced fields in the form of absorption. As shown in equation 1.85, the projection of the Green's tensor along a given direction is the EMLDOS. For this reason, EELS is sometimes said to measure the partial, or projected, EMLDOS integrated over z , or the z -EMLDOS, which is probably the closer defined physical quantity related to what is probed by EELS [88–90].

Low-loss & core-loss EELS

Although the presented equations are generally valid, as previously mentioned, EELS is usually divided between inner-shell and outer-shell excitations, or core-loss and low-loss EELS, respectively. Most of the electrons interact with the outer atomic shells of the sample, which are responsible for the observed energy losses up to ~ 100 eV. This division is generally performed because the EMLDOS can be better explained case-by-case, dependent on the absorbed energy range. For low-losses, for example, the optical properties of the sample are used to model the observed spectral features, even containing many theoretical overlaps between light-based and electron-based spectroscopies. In the core-loss, the strong spatial localization of such high energies allows unveiling details of the chemical bonds and chemical mapping in the atomic-resolved scale. Inner-shell spectroscopy is also largely associated with X-ray emission from the sample, as the de-excitation process must fill the vacant electron with an outer electron with a subsequent probability of photon emission. This has been briefly mentioned in an earlier section. It is called electron-dispersive X-ray spectroscopy (EDX) but has not been performed in this thesis.

1.4.2 Cathodoluminescence

CL is the process of light emission by a sample under an electron beam excitation. For coherent processes, CL can be determined by integrating the energy flux along the entire radial direction \mathbf{n}_r in the far-field, or in the limit of $kr \rightarrow \infty$. In Maxwell's equations, the energy flux is given by the Poynting theorem in equation 1.14. CL is generally written [87, 89] as

$$\Gamma_{CL}(\omega) = \frac{c}{4\hbar\pi^2\omega} \lim_{kr \rightarrow \infty} \int r^2 \Re\{\mathbf{u}_r \cdot (\mathbf{E}^{ind}(\mathbf{r}, t) \times \mathbf{H}^{ind}(\mathbf{r}, t))\} d\Omega. \quad (1.95)$$

Equation 1.95 is an analytical expression for coherent cathodoluminescence, which includes surface plasmon resonances and transition radiation, for example. Incoherent cathodoluminescence is generally associated with the creation of electron-hole pairs, in which photon emission is a consequence of their recombination and is generally said to be spatially delocalized thanks to their diffusion length. Incoherent cathodoluminescence is a very broad and active field of study in electron microscopy e.g. the study of spatially-dependent quantum confinement effect [91, 92] and single-photon sources [93]. Most of the work in this thesis, however, was performed under the coherent excitation picture. The exception is the last chapter, in which cathodoluminescence excitation spectroscopy (CLE) provides a new way of understanding incoherent CL processes.

Light emission in a CL process is associated with the spontaneous decay described in section 1.2.3, and thus also with the second equation in the set 1.79. Spontaneous emission does not depend on the current photon population and only

requires an excited atomic state. Within this picture, CL can be understood as a two steps process. The fast-electron induces the electric field in the sample and measures the EMLDOS projection in EELS. If there is a non-zero net dipole moment in the near-fields, there is also a non-zero Poynting vector in the far-field condition ($kr \rightarrow \infty$) and thus CL is expected. As it was seen in section 1.2.2, the effect of an emitted radiation by a dipole is mathematically equivalent to a damped undriven harmonic oscillating dipole, which is called radiation damping. The total losses of the system (ohmic, radiation damping, etc) explain the well-known energy shift between near-field and the far-field resonances, i.e. a peak shift between EELS and CL [94, 95].

Finally, light collection devices in a STEM are not as standard as EELS. It requires lenses or mirrors, optical spectrometers, and suitable electron microscopes (large polepieces, available windows, etc.). Since the pioneering work of Yamamoto *et. al.* [96], CL systems in electron microscopes have been increasingly popular [87, 97]. It is worth mentioning that CL systems in scanning electron microscopes (SEMs) are much more widespread, which allows to perform experiments with higher currents, and in thick samples, although with a reduced spatial resolution [98, 99].

1.4.3 Electron Energy Gain Spectroscopy

EEGS is based on an intermediate concept between EELS and CL. Instead of using either the electron energy-loss or the far-field radiated field to do spectroscopy, an intense laser pulse is shone onto the sample and the incident fast electron interacts with the induced fields by the optical external field. This interaction is manifested by the probability of a stimulated energy loss or gain by the swift electron, which can be directly measured in the EELS spectrometer at both sides of the ZLP. As the probability of stimulated gain and loss peaks is proportional to the intensity of the induced fields by the external illumination, the spectral resolution of the technique is given by the linewidth of the light field. This laser-assisted high spectral resolution represents an increase of at least a factor of 100 concerning the modern electron monochromators, as discussed in section 1.3.2. Since its first description in 2008 [3], the technique contemplates the acquisition of the so-called EEGS, in which a series of EELS spectra is acquired, each one for a unique narrow-band laser wavelength. The objective of this section is to give a simplified mathematical description of the problem. Further discussion is given at the dedicated chapter later on in this thesis.

The unperturbed electron wavefunction can be written as a moving envelope function $g(z, t)$ such that [100–102]

$$\psi(z, t) = g(z - v_e t) \exp[i(k_e z - \omega_e t)], \quad (1.96)$$

where v_e is the electron velocity, z is the electron position, k_e and ω_e are the electron wavenumber and its angular frequency, respectively. Using equation 1.60

within the Coulomb gauge condition ($\nabla \cdot \mathbf{A} = 0$), the interaction Hamiltonian can be written as

$$H_{int} = -i \frac{q\hbar}{2m_e} \left(\frac{\hat{\mathbf{E}}^+}{i\omega_p} - \frac{\hat{\mathbf{E}}^-}{i\omega_p} \right) \cdot \nabla, \quad (1.97)$$

where ω_p is the angular frequency of the external light illumination. Electrons can interact with the scattered field by either absorbing ($\hat{\mathbf{E}}^+$) or losing ($\hat{\mathbf{E}}^-$) a photon energy $\hbar\omega_p$ [100], as already demonstrated in equation 1.69. To derive a probability expression for the observed stimulated gain and loss peaks, the electron wavefunction and the external light field are both modeled as Gaussian envelopes with durations σ_e and σ_p , respectively. This allows modeling the electron-photon interaction under multiple illumination conditions, such as in continuous regimes, fast pulses (nanoseconds), and ultrafast pulses (picoseconds and femtoseconds). The electron envelope can be written as

$$g(z, t \rightarrow -\infty) = \left(\frac{1}{\sqrt{2\pi v_e \sigma_e}} \exp \left[-\frac{z^2}{2(v_e \sigma_e)^2} \right] \right), \quad (1.98)$$

and the light field as

$$E = E_0 \exp \left[-\frac{(z - c(t - \tau))^2}{4c^2 \sigma_p^2} \right] \exp[i(k_p z - \omega_p t)]. \quad (1.99)$$

Solving the time-dependent Schrödinger equation, $i\hbar(\partial/\partial t)\psi = H_{int}\psi$ and after a long demonstration², the final electron wavefunction reads as

$$\psi(z, t) = g(z - v_e t, -\infty) \sum_{n=-\infty}^{+\infty} \xi_n(z - v_e t) \exp \left[i \left[\left(k_e + n \frac{\omega_p}{v_e} \right) z - (\omega_e + n\omega_p) t \right] \right], \quad (1.100)$$

where the amplitude coefficient is given by

$$\xi_n(z) = \left(\frac{F_z}{|F_z|} \right)^n J_n \left(\frac{q}{\hbar\omega_p} F_z \exp \left[-\frac{(z + v_e \tau)^2}{4v_e^2 \sigma_p^2} \right] \right), \quad (1.101)$$

and the EEGS field is defined as

$$F_z \left(\frac{\omega_p}{v_e} \right) = \int_{-\infty}^{\infty} dz E_z(z, 0) \exp \left[-i \frac{\omega_p}{v_e} z \right]. \quad (1.102)$$

First, note how the EEGS field F_z is the Fourier transform of the scattered electric field along the electron propagation direction. The phase-matching condition can be seen in the exponential term of equation 1.102, as the momentum transfer must satisfy $k_p = \Delta k_e$ and thus the photon phase velocity must be equal

²Complete, and identical, solutions can be found in references [100, 101].

to the electron group velocity ($v_p = \omega_p/k_p = \omega_p/\Delta k_e = v_e$) to achieve a maximum EEGS intensity. The resulting electron wavefunction in equation 1.100 suggests the presence of infinite stimulated electron energy-gain and losses side bands (positive and negative terms of n in the summation) at energies $n\hbar\omega$. The intensity of these side bands are modulated by the amplitude coefficient expressed in equation 1.101, which follows a Bessel function of the first kind of order n .

In the absence or in the low light-intensity regime, $F_z \rightarrow 0$ and $J_n \rightarrow 0$ for $\forall n \neq 0$, meaning only unscattered electrons contribute to the observed spectra. As soon as the external electric field increases, scattered electrons contribute to the amplitude of sidebands, while the unscattered amplitudes reduce. This oscillatory behavior of the amplitudes of the sidebands has already been reported [5], essentially validating the set of equations described in this section.

EEGS is thus essentially measuring the intensity of scattered electrons by the external light field, which means its probability is dependent on the laser intensity, and its central wavelength and linewidth. Modern electron monochromators can reach, at its best, 2-5 meV, which would be equivalent to a linewidth of ~ 0.5 nm centered at 580 nm, while ns laser sources can reach as low as 2 pm. Besides, EEGS is capable of increasing the desired signal by increasing the amplitude of the external signal i.e. the laser power, especially important for weak scattered fields.

1.5 The microscopes

As in most of the experimental physics projects, many tools have been used along with this thesis. Extensively detailing of all of them is impractical and uninteresting. Two of them, however, are worth the effort. The first is a modified Vacuum Generators model HB 501 (VG) microscope, one of the first commercially available dedicated STEM microscopes, more than 40 years old, in which all of the instrumental development of this thesis has been performed. The second is a modified Nion Hermes200 STEM, called ChromaTEM, which is one of the most advanced STEM at the time of writing. Many chapters in this thesis use both microscopes and performance differences can not be stressed enough. ChromaTEM reflects all the astonishing advances in microscopy, but with performance comes complexity, making tests and developments unattainable. It is expected that the reader appreciates the VG as much as it deserves, as every chapter in this thesis would not be possible without it. Pictures of both microscopes can be found at the appendix of this work.

Vacuum Generators HB501

The VG used has been extensively modified along with its lifespan. Better PMTs are used in both ADF and BF imaging systems, the serial EELS detector has been replaced by a parallel acquisition system, and most parts of the analog panel, used

to control objective lenses, stigmators, the electron spectrometer, *etc.* have been replaced by a custom-made scanning unit developed by Marcel Tencé over the past years. Many key group developments have been performed in this microscope, which includes the development of 3D datasets, or hyperspectral images [103], single-atom EELS measurements [104] and an in-house-built cathodoluminescence system [92]. The latter has also triggered many important studies, such as the observation of single-photon generation under electron excitation [105], photon-bunching in cathodoluminescence [106] and, more recently, the study of single-photon emitters in individual defects in hexagonal boron nitride [93].

The microscope uses a cold field emission gun, which allows one to reach currents up to ~ 250 pA in a sub-nanometer probe size with a spectral resolution of ~ 300 meV at full-width at half-maximum. The EELS spectrometer is a Gatan 666 model, with electron aberration correctors up to the second-order controlled by homemade electronics. For low dispersion, EELS is limited by the point spread function (PSF) of the electron spectrometer at ~ 5 pixels, mostly due to photon backscattering between the scintillator and the CCD layer. The microscope also has a light-collection device based on a high numerical aperture parabolic mirror that can be positioned within a micrometer range by a set of micrometer positioners. The CL signal is gathered in an optical fiber bundle directly coupled to an optical spectrometer. This prototype has developed into a commercial solution by Attolight (Mönch actuator) [107]. For this thesis, an optical table has been attached close to the CL system to perform light injection and collection with more degrees of freedom on the alignment. As it will be seen later in this work, this has allowed several single-fiber experiments that would otherwise be impossible.

As it will be shown, I have also actively developed this microscope using Python3 within the interface of the open-source software NionSwift [108]. Implementations details are given in the next chapter.

ChromaTEM

ChromaTEM is based on a Nion Hermes200, a C_s -corrected microscope that operates between 30 and 200 kV. The stabilized cFEG allows reaching currents as high as ~ 1 nA with a 0.2 nm probe size. The microscope also has an electron monochromator (α -filter) capable of reaching down to ~ 5 meV spectral resolution at the electron acceleration of 60 kV. The improved spectral resolution allows the microscope to access the far infra-red region of the energy-loss spectrum, down to the 40 meV or less, and essentially opening an entire branch of optical excitations vastly unknown by the electron microscopy community. This is an immense contrast concerning VG microscopes, in which having reasonable signal-to-noise even at the 1.5-2.0 eV range can be challenging due to the ZLP tail and high-voltage instabilities. Naturally, ChromaTEM has triggered multiple works in the infra-red regime, specially on phonons [81, 109, 110] and plasmons [111–113]. The CL system in ChromaTEM uses the commercial solution from Attolight and has also triggered recent works involving the relation between EELS and CL [16, 114] with

a much better EELS spectral resolution than previous studies. Mirror positioning is made by a set of three encoded stepper motors that translates into a spatial resolution of ~ 50 nm. Note that although an optical table close to the CL is unpractical, it is possible to attach small optical setups directly at the CL system, as shall be seen in later chapters.

1.6 Numerical Methods

There are many available computational tools to solve classical problems in electromagnetism, all of them rely on results of the Maxwell's equations discussed above. These can be used to determine, for example, light propagation in a non-trivial medium, in which analytical solutions are non-existent, but can also be used to determine the induced fields upon a point charge excitation, mimicking the fast electron.

The EELS retarded field response of nanoparticles has been modeled using the boundary element method (BEM) [115, 116], which takes its name due to the algorithm functioning, full-filling the problem boundary conditions. Later, the EELS response of metallic nanoparticles has been scrutinized using dipole discrete approximation (DDA), a more general method capable of simulating materials of arbitrary geometry [117, 118] and finite-element method (FEM) [119, 120]. More recently, more sophisticated and user-friendly software has been developed, most notable by MNPBEM, an efficient MATLAB toolbox that uses BEM to simulate EELS of metallic nanoparticles [121, 122].

In this thesis, finite-difference time-domain (FDTD) has been used [123, 124]. Different from BEM, FDTD makes no assumption of the system e.g. boundary conditions, which makes it a very straightforward simulation tool, with little to no need for previous experience. Besides, as it will be later discussed, one of the most important samples used throughout this work is optical resonators, which are most commonly studied under FDTD because the time-domain provides one of the most critical parameters for these devices, i.e., the quality factor. Thanks to that, EELS has also been studied under this picture, in which a brief discussion is provided.

Finite-difference time-domain

In FDTD, the space is divided into a discrete mesh and time evolves in discrete time steps. The space cells are also called Yee's cells. As it was seen in Maxwell's equations 1.1, the time variation of the electric field (or magnetic field) depends on the curl of the magnetic field (electric field). This relationship is the basics of FDTD: the updated value of the electric field (magnetic field) is its current stored value added to the curl of the magnetic field (electric field).

To find an expression more suitable to FDTD, equation 1.38 can be substituted in equation 1.94, and, to be consistent with most EELS literature, the inward

solution of 1.29 was written in Gaussian units

$$\Gamma_{EELS}(\omega) = \frac{e^2}{4\pi\omega^2} \int \int \cos\left(\frac{\omega(z-z')}{v}\right) \times \Im\left\{\frac{E_z^{ind}(z,\omega)}{p(z',\omega)}\right\} dzdz', \quad (1.103)$$

where z' is the position of the calculated field, z is the dipole charge position, and $p(z',\omega)$ is the amplitude of the dipole. The simulation is performed by displacing a dipole along the electron direction in the finest possible step size dz . For every point, the induced fields are calculated along the same trajectory z' . The only output from the simulation is the ratio E_z^{ind}/p in equation 1.103. To obtain the induced fields, the simulation must be performed twice: once with and once without the scattering structure. Finally, note how the electron velocity only enters in the cosine term of equation 1.103, making it a trivial tool for studying the electron phase-matching conditions in optical resonators because arbitrary electron velocities can be determined with a single FDTD simulation.

EEGS with a monochromated and continuous electron beam

2.1 Introduction

The idea of reversing the process of energy loss upon using an external light field has its first appearance in a small paragraph of a seminar given by Archie Howie [1, 2]. It was suggested as “electron probe excitation with photon emission” and briefly discussed the surprising lack of works using cathodoluminescence (CL) in transmission electron microscopes, despite being already popular in scanning electron microscopes [125], and the pioneering works of Yamamoto [96, 126]. Howie proposed the illumination of a sample using tunable light sources to populate defect states and that an energy-gain and loss peak would rise although very weak. The electron energy-gain peak was not, however, a complete stranger to the community. A few experiments dating from the 60s and 70s have already reported electron acceleration as a consequence of the sample’s temperature-dependent phonon energy [127, 128]. These works reverberate until today, with the potential use of electron probes as local thermometers [129].

In 2008, electron energy-gain spectroscopy (EEGS) arose as a promising technique that could overcome the poor spectral resolution endured by electron energy-loss spectroscopy (EELS) and the lack of signal by CL, ultimately combining the sub-meV spectral resolution from modern laser sources with the spatial resolution of electron microscopes [3]. EELS and CL, more traditional electron spectroscopies, are depicted in Figure 2.1a. They rely on the energy lost by a fast-electron, which could be detected by EELS and, if any light is emitted, by CL. Stimulated EEGS/EELS (that can be also written as sEEGS and sEELS) are shown in Figure 2.1b, where an intense external optical pulse excites the sample and interacts with the incoming electron. Figure 2.1c schematizes typical results from these spectroscopies. In energy-gain, resonances can be found at the left of the zero-loss peak (ZLP) at multiples of the photon energy, indicating that the electron has gained energy. As the left side of the ZLP is expected to display peaks strictly related to

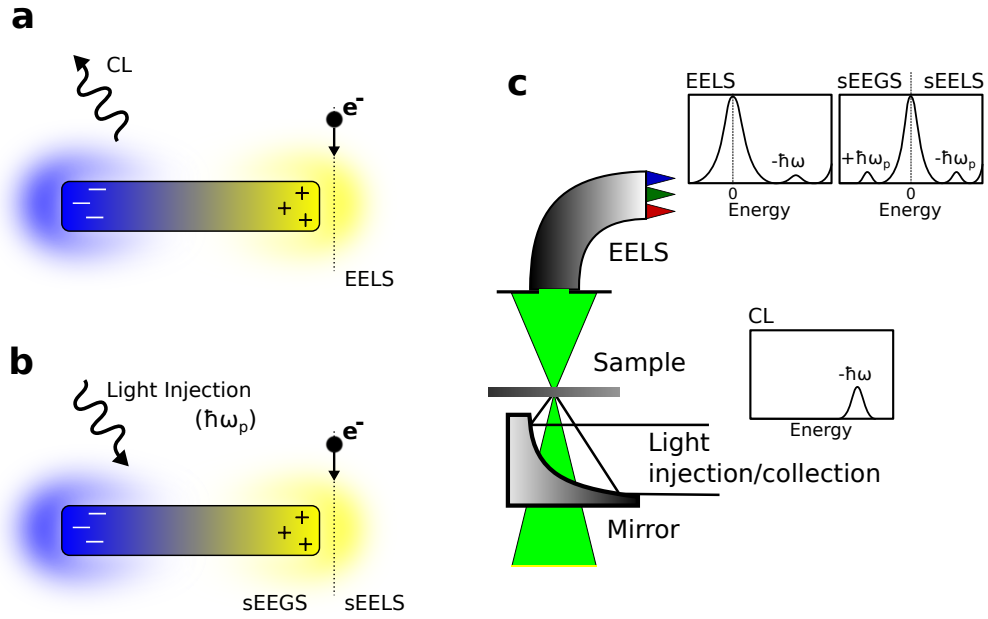


Figure 2.1: Scheme of some of the experimental techniques performed during this thesis. (a) An incoming electron lost energy (EELS) upon interaction with the sample, which could trigger a photon emission (CL). (b) Upon light injection, the electron can interact with the induced fields and has a probability of being accelerated (sEEGS, or energy-gain) or decelerated (sEELS, or energy-loss). (c) The experimental scheme and how the mentioned techniques in (a) and (b) are measured in a scanning transmission electron microscope.

the external field, the analysis of this side of the spectrum is prioritized and thus sEEGS/sEELS is generally called simply EELS.

The evident energy-momentum mismatch constraint between photons and fast electrons can be rather easily lifted when considering bounded evanescent optical fields, and thus the complex nature of their wavevectors, similarly to what has already been seen in the Smith-Purcell effect [130, 131]. Alternatively, the energy-momentum match can be seen in terms of the phase and group velocities of electrons and photons. The relativistic electron energy is given by

$$E_e = \sqrt{c^2 p_e^2 + m^2 c^4}, \quad (2.1)$$

where c is the speed of light in vacuum, p_e is the electron momentum and m is the electron rest mass. The photon energy for a media with an index of refraction n is

$$E_p = \frac{c}{n} p_p, \quad (2.2)$$

and for a photon propagating in a direction that makes an angle θ with the electron propagation direction, an electron energy gain of δE_e must be followed by a proper increase of electron momentum of $\delta p_e = \delta E_e / v_{g,e}$, where $v_{g,e}$ is the electron group

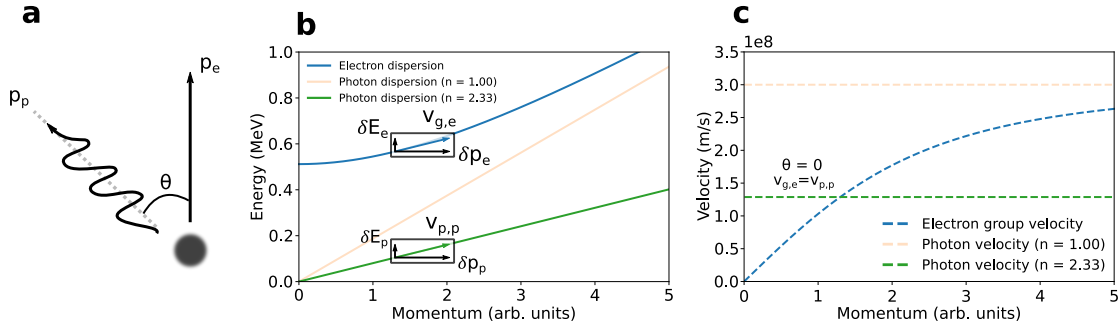


Figure 2.2: Dispersion curves for electrons and photons. (a) Scheme of the electron and photon momentum and their relative angle of propagation θ . (b) For a given electron energy, the electron-photon coupling condition must satisfy the energy-momentum match. This means for a given δE energy increase of the free-electron, a well-defined momentum increase of δp must follow. In other words, the coupling can happen when the electron group velocity ($\frac{\delta E}{\delta p}$) is equal to the photon phase velocity. (c) The electron group velocity as a function of its momentum (or energy) along with the photon phase velocity in free space ($n=1.00$) and a media with $n = 2.33$. Electron-photon energy-momentum match means that curves must cross.

velocity. The propagating photon with energy δE_p provides a momentum of $\delta p_p = \delta E_p/v_p$, but only the momentum component aligned with the electron propagation direction can be transferred, as shown in Figure 2.2. The energy-momentum match condition is, therefore, $\delta E_e = \delta E_p$ and $\delta p_e = \delta p_p \cos \theta$, which translates to

$$v_{g,e} \cos \theta = v_p, \quad (2.3)$$

in which equation 2.1 can be used to reach the following expression

$$\frac{p_e c^2}{\sqrt{c^2 p_e^2 + m^2 c^4}} \cos \theta = c/n. \quad (2.4)$$

The matching condition is shown in Figure 2.2c for a media of index of refraction $n = 2.33$ and $\theta = 0$. By what was stated before, the electron-photon cannot directly couple in the free-space because the electron group velocity does not ever reach c . Additionally, condition 2.4 is satisfied for every photon energy in a given medium because phase and group velocities are identical and constant for a given index of refraction.

In 2009, the pioneering work of Barwick *et al.* experimentally demonstrated the interaction of photons and electrons by using carbon nanotubes and silver nanowires [4]. The technique was baptized Photon-induced near-field electron microscopy (PINEM) and could map in real space the evanescent fields of the sample upon interaction with an external light field. An intense 220 femtosecond laser pulse was used to shine both the microscope electron gun and the sample, but with an optical path control between them to create a fine-tuning time delay line. Although the pulse was not short enough to grasp the dynamics of the evanescent

fields, which lies in the tens of femtoseconds for plasmonic nanoparticles, they have successfully shown the feasibility of this experiment, paving the way for high spectral resolution, time-resolved, electron spectroscopy. The experimental results led to a few other impressive theoretical works that provided insightful results both in the classical and quantum formalism [100–102].

However, one important question remains open. The probability of the gain signal depends on what? Most certainly in the light intensity, as already discussed by Barwick. For a plasmonic nanostructure, however, the field intensity scattered by the nanoparticle for a given $\mathbf{E}_{ext}(\omega)$ is proportional to the particle-induced dipole moment $\mathbf{p}(\omega) = \alpha(\omega)\mathbf{E}_{ext}(\omega)$, where $\alpha(\omega)$ is the structure polarizability. For a constant $\mathbf{E}_{ext}(\omega)$ across multiple wavelengths, the electron energy-gain probability is thus dependent on the external illumination wavelength. The femtosecond laser source was very prone to high-intensity signals due to the high peak field intensities while maintaining a small average power, crucial for preventing sample destruction. However, femtosecond laser sources suffer from a bad spectral resolution due to their short pulse duration, which is sometimes called the transform limit and it is a consequence of the Fourier transform of the signal from time to frequency domain. To give an order of magnitude of the problem, a 100 fs laser source would have a minimum bandwidth of ~ 20 meV. Nevertheless, 20 meV energy resolution is more than enough to reveal spectral features of broadband optical transitions, such as surface plasmon resonances, which has already been shown [6]. Another strategy to achieve an improved spectral resolution from pulsed laser beams is by time-modulation or beam chirping. With this, adjacent Mie modes of large silica spheres ($> 1 \mu\text{m}$ in radius) have been successfully extracted [13]. Spectral and momentum-resolved experiments have also been performed in photonic crystals: the well-defined band structure can be entirely mapped by controlling both the excitation wavelength and the angle of the incident light. Moreover, distinct quality factors have been identified by sweeping the time-delay in the femtosecond range [132]. Apart from an improved laser-assisted spectral resolution, several other outstanding works have explored PINEM with distinct objectives. Attosecond coherent control of the free-electrons was performed by modulating the quantum wavefunction of the fast electrons by the optical phase of the incident field. These functions were demonstrated to be modulated by the intensity of the external light by following the characteristic Rabi frequency oscillations [5, 7]. More recently, phase-matching of the electron and the optical field over hundreds of micrometers led to high energy gain/loss bandwidth, up to 1700 eV [133].

The aforementioned studies, although relevant for the development of laser-assisted spectroscopy with a high spectral resolution, cannot match the typical spectral resolutions of continuous or nanosecond-pulsed laser sources. Besides, electron monochromators have undergone massive improvements in the past few years, reaching a spectral resolution as low as tens of meV [81], similar to CL systems. The systematic meV spectral resolution in EELS and CL have undermined the applicability of laser-assisted spectroscopy using femtosecond laser sources,

remaining an option mostly for microscopes without an electron monochromator nor a light collection device. Photo-emitted emission guns do not have, up to date, available electron monochromators, and, perhaps even more critical, they are mostly using thermionic or Schottky FEGs (except [134]), severely crippling the ultimate microscope brightness and, therefore, its spatial resolution.

The first step towards a real improvement of the spectral resolution was done in 2019 by Das *et al.* A dye laser with tens of picometer linewidth, equivalent to $\sim 10 \mu\text{eV}$ at 585 nm, was used together with a rather intricate detection and synchronization system [8], as schematized in Figure 2.3. A pair of electrostatic blanking plates, running on typical voltages of hundreds of volts and maximal repetition rates of ~ 20 kHz, was used to deflect the incident electrons on the detector with a temporal resolution of tens of nanoseconds. The pulsed laser source is focused on the sample by a high-numerical-aperture parabolic mirror, identical to the one usually used for CL experiments, employing a typical repetition rate of 10 kHz and a pulse duration of ~ 30 ns. The proof of concept of this system was performed in the Vacuum Generators model HB 501 (VG) microscope and the gain peaks were only observed when the synchronization system was employed: a digital signal is sent to both the laser and the blanking plates aiming to only detect incident electrons that crossed the sample while the laser was shining. To account for the effective response time of the laser and the fast blanker (electric travel time through cables, laser electronics, light path, *etc.*), a tunable delay time was set between both input triggers, which is represented by Δt in Figure 2.3. The signal to the blanking plates is not only affected by Δt , but also by the duty cycle of the periodic input trigger. The digital “high” corresponds to the time the electrons will effectively reach the detector and so for the typical 30 ns pulse duration and 10 kHz repetition rate, the total number of detected electrons is reduced by a factor of $\sim 30 \text{ ns} / 100 \mu\text{s} = 3 \times 10^4$. In his work, Das *et al.* have demonstrated the feasibility of this approach for a single wavelength, lacking hence the spectroscopic potential of the technique. More importantly, however, the work has shown experiments in an entirely different regime from the previously mentioned studies. The synchronization is done at the detection level, and not by controlling the photo-emitted electron such as in the pulsed electron microscopes and hence opening the way to perform gain spectroscopy using continuous electron sources and, consequently, to explore the vast instrumentation advances in the past few years, most notable electron monochromators and sub-atomic electron probe sizes.

A few months later, Liu *et al.* have shown gain experiments using continuous laser and electron sources, well-known to have the best achievable spectral resolution [135]. The very low maximum light irradiance before sample damage occurs forced the use of monochromated electron sources to improve the signal-to-noise ratio to detectable levels. Although other experiments in such conditions have been performed [136], multiple wavelengths experiments have not been reported. Much more recently, however, an outstanding spectral resolution of approximately

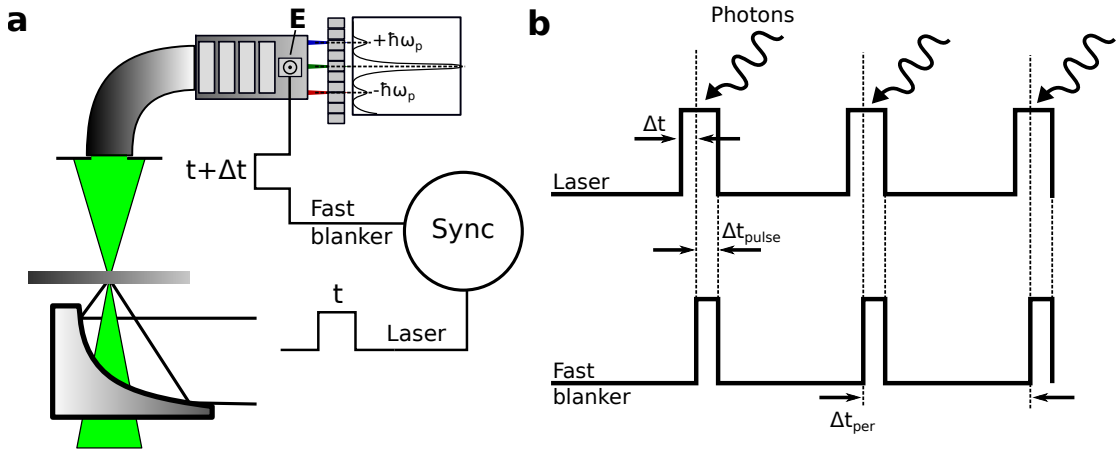


Figure 2.3: Performing EEGS experiment in a continuous electron gun. (a) The nanosecond laser source is focused on the sample by a parabolic mirror. A synchronization electronics triggers both the laser and the blanking plates within a user-defined time interval Δt . (b) The time evolution for three trigger cycles to the laser and the fast blanker with a periodicity Δt_{per} . The fast blanker has an additional parameter that controls the pulse duration Δt_{pulse} .

$3 \mu\text{eV}$, a factor of 1000 improvement from the best available electron monochromators, has been shown by using resonators with high quality factors [137]. The huge field amplification sustained by the high quality factor resonator allowed the experiment to be performed with a tunable continuous laser source without an electron monochromator. The very high photon orders (> 500) relaxed the monochromator condition as the electron energy change goes as high as 200 eV. The number of photon orders also enables the identification of the electron-photon coupling parameter, which was also mapped spatially around the resonator.

A pertinent question is, therefore, what else must be done? Albeit EEGS with μeV spectral resolution has been demonstrated, many points remain to be cleared out. First and most important, achieving such spectral resolution using cold field-emission guns (cFEGs) have immense experimental impacts. Not only by the obvious improvement in gun brightness but by the conceptual achievement of atomic-resolved EEGS when aberration-corrected microscopes are employed. Moreover, it is easy to underestimate the importance of a monochromated electron source in laser-assisted experiments, especially because the ultimate spectral resolution is going to be limited by the light source rather than the electron source. As discussed, however, EEGS maps the induced field as a response to the exciting wavelength, while EELS provides the entire absorption information over a much broader spectral range. The techniques, therefore, are not meant to be redundant but rather give complementary information about the sample. Lastly, EEGS results have found success in optical cavities, such as surface plasmon resonances and high quality-factor silica-based resonators, but still, there is much to perform in non-coherent optical excitations present, for example, in semiconductor samples.

2.2 Instrumental developments

After the proof-of-concept experiment performed by Das *et. al.*, several problems arose in the experimental setup. The most severe of them involves the multimode fiber-coupled injection system and the spatial profile of the output light beam. The beam profile of a multimode optical fiber displays a well-known so-called speckled pattern [138–140], a consequence of interference between the high number of modes that can propagate in these fibers. The amount of propagating modes can be determined by

$$M \sim \frac{V^2}{2}, \text{ with } V = \frac{2\pi a}{\lambda} NA, \quad (2.5)$$

where V is called V-number, a is the fiber core radius, λ is the light wavelength and NA is the numerical aperture of the fiber. Using the equation above, the number of modes in the waveguide used in ref. [8] is ~ 240000 ($\varnothing = 600 \mu\text{m}$, $NA = 0.22$, $\lambda = 0.6 \mu\text{m}$). Similar to the electron microscope, the focal plane of a laser focused by an optical thin lens represents the Fourier transform of the beam. By using a small round aperture in the Fourier plane, for example, one is applying a low-pass filter, letting it through only small spatial frequencies, which is precisely the principle of laser pinhole mode cleaners. With this in hand, it is easy to understand that using a large multimode fiber is very detrimental to the experiment because the focused laser spot in the sample is very large, especially useless for a nanometric electron probe. The practical impact of such a setup is that most of the input power is being used to destroy the sample rather than contributing to the electron energy-gain.

The experiment's feasibility was also severely undermined by the lack of communication and automatization between the laser source, optical components, and the microscope. Stimulated emission from organic dyes, for example, are known to have a very non-uniform response over the emitted wavelength [141–143]. As the stimulated gain peaks are dependent on the injected light intensity, the gain-spectroscopy within the assumption of constant light intensity must be performed with some sort of control system. The problem became even more obvious if one consider the response function of the optical setup, which includes the chromatic aberrations and the wavelength-dependent transmissibility/reflectance from the optical components. On the microscope side, the laser wavelength control must be synchronized with the EELS detection system. As the experiments evolved, many other instrumental advances have shown to be very convenient. Additionally, a multi-microscope-compatible platform was also intended because the instrumental developments performed in a dedicated machine would be immediately ready to be performed on any machine running a similar software. More specifically, the ChromaTEM microscope was the main goal. Based on these considerations, it was decided to program the entirety of the microscope from scratch using the recent microscope software developed by Nion Company, the Nionswift [108].

2.2.1 Controlling the electron microscope

Nionswift is an open-source, cross-platform, python-based imaging software focusing on scanning transmission electron microscopes (STEMs). It encourages the creation of microscope instruments, or controllers, that are registered as hardware components in the environment. Within this picture, several controllers were developed, most notably for the electron spectrometer, the optical spectrometers, the sample stage, the collection of magnetic lenses, the apertures, and for the scanning unit. Most of them are serial-based communication (through RS-232 ports), such as the current-controller power supply of the electron spectrometer/electron lenses and the apertures. They were developed around the PySerial library [144] and, although not part of Python3 standard library, it is reliable because it was wrapped around Microsoft .NET framework System.IO.Ports, the still standard Microsoft module for serial communication (recently made cross-platform through Linux distributions). A base class was developed for most of the controllers, in which particular methods are instantiated: the EELS spectrometer, for instance, has a value setting method to control the current of the optical elements and a few others controlling the wobbler conditions. When registering a controller, one must only inherit the base class and define very few methods, called abstract methods in Python3, to have the entire controller working properly. In the electron spectrometer, this method is only the value set, as the wobbler is derived from it. This allows a much more flexible software architecture: if another user has an EELS spectrometer controlled by Transmission Control Protocol (TCP) rather than serial, there is a single method that must be re-written. Analogously, this permits the development using dummy methods, in which software tests can be done without the actual hardware connected to it.

The instruments cited above have little-to-no support from Nionswift. This is of course understandable, as one can create and instantiate virtually anything that the user wishes to be working together within the microscope environment. Scan units (SUs) and detectors, however, are mandatory in any scanning microscope. These have special base classes that must be inherited to have the myriad of already-implemented functionalities, most notable regarding the interaction in the graphical user interface (GUI). This, however, does not exempt the development of libraries for both of them but reduces the arduous task of producing consistent GUIs. The SU used in this work is a custom-made FPGA-based solution controlled through USB by a set of C/C#/C++ libraries [145], in which a Python3 wrapper was written to make it compatible with Nionswift. The SU not only controls the electron probe rastering but also possesses multiple general-purpose input/output (I/O) pins, which are used, among other things, to perform hyperspectral image synchronization between the detector and the SU. Camera components in Nionswift also profit from base classes that can be conveniently inherited by the user. When the camera component is identified as EELS, for example, complete binning in the non-dispersive direction is automatically available.

Finally, another important instantiation is the so-called STEM Controller. It

is designed in such a way that accessing the other controllers and camera/SU components are made easy and thus methods that are meant to be dependent on the multiple components of the microscope are stated there. As an example, note how the sample stage is usually set to move as a specific fraction of the current field of view of the current scanning settings. Additionally, the electron spectrometer defines the experiment dispersion, in units of eV/channel, and this must be informed to the current EELS detector, while other experiments, such as CL, have associated cameras in which their dispersion is linked to other controllers (an optical spectrometer in this case). These co-dependencies, of course, happen all the time in an electron microscope and they are all taken care of inside the STEM Controller.

The entire microscope control project has been made open-source and available under MIT license [9]. The user-interface snapshot of some developed modules can be found at the appendix of this work.

2.2.2 EEGS experiment

In this section, it is described how the flexibility of the Nionswift software has allowed the integration of multiple inter-dependent hardware to create an EEGS experiment within the microscope software environment. Before describing each one of the components and how they are related to the experiment, the used laser, unarguably the most important of them, is discussed in detail.

The dye laser

The Laser (light amplified by the stimulated emission of radiation) is one of the most research-widespread quantum mechanical devices. The key quantum effect that enables the existence of the laser is the stimulated emission (SE). SE is normally explained in terms of its quantum-similar effects: the spontaneous decay and the stimulated absorption, all of them described in Chapter 1 (see Figure 1.2). In the SE, an incident photon triggers an atomic decay from the excited to the ground state and is followed by a photon emission, coherent, in-phase, with the former photon. This description is enough to understand the first condition (i) for the existence of the laser: population inversion. If the excited state is not more populated than the ground state, an incoming photon would be more likely to be absorbed. Thus, when population inversion is maintained, a gain medium exists, such that incoming photons are likely to trigger new photons by the cost of an atomic relaxation. The second laser condition (ii) is the presence of an exciting source, capable of sustaining the population inversion from the gain media even when other photons are relaxing these states through SE. This can be done in a variety of ways, such as by direct light excitation (in which case the pump light source usually have higher-energy photons than the emitted from the gain media), by electron collisions (gaseous lamp, for example), or by chemical reactions producing molecules in their excited state. The third condition (iii)

is the presence of a resonant cavity to efficiently harvest the photons from the gain medium. For pulsed lasers, there are two ways of doing it: either by using pulsed exciting sources, in which laser output will have the lifetime limited by the excitation lifetime, or by allowing light circulation in the cavity for a finite amount of time, called Q-switch operation [146, 147]. This technique was initially developed for the freshly-designed ruby laser [148]. The long-lived gain medium excited state, around 2-3 milliseconds lifetime, is pumped by a lamp source with a similar pulse duration inside a low quality factor (Q factor) cavity, which means excited states do not efficiently decay into the ground state because of the poor photon circulation. This creates a heavily-populated excited state and, when the cavity is switched to a higher-Q value, the entire energy is quickly harvested, generated initially by the spontaneous emission of the gain media and efficiently de-excited by the circulating photons. This process creates pulses much shorter than the actual lifetime of the excited state, in the order of tens of nanoseconds for the ruby laser.

As a pump source, a Q-switched neodymium-doped yttrium aluminum garnet (Nd: YAG) laser [149] is used. Although with an excited state lifetime of approximately 230 μs , the Q-switch operation allows the creation of 20-40 ns pulses at a maximum of 10 kHz repetition rate at 532 nm. The gain media in this work is composed of an organic dye solution, mostly known as dye-lasers, first demonstrated in 1966 by Sorokin *et al.* [141, 150]. The complex chemical structure of organic dyes has as a consequence an intricate energy diagram containing multiple overlapping excited states, which have placed dye-lasers as important devices due to the continuous tunability of the output photon wavelength. Wavelength tuning is achieved by placing diffraction gratings as part of the resonant cavity, which can be used to select the energy of the circulating photon by adjusting the angle of incidence [151]. Even the most up-to-date design of dye cells is close to the impressive results obtained by Litman and Metcalf back in 1976, achieving 1.25 GHz spectral halfwidth ($\sim 5 \mu\text{eV}$) thanks to the grating-grazing incidence and a tuning mirror [152]. More than the constant tuning of a single dye laser, commercially available dye-lasers often also possess easily changeable dye cells, allowing one to choose between the hundreds of available dyes. Although several have been used in this thesis, such as DCM and Pyrromethene 580, Pyrromethene 597 was by far the most utilized organic dye. It outputs light between 566 and 611 nm with a peak efficiency conversion of $\sim 25\%$ at 583 nm [153]. Albeit organic dyes are known to be very prone to photo-bleaching, reducing efficiency conversion as fast as 20 minutes for the most fragile ones, Pyrromethene 597 is a robust dye, lasting more than over a month even under heavy utilization. The dye cell grazing-grating used has 1800 lines/mm, leading to $\sim 2.8 \text{ pm}$ laser linewidth at 595 nm, or 10 μeV spectral resolution. Tuning range is from 560 nm to 900 nm, typical grating efficiency is in the order of 10% and laser output is linearly polarized.

Controlling the experiment

The elements of the experimental setup are shown in Figure 2.4. The optical setup is divided between two main parts: the coupling of the dye-laser light beam into the optical fiber, as shown by Figure 2.4a, and the other side of the optical fiber, attached to the microscope light injection (or collection) system and shown in Figure 2.4b.

The first control developed is concerning the laser function. The laser power supply has several serial-based commands, in which pump laser current, repetition rate, and Q-switch operational condition is configured. The first two are directly controlled in the Nionswift plugin, while Q-switch operation is set to manual triggering, meaning that an external TTL pulse is responsible for the Q-switch and consequent pump laser pulse into the dye cell. This manual laser triggering is key to the experiment, as it is used to create the delay line between the laser pulse and the fast blanker aforementioned.

The achromatic lenses L1 and L2 in Figure 2.4a have the same focal point (and thus produce a telescopic imaging system with unity magnification) and are used to produce a cross-over in which the continuous neutral density gradient wheel is placed. The gradient wheel is linked to a servo motor by a mechanical belt and two homemade 3D printed rotating shafts. Additionally, an Arduino UNO is used to control the servo motor by using the microcontroller standard library [154]. The beamsplitter cube BS1 reflects 90% of the incident light, and the 10% left is sent to the power meter PM1 (Thorlabs S120C sensor with Thorlabs PM100USB interface). The power meter can be controlled by SCPI (standard commands for programmable instruments), an ASCII-based command language, through its USB 2.0 interface [155]. PM1 is mostly used to determine transmission percentage across the optical fiber, which helps during alignment and to estimate the reminiscent chromatic aberration of the optical system. The silver mirror M1 and the achromatic aspheric lens L3 are used to focus the laser beam onto the fiber. In M1, there are two angular degrees of freedom controlled by piezoelectric actuators (Thorlabs PIAK10 [156]), while L3 is mounted in 5 degrees of freedom lens mount (3 spatial and 2 angular). The fiber uses a standard fiber SMA connector and is mounted in a 3-axis NanoMaxTM flexure stage [157] using manual differential micrometers. The alignment is done mainly by playing with M1 and the fiber 3-axis stage. For a monomode fiber, typical transmission values are $\sim 8-10\%$. For the Pyrromethene dye range (566-611 nm), residual chromatic aberration produces a transmission curve as a function of the laser wavelength with $\sim 20\%$ power fluctuation.

The other side of the fiber, shown in Figure 2.4b and 2.4c uses an achromatic aspheric lens L4 to collimate light from the fiber. It is mounted in a cage system and has two spatial adjustment knobs. The silver mirror M2, which contains two angular degrees of freedom, reflects the light to the parabolic mirror inside the microscope after traversing a silica vacuum window, called the microscope edge (ME, cannot be seen in Figure 2.4c). Analogously to BS1 and PM1, there is

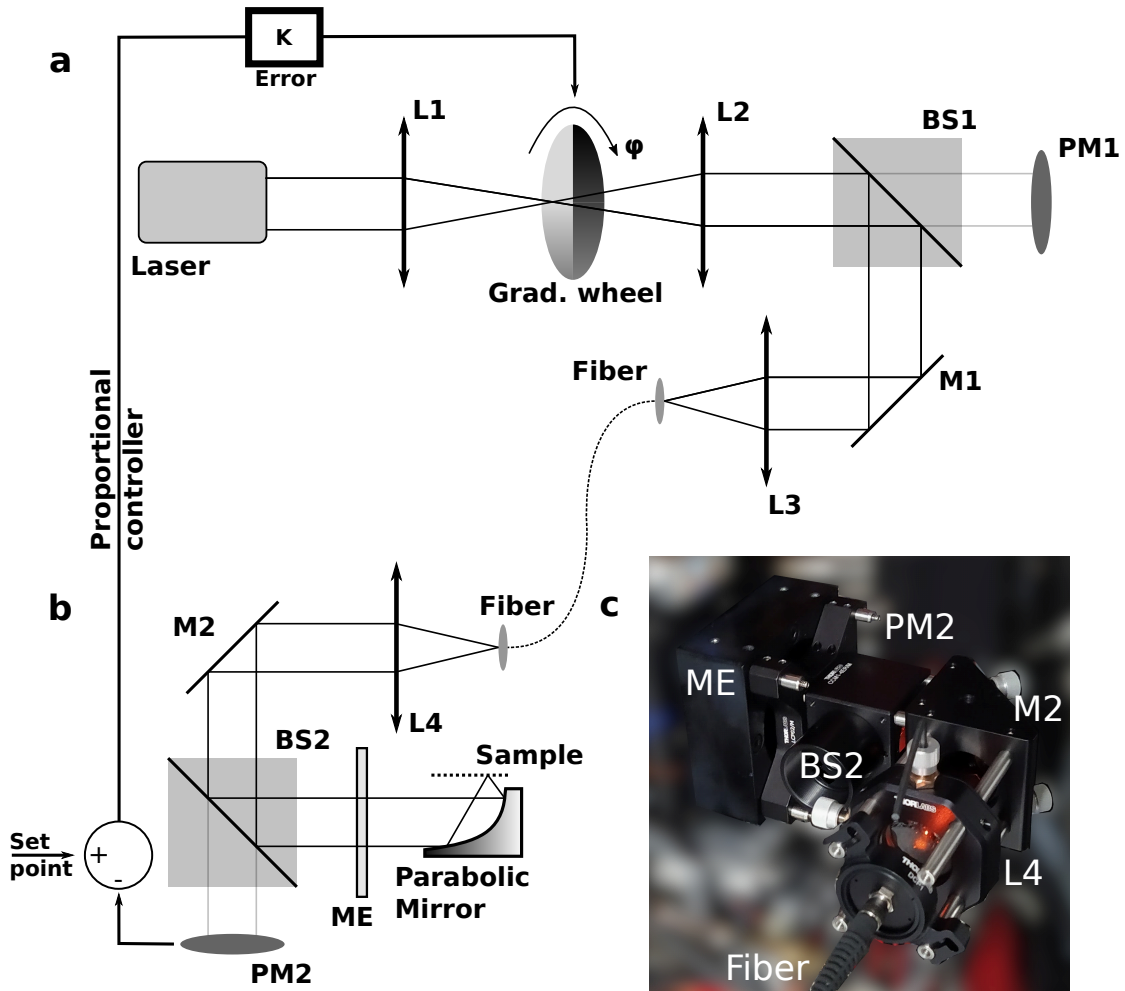


Figure 2.4: Scheme of the optical components of the EEGS experiment. (a) The laser output is focused on a gradient wheel density filter. The telescopic lenses L1 and L2 produce an output with unity magnification. The beamsplitter BS1 is used to collect 10% of the incident power in the power meter PM1. Finally, the laser beam is focused on the optical fiber. (b) The other side of the output fiber is coupled with L4. M2 and BS2 are used to send the light beam to the parabolic mirror, focusing the beam on the sample plane (dashed line). The boundary between atmosphere and vacuum (inside microscope) is represented by the microscope edge ME. (c) A photo of the partial scheme shown in (b). The gradient wheel angle φ is controlled by an Arduino UNO, which is in turn controlled by a proportional controller with a pre-determined set point and an actual measure given by PM2. L1, L2: achromatic lenses; L3, L4: achromatic aspheric lenses; BS1, BS2: 90:10 beamsplitter; M1, M2: silver mirror; PM1, PM2: power meters.

a cube beamsplitter BS2 in the light path which transmits 10% of the incident light to the power meter PM2 (Thorlabs S120C sensor with Thorlabs PM100USB interface). Additionally, note how there is a scheme of a proportional controller between PM2 and the gradient wheel in Figure 2.4. During EEGS acquisition, laser power must be constant across the different wavelengths, which is not the case for organic dyes. Even using a pre-calibrated dye efficiency correction proved to be a poor solution due to the chromatic aberration of the system, meaning that a robust solution necessarily involves a control system, independent from the current state of the optical system. The power control is performed within the Nionswift environment as a thread running only during data acquisition.

The third part of the experiment that must be controlled is the fast blanker and its synchronization system with the laser pulses, as mentioned in the introduction and shown in Figure 2.3. The fast blanker uses a pair of copper plates that can deflect the electron beam by a few millimeters (size of a typical EELS detector) and can reach a maximum repetition rate of 20 kHz. The typical applied voltages are ± 400 V when using 100 keV electrons, for example. Further details on the blanker instrumentation can be found in references [8] and [158]. In this scenario, three signals must be controlled in the nanosecond time-precision range: each one of the plates and the laser Q-switch input. For this, the custom-made scanning unit developed by Marcel Tencé [145] was used. The unit not only has the necessary control for the scanning coils of the microscope, but it also has multiple input/output (I/O) lines that are available to be programmed running in a 200 Mhz clock (5 ns temporal resolution). As both the signals in the fast blanker plates are subjected to identical electronics, the impulse response function of the electronics is expected to be similar. The laser Q-switch signal, on the other hand, is subjected to unknown electronics and physical processes, not to mention distinct cable lengths, *etc.* To account for all those variations, a signal delay parameter must be integrated into the software, which is easily done in the SU FPGA with the same 5 ns temporal resolution. Additionally, a time width parameter is added to the equation to determine the exposure of the camera to the temporally selected electrons. Ideally, this value must be identical to the laser pulse duration to have an optimal signal-to-noise ratio.

The alignment procedure of the laser-fiber coupling in Figure 2.4a has been described and it follows a standard interactive process performed in the elements M1 and L3, aiming to maximize the transmitted power through the fiber. The most challenging part, however, is the alignment of the single fiber relative to the sample plane in Figure 2.4b. This alignment is performed in two steps: alignment of the mirror relative to the sample and alignment of the fiber relative to the mirror. This was first achieved and improved in the available VG microscope by placing an optical table close to the CL system, as previously stated. The resulting system has been transferred to ChromaTEM and is shown in Figure 2.4c.

The entire laser, optics, and fast blanker control project has been made open-source and available under MIT license [10]. In the appendix, the reader can have

more details on how EEGS experiments can be performed with the instruments (laser, optical components, *etc.*) far from the microscope control computer. Additionally, a picture of the laser and the user interface developed for the EEGS experiment control is displayed.

2.3 Methods and results

In this chapter, the alignment of the optical setup shown in Figure 2.4b&c is described in detail. It is demonstrated that a sub-micrometer spot size is conjugated at the sample plane when the sample is illuminated by a monomode optical fiber. Finally, I discuss the limitations of using waveguides for the present work, as well as suggestions to circumvent such problems.

2.3.1 Alignment

As mentioned in early sections, a robust alignment of the light injection system must encompass both the alignment of the mirror relative to the sample and the alignment of the fiber relative to the mirror, sketched in Figure 2.5a. In light-collection experiments, large-core fibers or fiber bundles relax the fiber-mirror alignment because of their large surface area. For single fibers, fiber-sample alignment is critical and a maximum transmitted power happens when both alignments are properly performed.

The alignment procedure thus consists of reducing progressively the fiber core size from $\sim 600 \mu\text{m}$ to $10\text{-}25 \mu\text{m}$ while carefully adjusting the x-y fiber position and the mirror z-axis (see Figure 2.5a for axis direction). Despite this method being reliable after a bit of experience, I have developed an experiment to measure the field-of-view of the fiber, which in turn means that it is possible to objectively determine the beam size in the sample plane during the light injection. The mechanical spectral-image, so-called like this because of its 3D dataset containing two spatial coordinates and one spectral component, is performed by rastering the light point source position in the x-y plane (or, equivalently, rastering the mirror), and, for each of its position, collect a CL spectrum. In other words, a light spectrum is collected for multiple uniformly-spaced d values, in both x and y directions, as shown in Figure 2.5a. The total light intensity 2D histogram corresponds to the fiber field-of-view in the current fiber and mirror positions. The results for multiple fibers with different core radii are shown in Figure 2.5b. Measurements were performed by scanning a nano-diamond of $\sim 100 \text{ nm}$ size containing multiple nitrogen-vacancy emission centers. The $200 \mu\text{m}$ fiber shows a field-of-view of approximately $13 \mu\text{m}$, meaning that if light was injected through this fiber, the light spot at the sample plane would have a similar size. For a monomode fiber, the determined spot size was approximately 800 nm , which allows a much higher power density at the sample plane if compared to the early experiments using $600 \mu\text{m}$ core fibers.

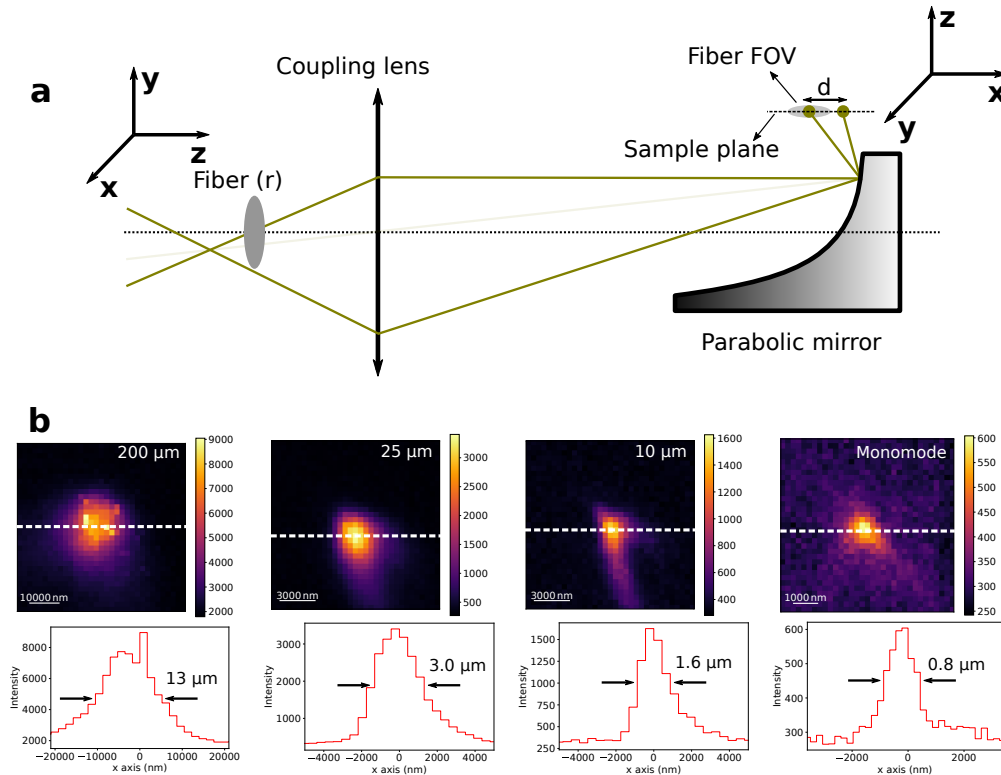


Figure 2.5: Scheme of the fiber-mirror alignment. (a) The fiber, with core radius r , produces a field-of-view (FOV) at the sample plane after the coupling lens and being focused by the parabolic mirror. If a point emitter is displaced by a distance d greater than the FOV, the light emitted from the point is not collected. (b) The field-of-view for different fiber radii. These 2D histograms are formed by rastering the point emitter position around the focal point of the parabolic mirror and acquiring a spectrum for every pixel. The integrated photon intensity across all wavelengths is shown.

2.3.2 Preliminary experiments

Although most of this thesis has been developed in the instrumentation-dedicated VG microscope, no results obtained in this machine will be shown in this section. Not for a lack of interesting data, but rather by the existence of gain experiments performed in the new generation of the microscope, much harder to obtain due to the complexity of the machine and the technical constraints. A small discussion is nevertheless presented in the next section regarding what has been done in the older microscope to put the improved experiment in perspective.

Early results

The very first EEGS experiments were performed by directly coupling the laser into a big 600 μm optical multimode fiber. As discussed before, these fibers sustain a huge number of modes and thus limit the size of the focused spot. Additionally,

they output speckled beams, which makes the gain experiment virtually impossible in both the spatial domain and in the energy domain thanks to the dependency of the speckled pattern on the laser wavelength. Because of the large laser spot and the consequent poor power density, electron energy-gain signal was only observed with laser powers as high as ~ 100 mW. Most of the deposited energy contributed to heat-induced sample damage without contributing to the energy-gain signal. More information on these early experiments can be found in references [8, 159].

The natural development of the experiment was to perform it using free-space optics. The improvement has allowed injecting a Gaussian beam into the mirror and thus perform meaningful spectral images, as well as, for the first time, laser-assisted spectroscopy, or EEGS. Most of the experiments were performed using ~ 1 mW laser power, a two order of magnitude improvement in power density. Polarization-resolved experiments were also performed, confirming the feasibility of this experiment despite using a parabolic mirror as a focusing optical device. These results are extensively discussed in reference [159].

Unarguably the most flexible way of working with laser beams, free-space optics, however, can impose constraints. In the ChromaTEM, the presence of an optical table attached to the CL system is impossible due to the poor mechanical stability of this system. Additionally, the laser cannot be placed close to the microscope because of the noise induced by the cooling systems and the dye circulator pump. The solution found was to use a fiber-based miniaturized optical setup, as shown in Figure 2.4c. The dye laser has remained in another room, mechanically decoupled from the microscope. The optical fiber used has ~ 40 m in length in order to connect both ends (between Figure 2.4a and 2.4b).

ChromaTEM results

The experiments in ChromaTEM shown are all carried out using the electron monochromator, in which the spectral resolution was set between 30 - 100 meV depending on the needs and the electron energy (30 meV was only achieved in 60 keV electrons). The standard sample used to perform the experiments is a lacey carbon in which a 50-200 nm layer of silver is deposited by Joule deposition. The silver-carbon lacey itself is enough to have multiple energy-gain hotspots but more controlled samples can be produced by shining single intense laser pulses to produce silver spheres ranging from 50 to 200 nm in diameter. The first gain signals were, therefore, obtained in very similar conditions when compared with the experiments in the VG microscope using the optical fiber; the unique difference being the expected difference in the time delay parameter because the laser was kept in the optics room, both for convenience and for isolating it from the microscope. The total distance between the microscope control and laser control was ~ 40 m and thus an optical fiber and the Q-switch co-axial signal cable with the appropriate length was used.

Initial ChromaTEM measurements were performed aiming to characterize the fast blanker. The best achieved ZLP at 100 keV with the blanker on is ~ 60

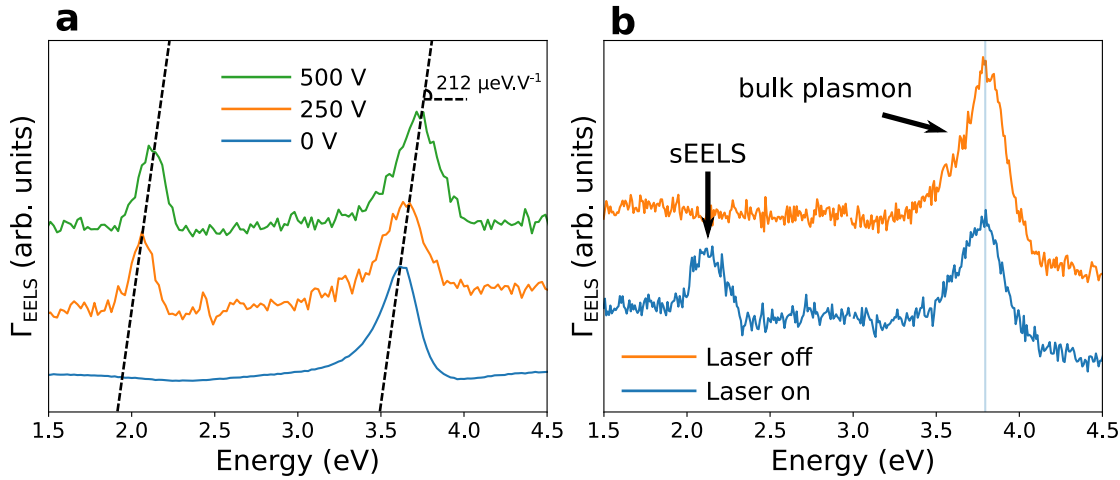


Figure 2.6: The impact of the blanking plates in ChromaTEM. EELS resolution is ~ 60 meV and the microscope voltage is set at 100 keV. (a) The pair of copper plates of the fast blanker acts as a quadrupolar element, which changes the EELS dispersion. (b) Laser on and off with the fast blanker on. Silver bulk plasmon energy does not change as a function of temperature.

meV, significantly higher when compared with the normal EELS spectrum, which was first attributed to a non-perfectly aligned blanking plate relative to the non-dispersive axis of the spectrometer. EELS dispersion, however, was found to be dependent on the voltage supplied to the fast blanker, suggesting the plates are acting as a quadrupolar element, as can be seen in Figure 2.6a by the energy shifting of both the simulated energy-loss peak¹ and the silver bulk plasmon. The energy shift in the bulk plasmon, however, can be due to the laser presence, as both bulk and surface plasmons resonances are known to be temperature-dependent [160–162]. In Figure 2.6b, no bulk plasmon energy shift is obtained as the laser is switched on and off, which reinforces the quadrupolar hypothesis.

The microscope at 60 keV not only has an intrinsic better spectral resolution but also the fast blanker uses a smaller voltage for a complete deflection of the beam from the EELS detector, which in turn alleviates some of the perceived problems. Figure 2.7a shows a typical gain curve for a constant average laser power of ~ 2 mW rastering between 575 nm and 605 nm within a 0.5 nm step, meaning an approximate ~ 1.5 meV spectral distance between adjacent laser wavelengths. Acquisition time per spectrum was 500 ms, with an average of 25 spectra per laser wavelength, and hence roughly 12.5 minutes total acquisition time. Sample contamination was not a problem under the aloof electron probe and the good vacuum conditions of ChromaTEM. The microscope was at 60 keV and a spectral resolution of ~ 30 meV was achieved, which unveiled the presence of multiple sub-replicas spaced by approximately 60 meV (~ 14.6 THz or 490 cm^{-1} , as shown by δ_1 and δ_2 in Figure 2.7c) due to Stimulated Raman amplification in silica, and

¹Remember EEGS experiments actually produces resonances at both sides of the ZLP.

which is discussed in the following paragraphs. However, this experiment shows with remarkable clarity the principle of gain spectroscopy: thanks to the 30 meV spectral resolution, the resonance position of the gain peaks follows the energy of the photon shone onto the sample. To better grasp the technical improvement relative to the previous experiments in a non-monochromated cFEG STEM, Figure 2.8 compare experiments in similar laser rastering conditions, from 575 nm to 605 nm with a spectrum dwell time of 500 ms, and similar energy-gain amplitudes. For the non-monochromated machine, 100 spectra are taken for each laser wavelength using 1.0 nm steps. For ChromaTEM, the number of averages is 25 and the laser

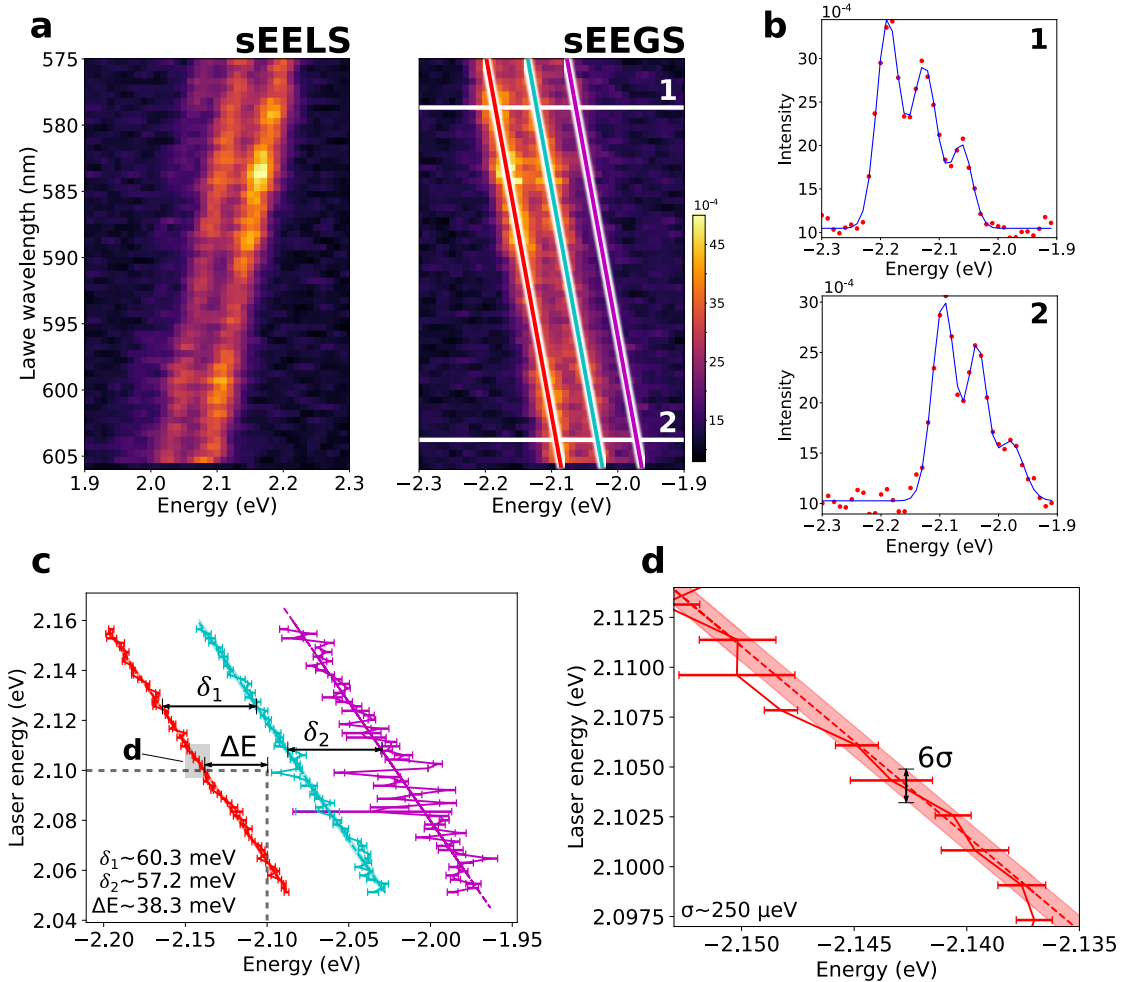


Figure 2.7: Energy-gain results in ChromaTEM with a spectral resolution of ~ 30 meV (at 60 keV). (a) Gain spectroscopy curves for the loss (left) and the gain (right) side of the ZLP, showing the multiple sub-replicas found during the experiments. (b) Two examples of fitting for the white horizontal lines in (a). A triple Gaussian model was used. (c) The mean of the three Gaussians for every laser wavelength. (d) The filled curves describe the measurement uncertainty over a $\pm 3\sigma$, displaying an unequivocal correspondence between EELS and the laser wavelength in approximately ~ 250 μ eV.

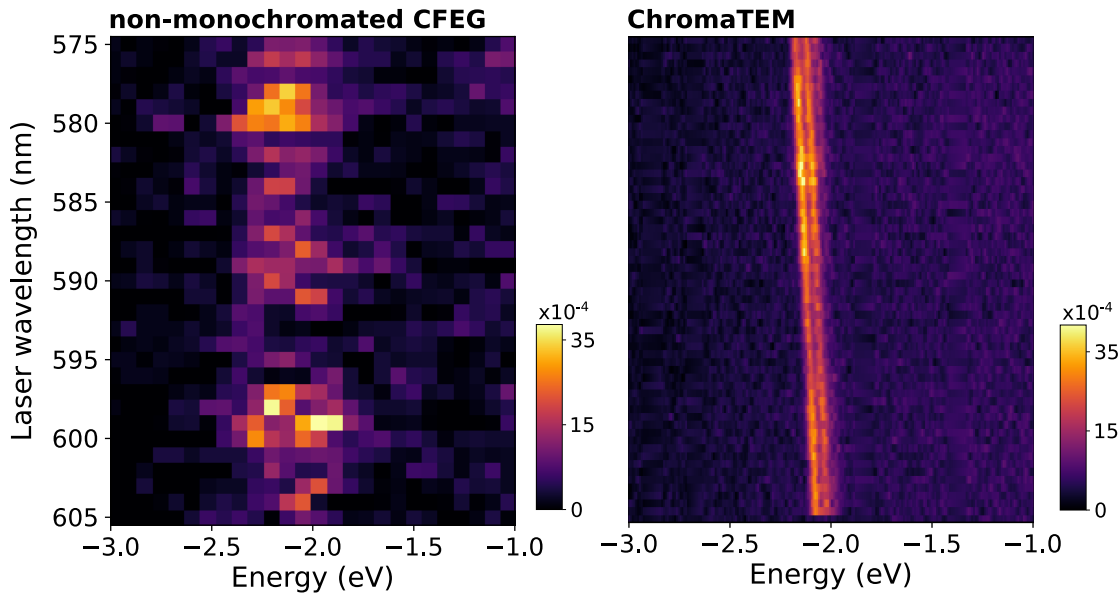


Figure 2.8: Comparison of EEGS curves for two microscopes in a similar acquisition condition, from 575 to 605 nm and 500 ms dwell time per spectra. In the left, the VG microscope is used, which has a cFEG electron source but not an electron monochromator. Each wavelength is averaged 100 times and the laser step is 1.0 nm. In the right, the measurement is performed on ChromaTEM. In this case, each wavelength is averaged 25 times and the laser step is 0.5 nm.

step wavelength is 0.5 nm. Note, however, that the studied sample is different in each case and thus the objective is not to compare the spectral features, but rather the increase of signal-to-noise ratio in ChromaTEM due to its improved spectral resolution.

Each laser wavelength curve in Figure 2.7a was fitted using an unconstrained triple Gaussian model. Two of these fitting results are shown in Figure 2.7b, associated to the horizontal white lines named “1” and “2” in Figure 2.7a. The mean of the Gaussians is displayed in Figure 2.7c. The filled regions represent the uncertainties of the results over three standard deviations ($\pm 3\sigma$). As expected, the standard deviation increases as long as lower-intensities sub-replicas are considered, which is just a matter of uncertainty propagation from the Gaussian fittings. The achieved standard deviation here is used as a suggestion of the effective spectral resolution of the gain spectroscopy. In the present case, EELS can unequivocally be associated with a well-defined laser wavelength within $\sim \sigma \pm 250 \mu\text{eV}$, for the most energetic and intense sub-replica. This value is already more than 10x smaller than the fwhm of the ZLP, but still not yet the laser linewidth of $10 \mu\text{eV}$, which is attributed to the low gain signal, in the order of 10^{-3} of the ZLP. Unfortunately, increasing this value by simply increasing laser power, as it should be done, is not possible because the stimulated Raman amplification is destroying the spectral density of the laser beam. Finally, note the 38.3 meV spectral

shift between the electron and the laser energies, depicted by ΔE in Figure 2.7c. The laser has been calibrated within a 0.1 nm spectral resolution using an optical spectrometer, or around 360 μeV at 580 nm, and thus suggesting a possible miscalibration of the electron spectrometer. This value must be carefully re-measured in the near-future, as it could have important consequences for EELS experiments.

Raman response function of silica-core fibers was extensively studied in the past, with extraordinary contributions from Stolen *et al.* during the AT&T efforts in fibered communications [163–165]. Figure 2.9a exemplifies the problem. The dye laser employed has a very high spectral density, meaning all its power is comprised in ~ 2.8 pm linewidth. Upon interaction with silica, Raman scattering produces multiple replicas equally-spaced in energy, also called Stokes orders. These higher-order peaks are more than 100x broader than the pump wavelength, which destroys the laser spectral density. This effect is severely worsened by the use of a monomode optical fiber, which has a small core size, and by the 40 m long fiber. In Figure 2.9b, the spectrum of ~ 8 mW laser output from the fiber is shown, which confirms the multiple Stokes orders. In Figure 2.9c, the relative intensity of each of the multiple Stokes shifts is shown as a function of the output power, which follows a Poisson distribution, given by

$$f(k, \lambda) = \frac{\lambda^k e^{-\lambda}}{k!}, \quad (2.6)$$

where λ is the average number of events and k is the number of scattering events. For the fundamental laser, the number of Raman scattering is zero, thus associated with k_0 . The k parameter increases by an unit for successive higher-order Stokes peaks, as shown in Figure 2.9b. In Figure 2.9c, the k value is determined for each curve, giving the ratios of $k_3/k_1 \sim 2.9$ and $k_2/k_1 \sim 1.8$. For the unscattered peak, the fitting gives $k_0 \rightarrow 0$, which approximates to an exponential decay in 2.6. For intense optical pulses, only 20% of the laser power is output at the initial and narrow laser wavelength, which severely cripples the experiment. Unfortunately, the intensity of these features as a function of laser wavelength is difficult to interpret because although the laser power at the sample is constant across wavelengths, the necessary input power before fiber coupling is not. Equivalently, the transmission efficiency of the optical setup is wavelength-dependent. It can be stated, therefore, that there are no solutions apart from mitigating the stimulated Raman scattering from the input light field.

In this scenario, few solutions are possible to reach more meaningful EEGS experiments. First is shortening the optical fiber, which can be done by moving the laser closer to the microscope. This is currently a non-ideal solution considering the demanding microscope environment: the high current used in the pump Nd: YAG laser and the mechanical noisy power supply and pumps can be very detrimental to ChromaTEM performance. An alternative solution involves using multimode fibers to transfer most of the laser power, and includes an optical setup system to spatially filter laser modes before injecting them onto the sample. Other fiber

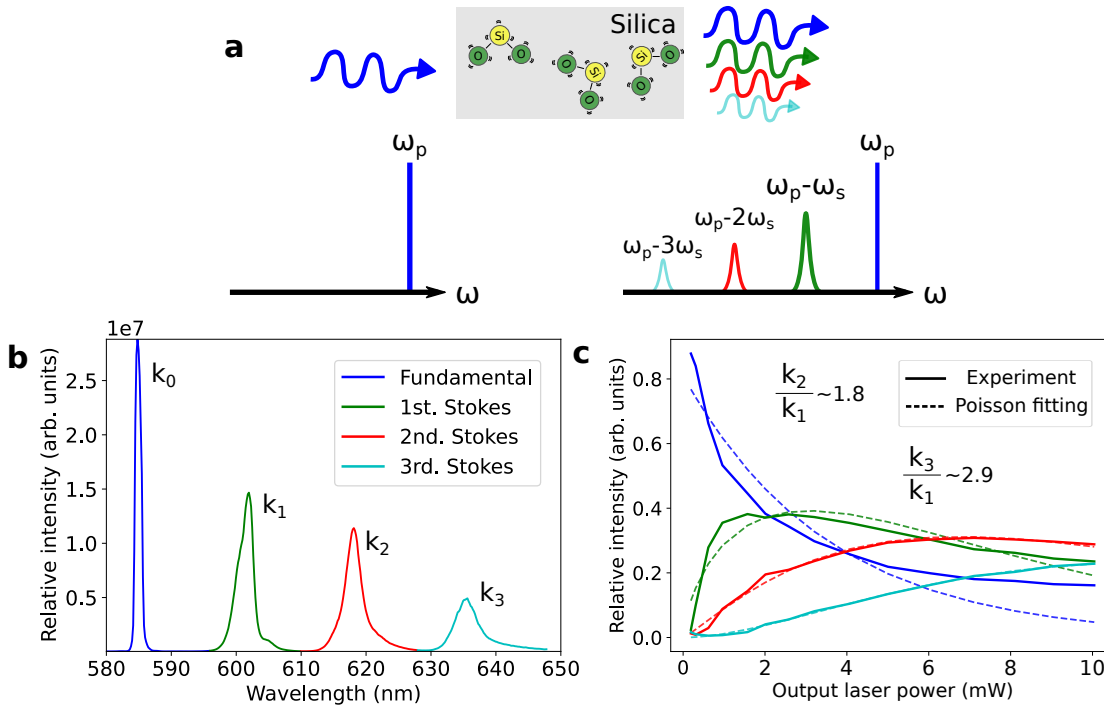


Figure 2.9: Stimulated Raman amplification in mono mode silica fibers. (a) A narrow-band laser interacts with silica, the core material of optical fibers. Raman scattering in silica outputs a light beam containing multiple wavelengths, or Stokes shifts, that are not useful for electron energy-gain spectroscopy. (b) The spectrum of the laser beam immediately before being shone into the sample. The output power is ~ 8 mW, a typical value used in EEGS. (c) The ratio between the replica intensity relative to the total spectrum intensity shows the Poissonian nature of these Stokes shifts.

technologies can also be utilized, especially hollow photonic crystal fibers which would prevent stimulated Raman for obvious reasons. Despite the many available options, the solution decided to be explored within the thesis period was to use ultrashort picoseconds laser sources. The natural broadening of the laser linewidth reduces the power spectral density and, for the same average power compared with the nanosecond dye laser, no stimulated Raman peaks were observed in the 40 m silica core optical fiber.

2.3.3 Gain without the fast blanker

In the previously mentioned ChromaTEM experiments, the fast blanker is used to synchronize the laser pulse with electron detection, drastically increasing the signal-to-noise ratio. The fast blanker, however, can present a few experimental inconveniences, such as losing the EELS loss signal, the change in electron dispersion due to its quadrupolar effect, and its limitation in the maximum repetition rate, currently around 20 KHz. This section explores options in which EEGS can be performed without the fast blanker

Using electron monochromators

Gain experiments with a monochromated electron beam were systematically performed without the fast blanker and using the nanosecond dye laser. Due to the Raman amplification and consequent small power spectral density, gain peaks were limited in intensity, displaying nevertheless easily-seen resonances after a few seconds of acquisition time, with probabilities around 10^{-7} , which are 10^4 weaker compared to the blanker-on counterpart, as expected. These experiments have been much easier to perform after the installation of the Medipix3 direct electron detector, which has virtually no readout noise, and thus spectra accumulation is performed with no additional cost.

For the experiments, a supercontinuum white laser (SuperK FIANIUM, from NKT Photonics) was used. Much more convenient than the dye laser, it provides fiber-coupled diffraction-limited output from 400 to 2400 nm range. The pulse width is approximately ~ 15 ps with a tunable repetition rate from 150 kHz up to 78 Mhz. In the maximum repetition rate, the laser duty cycle (on-to-period rate) is approximately $\sim 10^{-3}$, similar to the dye laser $\sim 0.3 \times 10^{-3}$, which means that the laser peak power per pulse is also similar for the same average laser power. The SuperK FIANIUM also has available multi-line filters, capable of output up to 8 different wavelengths simultaneously with bandwidths ranging from 2.0 nm in the UV range from 15 nm in the infrared range. Several energy-gain spectra for distinct laser wavelengths are shown in Figure 2.10. They were obtained using the maximum repetition rate of 78 Mhz and an average power of $\sim 1.5 \pm 0.5$ mW. The interest in using such lasers lies in their flexibility when compared to organic dyes. Not only the available energy range is much broader, but output power along them is also very stable. Finally, the fiber-coupled system can be directly used with the alignment procedure described early on. As a drawback, EGGS using picosecond laser sources in a continuous electron gun can only be performed in a microscope with an electron monochromator due to the absence of beam blanker in ChromaTEM working in such high repetition rates. Additionally, the spectral broadening of such sources is in the order of \sim meV, meaning no μ eV spectroscopy can be performed.

Exploring the temporal resolution of such devices might be possible under specific circumstances. As is discussed in the next paragraphs, a new generation of event-based electron detectors is emerging. These are capable of collecting the temporal information of all the individual electrons hitting the EELS detector. Additionally, some of these detectors have time-to-digital converters (TDCs), allowing external signals to imprint timestamps signatures in the normal electron data flow.

Using Timepix3

Timepix3 (TPX3) is a hybrid pixel detector capable of detecting electrons without the need of a scintillator layer and is thus known as a direct electron detector.

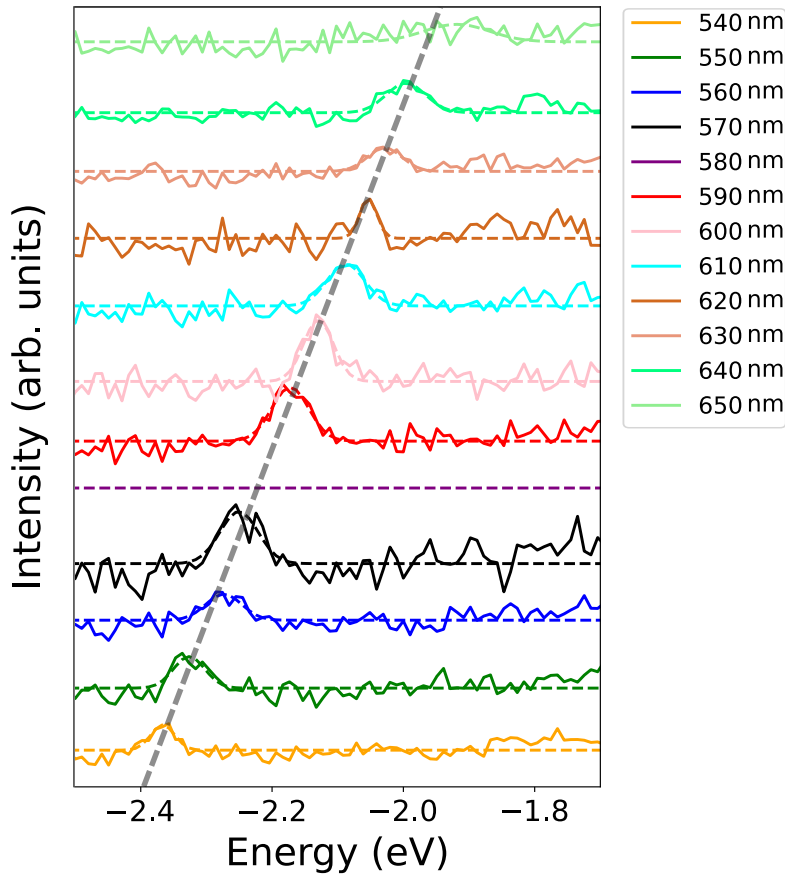


Figure 2.10: EEGS performed using a 15 ps laser pulse at 78 Mhz repetition rate without the fast blanker. Spectral bandwidth in these conditions depends on each wavelength but is roughly ~ 10 nm. Peak intensity is approximately 10^{-7} relative to the ZLP and no higher-order replicas have been observed.

Every pixel has a counting threshold, effectively detecting a hit only if the incident signal surpasses a certain intensity. Therefore, it offers a noiseless, high-quantum-efficiency, low point spread function (PSF) way of performing EELS. TPX3 will be extensively discussed throughout this work, including in its own chapter later on. This section, however, is going to provide a glimpse of its capabilities, showing that EEGS can be performed in a continuous electron gun without neither an electron monochromator nor a fast blanker.

Gain experiments were performed using the dye laser at 10 kHz repetition rate and with the CheeTah TPX3 solution from Amsterdam Scientific Instruments [166] in the VG microscope and, therefore, without an electron monochromator. The electrons that arrive in the detector are individually identified in the raw data. Each one contains multiple information but, in the current experiment, only one spatial coordinate (in the dispersive axis direction) and the time of arrival are relevant. In addition to the electron events, CheeTah also has two TDCs, which allows two TTL-based signals to be plugged in. These work as supplementary

events and the readout board is capable of creating timestamps for both the rising and the falling edge of these signals. The interesting part of the CheeTah solution is that both the electron and the supplementary events are read relative to the same clock, defined as 40 Mhz in the readout FPGA board. The Q-switch signal can be simultaneously sent to both the laser and one of the CheeTah TDCs. Electron energy-gain resonances are expected to happen at a constant time delay from the Q-switch timestamp and must last approximately the laser pulse duration. Figure 2.11a shows this concept for a laser power of ~ 25 mW and the dye laser set at 585 nm of approximately 1 s acquisition time. At time delay defined as 0 ns, four gain replicas can be seen, lasting between 20 ns and 30 ns. In Figure 2.11b, the time of arrival relative to the last Q-switch signal is plotted for the electrons at the left of the ZLP (and hence the gain side) for distinct pump laser currents, which are seen to change the laser pump delay time and, to a lesser extent, the laser pulse duration, as can be seen in Figure 2.11c after performing a Gaussian fit in each one of the curves. This experiment can be regarded as a form of coincidence experiment, relating electrons with external events in the time domain. One can think of studying the EELS loss spectrum side as a function of the laser pulse intensity, such as variations in the dielectric response function of the sample. Alternatively, temperature-dependent measurements can be performed if the EELS spectrum is studied as a function of the time delay, in which the sample goes from high temperatures during the laser pulse but relaxes to the environment conditions afterward.

Using TPX3 instead of the fast blanker has proved to be a much better solution in many aspects. As it will be seen in the TPX3 chapter in this thesis, an acquisition software capable of translating raw individual electron data to frame-based conventional data in a live fashion was developed, exempting the user from the burdening task of post-processing for every acquired data. The live signal allows switching between time-resolved and conventional spectra as fast as when using the fast blanker. In this scenario, TPX3 does not suffer from all the aforementioned fast blanker issues (quadrupolar effect and misalignment relative to the detector) and, more importantly, the electrons are not prevented to arrive in the detector; they are just not shown for the user. This means that spectral images can be reconstructed for both gain-resolved and using all the available electrons simultaneously. Signal saturation, however, is the single drawback of using TPX3 rather than the fast blanker. As it will be discussed later, TPX3 has three distinct and independent saturation bottle-necks: pixel-wise due to the inherent dead-time that must be elapsed between successive hits; column-wise due to the way data outputs from the detector and detector-wise thanks to the limited bandwidth that can be transmitted between the FPGA and the client computer. During EELS measurements, column saturation is usually the bottleneck and thus ZLP intensity can become meaningless during gain acquisition, although it can be estimated by proper detector masking.

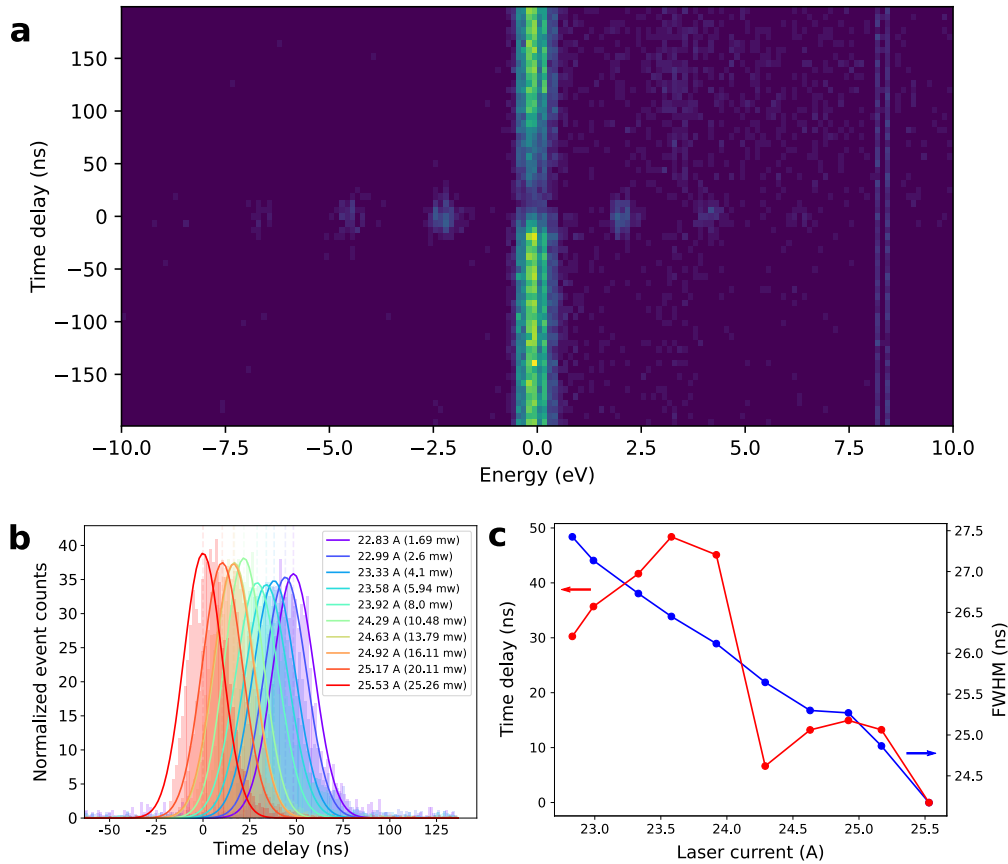


Figure 2.11: Electron energy-gain measurements using TPX3. (a) The laser Q-switch is sent to the TDC, creating timestamps that can be compared to the time of arrival of individual electrons, as seen by the histogram of the time difference as a function of the electron energy. (b) The number of hits in the left side of the ZLP as a function of the time elapsed from the last TDC for multiple laser currents, or powers. A dependency of the laser pulse arrival time on the pump laser current was observed. Pulse width changes slightly but is roughly ~ 26 ns. (c) Gaussian fitting results of the curves in (b).

2.4 Conclusions & prospects

In this chapter, EEGS performed with a continuous electron gun was extensively discussed. The technique is still much more challenging when compared to the energy-gain experiments performed in ultrafast electron microscopes. The energy-gain with the continuous gun, however, allows the use of narrower linewidth laser sources, such as the nanosecond dye lasers used in this work, and can benefit from a huge number of modern microscope technologies that are not normally available in pulsed electron guns. These can be as fundamental as the electron gun, in which cFEGs are the current standard and can reach higher brilliance relative to thermionic or Schottky FEGs used in pulsed guns; or more complex microscope features, i.e. aberration correctors and electron monochromators.

The instrumental developments in this thesis have allowed to systematically perform gain experiments using fibered solutions in ChromaTEM, a cutting-edge microscope capable of reaching ~ 5 meV spectral resolution. CL experiments are used to align the high-numerical-aperture parabolic mirror within $1 \mu\text{m}$ of the microscope central field of view to perform the light injection. Initial results with the electron monochromator have shown details of the fast blanker operation, unveiling a quadrupolar effect. EEGS was performed at best with 30 meV spectral resolution, clearly showing the dependency of the resonance position on the external laser wavelength. Unfortunately, further results were undermined by the presence of a strong stimulated Raman effect in the 40 m long monomode silica fiber. Energy-gain without the fast blanker was briefly discussed, in special exploring the ultrafast laser sources with similar duty cycles and by using an electron detector capable of output the temporal information of the electron events.

The EEGS development was first designed to be tested on high quality factor microcavities, such as whispering-gallery mode resonators (WGMRs) or photonic bandgap crystals. Although this experiment has not yet been performed in ChromaTEM, the next chapter nonetheless shows one example on how EEGS can be used when EELS and CL do not provide the necessary spectral resolution. Future experiments also include the study of metallic nanoparticles by EELS, CL and EEGS, which has not already performed within the same machine and using an electron monochromator. This could experimentally validate many theoretical aspects of these spectroscopies. Finally, many developments are underway to systematize EEGS with sub-meV spectral resolution as a standard spectroscopic technique, which can be performed in the current system by mitigating the stimulated Raman from the input light. Additionally, it is expected to run ChromaTEM with TPX3, which would allow a myriad of different time-resolved experiments to be performed.

Although it was suggested the usage of TPX3 as a possible solution to perform EEGS experiments without a beam blanker, many interesting applications can emerge by improving the 5 ns temporal resolution of the fast blanker used beyond the TPX3 time bin of 1.5625 ns. Similar to energy-gain experiments in ultrafast electron microscopes, in which a laser pulse is sent to the electron gun and the sample within an adjustable time delay in-between, ultrafast gain experiments in a continuous electron gun could be performed by using photo-activated ultrafast beam blanker, instead of the 5 ns static plates used, in the detection system, as depicted in Figure 2.12a. Such a system has already been implemented [167, 168], achieving a deflection voltage of 10 V with repetition rates as high as 100 Mhz, and a temporal resolution of ~ 100 fs, the same order of magnitude of EEGS in ultrafast electron microscopes. Additionally, the event-based nature of TPX3 could be used to improve the temporal resolution at least by two orders of magnitude of the variety of beam blanker designs intended to be used in continuous electron gun microscopes [168–170]. To do this, one can use the non-dispersive direction of the detector, as shown in Figure 2.12b. As in TPX3 the x , the y and

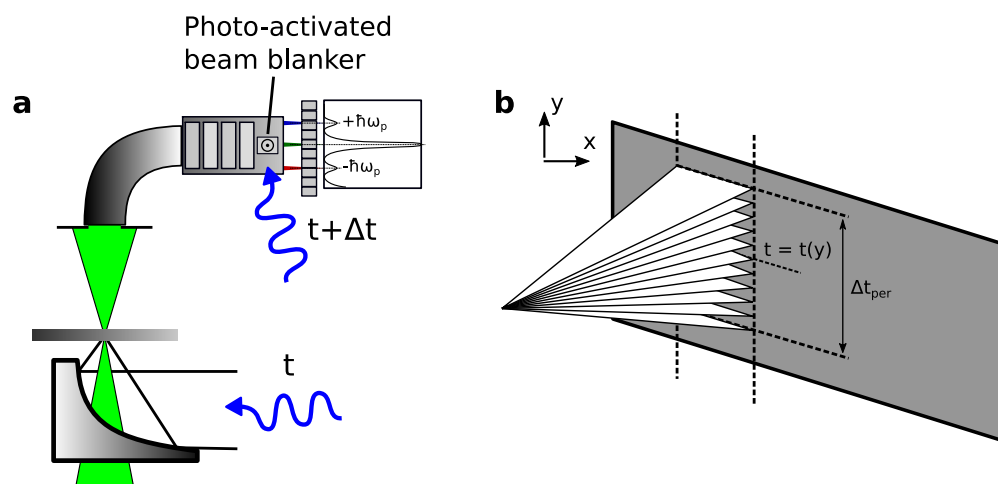


Figure 2.12: Ideas for improving the temporal resolution of EEGS experiments. (a) Using a photo-activated beam blanker allows to send the same laser beam to the sample and to the blanker with an optical delay line between them, similar to what is performed in ultrafast electron microscopes. (b) With an event-based detector, the blanking repetition rate, associated with the period Δt_{per} , can be sampled an additional factor of 256, the non-dispersive direction of the detector, in the limit of a single-line ZLP.

the electron time of arrival (ToA) are simultaneously known, the detector rows can be used to further sample the repetition rate of the fast blanker, and hence a thin ZLP in the non-dispersive direction is ideal. In this scenario, TPX3 and fast blanker synchronization must be done, similar to what is described in chapter 4 between the TPX3 and the microscope scanning unit, as will be seen later on this work.

Optical microcavities & electron beams

3.1 Introduction

The past few years have witnessed unprecedented advances in photonic technologies. In particular, plasmonics has attained the precise engineering of absorption and scattering properties of metallic nanoparticles (MNPs) due to improvements in synthesis methods [171–174]. Indeed, the surface plasmon resonances are dependent on a variety of parameters of the MNPs. Concurrently to this emerging technology, fabrication techniques have allowed the widespread use of optical microcavities, such as whispering-gallery mode resonators (WGMRs) and photonic bandgap crystals, which have attracted strong interest in the context of quantum electrodynamics, [175, 176] optomechanics, [177, 178] and sensing applications [179–181]. The tuning capability of all these devices makes the study of coupled systems particularly interesting as we discuss throughout this work.

Similar to a musical instrument, optical microcavities have a size-dependent resonant spectrum. These have a variety of possible designs, such as the already-mentioned WGMR, a pair of parallel reflecting surfaces, also called Fabry-Perot resonators [182, 183], or microdisks or toroids in which a single circulating plane is defined [184–186], to name a few. In the simplistic geometrical optics frame, the light in such structures is trapped due to successive total internal reflections. Unable to leave the optical resonator, the light would be circulating indefinitely, and, due to the well-defined size of the device, the circulating wavelength would also be perfectly defined. In wave optics, however, perfect spherical resonators do not exist, nor completely non-absorbing media. To account for such imperfections, a quality factor (Q factor) is usually defined for each resonant mode. For a resonant mode at the angular frequency ω and linewidth $\Delta\omega$, the Q factor is defined as

$$Q = \frac{\omega}{\Delta\omega} = \omega \frac{E_T}{P_{loss}} = \omega\tau, \quad (3.1)$$

where E_T is the total energy stored in the cavity, P_{loss} is the dissipated power and

τ is the cavity ring-down time or the photon lifetime. Since the first theoretical description [187] and their experimental observations [188, 189], the quest for high Q factor resonators has begun. Initially used for particle-size, material, and temperature identification, these high-Q devices were later explored in fluorescence [190, 191], lasing [192, 193] and cavity quantum electrodynamics through both strong [194, 195] and weak [196, 197] coupling. In a general way, the Q factor follows an inverse sum law [11] such as

$$Q^{-1} = Q_{int}^{-1} + Q_{rad}^{-1} + Q_{sur}^{-1}, \quad (3.2)$$

where Q_{int} , Q_{rad} and Q_{sur} represent, respectively, the Q factor related to internal, radiative, and surface losses. For silica and quartz resonators, the absorption in the IR and VIS region of the spectrum is minimal and thus Q_{int} can reach Q factors as high as 10^{11} , much higher than the highest reported experimental values of 10^{8-9} [18, 198, 199]. Q_{sur} is generally associated with surface roughness or material adsorption, which are usually small for modern synthesis techniques and high-vacuum measurements. However, some of the resonators scrutinized in this work were deposited onto a thin amorphous carbon membrane of approximately ~ 20 nm, which certainly impacts the ultimate Q factor obtained. Additionally, resonators in which a MNP is attached to its edge, also called coupled resonators, are also subjected to a strong reduction of their Q_{sur} , especially for lossy adsorbed materials such as metals. Finally, Q_{rad} is related to the a/λ ratio in WGMRs, where a is the sphere radius, meaning it could be made arbitrarily high by increasing the sphere radius. Spheres of $40 \mu\text{m}$ have theoretical values of $Q_{rad} \sim 10^{23}$ for modes close to $\lambda = 1550$ nm, for example. In photonic bandgap crystals, point defects can be engineered by disturbing the periodic lattice, which allows light to be confined in a small mode volume V . The Q_{rad} related to these point defects are usually limited by the in-plane radiation leaking [200], and thus many efforts have been put to design the lattice disturbance with the highest possible Q_{rad} . Figure 3.1(b&c&d) show a scheme of a WGMR, a coupled WGMR and a photonic bandgap crystal with a missing hole, associated with a point defect.

The aforementioned mode volume V is another important figure of merit of all optical microresonators, which can be described as the electromagnetic field localization or the energy stored per unit volume in the cavity [181, 199]. For Fabry-Perot resonators, a typical mode volume for a resonance of $Q \sim 10^5$ is $V \sim 10^5 \mu\text{m}^3$ [201]. For WGMRs, modes of $Q \sim 10^9$ are associated with mode volumes of $V \sim 10^3 \mu\text{m}^3$ [199]. For photonic bandgap crystals, the extreme mode localization means they have the smallest possible mode volume, even for relatively low quality factors. For resonances of $Q \sim 10^4$, mode volume can reach values as small as $V \sim 10^{-1} \mu\text{m}^3$ [200].

As a final relevant common property of optical microresonators, the resonances are characterized by their transverse electric (TE) or transverse magnetic (TM) polarization, in which the electric and magnetic field have no radial components relative to the confined mode wavevector, respectively ($\mathbf{r} \cdot \mathbf{E} = 0$ for TE and

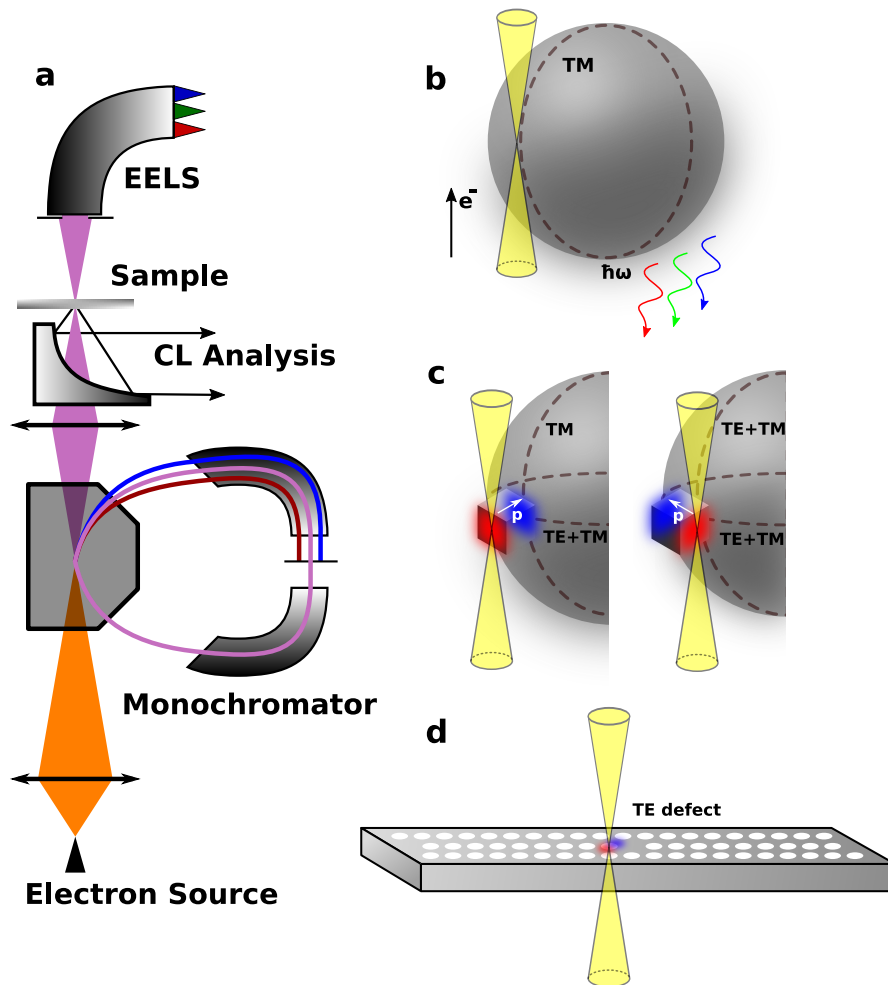


Figure 3.1: Configuration used to study the coupling between electrons and microcavities. (a) Scheme of an electron microscope containing an electron source, an electron monochromator, a cathodoluminescence (CL) mirror, the sample and an electron spectrometer. (b) Scheme of an electron beam and the excited TM mode (dashed line) in a bare dielectric sphere. (c) Through the addition of a metallic nanocube, the polarization of the excited WGM can be controlled by the electron-probe position. (d) The missing hole in a photonic bandgap cavity opens a single-defect state that can be spatially described by electron energy-loss spectroscopy (EELS).

$\mathbf{B} \cdot \mathbf{E} = 0$ for TM). A fast electron excites TM modes much more efficiently than TE modes, which can be understood by the absence of a radial electric field component in TE modes [87, 202]. Point defects in photonic bandgaps, for example, have TE polarization as the electric field is in the plane of the 2D periodic structure. As already seen in chapter 1, EELS measures the EMLDOS in the direction of the electron propagation, and, since there is a weak net electric field in this direction, this sample must be tilted in order to effectively probe such point defects. The dependence of EELS on the cavity mode polarization is further

discussed in the text for both WGMR and photonic bandgap crystals.

There is an understandable scarcity of works concerning electron beams and microcavities, most of them due to the lack of sufficient spectral resolution in previous electron microscopes. Figure 3.2 shows selected works using the three spectroscopic techniques used in this thesis, in which other optical excitations are included for comparison purposes, such as measurements of defects in semiconductors [92], different from all the others for being non-phase-locked with the exciting fast electron, and surface plasmon resonances [112, 204]. Henke *et. al.* have measured a whispering-gallery resonance in ring resonators with Q factors two orders of magnitude greater than all previous works [137] by electron energy-gain, demonstrating for the first time the outstanding potential of such technique. As a downside, if any, electron energy-gain spectroscopy (EEGS) measures a narrow-band energy range relative to what EELS and CL can typically do, and thus the number of identified modes are generally reduced [13]. Wang *et. al.* have measured the band structure of photonic bandgap crystals by EEGS by controlling both the excitation wavelength and the photon incident angle [132]. Cathodoluminescence experiments have a much greater potential for mapping several modes

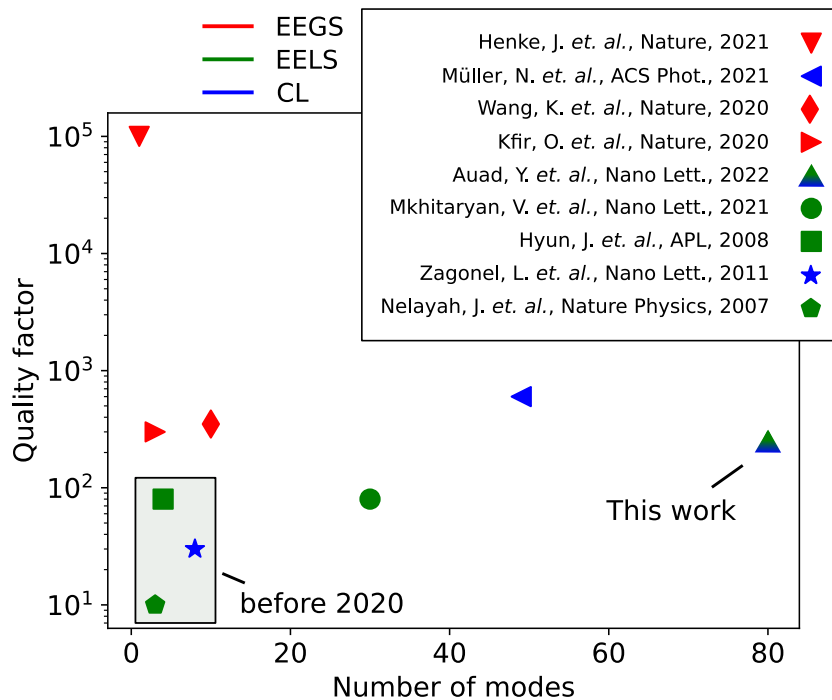


Figure 3.2: Selected works of measured optical excitations in an electron microscope using EEGS, EELS and CL. EEGS was used to map WGMRs by Henke *et. al.* [137] and Kfir *et. al.* [13] along with photonic bandgap crystals by Wang *et. al.* [132]. CL was used to identify defects in semiconductors by Zagonel *et. al.* [92] and whispering-gallery resonances by Müller *et. al.* [203]. EELS is used to identify several surface plasmon modes [112, 204], a few low-Q whispering-gallery resonances by Hyun *et. al.* [14] and multiple higher Q gallery-modes, as shown in this chapter [16].

with reasonable quality factors, as shown by the work of Müller *et. al* [203]. CL, however, can only identify modes in the visible range, and higher Q mapping usually comes with a reduced field-of-view of the optical spectrometer. EELS can measure gallery-modes even close to the silica bandgap at ~ 9 eV, as shown by Hyun *et. al* [14], but, with an extreme degree of monochromaticity, much smaller energies modes can be mapped, from 1.5 eV up to close to the silica bandgap [16], as shown later in this chapter. Finally, by combining EELS and CL, one can map the same resonance with different techniques, and thus with different attainable Q factor mapping, providing complementary information of the WGMR, either coupled with a MNP or not [16].

In this chapter, microresonators are scrutinized under electron beams in a highly monochromatic electron microscope. Especially, WGMRs of $\sim 2 \mu\text{m}$ radius are studied, both bare and coupled with MNPs, by EELS, CL and EELS. In the bare resonators, more than 80 resonant modes have been observed, from 1.5 to 7.0 eV. In the coupled resonators, which are simply bare resonators with MNPs attached to their edge, these modes interact with the modes of the nanoparticle by weak-coupling, leading to a dependence of the coupling strength on the selected mode order. A few preliminary results of EELS in photonic bandgap crystals are also discussed. More specifically, the spatial mapping of a single missing hole defect is identified, which should lead to important insights to map ultrahigh-Q photonic crystals. These experiments are sketched in Figure 3.1.

3.1.1 Whispering-gallery mode resonators

A physical description of whispering-gallery modes was first proposed by Lord Rayleigh using acoustic waves circulating the dome of St. Paul's Cathedral [205]. To obtain the electromagnetic-wave analog of this system, the diameter of tens of meters of the cathedral must be scaled down to the micrometer range e.g. in circular or spherical microstructures. Resonances are characterized by their transverse electric (TE) or magnetic (TM) polarization and a set of angular, radial, and azimuthal mode numbers (l , q , and m). Besides, WGMRs made from materials with low intrinsic loss, such as silica, can sustain modes that have exceptionally high Q factors [175].

The analytical solution to explain WGMRs are long to obtain, although it starts from the relatively simple Maxwell's equations. The Helmholtz's equation for the electric and magnetic field can be obtained from the vector identity $\nabla \times (\nabla \times \mathbf{E}) = \nabla(\nabla \cdot \mathbf{E}) - \nabla^2 \mathbf{E}$, and in the absence of charges,

$$\left. \begin{aligned} \nabla^2 \mathbf{U}(\mathbf{r}) + k^2 \varepsilon \mu \mathbf{U}(\mathbf{r}) &= 0, \\ \nabla \cdot \mathbf{U}(\mathbf{r}) &= 0, \end{aligned} \right\} \quad (3.3)$$

where \mathbf{U} can be both \mathbf{E} and \mathbf{B} . To solve this problem, the above vector equation is substituted by three scalar wave equations with solutions as $\Psi(\mathbf{r})$. They are subsequently written in spherical coordinates, in which variables can be separated

($\Psi(r, \theta, \varphi) = \Psi(r) \times \Psi(\theta) \times \Psi(\varphi)$), and, with the appropriate boundary conditions, three independent solutions of this system are found in terms of the vector spherical harmonics [25]

$$\left. \begin{aligned} \mathbf{X}_l^m &= \nabla Y_l^m \times \mathbf{r} / \sqrt{l(l+1)}, \\ \mathbf{Y}_l^m &= \nabla Y_l^m r / \sqrt{l(l+1)}, \\ \mathbf{Z}_l^m &= Y_l^m \mathbf{r} / |\mathbf{r}|, \end{aligned} \right\} \quad (3.4)$$

in which the electric field, for both polarizations, are [206–208]

$$\left. \begin{aligned} \mathbf{E}_{lm}^{TE}(\mathbf{r}) &= \frac{1}{kr} E_0 f_l(r) \mathbf{X}_l^m(\theta, \varphi), \\ \mathbf{E}_{lm}^{TM}(\mathbf{r}) &= \frac{1}{n^2} E_0 \left(\frac{\partial f_l(r)}{\partial r} \frac{1}{k^2 r} \mathbf{Y}_l^m(\theta, \varphi) + \sqrt{l(l+1)} f_l(r) \frac{1}{k^2 r^2} \mathbf{Z}_l^m(\theta, \varphi) \right). \end{aligned} \right\} \quad (3.5)$$

Inside the resonator ($r < a$), $f_l(r) = \psi_l(kr)$, and, outside, $f_l(r) = C_1 \psi_l(kr) + C_2 \chi_l(k_0 r)$, where ψ_l and χ_l denote, respectively, the first and second type Riccati-Bessel functions, C_1 and C_2 are coefficients to be determined, n is the refractive index of the resonator, and a is its radius.

The solutions of $f_l(r)$ also respect a radial equation [206, 207], which was used by Nussenzveig as an analogy with the time-independent Schrödinger equation [209], in which the effective potential is equivalent to considering the trapped light as a bounded state. Higher values of l produce evanescent fields that leak very little to the exterior of the resonator and could only escape by tunneling through the potential barrier. These low-leaking modes will circulate many turns and, consequently, have high Q factors.

Resonant frequencies

The multiple resonant mode frequencies can be obtained from this mathematical model by solving the spherical boundary conditions i.e. the continuity of the tangential components in the set of equations 3.5

$$\left. \begin{aligned} C_1 \psi_l(kr) + C_2 \chi_l(k_0 r) &= \chi_l(ka), \\ C_1 \psi_l'(kr) + C_2 \chi_l'(k_0 r) &= P \chi_l'(ka), \end{aligned} \right\} \quad (3.6)$$

where $P = n$ or $P = n^{-1}$ for TE and TM polarization, respectively. Assuming large ratios of a/λ , an expression for the resonant condition can be written in terms of the Bessel (J_u) and Neumann (N_u) functions [206, 207] such as

$$P \frac{J'_{l+1/2}(nx)}{J'_{l+1/2}(nx)} = \frac{N'_{l+1/2}(nx)}{N'_{l+1/2}(nx)}, \quad (3.7)$$

where $x = 2\pi a/\lambda$ is usually called the size parameter. By solving this equation, one can define a free spectral range as the spectral distance between adjacent modes of the same polarization and radial order as

$$\Delta\nu_{q,l}^{\Delta l=1} \approx \frac{c}{2\pi na}, \quad (3.8)$$

and also derive the spectral distance between modes of the same radial and angular order but with distinct polarization

$$\Delta\nu_{q,l}^{TM-TE} \approx \frac{c}{2\pi na} \frac{\sqrt{n^2 - 1}}{n}. \quad (3.9)$$

Alternatively, the scattering of a plane wave by a dielectric sphere can also be studied under the Mie-Lorentz theory. In this picture, Mie efficiencies for the light extinction, scattered, absorbed, and backscattered can be calculated from a pair of coefficients [25, 202, 210, 211] that can be written such as

$$t_l^M = \frac{-j_l(x)x_1 j_l'(x_1) + x j_l'(x) j_l(x_1)}{h_l^+(x)x_1 j_l'(x_1) - x [h_l^+(x_0)]' j_l(x_1)}, \quad (3.10)$$

and

$$t_l^E = \frac{-j_l(x)[x_1 j_l(x_1)]' + \varepsilon [x j_l(x)]' j_l(x_1)}{h_l^+(x)[x_1 j_l(x_1)]' - \varepsilon [x h_l^+(x_0)]' j_l(x_1)}, \quad (3.11)$$

where $x_1 = 2\pi a/\lambda\sqrt{\varepsilon}$, ε being the dielectric function inside the resonator, h_l^+ and h_l^- are the spherical Hankel functions, outgoing and ingoing waves for the + and – superscripts, respectively, and j_l^+ and j_l^- are spherical Bessel functions, following the same propagation convention as the spherical Hankel functions.

EELS & CL in WGMRs

The analytical solution of the energy loss and radiation emission probability of a fast electron upon interaction with a spherical dielectric body can be written as [87, 202, 212]

$$\Gamma_{\text{loss}}(\omega) = \frac{1}{c\omega} \sum_{l=1}^{\infty} \sum_{m=-l}^l K_m^2 \left(\frac{\omega b}{v\gamma} \right) \times [C_{lm}^M \Im\{t_l^M\} + C_{lm}^E \Im\{t_l^E\}], \quad (3.12)$$

and

$$\Gamma_{\text{rad}}(\omega) = \frac{1}{c\omega} \sum_{l=1}^{\infty} \sum_{m=-l}^l K_m^2 \left(\frac{\omega b}{v\gamma} \right) \times [C_{lm}^M |t_l^M|^2 + C_{lm}^E |t_l^E|^2], \quad (3.13)$$

where K_m is a modified Bessel function of order m , b is the electron impact parameter relative to the sphere center, t_l^M and t_l^E are the Mie scattering coefficients

aforementioned, which depend exclusively on the sphere radius and its dielectric function, and C_{lm}^M and C_{lm}^E are coupling coefficients that depend on the ratio of electron to light velocities v/c and can be found in ref. [212]. These simple results show that EELS and CL are well-fitted tools to study extinction and scattering spectroscopy at the nanometer scale. Note that, for lossless media, the dielectric function is real and by using mathematical properties of the spherical Bessel functions, $\Im\{t_l^{M,E}\} = |t_l^{M,E}|^2$, which means $\Gamma_{\text{loss}}(\omega) = \Gamma_{\text{rad}}(\omega)$. For complex dielectric functions, $\Im\{t_l^{M,E}\} \geq |t_l^{M,E}|^2$ and hence $\Gamma_{\text{loss}}(\omega) \geq \Gamma_{\text{rad}}(\omega)$. In other words, the energy lost in the form of radiation is always smaller than the total energy lost by the incoming electron [202].

3.1.2 Whispering-gallery mode resonators & metallic nanoparticles

Due to their high Q factor, coupling light to a WGMR is a challenging task. Efficient methods almost always rely on evanescent fields using gratings, prisms, or tapered fibers [11, 209, 213, 214], as shown in Figure 3.3(a&b). In particular, fiber tapering can reach coupling efficiencies as high as 99% but requires active positioning to maintain this level of performance over long periods. Free-space light is an alternative to evanescent coupling, but it has only encountered partial success with spheres [12, 215] and asymmetric cavities [216, 217] having high radiative losses due to the bounded nature of the gallery modes.

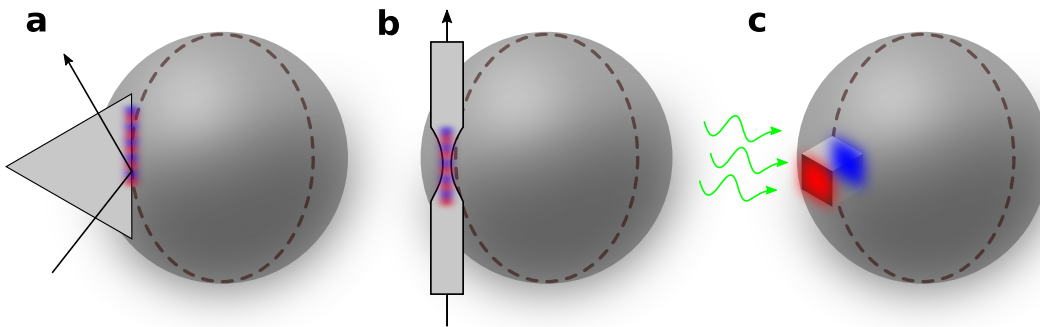


Figure 3.3: Methods of exciting WGMRs. (a) Using frustrated total internal reflection in a glass prism. (b) Using tapered optical fibers. (c) Using nanoparticles attached to the edge of the resonator in order to couple far-field radiation.

A practical solution to the problem is to couple an intermediate (e.g., plasmonic) nanoparticle to the gallery modes and to employ it as an evanescent light coupler into the WGMR microresonator [218–221], sketched in Figure 3.3c. This approach has been successfully used to detect and characterize the nanoparticle using mode energy shifting [17, 222, 223], splitting, [18, 224] or broadening [225, 226] of the unperturbed resonances. Single-metallic-nanoparticle and gallery-mode coupling using far-field light has been studied for applications in photocatalysis, [227]

as well as for engineering ultranarrow plasmonic resonances [228, 229]. Selective coupling into TE and TM modes depending on the incident free-space light polarization has also been observed [230], finding interesting applications in sensing thanks to the clearer mode identification enabled by this method [181]. However, a sufficient degree of spatial resolution to study the induced near electric field is still lacking in all of the mentioned studies.

An alternative to studying nanoparticles with high spatial resolution is to use a scanning transmission electron microscope (STEM). EELS and CL spectroscopy are techniques that can be performed inside the STEM and can combine the sub-nm probe size with high spectral resolution (<10 meV) when monochromatic electron sources are used. EELS and CL have been extensively explored to study small (radius < 150 nm) spherical particles [88, 97, 231], including the observation of low-order optical modes in SiO₂ spheres by Hyun *et al.* [14]. Large spheres (radius > 1.5 μm) have been studied with electron beams by using photon-induced near-field electron microscopy [4], in which a few gallery modes have been observed due to the interaction of an externally applied optical field with the free electrons [13]. More recently, Müller *et al.* have measured broadband light emission from high-Q WGMRs using fast electrons [203], but without the complementary information obtained from EELS. Most of these examples, however, could not resolve a large number of modes. Besides, the bare resonators did not offer much to be spatially explored due to their spherical symmetry.

3.1.3 Photonic crystals

The seminal work of Eli Yablonovitch entitled “Inhibited Spontaneous Emission in Solid-State Physics and Electronics” [39] has shown that carefully designed periodic dielectric structures can forbid light propagation in a band of the electromagnetic spectrum and hence they exhibit the so-called electromagnetic bandgap. Yablonovitch’s work marks the beginning of the blooming era of photonic bandgap crystals [232, 233].

The origin of the photonic bandgap can be more easily understood in 1D periodic structures, such as the one shown in Figure 3.4a. For a periodicity of d , the primitive reciprocal lattice vector is $(2\pi/d)\mathbf{z}$ and the Brillouin zone comprises $-\pi/d \leq k \leq +\pi/d$. Because the wavevector repeats itself outside the Brillouin zone, the light line folds at $k = \pi/d$, which explains the wavevector range shown in Figure 3.4(a&b). For the case of $n_1 = n_2$, at the edge of the Brillouin zone, $\lambda = 2d$ and there are two possible phase configurations of the propagating electric field, as depicted by the purple and the red curves in Figure 3.4a. When there is an index of refraction contrast, i.e. $n_1 > n_2$, the electric field profile is forced to change. It is possible to show that for such a case, the low-frequency modes concentrate their energy in the media with the highest index of refraction [234]. In other words, the spatial energy redistribution due to the index of refraction contrast splits the allowed frequencies, creating an electromagnetic bandgap. For

consistency with most available textbooks, it is worth mentioning that the upper and the lower bands are also sometimes referred to as air and dielectric bands.

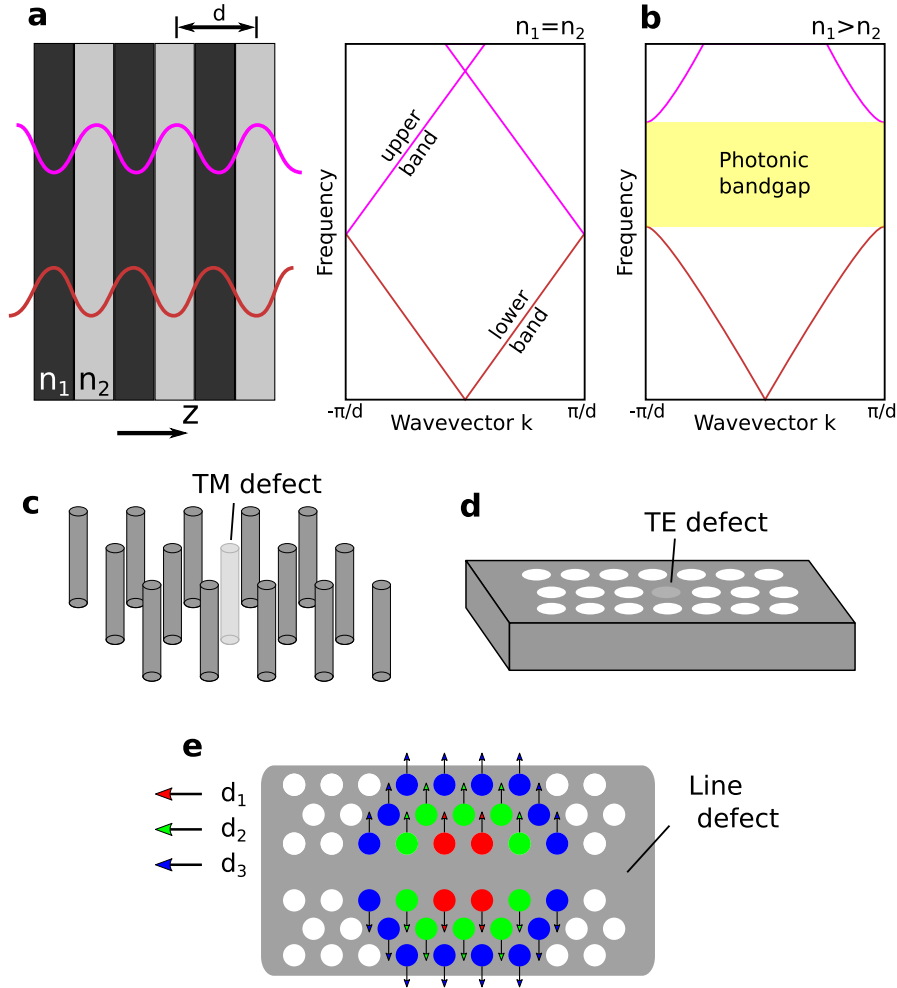


Figure 3.4: Properties of photonic bandgap crystals. (a) The periodic sheets have a periodicity of d and the electric field amplitude for the upper band (purple curve) and the lower band (red curve) are shown for $k = \pi/d$ and $n_1 = n_2$. (b) If $n_1 > n_2$, the energy redistribution between the dielectric sheets split the allowed light frequencies, and an electromagnetic bandgap is opened. (c) A 2D periodic structure of pillars is prone to exhibit a TM bandgap. (d) Conversely, an array of holes is prone to display a TE bandgap. (e) The photonic bandgap design by Kuramochi *et. al.* [235] tried in this work. The distance of neighbor holes of a line defect are modulated by different distances d_1 , d_2 , and d_3 .

2D periodic structures are subjected to similar reasoning, although in this case the bandgap band structure must be independently determined for each TE and TM polarization. In general, a periodic structure of dielectric rods with air gaps between them is much more prone to exhibit a TM bandgap; TE gaps being difficult to open. Conversely, a periodic array of holes is usually associated with

TE band gaps, as shown in Figure 3.4(c&d). A complete photonic gap, with simultaneous TE and TM band gaps, can be fabricated by carefully designing the crystals with large holes and thin veins connecting the structure, although experimentally challenging. The reason behind the relation between design and either TE or TM gap is complex [234], but can be more easily grasped by a similar argument as for the 1D structures: large band gaps are related to the contrast of the energy density of the fields between the dielectric (high ε) and the air layer (or the low ε). In the set of dielectric rods within an air media, TE polarization fields are both weak media because they are forced to penetrate low- ε regions. In the complementary structure, the continuous presence of material provides high- ε paths for the fields to propagate on and thus a much higher contrast of the fields between the dielectric and the air region [234].

Extreme light-localization can be achieved by perturbing the dielectric periodicity of the crystal by a single or multiple lattice site. These are most known as point defects and are the equivalent of having a single state within the forbidden electromagnetic bandgap. There are several ways of designing such defects in 2D photonic crystals, ranging from local lattice radius adjustment [236–239], by removing them completely [240], by removing sites and perturbing the periodicity [200], or by complete line defects [241]. These outstanding and numerous examples engineered photonic crystals with Q factors as high as 10^5 . More recently, Kuramochi *et. al.* have designed an ultrahigh-Q cavity ($Q \sim 10^6$) by modulating the local width of a line defect [235], which is sketched in Figure 3.4e and is the base design studied in this thesis.

3.2 Results

3.2.1 Bare microspheres

Non-functionalized SiO_2 spheres from BangsLabs Inc [242] ranging from $1.5 \mu\text{m}$ to $2.0 \mu\text{m}$ in radius have been used for the experiments. The microscope is a modified Nion Hermes 200 fitted with an Attolight Mönch CL system, known as ChromaTEM throughout this thesis. Experimental results were interpreted by energy-loss simulations done by using a 3D finite-difference time-domain (FDTD) method available in Ansys Lumerical [124] and based on the work from Cao *et. al.* [243] by using custom-made Lumerical and Python3-based post-processing scripts. Mie scattering calculations were used to estimate the sphere radius [210, 244]. The dispersion values for the SiO_2 response were taken from Malitson’s work [245].

Figure 3.5 shows the combined results of EELS and CL using acceleration voltages of 200 kV and 100 kV for one bare sphere suspended on a carbon membrane of ~ 20 nm thickness. More than 80 resonances were observed in the broadband excitation using 200 keV electrons in EELS, while no energy loss was observed for 100 keV due to the reduced coupling for slower electrons. In both the experimental results and the FDTD simulations, TE polarization is poorly excited by the fast

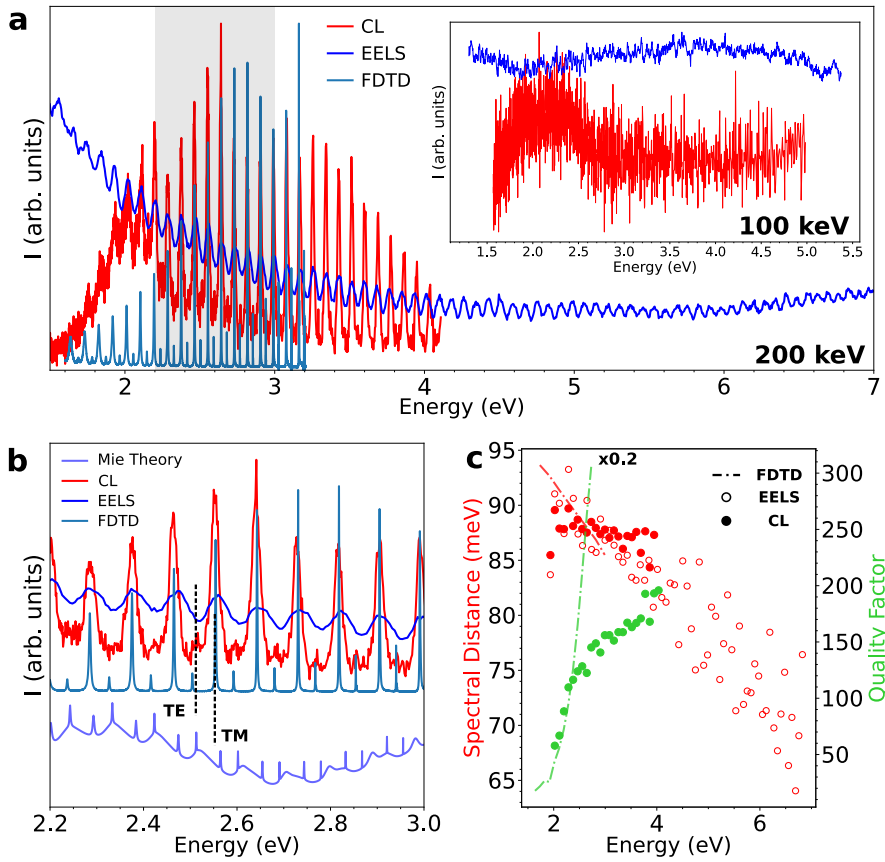


Figure 3.5: Emergence of optical modes in a SiO_2 sphere of $1.595 \mu\text{m}$ radius. (a) EELS and CL spectra were measured by using 200 keV electrons, compared to FDTD simulations. The inset shows measurements at 100 keV, lacking any visible resonances. (b) Zoomed area around the highlighted gray rectangle in (a). (c) Measured CL and simulated FDTD Q factors, plotted along with the spectral distance from EELS, CL, and FDTD. The FDTD Q factor is divided by a factor of 5 for readability.

electron, also as a consequence of equation 3.12 due to the smaller coupling terms of TE in comparison with TM for these electron energies.

Each resonance in EELS and CL was fitted with a Gaussian and the obtained center subtracted from the adjacent mode to form a spectral distance curve, which was subsequently compared with the theoretical free spectral range (FSR)[207, 246]. These values were used for modes from 2.0 eV to 3.0 eV to extract the effective index of refraction. The index was calculated to be 1.398 at 2.0 eV and 1.409 at 3.0 eV, which are values that agree within $\approx 95\%$ with reference values [245]. Beyond 3.0 eV, modes have Q factors exceeding 10^5 from Mie Theory, which would be easily washed out by losses and finite energy resolution of our experimental setup. This is especially important for the far-UV resonances observed in EELS, as multiple sets of radial orders combined with the limited spectral resolution of the electron beam undermine mode order identification and the estimative of the index of refraction.

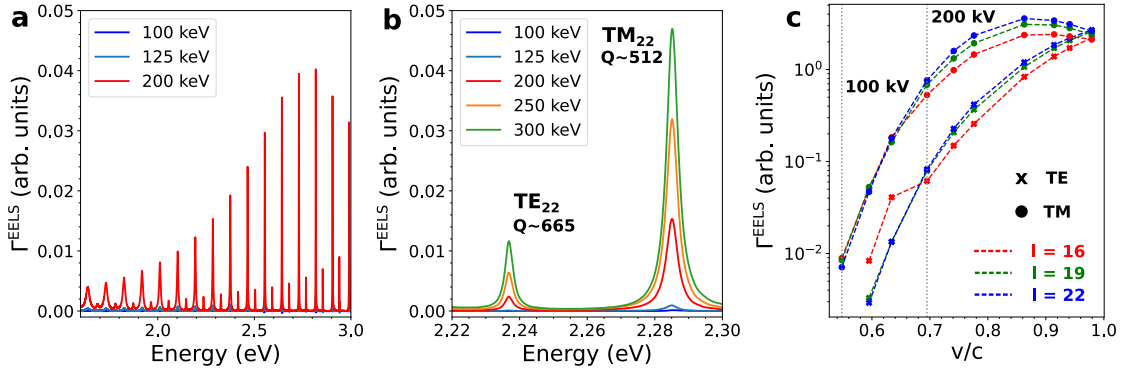


Figure 3.6: FDTD simulation results for a bare SiO_2 sphere. (a) EELS probability over a broadband energy range for 100 keV, 150 keV, and 200 keV electrons and a sphere of radius $\approx 1.60 \mu\text{m}$. (b) Details of the TM_{22} and TE_{22} resonances for multiple electron kinetic energies. (c) The probability for three TM and TE resonances as a function of v/c .

The Q factors from FDTD follow an exponential-like profile as radiation leakage is the only source of loss in the simulation, similarly to what has been already discussed in section 3.1.1. The inflection point near 2.8 eV in the experimental Q factor from CL can be attributed to a combination of experimentally induced losses, such as the effect of the carbon membrane and surface inhomogeneities, [207, 247] as well as the expected quality factor reduction from the increased radial order.

The EELS probability for a bare resonator was FDTD-simulated for several v/c ratios, as shown in Figure 3.6. A few angular order peaks close to the visible range for a sphere of $\approx 1.60 \mu\text{m}$ were inspected. For the TM_{22} mode, for example, the EELS probability increases approximately two orders of magnitude as the electron energy is increased from 100 keV to 200 keV. Also, the loss probability for the TE modes approaches the TM ones only when $v \sim c$, as expected [202]. The quality factor for the TM polarization is slightly smaller than the TE one, which is also an expected result when only radiation losses are taken into account [207].

3.2.2 Coupled microspheres

To study the coupling of nanoparticles with WGMRs, silver nanocubes of $\approx 100 - 120 \text{ nm}$ side length, synthesized by seed-mediated growth, [248, 249] have been drop-casted on the sample grid containing the SiO_2 spheres. To mitigate the direct coupling of the electron beam with the WGMR, the electron acceleration is kept at 100 keV, where the coupling terms for angular modes $l \approx 20$ are reduced by two orders of magnitude, as shown in Figure 3.6. In theory, for a lossless Drude Metal, bare nanocubes are known to support an infinite number of optical modes [250, 251], which are conventionally divided into corner (C), edge (E), and face (F) modes [113, 252–254]. The presence of the SiO_2 sphere, as a substrate, induces

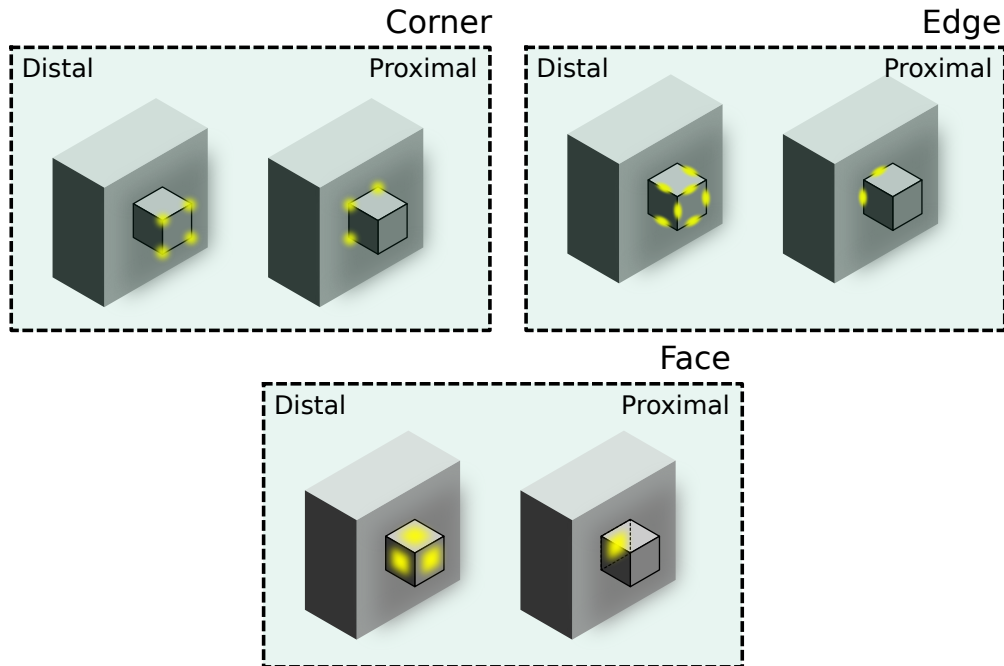


Figure 3.7: Hybridization of the silver nanocube corner, edge and face modes into distal and proximal resonances due to the substrate presence.

mode hybridization for each of the C, E, and F modes, leading to the so-called proximal (P) and distal (D) splitting in reference to the induced fields concentrated close or opposite to the substrate [15, 255], respectively. An illustration of the field amplitudes for these hybridized modes is sketched in Figure 3.7. Figure 3.8 shows the most notable of these modes identified simultaneously by EELS and FDTD simulations, done by placing a 100 nm Ag nanocube on a 500 nm thick SiO_2 plane substrate to observe the cube-substrate hybridization. Weak coupling between the gallery modes circulating in the sphere and the cube surface plasmons is observed in the spectral range of the dipolar mode (Dip) and, to a lower extent, in the first observed distal corner (DC_1) resonance, as shown in Figure 3.8a

Loss spectra were studied with the electron probe positioned at the cube top (opposite edge from the substrate), side (lateral edge), distal corner (opposite corner from the substrate), and proximal corner (closer corner to the substrate) positions, which contain all possible symmetries of the problem. No gallery modes were observed in the proximal corner mode PC_2 , the second distal corner DC_2 , the proximal and distal edge modes (PE and DE, respectively), and the distal face mode DF, even though similar bare resonators exhibited detectable modes up to 7 eV under 200 keV electron excitation. This behavior can be attributed to the near-zero net dipole moment of these higher-order modes, and thus, the resulting electric field is not enough to be observed in the EELS spectrum. Figure 3.8c shows filtered spectral maps of the cube modes, which match the already-known tomographic reconstructions of this system [15] and were also observed in

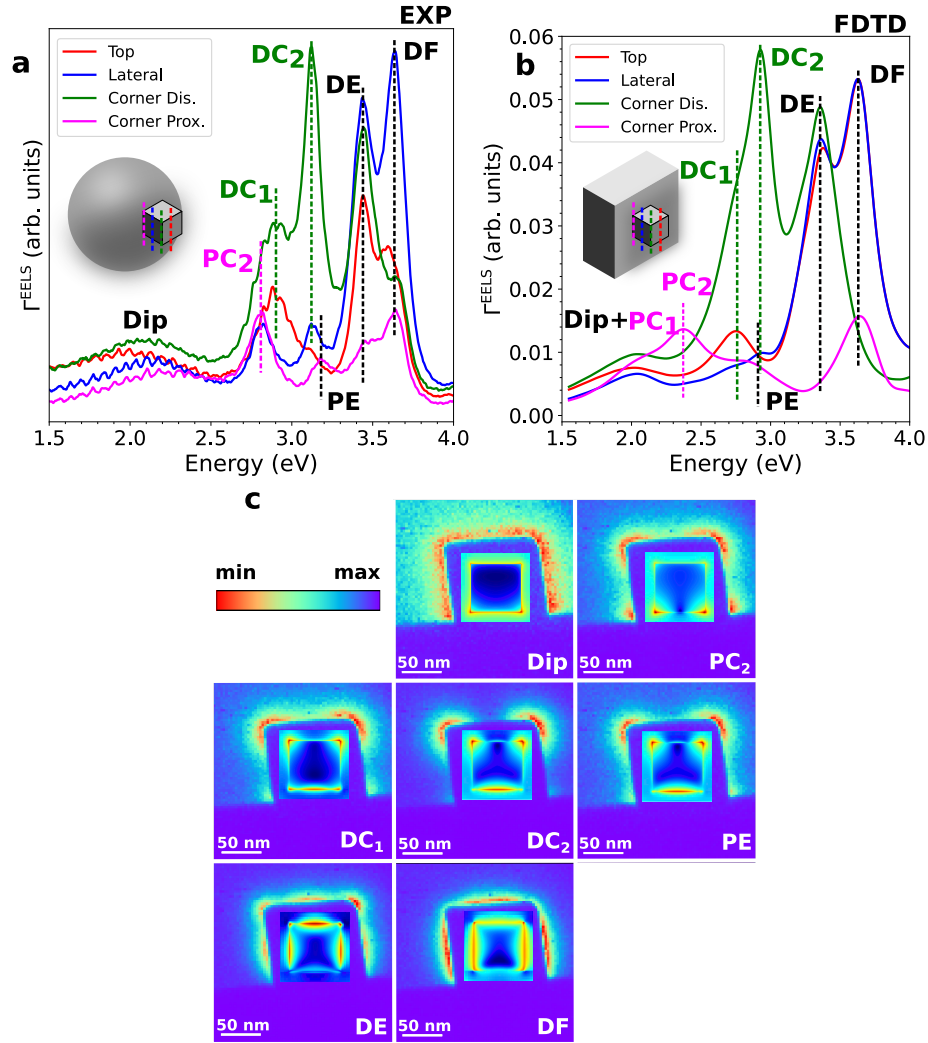


Figure 3.8: Characterization of MNP-WGMR coupling. (a) Experimental electron energy-loss spectra of a silver nanocube of ≈ 105 nm side length placed on a silica sphere for four different probe positions as indicated by the inset scheme. (b) FDTD simulated electron energy-loss spectra of a silver nanocube of 100 nm on a SiO_2 planar substrate for similar probe positions. (c) Spectral maps obtained by EELS for all identified modes and, superimposed, the FDTD-simulated relative value of the electric field.

the FDTD simulations, as shown in the appendix of this work. The relative value of the electric field obtained from FDTD for each of the cube modes is shown in the respective experimental cube map.

Due to the much more complex distribution of the local electric field associated with these higher-order modes, the analysis has focused on the cube's dipolar mode (Dip), which is characterized by dipole moments along with the three main symmetry directions. Within the dipolar picture, it is suggested that different probe positions, that translate into distinct net dipolar moment directions, induce different gallery-mode polarizations. As TE modes have no radial electric fields

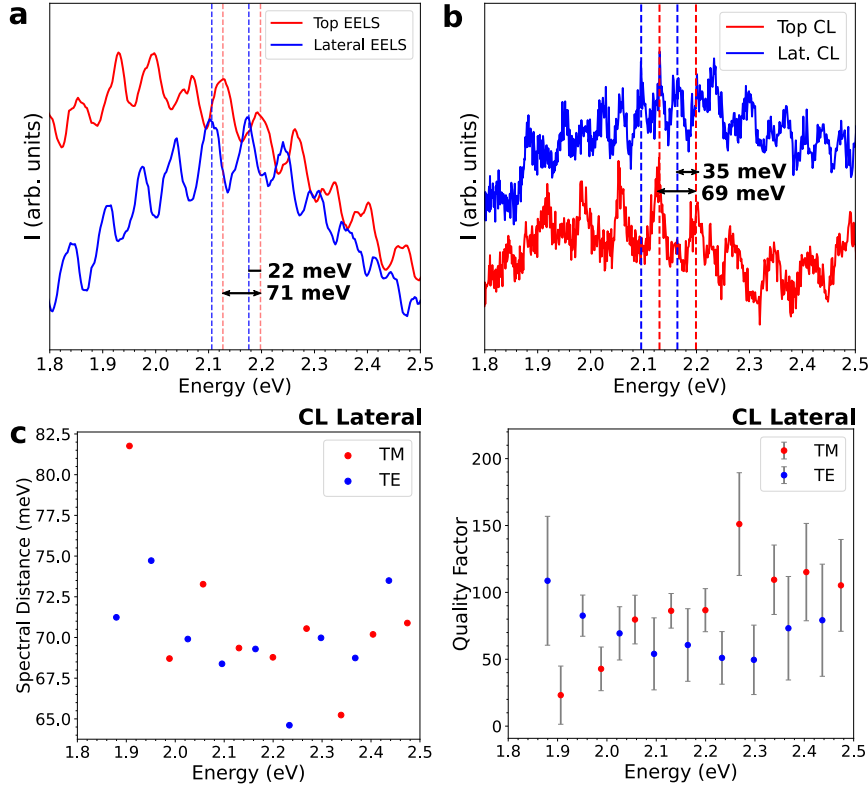


Figure 3.9: Polarization dependence of the MNP-WGMR coupling. (a,b) Polarization dependence on the probe position as observed in the EELS (a) and CL (b) signals associated with the dipolar mode. TM and TE modes are simultaneously observed in CL for the lateral probe position, while they were not seen in EELS due to the limited spectral resolution of the technique. (c) Spectral distance and quality factors for the resonances found with the lateral probe position. The uncertainty in the spectral distance is < 1 meV for all data points.

($\mathbf{r} \cdot \mathbf{E} = 0$), the top probe position primarily excites TM modes. If the probe is placed laterally to the cube, the resulting electric field is mostly tangential to the sphere surface and can thus excite both TE and TM modes [230, 256], as has been already shown in the set of equations 3.5. The experimental results from EELS show resonances that are equally spaced by ~ 71 meV for each top and lateral probe position, but shifted ~ 22 meV between each other, as shown in Figure 3.9. This value is smaller than the fwhm derived from the EELS spectra and therefore limits the resolution of possible neighboring TE and TM resonances. CL offers a simple solution to further explore the problem thanks to its superior spectral resolution.

The employed CL system is angle-selective and can only detect gallery modes that circulate close to the plane containing the electron trajectory due to the mirror position relative to the sample and the electron beam direction, as can be seen in the microscope sketch in Figure 3.1. Experimental CL results are shown

in Figure 3.9b. For the top probe position, which induces a strong radial electric field, TM polarization is more clearly resolved, while for a lateral probe both sets of TM and TE resonances can be observed. The measured FSR is ~ 69 meV and the TE-TM spectral distance can be directly determined with the lateral probe spectrum as ~ 35 meV.

The measured resonances have been fitted for the lateral probe position and divided into two different sets. Consecutive modes were subtracted to obtain a spectral distance curve and the standard deviation was used to estimate Q factors. Uncertainty bars for the Q factor are also included due to the non-negligible fitting uncertainties. The spectral distance curve shows no notable difference between polarizations, as expected from its definition. The Q factor for TE modes has a minimum value centered on the cube dipole resonance, which is expected because cube-induced losses are then maximal. For the TM modes, a steady Q factor decrease down to the lowest energy resonance at ~ 1.9 eV is observed, but not a clear minimum. Unfortunately, the low emitted light intensity and the impossibility of easily changing the electron acceleration preclude further exploration of the coupled system.

It is worth mentioning that CL results outside the dipolar energy range were also obtained. While induced gallery modes were not observed in EELS for DC₂ (Figure 3.8a), CL displays a coupling component, as shown in Figure 3.10. This observation reinforces the argument that the coupling strength is dependent on the net dipole moment. Since CL measures the radiative component of the coupled plasmon-WGM mode, induced gallery modes can be observed. In addition, EELS is a combination of radiative and non-radiative losses and, because the non-radiative contribution only contains plasmonic losses and dominates over the

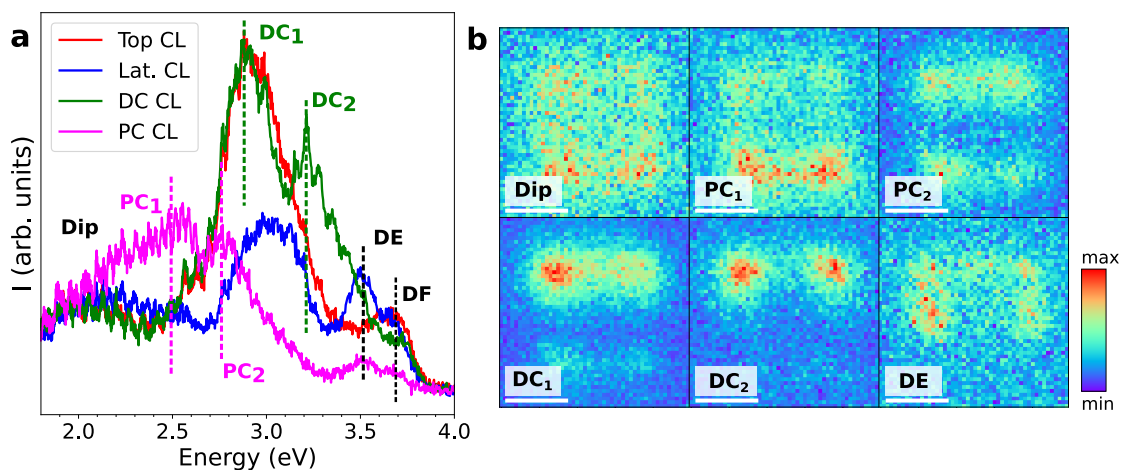


Figure 3.10: Experimental CL results. (a) CL spectra for the cube-substrate system at four different probe positions. (b) Spectral maps for the dipolar (Dip), first and second proximal corner (PC₁ and PC₂), first and second distal corner (DC₁ and DC₂), and distal edge (DE) modes. Scale bars are 50 nm.

radiative component, gallery modes are difficult to resolve in the EELS spectra. Most of the identified modes revealed by EELS have been also seen in CL, including the first-order proximal mode PC_1 that was difficult to resolve in EELS because of its closeness to the dipolar mode (Dip) and the tail of the much stronger PC_2 . Additionally, PC_1 and PC_2 can be better spatially resolved because thick regions of the sample can be probed in CL, differently from EELS, in which penetrating trajectories in such a thick sample is difficult. Note that PC_2 radiates less than PC_1 due to its higher-order, analogously to what happens to DC_2 relative to DC_1 .

To obtain further insight into the physics of the nanocube-sphere system, the effective polarizability modified by the non-homogeneous environment (section 1.2.2) is used. The polarizability $\alpha(\omega)$ is calculated from a finite-difference method (see appendix) and the Green's tensor $\vec{G}(\omega)$ using the boundary-element method [87]. This theoretical formulation was mainly performed by Vahagn Mkhitarian and F. Javier García de Abajo, with a common discussion between me and the other co-authors of the associated published paper in ref. [16].

These elements are represented in Figure 3.11b, where $\text{Re}\{\alpha^{-1}\}$ is found to change its sign around 2.5 eV, indicating the emergence of a prominent particle plasmon, whereas \vec{G} displays sharp oscillations revealing the effect of coupling to the Mie modes of the sphere. For comparison, the featureless profile of the Green's tensor for a planar silica surface is also shown. From these considerations, the weak-coupling regime is certainly the case, as the lifetime of the MNP dipole is much smaller than that of the whispering-gallery modes, so that the imaginary part in the denominator of α^{eff} remains relatively large and dominated by the nanocube component. Then, the optical response of the MNP-sphere hybrid system is enhanced at the points in which the real part of the denominator is canceled, as indicated by the crossings between $\Re\{\alpha^{-1}\}$ and $\Re\{G_{zz}\}$ in Figure 3.11b. The effective dipole induced on the particle receives contributions associated with different scattering paths, as schematically shown in Figure 3.11a. Namely, it is contributed by the direct field produced by the electron ($\mathbf{E}_{\text{EB}}^{\text{dir}}$), as well as by the scattering of this field at the sphere ($\mathbf{E}_{\text{EB}}^{\text{reff}}$) and the scattering of the dipole field at the sphere acting back on the dipole ($\mathbf{E}_{\text{dip}}^{\text{reff}}$); these contributions are all captured in α^{eff} .

To calculate EELS in this model, the multiple-elastic-scattering of multipole expansions (MESME) method [257] with the sphere and the MNP acting as scattering centers has been used. In particular, the sphere is described by multipoles up to order > 30 and the MNP through the electric dipolar components of the scattering matrix. This method captures all scattering paths schematically represented in Figure 3.11a. The results presented in Figure 3.11c confirm the analysis based on α^{eff} : the EELS probability with the MNP alone exhibits a prominent plasmon, but it is modulated through coupling to Mie resonances of the sphere in a way similar to that observed in the experiment. Note that the model successfully describes the sphere and MNP coupling within the dipolar picture, but it does not account for higher-order plasmon modes. In this sense, although Figure 3.11 shows

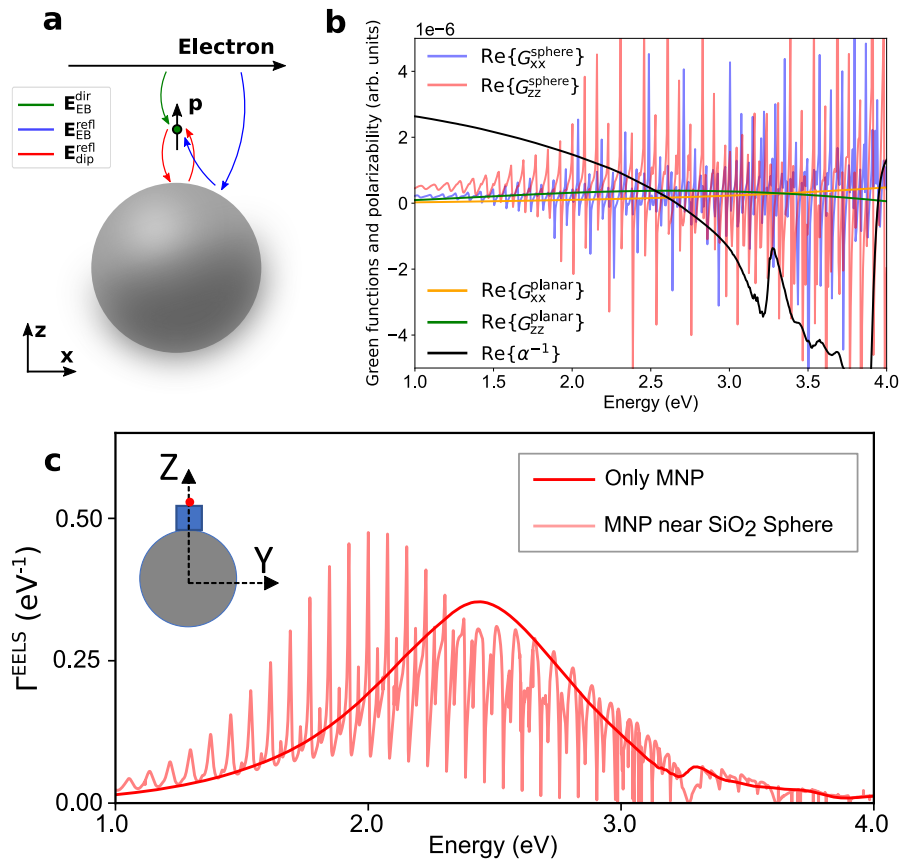


Figure 3.11: Analytical description of free-electron interaction with a MNP-WGMR hybrid system. (a) Electric field contributions to the self-consistent dipole model (see main text), where the MNP is treated as a dipolar scatterer. (b) Calculated electromagnetic Green's tensor components for the self-induced field produced by the particle dipole on itself due to the presence of the dielectric sphere, compared with the real part of the inverse of the MNP polarizability. (c) Model calculation of the EELS probability corresponding to the nanocube alone and the nanocube placed near the sphere for the electron beam position shown in the inset.

gallery modes along the entire displayed energy range, they are not observed in Figure 3.8a because higher-order modes mask the tail of the dipolar resonance. Further discussion of the analytical model can be found in the appendix of this work.

EEGS on the coupled system

One suggestion to increase the resonance Q factor is to increase the sphere radius, as Q_{rad} scales exponentially for a given resonance wavelength. However, as can be seen in equation 3.8, the spectral distance between adjacent modes is inversely proportional to the sphere diameter, and hence the finite spectral resolution of EELS hinders mode identification. Besides, CL becomes a less viable spectro-

scopic technique because increasing Q_{rad} is equivalent to reducing the leaking of the confined modes to the far-field. Such a scenario is precisely where EEGS is supposed to replace EELS and CL. As already discussed, energy-gain experiments in WGMR were performed by Kfir *et. al.* [13], although not in the larger spheres as reported here, and by using a chirped light pulse rather than scanning the laser wavelength.

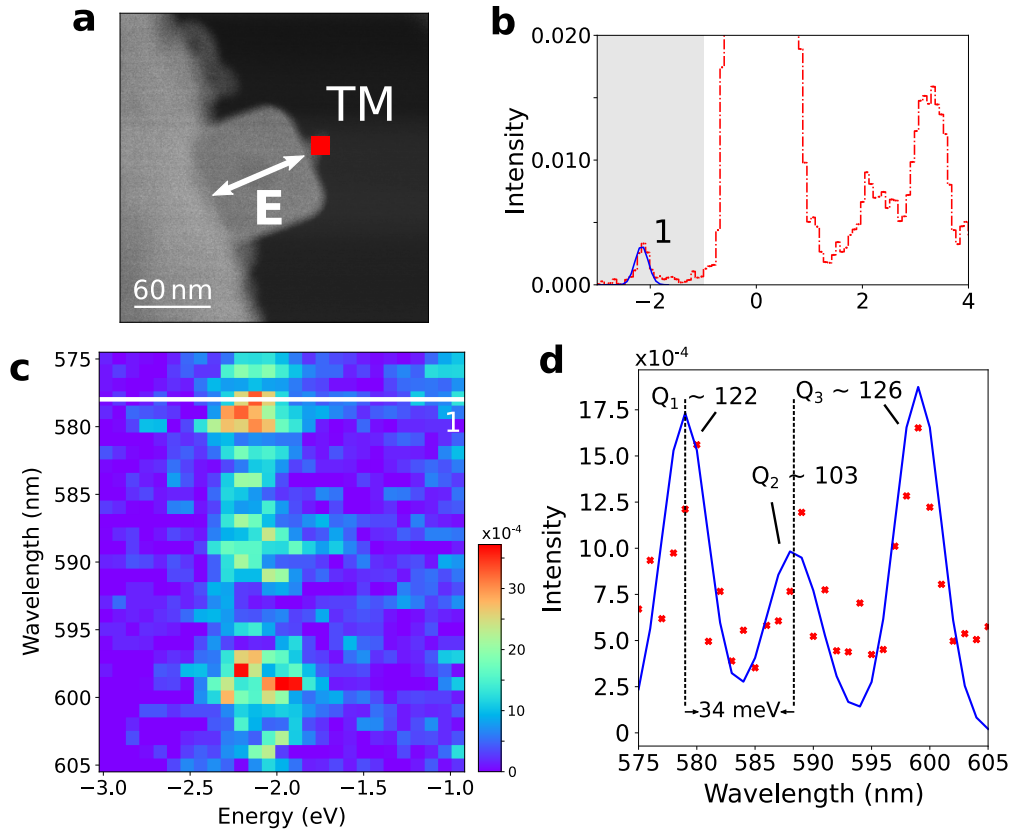


Figure 3.12: EEGS performed in a 4 μm radius silica sphere. (a) The annular dark-field (ADF) image shows the cube and the electron probe position of the EEGS measurement. In this position, only TM modes are excited because TE modes do not have a radial component of the electric field. (b) A single EEGS spectra for a laser wavelength of 577 nm, showing the fitted resonance in the blue curve. (c) The bi-dimensional histogram of the laser excitation wavelength and the energy-gain spectra for the energy range defined by the gray rectangle in (b). Additionally, the horizontal white line 1 corresponds to the spectrum displayed in (b). (d) Every laser wavelength in (c) was fitted with a Gaussian and their intensity is displayed in the red dots. These have been again fitted with three Gaussians, shown by the continuous blue curve.

EEGS was performed in the Vacuum Generators model HB 501 (VG) microscope (a non-monochromated cold field-emission gun (cFEG) STEM), as the experiment was currently not feasible on ChromaTEM. The gain curves were performed rastering the laser wavelength between 575 nm and 605 nm with a step of 1

nm, ~ 3.5 meV spectral spacing between points. The sample is a sphere of approximately $4 \mu\text{m}$ radius, twice as big when compared to previous experiments. Figure 3.12 shows the histogram of the energy-gain peaks for multiple laser wavelengths, in which the curve in (a) is related to the horizontal white line “1” in (b). The electron probe position is indicated by the red square and is associated with the top probe position, and thus with the excitation of TM-only whispering-gallery modes. Every resonant peak (blue curve in Figure 3.12b) was fitted with an unbounded Gaussian and the intensity of them as a function of laser wavelength is shown by the red crosses in Figure 3.12d. Subsequently, a second model based on three Gaussians has been used to fit the encountered intensities, unveiling the three modes as indicated by the continuous blue curve in Figure 3.12d. The signals are rather noisy, which again reinforces the massive technical advantage of ChromaTEM for performing EEGS over the VG microscope, as has already been discussed in the previous chapter of this thesis. To sustain the meaningfulness of these curves, the free spectral range of the resonances were estimated based on equation 3.8, which thus must be twice as small as the ~ 69 meV for the TM-only modes in the previous experiments, as can be seen in Figure 3.9b. The measured value for the $4 \mu\text{m}$ sphere was determined in ~ 34 meV range, a great agreement with the expected value.

For a given resonance wavelength, Q_{rad} grows astronomically with the sphere radius, not compatible with the encountered Q factors of 122, 103, and 126, only slightly higher than the previous experiments. As the ultimate Q factor follows an inverse sum law, a single limiting factor is enough to prevent its increase, which is here attributed to the presence of the lossy metallic nanocube. Besides, the surface of these larger spheres has shown to have adsorbed material on it, reducing further the potential for high-Q applications. Placing the electron probe in the lateral of the cube would excite both TM and TE modes, and thus a richer EEGS spectrum could be retrieved. Unfortunately, these experiments have shown featureless curves, attributed to the high spectral density and the subsequent loss of contrast. This stands as a second example of the importance of cutting-edge microscopes for EEGS measurements, such as ChromaTEM: even if the spectral resolution is ultimately given by the laser linewidth, unstable zero-losses, poor spectral resolution, and poor electron spectrometers can effectively restrict the maximum observable Q factor.

As discussed, transferring the EEGS experiment to ChromaTEM is a work in progress. In such a case, spatial maps for specific resonances could be performed, which is expected to provide a very comprehensive dynamics of the coupling: TM modes would have energy-gain resonances all along the cube perimeter, while TE modes would be concentrated to the lateral edges of the nanocube.

3.2.3 Photonic bandgap crystals

Photonic bandgap crystals have also been subjected to study in ChromaTEM, in which its remarkable spectral resolution allows to resolve high-Q resonances to perform EELS measurements in the infrared spectral range, still vastly unexplored because the tail of the zero-loss peak (ZLP) normally hinders resonances in this energy range.

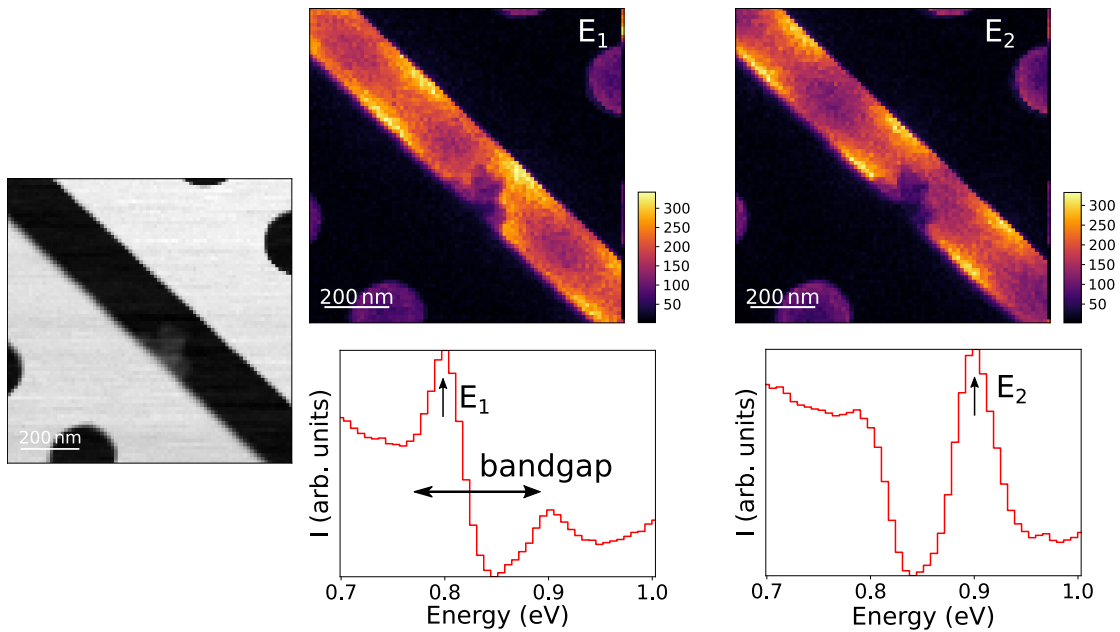


Figure 3.13: Preliminary measurements of the ultrahigh-Q slot cavity. The defect is designed by modulating the line width of a line defect. The slot, or the line defect, exhibits low-Q guided modes, which are at energies close to the expected bandgap of the photonic crystals. Their long tails and the unfortunate sample contamination prevented the ultrahigh-Q mode identification.

The photonic crystal sample is based on the ultrahigh-Q cavity obtained by modulation of the line width of a line defect [235], as sketched in Figure 3.14e, and in which Q factors as high as 10^6 have been experimentally observed [258, 259]. The line defect can be made into a slot, in which the fast electron can probe close to the maximum of the field intensity. These cavities have been produced and characterized in the Quantum dot & photonic nanostructures group in the center of nanosciences and technologies (C2N) by Xavier Checoury and have been observed in ChromaTEM. The slot cavity around the ultrahigh-Q defect is shown in Figure 3.13. The expected bandgap, from previous measurements at C2N, is between approximately 0.75 eV to 0.88 eV, in which EELS measurements seems to properly identify. Unfortunately, the cavity had a contaminant close to the defect site, which could interfere with the maximum attainable observed Q factor. Besides, guided modes were observed at E_1 and E_2 , close to the edges of the bandgap, and their long tails can also hinder the sharp spectral feature associated

with the ultrahigh Q factor of the cavity defect. Finally, Figure 3.13 shows a non-tilted measurement to properly show the spatial distribution of the guided modes. Measurements, however, were also performed with a tilted angle, with the rotating axis perpendicular to the slot, as high as 600 mrad (~ 34.4 degrees). No defects were identified within the photonic bandgap in any case. In this picture, the simplest defect, an individual missing hole in a completely periodic structure [200, 237, 241], has been studied. Missing holes can be found in any of these cavities as a consequence of a faulty fabrication processes. When far from the defect site, their impact are minimal in the attainable defect Q factor.

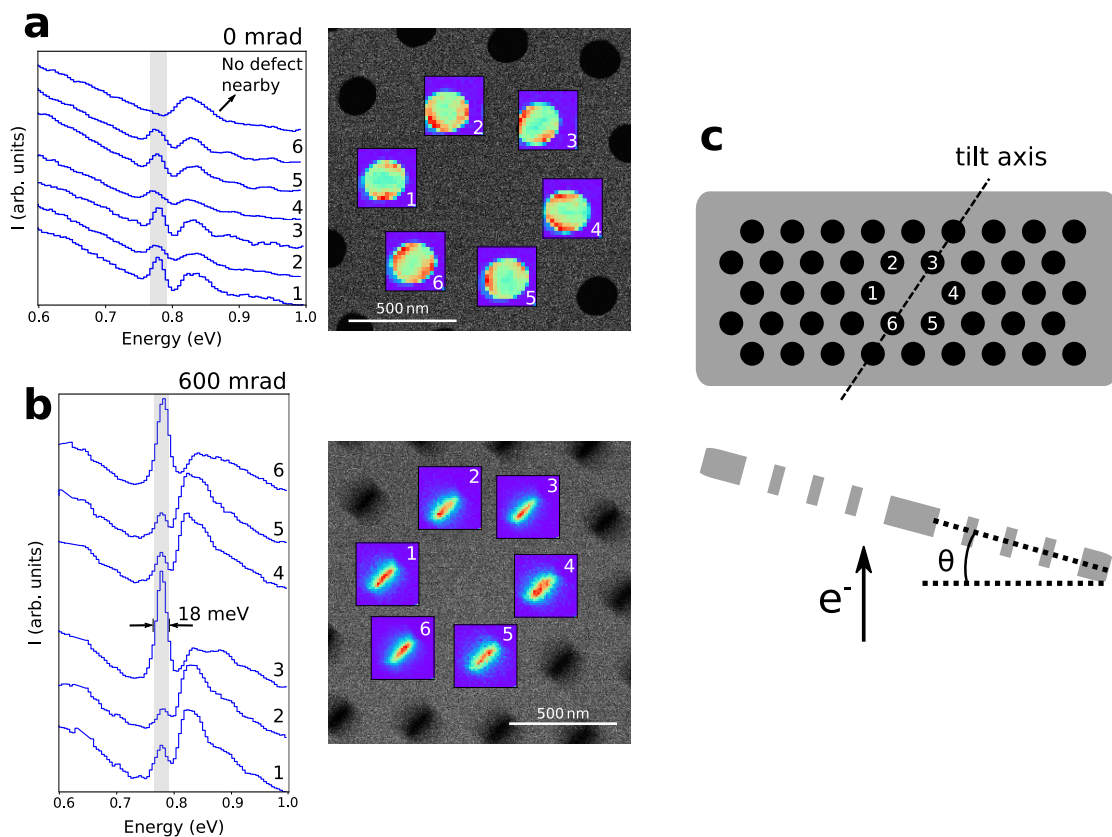


Figure 3.14: Preliminary measurements on a single-hole defect in a photonic crystal. (a) EELS measurements for the holes in the vicinity of the defect with the electron propagation perpendicular to the photonic cavity. (b) Same as (a) but with the cavity tilted by 600 mrad around the holes 3 and 6. (c) The scheme of the cavity and the missing-hole defect. The angular tilt relative to the incident electron is shown at the bottom.

As aforementioned, these defects have a TE polarization, meaning the electric field is mainly at the sample plane, orthogonal to the electron propagation direction. In Figure 3.14a, a hyperspectral image is obtained for every neighbor hole from the defect center, in which the fields at the electron propagation direction are mapped. When the sample is tilted by 600 mrad along the axis of rotation

shown in Figure 3.14c, the EELS intensity along the holes “3” and “6”, crossing the rotation axis, is much more intense, which is explained by the projection of the in-plane electric field. The spectral resolution of the microscope was ~ 18 meV, which would be capable of measuring Q factors as high as $Q \sim 43$ for resonances centered at ~ 0.78 meV. Even for these simple defects, expected quality factors are in the order of 10^3 [175, 237] and thus certainly limited by the microscope spectral resolution. Even at the best microscope condition, the maximum observable quality factor is ~ 150 for 5 meV ZLP fwhm. EEGS is, therefore, the natural solution for spatial mapping of these resonances.

The experimental observation of such resonances is important. Not only the expected quality factor is 1-2 orders of magnitude greater than the whispering-gallery resonators, but the volume of these modes is also much higher. For photonic crystals, mode volumes scale as $\propto (\lambda/n)^3$ and thus higher brightness electron guns are needed to achieve the appropriate spatial resolution.

Unfortunately, EELS can not appropriately map the maximum field intensity of such defects, which is positioned at the center of the missing hole, where the sample is too thick. For this, mode mapping must rely on the evanescent fields across the neighbor holes. Summed to the in-plane electric field for TE-based point defects, mode mapping in EELS is incomplete without simulations. This is also a work in progress, in which FDTD-based simulations, similarly to the ones performed for whispering-gallery microresonators, are underway.

3.3 Conclusions & prospects

Bare and metallic nanoparticle-coupled microspheres were studied with high spatial resolution using fast electrons, observed from energy absorption (EELS), light emission (CL), and, to a lesser extent, EEGS measurements. While CL can be used to improve the experimental spectral resolution, EELS provides rich and complete absorption information over a large spectral range: a compelling example of how EELS and CL can be used together to provide self-complementary information. EEGS measurements showed resonant modes in higher-radius spheres, which were not observed in EELS at ChromaTEM, although the lack of signal-to-noise ratio prevented a more comprehensive study, i.e. spatial maps for different TE and TM resonances. FDTD-simulated energy-loss spectroscopy, beyond its remarkable agreement with experiments, provided a deep physical insight into the coupling mechanism. Finally, the plasmon resonance excitation by the electron probe allows for the manipulation of the gallery-mode polarization by either coupling to TM or both TM and TE resonances. With the advent of a new generation of monochromated STEMs, experiments requiring such high spectral and spatial resolution are now possible.

Although the WGMR and MNP coupled system is an interesting one, the presence of a lossy nanoparticle disrupted the bounded modes to the point that the ultrahigh-Q factor is probably impossible, which has triggered the beginning

of the work on photonic crystals. For such a system, the sample can be studied stand-alone, without any loss on the expected Q factors due to experimental constraints. Observing ultrahigh-Q, however, is not an easy task because coupling and observing these modes require proper phase-matching and an extreme degree of monochromaticity of the electron beam. Naturally, and rather obviously, EEGS spectroscopy stands as the possible solution to this problem. During these trials, a work was published on a whispering-gallery micro-ring chip, performing for the first time μeV -resolution electron-based spectroscopy [137]. Fortunately, many things are still to be done. The spatial resolution of the small mode volumes created by ultrahigh-Q point defects in photonic crystals has not yet been reported and probably requires cFEG electron guns. Besides, photon emission of these structures can be efficiently studied in ChromaTEM, thanks to the efficient high-numerical-aperture parabolic reflector.

Finally, it is worth mentioning that these ultrahigh-Q photonic cavities have an even broader research interest. The phase-matched fast electrons travelling through the cavity slot shown in Figure 3.13 can strongly interact with the TE defect mode, leading to much higher EELS probabilities of the defect state. Additionally, for a high enough electron current, the long-lived ring-down time of these defects are expected to produce non-linear effects, such as the “spontaneous energy-gain”, in which the inter-arrival times of two electrons must be inferior to the lifetime of the defect state. In this case, the direct electron detector Timepix3 (TPX3) can provide valuable insights, as it is capable of output the electron time of arrival (ToA) and thus experimentally confirming the temporal correlation of a energy-gain event with a prior energy-loss event.

Event-based EELS: developments & applications in the nanosecond scale

4.1 Introduction

As should be clear up to this point, the transmitted electrons carry spectral information from the sample and are studied by electron energy-loss spectroscopy (EELS) with high spatial resolution, down to the atomic level. Data is usually acquired in the form of a hyperspectral image, a data cube indexed by one energy and two spatial coordinates.

One of the main concerns when performing EELS is that the energy-momentum transferred during the inelastic scattering of the electron may cause undesired effects in the sample, such as knock-on displacement, induced heating, and radiolysis [75, 260]. Several approaches have been proposed to diminish them, such as custom scan paths and fast scans combined with data reconstruction algorithms [145, 261–263]. Although effective, these solutions are limited by their frame-based nature, which have a minimum acquisition time given by the readout scheme, typically of a few milliseconds for charged-coupled device (CCD) cameras, for example.

Up until now, frame-based detectors have been the usual solution for EELS. These count the number of electrons hits in a given dwell time indiscriminately and thus the temporal information is limited by the spectrum acquisition time, as shown in Figure 4.1a. CCDs and complementary metal-oxide-semiconductor (CMOS) are the most widespread frame-based detectors for EELS [264, 265]. For both detectors, a scintillator and an array of optical fibers are typically used to convert the incident electrons into photons. These detectors have a variety of noise sources, such as dark and readout noises, and can dramatically degrade the spectral resolution due to the increased point spread function (PSF) imposed by the scintillator layer. A second kind of electron detection uses hybrid-pixel detectors (HPDs), in which the sensor layer and the readout chip (also called application-specific integrated circuit or ASIC) are manufactured independently from each other. Multiple successive generations of ASICs led to the spread of

HPDs in many different research subjects, such as space dosimetry [266], synchrotron source imaging [267, 268], X-Ray spectroscopies [269, 270] and electron microscopy, including diffraction [271, 272], imaging [273–276] and EELS [277, 278]. One of the most successful ASICs, the Medipix3, introduces several improvements relative to CCDs and CMOS for EELS acquisition. These include the practically zero readout noise, the improved PSF due to the direct electron detection and the readout time as low as $\sim 500 \mu\text{s}$ [279]. Despite their improved acquisition speed, the problems related to frame-based acquisition persist because scanning pixel time in a scanning transmission electron microscope (STEM) can go as low as tens of nanoseconds. This is much faster than the readout time of any commercially available frame-based detector.

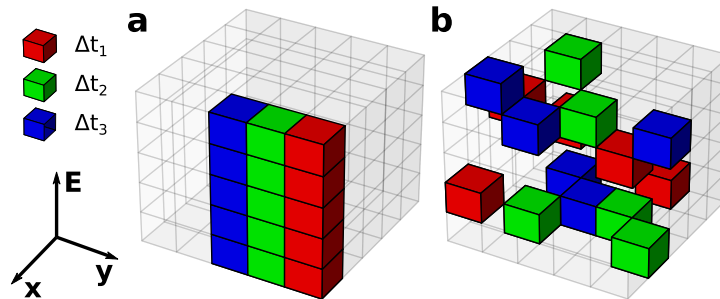


Figure 4.1: Comparison between frame-based and event-based hyperspectral acquisitions. (a) In the frame-based hyperspectral image reconstruction, the entire spectral dimension is acquired for each electron probe position. The minimum exposure time is given by the camera readout time, typically in the millisecond range for CCDs. (b) The event-based reconstruction places each electron in its corresponding data cube position when an electron hit is detected. Because of this, the electron beam can be rastered as fast as the time resolution of the event-based camera, typically in the nanosecond range. In both cases, the cube color code represents a typical acquisition time of a frame-based measurement ($\sim 1 \text{ ms}$). In such a time window, the scan unit can raster a great number of pixels.

A different concept of hyperspectral data acquisition for EELS can be defined when electrons are individually counted and can be unequivocally placed in the corresponding spectral and positional coordinates of the data cube. For example, one can consider a fast rastering electron beam with $0.5 \mu\text{s}$ pixel time. In such a time interval, for a probe with $\sim 50 \text{ pA}$ only ~ 150 electrons would hit the sample, most of them falling in the zero-loss peak (ZLP). For a single-pixel acquisition, there would not be enough electrons to produce a usable EELS spectrum. However, continuously scanning and adding the electrons in an event-based fashion can lead to a meaningful reconstruction of the data cube. We show such a scheme in Figure 4.1b. The Δt shown is a typical frame-based acquisition time ($\sim 1 \text{ ms}$). For the event-based acquisition, the SU rasters a great number of pixels within the time interval Δt that would be needed to collect a spectrum in the frame-based approach. Of course, contrary to the frame-based approach, the arrival time of

each of these hits is known with a precision much better than Δt . Also, during Δt , one acquires electron hits from different points of the data cube in space. One must therefore relate a given electron hit with the corresponding probe position to construct a hyperspectral image. In this case, hyperspectral images can be acquired with very fast scanning pixel dwell time and thus synchronously with the normal annular dark-field (ADF) imaging without any performance penalty.

In this chapter, the implementation of this concept for EELS is demonstrated, similarly to what was recently performed for event-driven 4D STEM acquisition [280]. The probe position and the electron hit can be related in the temporal dimension by using an electron detector capable of output such information. At first, details of the event-based hyperspectral EELS implementation is explained, describing, in particular, the Timepix3 (TPX3), the direct electron detector used throughout this chapter and the next, and the related features of the used readout board, called SPIDR (Speedy PIXel Detector Readout), that allowed timestamping supplementary events from the scan unit (SU) superimposed on the data flow of the electron events. To illustrate the problem, an event-based hyperspectral acquisition using 120 ns pixel time sampled over 512 x 512 pixels is shown. The last part of the chapter is dedicated to the application of this system to follow the decomposition of calcite (CaCO_3) into calcium oxide (CaO) and gaseous carbon dioxide (CO_2) under electron beam irradiation.

4.1.1 The Timepix3 and the CheeTah solution

To implement the event-based hyperspectral EELS, a TPX3 detector has been used. In its first version, Timepix was a simple modification of Medipix2, allowing one to increment the pixel counter by clock ticks instead of the number of events since a reference clock was distributed on each one of its pixels [281]. Timepix had thus the old functionality of counting hits but also the option of output either time of arrival (ToA) or time over threshold (ToT) values [282]. The former measures the time elapsed until a hit is detected, while the latter measures the time the hit stays over the pixel signal threshold. Its successor, the ASIC TPX3, was the first real data-driven detector in the entire Medipix/Timepix family, as a pixel hit in any of its 256x256 pixels is responsible for triggering data output from the chip. A voltage-controlled oscillator (VCO) running at 640 Mhz allows TPX3 to achieve a nominal temporal resolution of 1.5625 ns (called fine ToA) and, in contrast with the first Timepix generation, can simultaneously provide ToA and ToT [281, 283].

The obvious motivation from the architecture change from Timepix to TPX3 (frame to event-based) is the total data transfer time interval of the pixel matrix. In Timepix, this value is the readout time, as defined in this work, and is a constant value of $\sim 300 \mu\text{s}$ independent of the detector occupancy (defined as the percentage of pixels hit). In TPX3, for a given bandwidth Bw (the number of bits transferred per unit time) this interval is estimated to be

$$T_{transfer} = NS/Bw, \quad (4.1)$$

where N is the number of pixel hits and S is the size, in bits, of the individual packet sent. A single-chip TPX3 has 8 output links that can perform 640 Mbps data transfer, reaching thus a maximum transfer bandwidth of 5.12 Gbps. This means that for the standard packet size of 48 bits (Figure 4.2a), an occupancy of 50% of pixels has a data time transfer similar to the readout time for frame-based mode, as shown in Figure 4.2d. In this scenario, two important conclusions can be stated: (i) the detector has a better performance using event-based, or sparse readout, for occupancy rates smaller than to 50%, and (ii) the data-driven TPX3 has a much smaller dead-time between consecutive hits in the same pixel. Indeed, for the frame-based approach, the dead-time per pixel is given by the readout speed of $\sim 300 \mu s$ while in the event-based, this dead-time is reduced to 475 ns. As it is discussed better in the following paragraphs, the pixel hit is represented by its analog input, shown in Figure 4.2c. This pulse is responsible for determining both the ToA and the ToT, and the aforementioned dead-time of 475 ns is related to its duration: a second electron hit must arrive when the analog input has sufficiently decayed.

There are several packet formats for the output data. In this work, TPX3 was only used in the event-based operation with simultaneous acquisition of ToA and ToT, which leads to the packet data structure shown in Figure 4.2a. Pixel address is 16-bits long (16b) and contains the information of both the horizontal and vertical hit position, as shown in the chip illustration in Figure 4.2b. As the pixel matrix is 256x256, 8b is required for each positional value. ToA is 14b relative to the 40 Mhz reference clock, meaning it can count up to $2^{14} \times 25 \text{ ns} = 409.6 \mu s$. ToT is a 10b also relative to the 40 Mhz reference clock. Finally, fine ToA (fToA) is the value associated with the VCO signal running at 640 Mhz. Figure 4.2c sketches how the time-related values for a single pixel are determined. A pixel hit over threshold puts the pixel discriminator in a high state and immediately starts the VCO, which is asynchronous relative to the reference clock of 40 Mhz, and it runs “on-demand”, triggered by the high state of the discriminator. Additionally, the VCO is common for every array of 8 pixels, called super-pixels, and can only be accessed by one pixel at a time. It runs until the next rising edge of the reference clock, which latches the ToA time and starts the ToT counter simultaneously, running until the discriminator goes to the lower state. The global ToA (gToA) is a counter incremented every falling edge and is shared between every double column of TPX3. The latch is thus used to obtain the current gToA counter value for a single pixel.

For the development of the application, a solution from Amsterdam Scientific Instruments (ASI), called CheeTah, was used, which includes the SPIDR board [284] and the control software. The detector consists of four 256x256 chips mounted linearly adjacent to each other to form a 256x1024-pixel array, more appropriate to perform EELS. The packet structure described in Figure 4.2a is

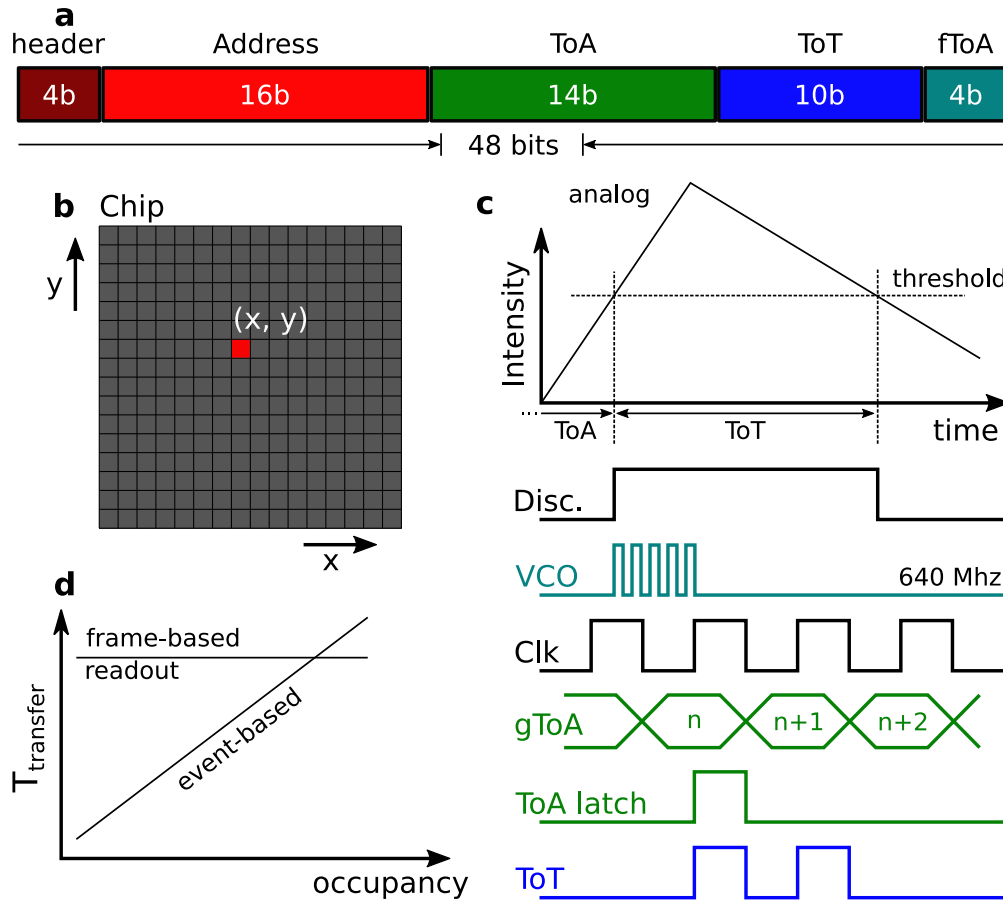


Figure 4.2: General aspects of TPX3. (a) Packet data structure for the event-based, simultaneous ToT/ToA mode. (b) The TPX3 chip. It is a 256 x 256 matrix containing 55 μm side-length pixel. The pixel address of the packet structure is related to the impact position of the hit, as shown by the red square. (c) Scheme of how the time-related quantities are obtained at the pixel level. If the hit signal in the analog input is higher than the set threshold, the signal discriminator goes high and the on-demand 640 Mhz VCO signal starts until the next rising edge of the 40 Mhz reference clock, which is also when the global ToA (gToA) is identified by the ToA latch. gToA is distributed every double column of the chip and is incremented at every falling edge of the reference clock. Finally, ToT counts the number of clock hits until the discriminator goes low, or the analog input goes below the threshold. (d) Shows the time of data transfer in the frame-based and event-based architecture. For the frame-based, this time is constant and is what has been called readout time. In the event-based, the sparse readout scheme means that for occupancy percentages lower than 50%, event-based is faster than frame-based.

slightly modified in CheeTah. Most notably, the electron ToA is extended by using a 16-bit counter, increasing the raw packet size from 48 to 64 bits. In this scheme, at each ToA overflow of 409.6 μs , the counter is incremented by a unit, which effectively increases the total measured time to $2^{16} \times 409.6 \mu\text{s} = 26.8435456 \text{ s}$. Additionally, data is sent by packet chunks for each one of the four TPX3 chips,

which are preceded by an extra 64 bits of data, called the header.

Another very distinct feature of CheeTah is the presence of two time-to-digital converters (TDCs). These are based on the same reference clock of 40 Mhz, but a set of six phase-locked generated 320 Mhz clocks allows to reach time discrimination within 12 bins in the 320 Mhz signal [284–286]. In practice, this translates into $1/12 \times (1/320 \text{ Mhz}) \sim 260 \text{ ps}$ time bins. The TDCs input lines are thus capable of creating timestamps of external signals, and, as the same reference clock is used, these signals can be time-related to the ToA of electron events. Equivalently, events in CheeTah can be either electron events, as already discussed, or TDC events, also called supplementary events. These work on the same reference clock and thus the absolute time of both can be retrieved. Finally, TDC events are time-only, and neither pixel address nor ToT applies. The 320 Mhz generated clock uses a 35-bit counter, reaching a maximum timestamp before overflow at $2^{35} \times (1/320 \text{ Mhz}) = 107.3741824 \text{ s}$. To reach the 260 ps temporal resolution, an extra 4-bit of data is provided (from 0 to 11).

4.2 Event-based hyperspectral EELS implementation

When TPX3 is used in EELS, therefore, one has access to each electron’s positional coordinates (the dispersive and non-dispersive directions) and the temporal coordinates, represented here by both ToA and ToT. To reconstruct the hyperspectral image, a way to correlate the temporal information of the electron events with the electron probe position must be found. One approach is to feed the SU reference clock signal into TPX3, which would require flexible and programmable SUs and TPX3 control boards. The employed solution is to create supplementary events in the TPX3 data flows, effectively exploring the two distinct kinds of events: one linked to individual electrons and another to reference timestamps of the microscope probe position.

In the following, the dispersive direction of the detector is denoted as α and the non-dispersive β . A custom-made SU solution that is based on a 25 Mhz clock and can scan as fast as 40 ns per pixel [145] was used. To synchronize the SU and the SPIDR clocks, the SU sends reference signals, or supplementary events, to the CheeTah, as demonstrated in Figure 4.3a. They contain only timestamps and can be represented by any input signal that can be used to unequivocally determine the electron probe position (x, y) . Although theoretically one could use a single signal indicating the start of the rastering, sending periodic reference signals prevents clock drift, which is especially important for long ($>10 \text{ s}$) acquisition times. In the present case, the beginning of a new scan row (y direction) as a trigger falling edge was used, while the end of a line is represented by a rising edge. The difference between a falling and a rising edge is the scanning flyback time setting.

The complete hyperspectral reconstruction principle is shown in Figure 4.3b,

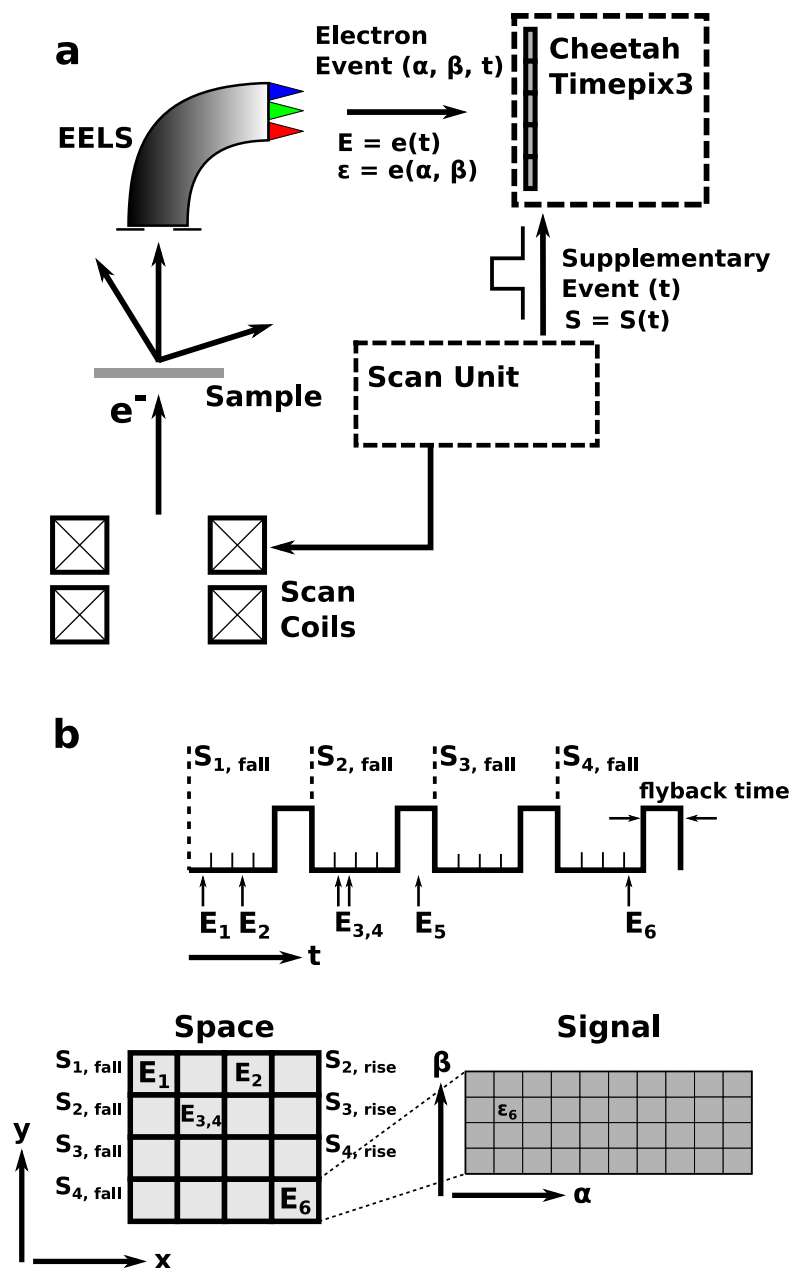


Figure 4.3: The hyperspectral data reconstruction process. (a) The scheme of the system used for data acquisition. The scan unit inputs temporal supplementary events, while individual electrons produce positional and temporal events. (b) A sketch on how the temporal information of both electrons and supplementary events can be used to arrange electrons in the reconstructed hyperspectral spatial data (x and y). The pixel address (α and β) is used to determine the spectral information of each probe position.

which depicts the timeline of the occurring events. For clarity, electron events e_n are further subdivided into $E_n = e_n(t)$ and $\varepsilon_n = e_n(\alpha, \beta)$ to explicitly indicate what information is used in each step of the reconstruction. As the received supplementary event $S(t)$ relates to the beginning of a new scan row, the number of columns (x direction) must be known by the software. This value is used as the number of time bins between a supplementary falling event and a successive rising event, as shown at the top in Figure 4.3b. As an example, it is possible to see that electrons e_1 and e_2 are in the same row because they are both after $S_{1,fall}$ but are in different columns because they are in different time bins within the scan row. It is important to note that electron emplacement in the hyperspectral spatial pixel (x and y) is only dependent on time. The pixel address of the electron event, ε_n , is only used to form the hyperspectral signal (α and β), as shown in Figure 4.3b at the bottom left by ε_6 . Additionally, the rising edge trigger input by the SU indicates the end of a scan row, meaning the high digital signal corresponds to the flyback of the electron probe; any electron event that arrives during this time interval is rejected, as illustrated by E_5 . As a final remark, it is important to clarify that the time t in $E_n = e_n(t)$ is simply the electron ToA corrected by the fine ToA, having a nominal temporal resolution of 1.5625 ns. Note also that the multiple electron-hole pairs created by a single impinging electron create multiple detector hits, called clusters. To circumvent the problem of multiple event counting due to clusters, a cluster-correction algorithm was implemented. It must use both the temporal and the spatial information of adjacent electron hits to be effective and is explained in detail later in this work.

A live acquisition program was coded in Rust [287] capable of translating the received events by the TPX3 to a variety of outputs, including the hyperspectral image illustrated in Figure 4.3 [19]. The software can be controlled in a user interface plugin developed for the Nionswift software [108], which is also used for data acquisition and for controlling the microscope. Other software features include the acquisition of single spectra, which uses the period of a TTL signal in the TDC line to determine the spectrum dwell time. The processed data is transferred by transmission control protocol (TCP) using a 10-Gbit optical fiber from the dedicated processing computer to the client computer. For a single spectrum, data is transferred in its entirety (1024-sized array for fully-binned measurements and 1024x256-sized for image measurements) with configurable bit depth to accommodate a high range of acquisition times. For the hyperspectral image, one must note that for a 512 x 512 image with 120 ns pixel time, an entire 512 x 512 x 1024 hyperspectrum is simultaneously reconstructed with the ADF, although very sparse. The transfer rate would need to be ~ 140 Gbit/s (using 16-bit integer) which is much higher than the transfer limit of the 10-Gbit Ethernet. In such cases, data can be transferred more compactly by sending a list of indices to be incremented in the datacube. As an example, for a hyperspectrum containing 64 x 64 spatial pixels, and considering the 1024 pixels in the detector row, these indices must be between 0 and 4194304.

Figure 4.4 shows an initial example of a live hyperspectral reconstruction. The pixel dwell time was kept at 120 ns in a 512 x 512 spatial sampling with a current of approximately 10 pA from a region of approximately $1.0 \mu\text{m}^2$. The flyback time is set at 28 μs but measured as $\sim 28.5 \mu\text{s}$ and thus a single frame takes approximately 46 ms to acquire. The sample contains some silver nano-cubes drop-cast onto a thin film of amorphous carbon. At the top, the ADF image obtained during data acquisition and three snapshots for different accumulation times of the energy-filtered hyperspectrum between 5 eV and 45 eV, comprising the strong carbon plasmon resonance peaked at approximately 22 eV. At the bottom, it is displayed the spectrum for the 8 x 8 pixel cell highlighted by the yellow square. In the first 2 s of acquisition, 43 complete ADF frames are accumulated and a minimal contrast shows up in the energy-filtered image. After 16 s and 76 s of acquisition (corresponding to, respectively, 347 and 1649 frames), the contrast is greater and the bulk plasmon of amorphous carbon resonance is much more distinguishable.

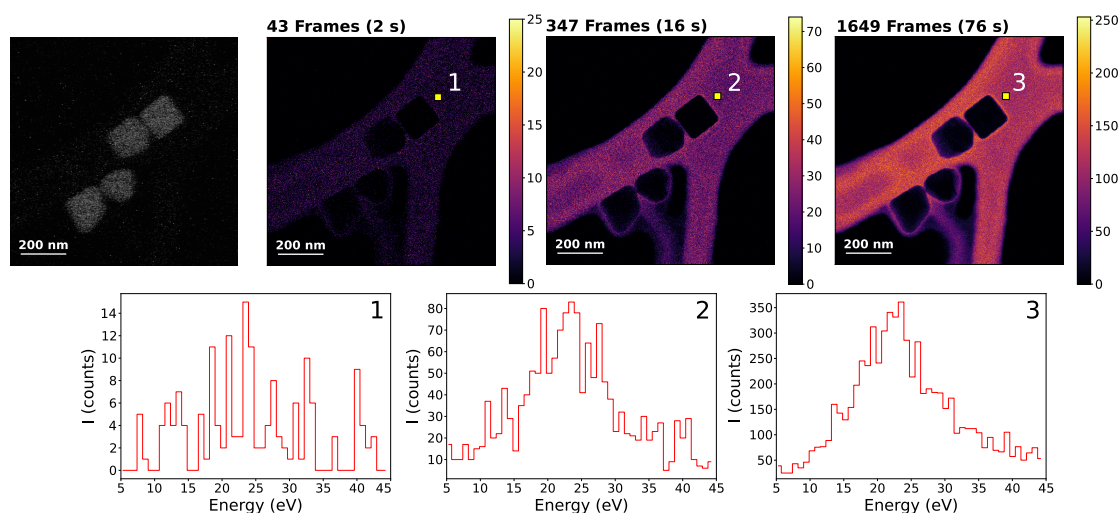


Figure 4.4: Energy-filtered hyperspectral image containing 512 x 512 pixels and using 120 ns pixel time between 5 eV and 45 eV for a sample of silver nano-cubes drop-casted over a thin amorphous carbon film. The ADF (top left) and three images (1, 2, and 3, at the top) and the corresponding spectra acquired inside the highlighted yellow square (8 x 8 pixels) taken after 43, 347, and 1649 complete ADF frames shows the time evolution and the event-based nature of hyperspectral data formation.

The developed software [19], as mentioned, provides live imaging capabilities, i.e. 2D and 1D EELS spectra, as well as the live reconstruction of hyperspectral images. Previous frame-based hyperspectral maps of 512 x 512 pixels would be acquired in at least 4 minutes considering a sub-ms readout time of the EELS detector. In this work, the same spatial sampled hyperspectral image is acquired every ~ 46 ms, which is almost $\times 10^4$ faster than the frame-based approach and is an important technical advance in EELS instrumentation. To provide a better understanding of the software scalability concerning the hyperspectral data reconstruction, the processing time for the equivalent of 5 s of acquired data is

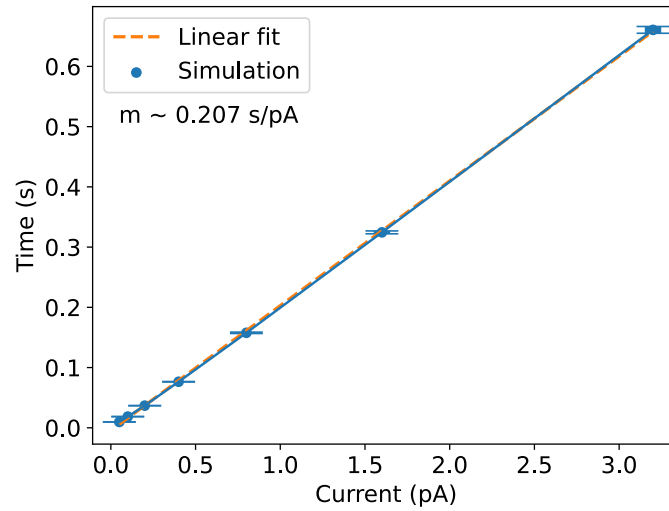


Figure 4.5: Processing time of a 256 x 256 hyperspectral image with 1 μs pixel dwell time for 5 s of data acquisition, showing the expected linear relationship. Approximately 24 pA is required to reach a processing time of 5 s, the same as the acquisition, meaning software would not handle live acquisitions from currents beyond 24 pA.

plotted as a function of the chosen current in Figure 4.5, considering a fixed pixel dwell time of 1 μs and a spatial sampling of 256 x 256 pixels. The performance was analyzed using *perf* [288], a performance analyzing tool available from the Linux kernel, and were repeated between 50-100 times to obtain more meaningful results. As expected from the event-based nature of TPX3, the processing time is linear with the current, with an angular coefficient $m \sim 0.207 \text{ s/pA}$. To reach the live processing limit, processing time must be equal or greater than the acquisition time, which happens for a current of $\sim 24 \text{ pA}$ in these conditions, five times higher than the maximum TPX3 throughput of 5 pA. Simulation performance for the pixel dwell time and the spatial sampling direction, as well as specifications of the used computer for the data processing, can be found in the appendix.

4.3 The calcite decomposition

In order to demonstrate the event-based hyperspectral image, a calcite (CaCO_3) sample is used and its well-known transformation to calcium oxide (CaO) and carbon dioxide (CO_2) under the electron beam irradiation ($\text{CaCO}_3 \xrightarrow{e^-} \text{CaO} + \text{CO}_2$) [289–291] is explored. The experiment was performed in a Vacuum Generators model HB 501 (VG) at 100 kV equipped with an LN_2 cold stage that stays at approximately 150 K. The acquired data had 4 μs pixel time with the 32 nm x 32 nm region sampled by 32 x 32 pixels. The convergence angle was 15 mrad and a collection aperture of $\sim 2 \text{ mrad}$ was used to have both an improved spectral resolution and to produce a non-saturated EELS dataset. The electron spectrometer

was set to a small dispersion of ~ 0.445 eV/pixel to monitor simultaneously the low loss region, the carbon K edge, and the calcium $L_{2,3}$ edges. In these conditions, one ADF image, and therefore one hyperspectral image, is completed every ~ 5 ms. Such a rate is comparable with that of a single energy-filtered transmission electron microscope (EFTEM) image, although in the present case the whole spectral range is gathered. The collected signal is extremely low at these rates, as the dwell time for the acquisition of each pixel's spectrum is $4 \mu\text{s}$, and some time-binning is needed for interpreting the data. Therefore, the total of 93 s of the acquisition was sliced into 232 hyperspectral images with intervals of 400 ms, which corresponds to roughly 80 complete ADF frames and an exposure time per pixel of $320 \mu\text{s}$. As it shall be seen, this temporal sampling is enough to unveil the calcite decomposition dynamics in the low-loss energy range. Data analysis in this work was done using the Hyperspy package [292].

4.3.1 Cluster correction

Before examining the data set, a custom-developed algorithm, implemented within the Rust-based live processing library, was used to identify and treat clusters from the hyperspectral time slices. To do so, both ToA and the pixel hit position are used: the set of pixels within a single cluster is counted as a single event carrying the average ToA and pixel impact position. A new cluster is created if the next electron event has a ToA superior to the previous one by > 200 ns or if the pixel distance is > 2 pixels in any of the α or β directions independently (see the appendix for further details on different parameters). Figure 4.6 shows the

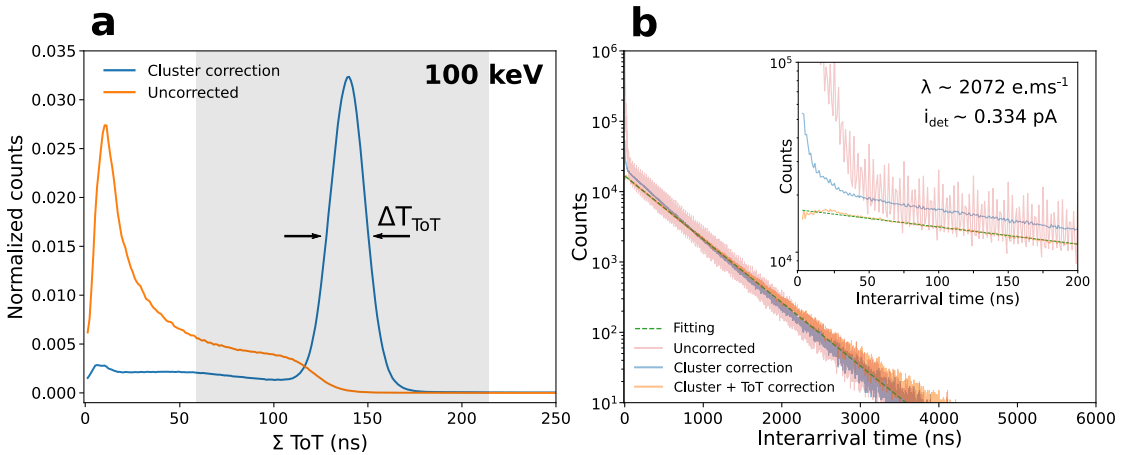


Figure 4.6: Impact of the cluster-correction algorithm in the EELS data. (a) The normalized frequency of the summed ToT before and after cluster correction. (b) The electrons inter-arrival times for the uncorrected, cluster-corrected and cluster+ToT-corrected data. Fitting was performed for the latter and provided an expected number of occurrences of $\lambda \sim 2072$ electrons.ms $^{-1}$, corresponding to a current in the detector of $i_{\text{det}} \sim 0.334$ pA.

impact of cluster treatment on the EELS hyperspectral data. In Figure 4.6a, the histogram of the ToT for all pixel hits before the cluster-correction (orange curve) and the histogram of the sum of the ToT of all the pixel hits that belong to a single cluster (blue curve) are plotted. A Gaussian fit to the distinct peak shown in the cluster-corrected data gives us an average value of ~ 139.13 ns and an equivalent full-width-half-maximum $\Delta T_{ToT} = 22.65$ ns, which is under the clock tick of 25 ns. In such a case, ToT-based spectroscopy has a resolution of approximately 16.18 keV and hence is difficult in the typical EELS range (< 1 keV). In Figure 4.6b, the time difference between consecutive events, called inter-arrival times (ITs), is plotted for the same electrons as in Figure 4.6a. A consequence of the independence of the events in a Poisson process is that the number of events as a function of the observed IT follows an exponential decay $e^{-\lambda t}$, where λ is the expected rate of occurrences in the Poisson process. The uncorrected curve (light red) seems to be properly following an exponential decay for ITs longer than 100 ns but has a steep increase of approximately two orders of magnitude for ITs shorter than 50 ns. After cluster-correction (light blue curve), the curve approximates to an exponential behavior for shorter times, despite a still visible deviation for ITs < 25 ns. Additionally, it is also shown (light orange curve) the IT for the electrons in which their cluster total ToT is between 60 and 220 (gray rectangle in Figure 4.6a), which follows a much-closer exponential behavior for short ITs. Identified clusters with small total ToT are primarily formed in between TPX3 chips and thus might be subjected to a different cluster formation dynamics that does not follow Poisson statistics. Finally, the current in the detector estimated by the number of hits after cluster + ToT correction is 0.322 pA. The fitting result (dashed line) gives $\lambda \sim 2072$ electrons.ms $^{-1}$, which corresponds to a current of ~ 0.334 pA and agrees within 96% with the electron hit estimate. Note that the Poisson statistics of the electrons is an indicative of the non-saturated regime of

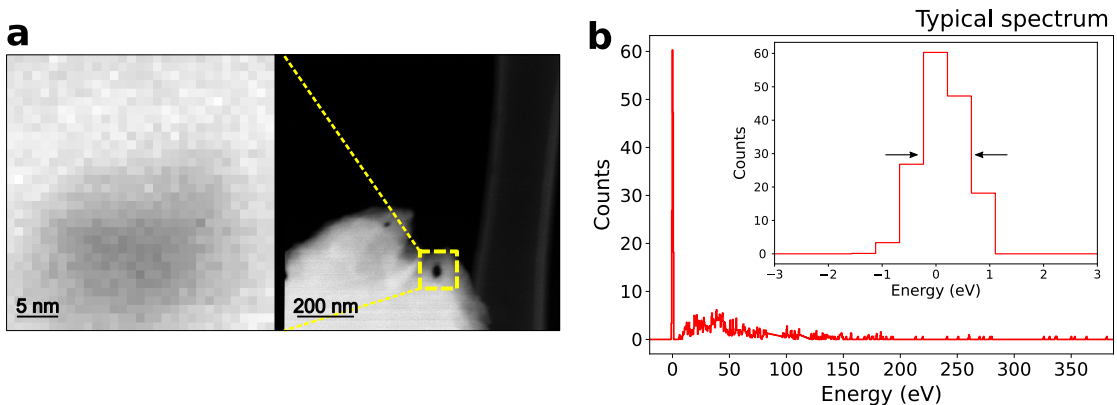


Figure 4.7: Typical acquisition conditions. (a) ADF images at approximately 25 s of acquisition time (left) and at the end of the acquisition after 93 s (right). (b) Typical EELS spectrum for a single pixel in a single time slice, showing a full-width at half-maximum of 2 pixels.

electron detection.

4.3.2 Results & discussion

Figure 4.7a displays one snapshot of the ADF at ~ 25 s of acquisition time (left), which already shows a contrast due to the accumulated sample damage. The ADF at the right shows a higher field-of-view image after the entire 93 s of acquisition. Figure 4.7b shows a typical single-pixel spectrum in one time slice ($320 \mu\text{s}$ pixel exposure time), displaying a ZLP with a maximum number of ~ 60 electron hits and a full-width at half-maximum of 2 pixels, a consequence of the improved PSF of direct electron detectors [277].

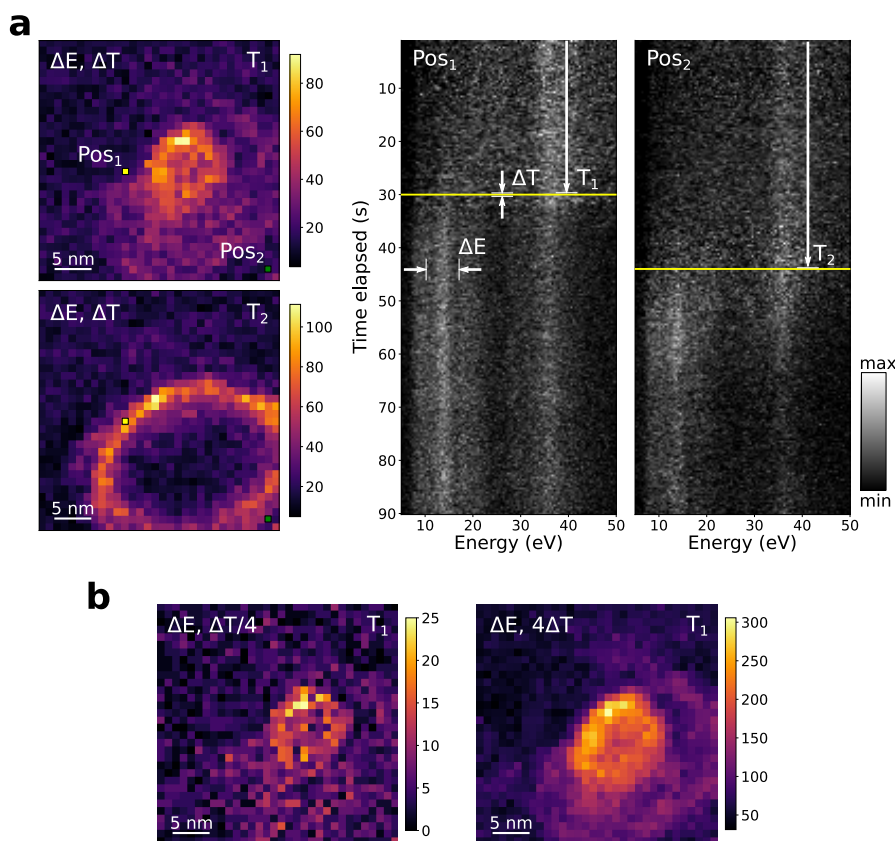


Figure 4.8: Hyperspectral EELS results for the calcite decomposition in the low-loss energy range. (a) Two energy-filtered snapshots centered at $E = 13$ eV accumulated in the energy interval ΔE for the time slices at $T_1 = 30$ s and $T_2 = 45$ s summed over the time interval $\Delta T = 400$ ms. The time evolution for two pixels, Pos₁ and Pos₂, is also shown. (b) Similar to the snapshots in (a), but for a time interval of 100 ms (top) and 1600 ms (bottom).

Figure 4.8a shows a few results from the time-resolved hyperspectrum after running the cluster-correction algorithm in the data set. Two energy-filtered images centered at the plasmon resonance feature at ~ 13 eV, indicated as ΔE and

associated with the CaO formation [290, 291], are shown at left for two distinct times (T_1 and T_2) within the same time interval $\Delta T = 400$ ms and thus depicts the CaO formation dynamics within ± 200 ms time resolution. The EELS spectra as a function of the total elapsed time for the pixel Pos₁ (yellow square) and Pos₂ (green square) are shown at the right. Note how Pos₂ is farther from where CaO formation starts and hence the transformation is triggered at a later time than at Pos₁. There is a clear transformation in the low-loss spectra, most notably around the aforementioned resonance at ΔE , successfully captured by the time-binning chosen. In Figure 4.8b, a similar energy-filtered snapshot is shown, but with time intervals of 100 ms and 1600 ms, demonstrating that the time-binning value can be arbitrarily picked as long as it is a multiple of a single-scan image acquisition time.

In Figure 4.9a, similar spectra for the core-loss energy range around the Carbon-K edge and the Calcium L_{2,3} edges are shown for the entire sample region. In Figure 4.9b, it is displayed the sum of the normalized signal between 286 eV and 305 eV (comprising thus the C-K edge) divided by the signal between 343.5 eV and 351.0 eV (Ca L_{2,3}). To have a better signal-to-noise ratio, time slices were binned by a factor of 8, and thus have a time resolution of ~ 3.2 s. The smaller proportion of carbon relative to calcium over time suggests the calcite decomposition is happening and, consequently, carbon content is reducing in the system.

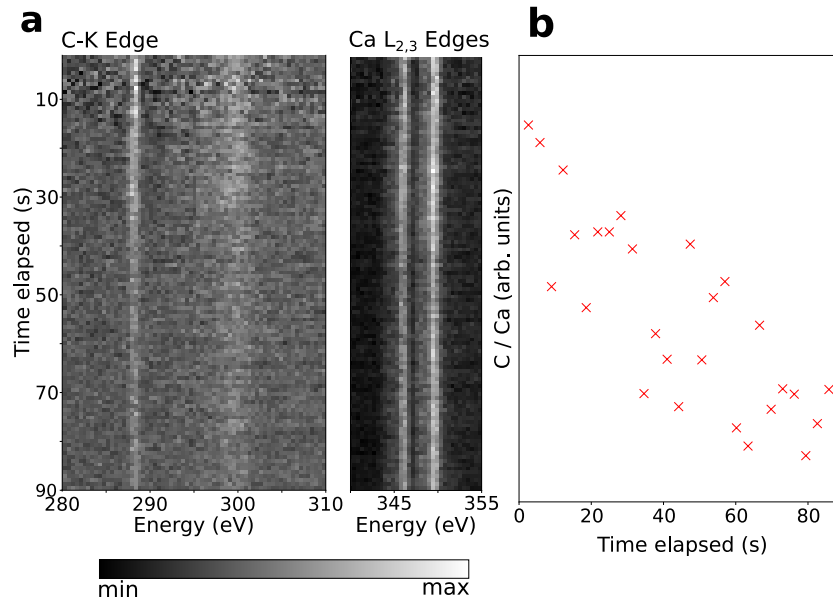


Figure 4.9: Hyperspectral EELS results for the calcite decomposition in the core-loss energy range for the entire sample region. (a) Time evolution around the C-K edge at the left while, at the right, we display around the calcium L_{2,3} edges. (b) The ratio between C-K edge (286 eV - 305 eV) and the calcium-L_{2,3} (343.5 eV - 351.0 eV). The diminishing proportion indicates that despite sample mass-loss, carbon content is reducing relative to calcium.

To extract more spectral information from the calcite decomposition dynamics, one could further increase the time interval of the hyperspectral slices, sacrificing time resolution for more signal per spectrum. More interesting, however, is to perform a low-rank approximation, such as singular value thresholding (SVT), a.k.a. PCA (principal component analysis), which can increase the signal-to-noise ratio [293, 294] without sacrificing time and spatial resolution. Figure 4.10 shows the result of SVT of the dataset with 3 components for a single spatial position close to the yellow square (Pos_1) highlighted in Figure 4.8. The time evolution shows the progressive reduction of the carbon content, followed by a more and more pronounced crystal field splitting of the t_{2g} and e_g peaks in the Ca $L_{2,3}$ edge due to the undistorted octahedral symmetry and change in length of the Ca-O bonds in CaO compared to CaCO_3 [291], as valence band shifts are expected to occur on those cases [295]. The SVT was performed with the ZLP and the pixels close to the chip edges masked. Finally, note that although the time slice interval has the unbinned value of 400 ms, single-pixel exposure time is $\sim 320 \mu\text{s}$.

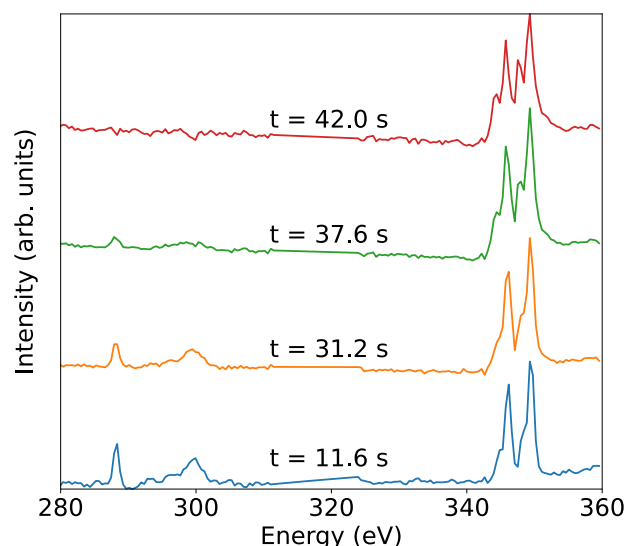


Figure 4.10: Set of spectra for a single pixel close to Pos_1 for four different times after PCA denoising. Carbon content is progressively reduced, while the crystal field splitting, associated with the Ca-O bonds, increases. Time slices are within the unbinned time interval of 400 ms and exposure time, per pixel, is $320 \mu\text{s}$.

4.4 Conclusions & prospects

In this chapter, event-based and frame-based detectors were compared, especially in the context of EELS. TPX3, an event-based direct electron detector was introduced, which is capable of acquiring energy-loss spectra with a practically noiseless readout scheme and with an improved PSF relative to scintillator-based indirect detection systems. TPX3 is capable of providing the ToA of the electron events

within 1.5625 ns temporal resolution. Additionally, the CheeTah solution has two TDC line inputs, which is the core of the event-based hyperspectral EELS implementation thanks to external events from the SU to add timestamps in the electron data flow. These enable the live acquisition of standard EELS spectra and hyperspectral 3D data, in which a software has been developed and is available under MIT licensing [19].

The acquisition of a hyperspectrum with scanning speed limited by the SU rastering time instead of the detection system was presented. To demonstrate our system capabilities, it was studied the decomposition of calcite into CaO and CO₂ under electron beam irradiation. After cluster correction and ToT correction, electron arrival times follow a Poisson distribution, which shows both the well-known statistics of the electron emission in a cold field-emission gun (cFEG) and the non-saturated regime of the data acquisition. Note that, in principle, hyperspectral images can be acquired with pixel times as low as 1.5625 ns (nominal temporal resolution of TPX3), although reaching this scan rate would need further TPX3 calibrations [296, 297] that are irrelevant for the present minimum rastering time of 40 ns. Time-resolved data is shown for the CaO formation in the low-loss and the core-loss energy range. For the latter, a single-pixel spectrum after performing signal decomposition was achieved in the hyperspectral slices, although meaningful spatial maps are working in progress in more controlled samples.

It is believed that event-based hyperspectra will become increasingly available in the microscopy community. They will effectively tackle several important problems that require both nanometric spectral resolution and nanosecond time resolution. Several applications can be contemplated with such systems, especially regarding optical excitations in the nanosecond timescale, which include high-Q optical resonators, already demonstrated in the previous chapter and that have been scrutinized under electron beams for multiple works [16, 137, 203], and accessing the chemistry of electron-irradiation sensitive materials like graphene oxide [298].

Cathodoluminescence excitation spectroscopy

5.1 Introduction

The second interesting application of Timepix3 (TPX3) in this thesis is the development of cathodoluminescence excitation spectroscopy (CLE), which was inspired by its powerful analog in optics: photoluminescence excitation spectroscopy (PLE). This chapter was developed in equal co-authorship with the post-doctoral Nadezda Varkentina.

In PLE, the exciting laser wavelength is rastered and the emitted photons are collected by using an optical spectrometer or in a selected energy range in a single-channel detector, such as a photomultiplier tube (PMT), making it possible to determine absorption curves related to a specific emission pathway, as shown in Figure 5.1. This has led to many successful measurements, such as the role of phonons in the absorption spectra of single carbon nanotubes [299] or the energy transfer in carbon nanotubes/porphyrin compounds [300]. More recently, PLE was used to determine the excitonic binding energies of monolayer transition metal dichalcogenides [21, 301]. However, being diffraction-limited, PLE is not suitable for studies in the nanoscale range.

One of the interesting properties of electron energy-loss spectroscopy (EELS) is that the electron travels at relativistic velocities, from $0.33c$ for 30 keV to $0.70c$ for 200 keV. When this fast-moving charge crosses the sample, the axial and radial electron fields have significant values only within a few hundreds of attoseconds interval. The Fourier-transform in the frequency domain shows that the electron contains energy contributions from a broadband range [302]. In the context of a possible CLE, however, this is a very poor property: how to relate the emission spectra, if any, in cathodoluminescence (CL) with the incoming electron? In other words, how to know which electron, and its corresponding energy, has triggered a photon emission? This is precisely what CLE is proposed to do.

To better grasp the idea of this concept, one can use some of the results already discussed in this thesis. For the measurements shown in chapter 3 for the spherical

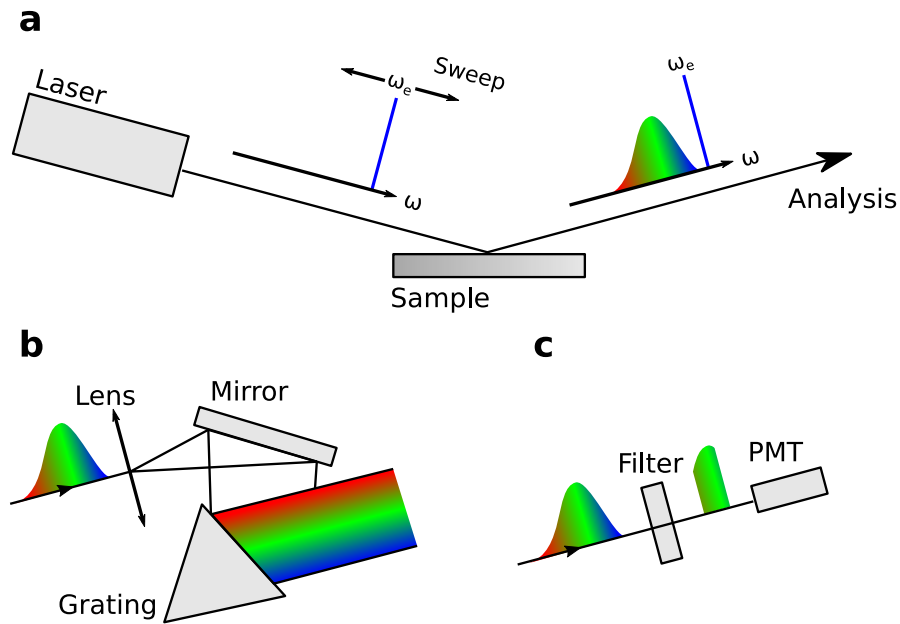


Figure 5.1: Sketch of the PLE experiments. (a) The photoluminescence spectrum of the sample is acquired for multiple excitation energies by rastering ω_e . The output light can be analyzed by using an optical spectrometer (b), acquiring an emission spectra for each laser wavelength or by using a filter and a single-channel detector (c), such as a PMT.

microresonators, EELS and CL spectra are temporally uncorrelated. Although, indeed, one represents the absorption spectrum (EELS) while the other the emission spectrum (CL), it is impossible to experimentally know which absorbed energy has triggered which photon emission. As the myriad of different processes that can happen between absorption and emission have different time-scales, one can state that these spectra are simply time-averaged.

In this chapter, CLE is demonstrated with nanometer-scale spatial resolution over a broad energy range, from the visible to the soft X-ray, 2 eV to 620 eV, in a scanning transmission electron microscope (STEM). The approach relies on a new coincidence scheme between inelastic electron scattering and photon emission events. If the temporal information of both these events is known, correlation can be performed to unveil the probability of each energy transfer pathway, and thus CLE spectra are constructed with EELS events that are time-correlated with an emitted photon, while the energy-dependent relative quantum efficiency spectra are given by the ratio of CLE and total EELS spectra. As a proof-of-principle of CLE, examples from the two main families of optically relevant materials were studied i.e., plasmonic nanoparticles, typically associated with phase-locked, relative to the exciting source, light emission processes, and defects in semiconducting materials, most usually associated with incoherent processes [87]. For the former, silica-shelled Au nanospheres were studied, in which two light emission pathways are identified: surface plasmons (SP) for the Au and transition radiation (TR)

for the SiO_2 and Au. The direct energy and time correlation between absorption and emission for these excitations, known to be coherent, is a confirmation of the relevance of CLE. For the latter, h -BN flakes were used, in which the decay pathways leading to the excitation and emission of the 4.1 eV defect were explored. All excitations, from the near-band edge (NBE) to the core-losses, including the bulk plasmon, are demonstrated to participate in photon emission. The bulk plasmon is experimentally confirmed as the main absorption pathway. Nevertheless, the relative quantum efficiency first peaks at the NBE energy and is followed by a linear increase up to the maximum energy in the soft X-ray energy range (620 eV), which had not yet been shown. Finally, spatially resolved CLE in h -BN reveals the spatial variation of the excitation and decay pathways with a 40 nm spatial resolution. STEM-CLE, on that account, has proven to be a nanometer-scale counterpart of PLE.

It is important to note that coincidence experiments in a electron microscope have already been performed in the past, especially by the pioneering experiments of Kruit *et. al.*, in which X-rays photons and electrons were time-correlated in the attempt of improving the EELS detection limits [303]. This work was performed before the widespread usage of parallel EELS detection, and thus a PMT as used. More recently, coincidence experiments using similar X-rays photons were performed using a TPX3 and hence a 2D EELS detector, which allowed to study a much broader energy range simultaneously [304, 305]. The coincidence of infrared photons and electrons was also performed [306], although the relative quantum efficiency as a function of energy and its spatial dependence has not been measured.

5.1.1 Light emission mechanisms

Before discussing the results of this chapter, it is instructive to introduce a more robust theoretical background relative to the light emission mechanisms because knowing the dynamics of CL provides insights regarding the associated absorption process. In the electron microscopy community, they are usually classified regarding the phase relation between the exciting source, the electron beam, and the emitted radiation. Following the nomenclature given by García de Abajo, coherent excitations are when the emitted light and the exciting electron are phase-locked, while, in an incoherent process, the emitted light has no phase relation with the electron beam [87, 97].

Coherent excitations

One of the simplest coherent light emission processes is Cherenkov Radiation (CR). It arises in dielectric media in which the electron travels faster than light, or, equivalently, $v_e > c/\sqrt{\epsilon}$ [87, 307, 308]. The light is emitted along the so-called Cherenkov cone, analogously to what happens to pressure shock waves created by supersonic sources. Another coherent process is TR, which is usually pictured

by the collapsing of the electron image charge when the fast electron crosses the sample. An effective dipole is created perpendicular to the sample surface, which produces an emission pattern with two lobes with a minimum at the electron propagation direction [87]. As expected from coherent processes, Cherenkov and TR are subjected to interference patterns, which has already been observed and discussed in the pioneering works of Yamamoto *et. al.* [309, 310]. However, as pointed by García de Abajo *et. al.*, whereas CR is connected to electrons propagating in an infinite media, TR is linked to the emission between an interface of two different media, and thus for finite media the distinction between them is not straightforward [307].

Finally, light emitted from SP is also coherent. In fact, the first spatial map of surface plasmons in individual nanoparticles in a STEM was done by CL rather than EELS [231], which would only make sense if EELS and CL were spatially correlated, as in coherent excitations. With the emergence of ultrahigh monochromated electron microscopes, such as in ChromaTEM, mapping surface plasmons in EELS had become an almost trivial task [16, 112]. However, CL still has a few

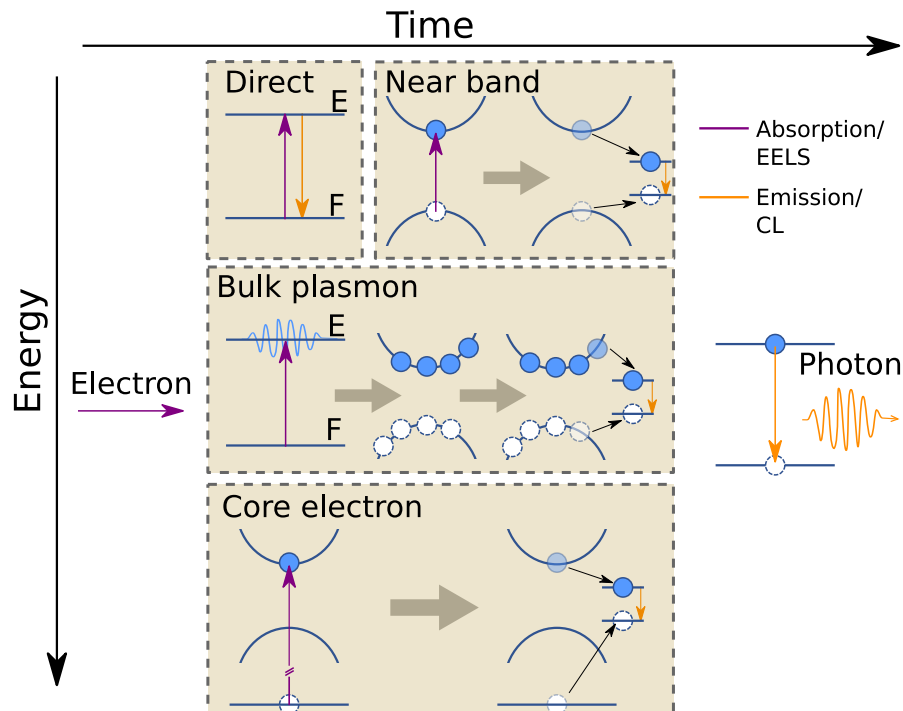


Figure 5.2: Photon emission pathways upon electron scattering. A relativistic inelastic electron scattering event in a solid can generate different excitations (vertical purple arrows): direct optical transition, NBE transition, bulk plasmon excitation, and core-electron excitation. Excitations not involving single particles (excitons, bulk and surface plasmons, etc.) are represented between a fundamental (F) and excited (E) state. These can relax through different pathways, leading to the excitation of a final optically bright energy level and photon emission (vertical orange arrows).

advantages with respect to EELS, especially because light manipulation is still much easier to do than with electrons, so polarization-resolved measurements are capable of providing directional information [311]. Besides, the spectral resolution of optical spectrometers routinely achieves 5-10 meV, which is cheaper and less complex than electron monochromators.

In the context of CLE, coherent cathodoluminescence is easily described because the emitted photon energy is close to the electron energy lost, being the difference due to total intrinsic losses of the system (i.e. ohmic losses and radiation damping mostly, as discussed in Chapter 1). These are the direct process, as depicted in Figure 5.2, in which vertical arrows depict optical transitions, purple for absorption and orange for emission, while relaxation pathways are illustrated by black arrows.

Incoherent excitations

It was stated previously that the electron beam could be seen as a broadband excitation source. What does this phrase mean exactly? Is the electron beam thus correspondent to a white-light excitation source? If this is true, CLE and PLE would be strictly equivalent. Electron beams can transfer momentum to the sample, which means they can excite non-direct energy transitions between the valence and the conduction band. Differences apart, an incoherent light emission process would be equivalent to what happens in photoluminescence: light is absorbed in a given energy, and then the excited state decays inelastically to produce photons in a different energy, inferior to the absorbed one.

Incoherent processes are most usually associated with the creation of electron-hole (e-h) pairs. For electron energies of typical microscopes, the bulk plasmon resonance is one of the most probable excitation [87, 97], which have picosecond lifetimes and rapidly decays into multiple e-h pairs. Subsequently, they diffuse in the material, in the tens of picoseconds timescale, until a radiation center is found, where light is effectively emitted. This behavior has been recently experimentally strengthened thanks to the observation of photon-bunching in CL experiments [106, 312, 313], meaning a single electron can trigger the emission of multiple photons.

Under this same logic, the pathways described in Figure 5.2 can be adequately described. In the near-band, the incoming electron can be absorbed, even in an indirect bandgap semiconductor such as *h*-BN [314]. Bulk plasmon, as already discussed, can excite multiples e-h pairs and, finally, core electrons, from the inner bands of the atom, can also excite electrons to the valence band, similarly to what is done in core-loss EELS.

5.1.2 Correlation algorithm

The temporal resolution of the electron events was obtained thanks to a TPX3 hybrid-pixel detector (HPD). All the libraries written for the acquisition of TPX3

live measurements [19], presented in the previous chapter, were used as a base to a post-processing library, which has currently two major capabilities. The first is the arbitrary time-slicing of hyperspectral data, as already discussed in the calcite decomposition. The second is the coincidence-seeking algorithm, which can process spatially-resolved CLE maps. Both are readily compatible with the optional cluster-correction, which is indeed applied throughout this chapter¹.

For the photon-electron coincidence, the time of arrival (ToA) of each electron event is compared with the ToA list from the photon events after both being sorted by time. A coincident electron is found when its time lies within a given time interval, ± 25 ns in this work, centered at the first-matching photon time. Instead of pairing every electron with all the elements of the photon list, a sliding window algorithm is performed, which allows increasing performance by as much as a factor of 10 due to the effective photon list's reduced size. Additionally, concurrency (using multiple cores of the computer) is implemented in parts of the code. The algorithm standard output consists of a list of energy-loss indices along with their associated time delay. For the hyperspectral dataset reconstruction, supplementary events from the microscope scanning unit are used. This procedure can be found in detail in ref. [20] and in the previous chapter. Time delay was set to zero at the maximum of coincidence counts. Its absolute value is meaningless as it includes electronic and propagation delays.

The typical photon rate is 8-10 kcounts/s or, equivalently, ~ 90 -100 photon events every MB of TPX3 raw data for the typical electron beam current used. Processing time depends on the desired maximum time width, in which an increased value improves overall performance, although it may take unnecessary space and memory of the computer. The processing time is in the order of ~ 10 s/GB of data in the mentioned acquisition conditions, and is roughly independent if the data is a 3D hyperspectrum or not. For the former case, typical EELS hyperspectral images have 50-100 GB of data, and hence can be processed in ~ 12.5 min. As a comparison, a Python3-based algorithm with similar logic can take more than 20 hours to process.

5.2 Results & Discussion

To give reference EELS and CL spectra, the silica-shelled gold nanospheres and the *h*-BN flakes were studied in ChromaTEM, which has an electron monochromator. The achieved EELS spectral resolution was approximately 15 meV and the results are shown in Figure 5.3. For the nanospheres, the EELS spectrum shows a strong SP resonance along with a weak TR, as expected from their respective oscillator strengths. The NBE of silica can be seen at roughly ~ 9 eV, which is also the expected value [245]. In the *h*-BN, absorption shows distinctly the NBE of the

¹The time over threshold (ToT) correction discussed in the previous chapter, however, is not applied.

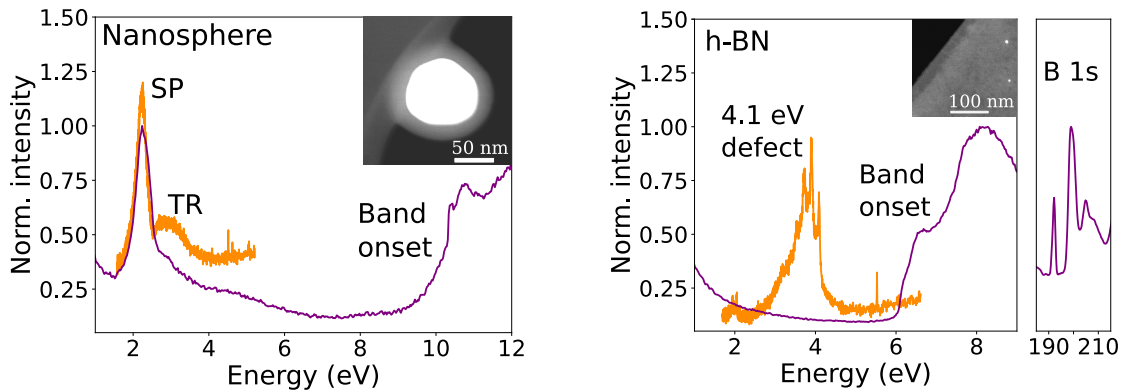


Figure 5.3: Time-averaged CL (orange) and EELS (purple) spectra of an Au/SiO₂ nanosphere and a thin *h*-BN flake show different absorption and emission features, described in the text. From these correlative time-averaged spectra, one cannot identify which absorption transitions lead to light emission. The small intensity emission at ~ 2 eV in the *h*-BN CL spectrum is a replica of the 4.1 eV defect emission due to the diffraction grating. The insets show images of the nanosphere and the *h*-BN edge. CL and EELS spectra have been normalized and shifted vertically for clarity. The spectra were acquired in ChromaTEM.

semiconductor in the low-loss regime. In the core-loss range, the Boron K edge at ~ 190 eV is observed. For the CL emission spectra in the Au nanosphere, SP and TR were both observed while, for *h*-BN, the well-known 4.1 eV defect is the sole feature. Being an incoherent source of light, one can only conjecture, based on theory or indirect evidence, which electron does trigger such emission, and, as depicted in Figure 5.2, NBE, bulk plasmons, core-hole excitation, or direct excitations could be all candidates for this. The weight of different pathways could not be measured in the past, which is precisely the main objective of this technique.

To achieve CLE, a temporal resolution below the time interval between events, given by the electron current (typically 1 electron every 25 ns for 10 pA), is required for all energy loss events of interest. The EELS-CL setup used for coincident measurements is displayed in Figure 5.4a. For EELS, a TPX3 detector, mounted in a non-monochromated cold field-emission gun (cFEG) electron microscope, was used [20], which provides sub 10 ns time resolution over arbitrary energy ranges determined by the resolution power of the electron spectrometer and the TPX3 pixel size. The EELS spectral resolution of the electron microscope is approximately 0.3 eV. Additionally, the particular detector used (CheeTah, from Amsterdam Scientific Instruments) has two time-to-digital converters (TDCs), allowing to append timestamps from external signals into the original electron data flow, as already discussed in the previous chapter of this thesis. Photon emission events were detected with a PMT working in the 2.0 to 5.0 eV energy range. The PMT output is directly connected to one of the TPX3 TDC lines. Electrons and photons' arrival times were stored in a list, along with the energy loss of the electron. The search

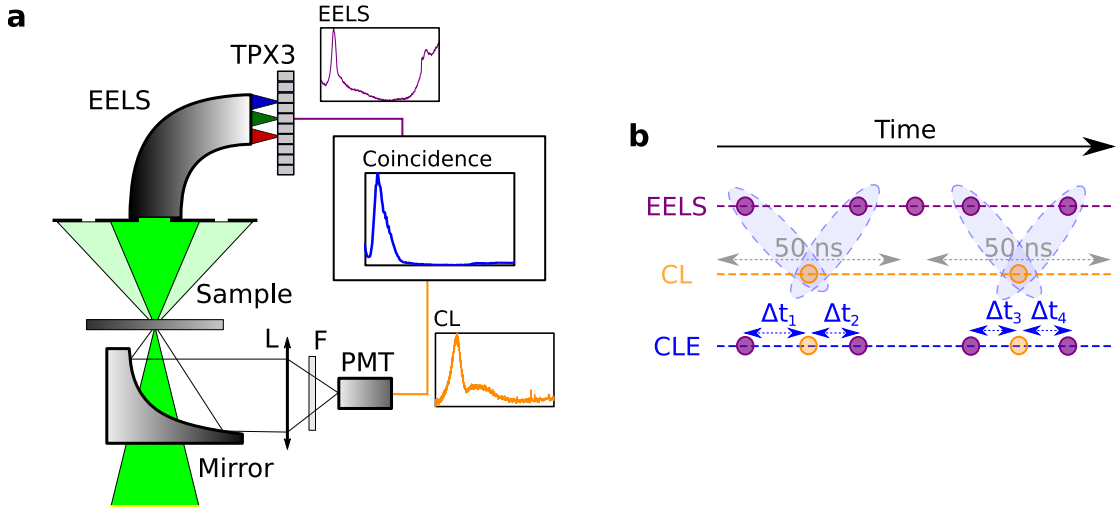


Figure 5.4: CLE in a STEM. (a) Sketch of the experimental setup: A 60-100 keV electron beam is focused in a nanometer spot that can be scanned along the surface of a sample. Time-resolved CL events (orange) are collected through a parabolic mirror and detected, after passing through an optical lens (L) and a bandpass filter (F), with a PMT, and time-resolved EELS events are measured by a TPX3 detector after an EELS spectrometer. These are stored in an ordered list, used to produce coincidence spectra (blue). (b) A search algorithm is used to find electrons that are within ± 25 ns of a detected photon.

algorithm described in section 5.1.2 is used to find electrons that are within ± 25 ns of a detected photon, from which a 2D histogram of time delay versus electron energy loss is reconstructed for a thin h -BN flake, as shown in Figure 5.5a. The number of detected electrons as a function of the observed time delay is shown by the red curve, in which the baseline count, representing the non-correlated

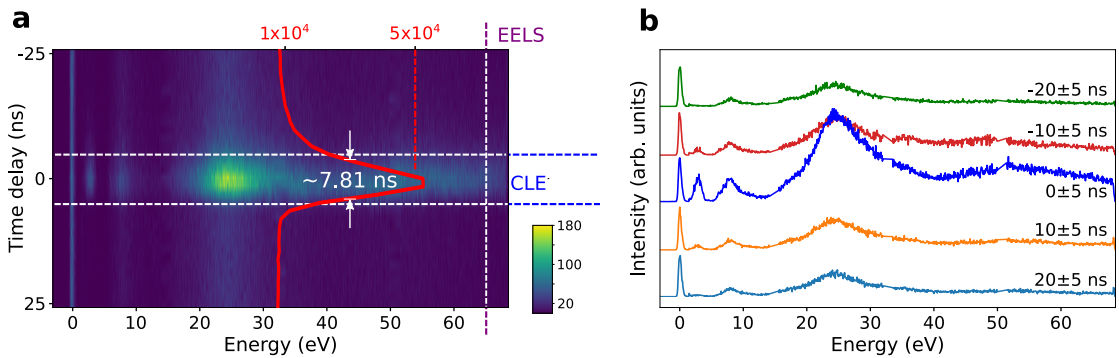


Figure 5.5: The photon-electron time-delay coincidence histogram for a thin h -BN flake. (a) The time delay between a photon and an electron as a function of the electron energy loss. The red curve is proportional to the number of coincident electrons in the time delay axis. (b) Series of spectra for multiple time delay windows. CLE, unless otherwise stated, is defined as 0 ± 5 ns.

photon-electron pairs, is approximately 10^4 , and it peaks at 5×10^4 counts at zero time delay. As already discussed in the previous chapter, reaching the ~ 1.56 ns temporal resolution in TPX3 requires a temporal calibration at the pixel level [296, 297], which was not performed, and hence the red curve full-width at half-maximum of approximately 7.81 ns represents the response time of the detection scheme. This 2D histogram shows the temporal evolution of the loss spectrum as a function of delay to a detected photon. In short time delay intervals (0 ± 5 ns, unless a wider time range is specified) a CLE spectrum is extracted. In Figure 5.5b, the same 5 ns time interval is used to plot several EELS spectra centered at distinct absolute time delays, from -20 to +20 ns, which clearly display changing features, most notable the intensity of the bulk plasmon at ~ 25 eV and the fading of the TR peak for long absolute time delays. The CLE spectrum resembles an EELS spectrum but is weighted by the photon emission probability, as shown in Figure 5.5b in the blue curve.

The ratio of the CLE and the non-coincidence EELS, therefore, provides the

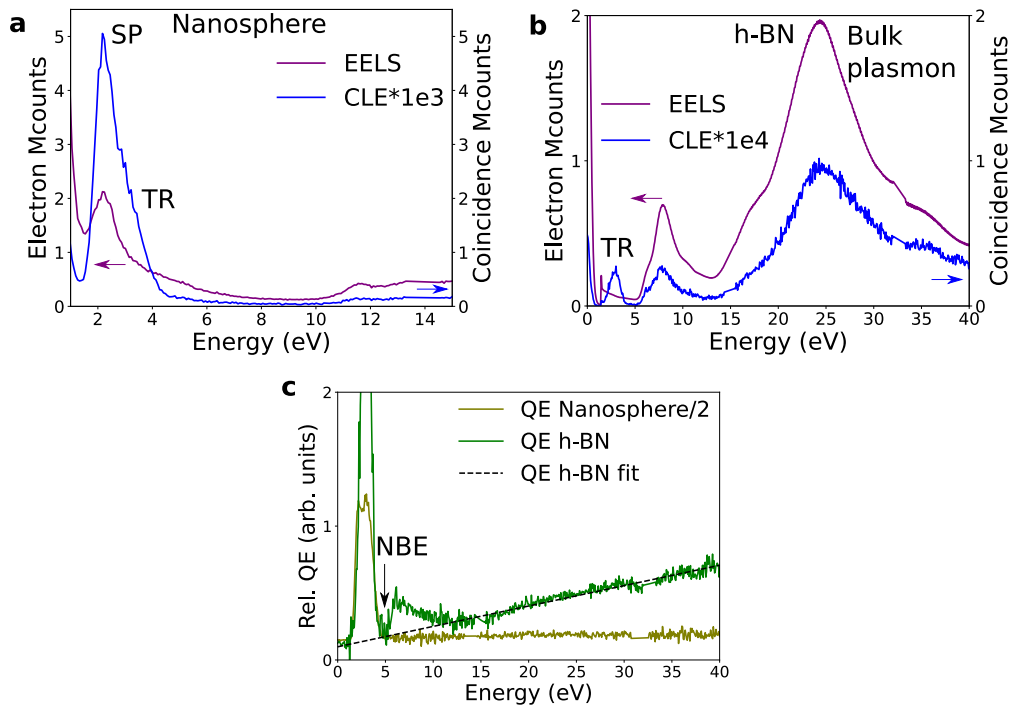


Figure 5.6: CLE results for silica-shelled gold nanospheres and *h*-BN flakes. (a) The total EELS (all detected electrons), and the CLE for the nanospheres. (b) Similar for the *h*-BN flakes. (c) The relative QE for both samples, defined as the ratio between CLE and EELS. For the nanosphere, the SP and TR decay channels are efficient photon emission pathways. For the *h*-BN thin flake TR, NBE, and all energies above it contribute to photon emission. NBE losses are more efficient pathways for light emission than energies below the bulk plasmon. Above 15 eV, the relative QE increases linearly. The nanosphere relative QE was divided by 2 for clarity.

relative quantum efficiency (QE) of different absorption processes. It highlights the differences between competitive radiative and non-radiative pathways, as displayed in Figure 5.6. For the nanospheres with the electron beam incident on the SiO_2 shell, the CLE spectrum shows that photon emission is due to the Au nanosphere SP decay (2.0-2.4 eV) and SiO_2 TR (2.6-4.0 eV), while higher energy losses do not contribute to light emission in the emission detection range. This is a reassuring observation, as photonic modes such as plasmons or TR are created in phase with the electron field and can only be created by loss events with energies in the same range as the emission ones [87]. A similar observation is reported by Feist *et al.* on micrometric photonic structures using an equivalent EELS-CL coincidence experiment [315]. The observation of these coincidence events and decay channels essentially validates the present methodology.

In a thin h -BN flake (<50 nm), the CLE and the relative QE spectra show contributions from TR, NBE, bulk plasmons, and higher energies towards the 4.1 eV defect and the TR. As discussed, the contribution from TR is usually missed in EELS spectra because of its small cross-section. As a matter of fact, they are invisible in the EELS and CL spectra of Figure 5.3. In the CLE spectra of Figure 5.6b, however, their contribution (at $1e-5$ event counts compared to the regular EELS counts, a typical 2 orders of magnitude better sensitivity than previously demonstrated) is revealed, as a signature of the remarkable sensitivity of CLE, much along the lines of PLE. From the CLE, it is experimentally proven that the common assumption that the bulk plasmon at ~ 24.4 eV is indeed the main source of electron-hole pairs which, after relaxation, triggers the 4.1 eV photon emission of the defect. Nevertheless, NBE absorption is demonstrated to be a non-negligible source of emission, with core-losses also a possible excitation path. The energy-

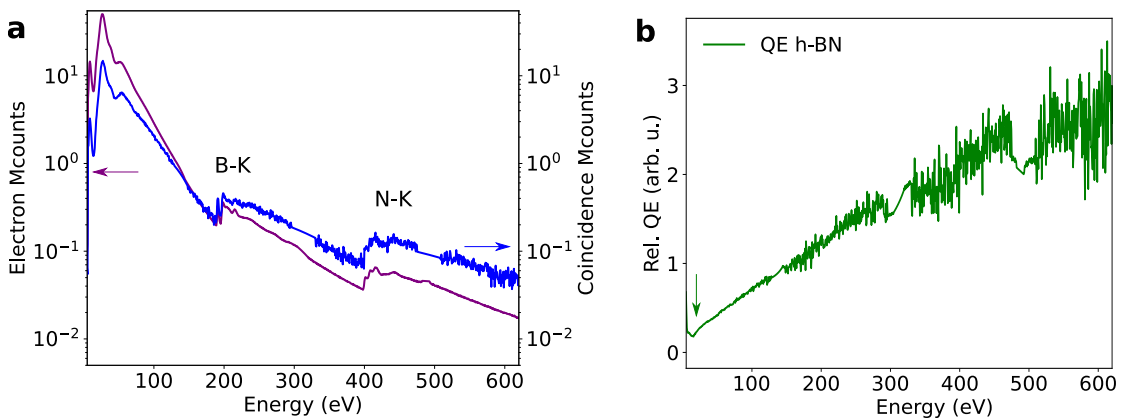


Figure 5.7: Core-loss spectra for a thin h -BN flake. (a) EELS and CLE of one h -BN flake measured up to 620 eV. B-K and N-K mark the boron and nitrogen EELS K edges. (b) Relative QE for the measured flake. The minimum of relative QE is visible at around 15 eV, as well as the decrease in relative QE between 6.5 and 15 eV (pointed by green vertical arrows). The CLE spectrum is integrated within the time range of ± 10 ns in this case.

resolved relative quantum efficiency in Figure 5.6c shows strikingly that NBE is a more efficient excitation channel than other excitations up to 15 eV. Above this energy, the efficiency for photon emission increases linearly, up to the maximum energy measured (620 eV), as shown in Figure 5.7, and highlighted by the green arrow in Figure 5.7b. The extrapolated linear trend at low energy crosses zero at the bandgap energy, in which the following dynamics can be suggested: each excitation at energy loss E can lead to the generation of at most N electron-hole pairs, where $N = E/E_g$, and E_g is the bandgap energy. Below the bandgap, the number of electron-hole pairs generated is zero. Assuming that the last step to the 4.1 eV defect emission is the NBE electron-hole pairs, the linear trend is deduced. With this, the peak in the relative QE at the NBE energy is reminiscent of an unforeseen resonant effect that will require further theoretical investigation. Direct resonant excitation of defect states by fast electrons has yet to be observed.

For the acquisition of the data displayed in Figure 5.4, the probe position

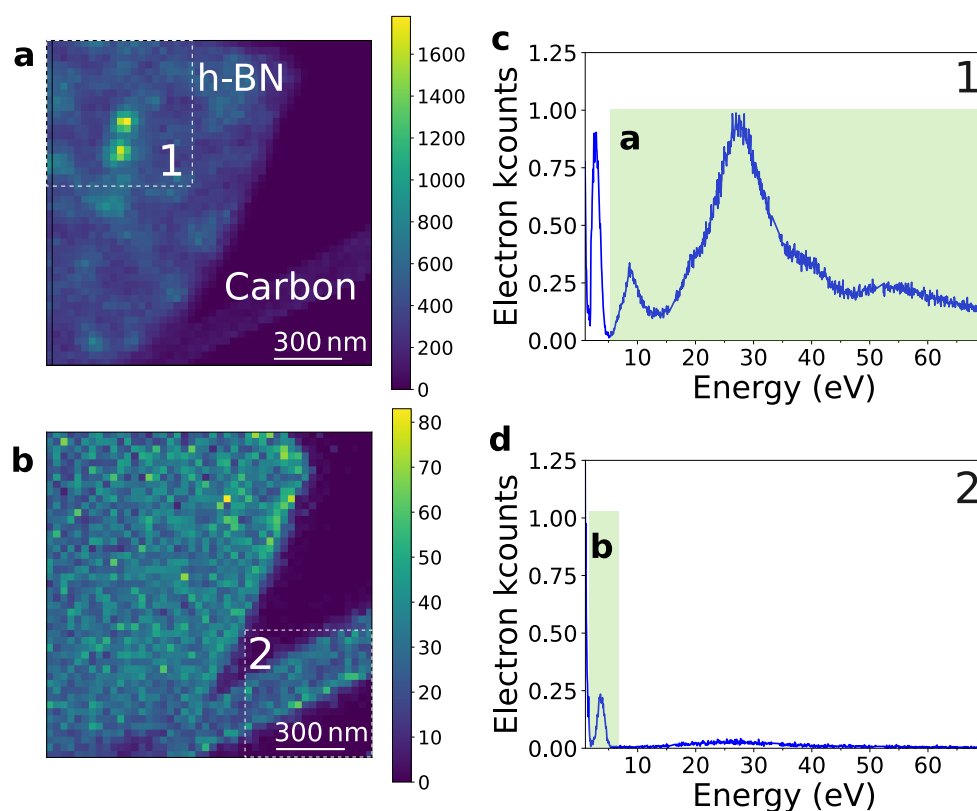


Figure 5.8: Spatially resolved CLE maps in h -BN. (a) CLE energy-filtered map above 6.5 eV, the NBE energy, showing multiple localized absorption maxima, that lead to the photon emission of the 4.1 eV defect. (b) CLE energy-filtered map between 2 eV and 5 eV, showing where TR occurs. Both the h -BN thin flake and the amorphous carbon support (lower right, which is the support for h -BN in the TEM sample) show absorption leading to photon emission. (c-d) CLE spectra of regions marked 1 and 2 in panels (a&b), with marked integrated ranges for maps a and b, respectively.

was standing still. As a single TDC in TPX3 was used, the other input line was available to perform event-based hyperspectral images, as discussed in the previous chapter. This allows one to map the different pathways directly in real space. The 4.1 eV emission in *h*-BN is known to arise from single point defects [93]. For each single defect, the CL excitation area forms an intensity spot $\approx 80 \times 80 \text{ nm}^2$ wide, as can be seen in Figure 5.8a. The CLE mapping was performed by rastering a nanometer-sized beam on the sample, and collecting the entirety of electron and photon events corresponding to emission in the 3.65-4.13 eV range at each pixel of the scan. From these, the same coincidence-seeking algorithm can be used to reconstruct CLE maps.

These time-resolved maps permit disentangling the different decay pathways in space and energy, with a 40 nm spatial resolution. Indeed, the CLE map filtered above 6.5 eV energy loss shows two sharply localized intensity spots consistent with the observation of 4.1 eV localized defects, as shown in Figure 5.8a. Conversely, the CLE map filtered between 2 eV and 5 eV, on the peak linked to TR, shows that both the *h*-BN flake and the thin amorphous carbon support exhibit coincidence events distributed in a relatively uniform manner, as shown in Figure 5.8b. It must be stated that the specific absorption signature of the defects at their absorption energy was not identified. Coincidence measurements with better EELS spectral resolution might reveal it in the future.

5.3 Conclusions & prospects

It was demonstrated spatially-resolved CLE, which includes the main advantages of PLE, i.e. the high sensitivity measurement of the relative quantum efficiency and the consequent insight between multiple light emission decay pathways with that of electron spectroscopies, i.e. the broadband excitation energy range, and the nanometer-scale spatial resolution. Numerous applications of CLE are expected for nanomaterials, ranging from the optimization of single-photon sources [316], the unveiling of the role of nanometer to atomic-scale features on the optical properties of transition metal dichalcogenide monolayers by mapping the excitons binding energy [21] to the characterization of new optical materials such as hybrid perovskites [317], and others yet to be discovered and understood. The spectromicroscopy scheme described requires only time-resolved electron and photon detectors, being implementable in any electron microscope. Therefore, it applies to any object compatible with STEM observation, should they present either coherent (plasmonics systems, photonic bandgap materials, waveguides *etc*) or incoherent (quantum wells, quantum dots, single-photon emitters *etc*) [97, 302] light emission processes. The current applications of the setup in the time domain are limited by the electron detector temporal resolution. Improvements in the near future are expected with a proper time calibration at the pixel level, which can be performed, for example, by acquiring CLE spectra of short-lived optical transitions, such as surface plasmons, in all the pixels of the 2D detector. Be-

cause they are coherent light emission processes, and because their decay time is in the femtosecond time range, the rising and falling edge of the coincident electrons are much faster than the TPX3 electron time bin of 1.5625 ns, and hence time correction is possible. Additionally, an improved temporal resolution is expected by the new Timepix4 detector [318], with fast deflectors or with the use of pulsed electron guns [4, 5, 134]. Photon and electron energy-resolved experiments in the core-level range with better temporal resolution should give further hints on the microscopic physics behind the relaxation pathways. Additionally, as the number of emitted photons per electron per energy is lost using single-pixel detectors, the use of multiple PMTs or 2D arrays of detectors solves this, giving access to excitation-energy-resolved Hanbury Brown and Twiss interferometry [105] for energy-resolved retrieval of quantum statistics, energy efficiency for total photon yield and excited-energy-resolved bunching experiments [106]. As for PLE, CLE resolved in emission and absorption energy will allow one to assign specific energy bands to each observed transition, but now with nanoscale spatial resolution. Finally, polarization-dependent EELS [319, 320] and CL can also be explored in the near-future.

General conclusions & prospects

In this work, I was mainly interested in instrumental developments in electron microscopy. Since the beginning of my Ph.D., it was clear how the standard, and commercially available, software tools in electron microscopes are very limiting to the more intrepid user. Deprived of developing more complex tasks, the microscopist is tied to writing a few simple scripts within the microscope environment, at best, which can lack the necessary control depth to automate more complicated routines. My first big project during my thesis was the attempt to transform electron energy-gain spectroscopy (EEGS) in a standard spectroscopic technique that could be as easy as electron energy-loss spectroscopy (EELS) and cathodoluminescence (CL) to perform. Albeit not yet the case, I am convinced that a significant step was taken. The most important aspect of such a step is the microscope control described in chapter 2. With it, a Vacuum Generators HB501 (VG) dedicated scanning transmission electron microscope (STEM) was controlled with Python3 within the Nionswift software. By using a modular scheme, other control interfaces were developed, most notably an application interface between Nionswift and a set of external instruments required to perform EEGS, such as the laser, the motor-driven optical elements, the power meters, *etc.* With them, I was able to architecture automated EEGS alignment and acquisition thanks to the control of the EELS camera, the sample stage, and all the aforementioned instruments with the microscope user interface. Additionally, as Nionswift currently runs in both the VG and the ChromaTEM, our recently acquired highly monochromated electron microscope, all the developments are interchangeable between these microscopes, which means more significant developments can be made before the experiments in ChromaTEM. Chapter 3 is mostly a consequence of these efforts. Initially, with the whispering-gallery mode resonators (WGMRs), in which ultra-high Q factors were not obtained, and thus EELS and CL had enough spectral resolution to unveil the gallery-modes, and later by attaching a single metallic nanoparticle (MNP) to the edge of the resonator. In the latter, the spherical symmetry of the problem was broken, and much more interesting spatial features were revealed, including the MNP-substrate hybridization and the energy-dependent

weak-coupling between the MNP and the WGMR. EEGS was performed in a larger microresonator, in which the increased mode density prevented the mode identification in EELS. Countless EEGS spectra were performed in such a system, varying the resonator and the MNP size and material. Although not shown in this thesis, these experiments were performed along with, and helped to polish, the instrumental developments. This is why I tend to arrange both chapters 2 and 3 within the same project. Chapter 3 is the physical problem that motivated the developments presented in chapter 2.

The second big project during my Ph.D. was the development of the live processing of the Timepix3 (TPX3) data, which has allowed me to better grasp the hardware world of electron microscopy instrumentation. I was able to project the so-called event-based hyperspectral EELS, in which complete 3D datasets can be acquired within tens of milliseconds. In this case, data acquisition speed is limited by the rastering speed of the electron probe, finally overcoming the long-lasting limitation of the readout time from frame-based parallel detectors, such as charged-coupled devices (CCDs). This means that hyperspectra can be obtained along with the traditional imaging systems, such as the annular dark-field (ADF), which is discussed in depth in chapter 4. Naturally, this development required a high-performance software, in which the Rust programming language was chosen. Additionally, several independent base libraries were developed, responsible for managing time-to-digital converters (TDCs) structures, reading raw packets, handling electron clusters, *etc*, which also led to the development of a high-performance post-processing library. Although the birth of cathodoluminescence excitation spectroscopy (CLE), discussed in chapter 5, could have used any programming language to post-process and seek the coincident electron-photon pairs, the usage of the recently developed Rust library sped up processing by at least a factor of 100: instead of more than 20 hours of data processing in Python3, the Rust-based algorithm was able to do it in a bit more than 10 minutes. This certainly impacted our understanding of the technique, as data were acquired and immediately analyzed, and thus tens of spectra could be done each day, exploring several samples within distinct experimental conditions. Beyond, all the already developed event-based hyperspectral EELS can be directly used, which has allowed performing CLE spatially resolved, less than 40 nm in the present case.

In each chapter, a conclusion and a few prospects are presented, albeit giving general future ideas is not difficult. The entire project gravitates toward high spectral & temporal resolved novel spectroscopic ideas in a continuous electron gun. The concept of μeV -based electron spectroscopy is extensively discussed in chapter 2, and nothing is preventing such experiments apart from ultrahigh Q factor samples, which is of course a considerable part of the problem. In the temporal resolution, however, much has to be done. The static plate beam blanker used is very far behind modern designs, capable of reaching down to 100 fs temporal resolution [168], more than four orders of magnitude faster than the 5 ns used in this work. Together with an event-based detector such as TPX3, further time

binning can be obtained in the non-dispersive direction of the detector, which can open the study of dynamics in the ultrafast time scale, an entire physics domain still vastly unexplored in continuous-gun electron microscopes. This would enable, among other things, the study of ultrafast optical excitations using EEGS, the proper study of the weak-coupling dynamics in high-Q systems, as presented in chapter 3, and the lifetime study of shorter-lived optical transitions in CLE, as discussed in chapter 5.

7.1 Concepts and Mathematical Tools

A - Fock states and the quantization of the electromagnetic field

The most common approach into the electromagnetic field quantization is the replacement of the potential vector into the potential operator ($\mathbf{A} \rightarrow \hat{\mathbf{A}}$). To do so, the classical field is compared to the quantum harmonic oscillator [46], with which it is assumed the reader is familiar. The potential vector must be expanded in terms of \mathbf{k} (k_x , k_y and k_z) and from the two transverse polarizations (λ_1 and λ_2) such that

$$\mathbf{A}(\mathbf{r}, t) = \sum_{\mathbf{k}} \sum_{\lambda=1,2} \mathbf{e}_{\mathbf{k},\lambda} A_{\mathbf{k},\lambda}(\mathbf{r}, t), \quad (7.1)$$

where the coefficients are

$$A_{\mathbf{k},\lambda}(\mathbf{r}, t) = A_{\mathbf{k},\lambda}(t)e^{i\mathbf{k}\cdot\mathbf{r}} + A_{\mathbf{k},\lambda}^*(t)e^{-i\mathbf{k}\cdot\mathbf{r}}. \quad (7.2)$$

The orthonormality can be stated in a single equation:

$$\mathbf{e}_{\mathbf{k},\lambda} \cdot \mathbf{e}_{\mathbf{k},\lambda'} = \delta_{\lambda,\lambda'}, \quad (7.3)$$

where $\delta_{\lambda,\lambda'} = 1$ for $\lambda = \lambda'$ and are zero otherwise. The Coulomb gauge condition ($\nabla \cdot \mathbf{A} = 0$ and $\nabla^2 \mathbf{A} - \frac{1}{c^2} \partial^2 \mathbf{A} / \partial t^2 = 0$) can be written identically to the simple 1D harmonic oscillator equation of motion as

$$\omega_k^2 A_{\mathbf{k},\lambda}(t) + \frac{\partial^2 A_{\mathbf{k},\lambda}(t)}{\partial t^2} = 0, \quad (7.4)$$

where $\omega_k = ck$. This mathematical equivalence allows quantizing the electromagnetic field in the same fashion as the simple harmonic oscillator. The solution of the equations above is

$$A_{\mathbf{k},\lambda}(\mathbf{r}, t) = A_{\mathbf{k},\lambda} e^{-i\omega_k t + i\mathbf{k}\cdot\mathbf{r}} + A_{\mathbf{k},\lambda}^* e^{i\omega_k t - i\mathbf{k}\cdot\mathbf{r}}. \quad (7.5)$$

In the absence of charges, the electric and magnetic field can be derived the gauge conditions $\mathbf{E} = -\partial\mathbf{A}/\partial t$ and $\mathbf{B} = \nabla \times \mathbf{A}$ and thus

$$\left. \begin{aligned} \mathbf{E}(\mathbf{r}, t) &= \sum_{\mathbf{k}} \sum_{\lambda=1,2} \mathbf{e}_{\mathbf{k},\lambda} E_{\mathbf{k},\lambda}(\mathbf{r}, t), \\ \mathbf{B}(\mathbf{r}, t) &= \sum_{\mathbf{k}} \sum_{\lambda=1,2} \frac{\mathbf{k} \times \mathbf{e}_{\mathbf{k},\lambda}}{k} B_{\mathbf{k},\lambda}(\mathbf{r}, t), \end{aligned} \right\} \quad (7.6)$$

in which

$$\left. \begin{aligned} E_{\mathbf{k},\lambda}(\mathbf{r}, t) &= i\omega_k [A_{\mathbf{k},\lambda} e^{-i\omega_k t + i\mathbf{k}\cdot\mathbf{r}} - A_{\mathbf{k},\lambda}^* e^{i\omega_k t - i\mathbf{k}\cdot\mathbf{r}}], \\ B_{\mathbf{k},\lambda}(\mathbf{r}, t) &= ik [A_{\mathbf{k},\lambda} e^{-i\omega_k t + i\mathbf{k}\cdot\mathbf{r}} - A_{\mathbf{k},\lambda}^* e^{i\omega_k t - i\mathbf{k}\cdot\mathbf{r}}]. \end{aligned} \right\} \quad (7.7)$$

The total electromagnetic energy in such a case is, from equation 1.12

$$U = \frac{1}{2} \int_V [\varepsilon_0 \mathbf{E}(\mathbf{r}, t) \cdot \mathbf{E}(\mathbf{r}, t) + \mu_0^{-1} \mathbf{B}(\mathbf{r}, t) \cdot \mathbf{B}(\mathbf{r}, t)]. \quad (7.8)$$

To solve the problem, a quantized cavity of volume $V = L^3$ is defined, and with a somewhat lengthy demonstration [46],

$$U = \sum_{\mathbf{k}} \sum_{\lambda} U_{\mathbf{k},\lambda}, \quad (7.9)$$

with the coefficients

$$U_{\mathbf{k},\lambda} = \varepsilon_0 V \omega_k^2 (A_{\mathbf{k},\lambda} A_{\mathbf{k},\lambda}^* + A_{\mathbf{k},\lambda}^* A_{\mathbf{k},\lambda}). \quad (7.10)$$

The Hamiltonian of the 1D quantum harmonic oscillator [45–47] is

$$\hat{H}_{HO} = \frac{\hat{p}^2}{2m} + \frac{1}{2} m \omega^2 \hat{x}^2 = \frac{1}{2} \hbar \omega (\hat{a} \hat{a}^\dagger + \hat{a}^\dagger \hat{a}) = \hbar \omega \left(\hat{a} \hat{a}^\dagger + \frac{1}{2} \right), \quad (7.11)$$

where \hat{a} and \hat{a}^\dagger are, respectively, the destruction and the creation operators. They satisfy the commutator $[\hat{a}, \hat{a}^\dagger] = 1$ and have the following property when applied to the eigenstate $|n\rangle$

$$\left. \begin{aligned} \hat{a} |n\rangle &= \sqrt{n} |n-1\rangle, \\ \hat{a}^\dagger |n\rangle &= \sqrt{n+1} |n+1\rangle, \end{aligned} \right\} \quad (7.12)$$

which allows to finally quantize the fields: the eigenstates are indicated by the subscripts \mathbf{k} and λ . The destruction and creator operators destroy and create one photon of energy ω_k in the mode $\mathbf{k}\lambda$. The eigenvalues of these operators, $n_{\mathbf{k},\lambda}$, designates the number of photons in our quantized cavity. All these properties can be synthesized in the set of equations below:

$$\left. \begin{aligned} \hat{a}_{\mathbf{k},\lambda} |n_{\mathbf{k},\lambda}\rangle &= \sqrt{n_{\mathbf{k},\lambda}} |n_{\mathbf{k},\lambda} - 1\rangle, \\ \hat{a}_{\mathbf{k},\lambda}^\dagger |n_{\mathbf{k},\lambda}\rangle &= \sqrt{n_{\mathbf{k},\lambda} + 1} |n_{\mathbf{k},\lambda} + 1\rangle, \\ \hat{n}_{\mathbf{k},\lambda} &= \hat{a}_{\mathbf{k},\lambda}^\dagger \hat{a}_{\mathbf{k},\lambda}, \\ \hat{n}_{\mathbf{k},\lambda} |n_{\mathbf{k},\lambda}\rangle &= n_{\mathbf{k},\lambda} |n_{\mathbf{k},\lambda}\rangle, \end{aligned} \right\} \quad (7.13)$$

in which these quantum eigenstates of light are more usually known as photon-number states or Fock states of the electromagnetic field. The Hamiltonian of the radiation field can be obtained analogously as performed in equation 7.11. Hence,

$$\hat{H}_R = \sum_{\mathbf{k}} \sum_{\lambda} \hat{H}_{\mathbf{k},\lambda}, \quad (7.14)$$

where

$$\hat{H}_{\mathbf{k},\lambda} = \frac{\hbar\omega_{\mathbf{k}}}{2} (\hat{a}_{\mathbf{k},\lambda} \hat{a}_{\mathbf{k},\lambda}^\dagger + \hat{a}_{\mathbf{k},\lambda}^\dagger \hat{a}_{\mathbf{k},\lambda}), \quad (7.15)$$

in which the subscript R stands for the radiation Hamiltonian. Direct comparison between the last equation and the total energy in a cavity obtained in equation 7.10, we can relate the vector potential amplitudes to the quantum mechanical mode operators such that

$$\left. \begin{aligned} A_{\mathbf{k},\lambda} &\rightarrow \sqrt{\frac{\hbar}{2\varepsilon_0 V \omega_k}} \hat{a}_{\mathbf{k},\lambda}, \\ A_{\mathbf{k},\lambda}^* &\rightarrow \sqrt{\frac{\hbar}{2\varepsilon_0 V \omega_k}} \hat{a}_{\mathbf{k},\lambda}^\dagger. \end{aligned} \right\} \quad (7.16)$$

Using the equations above to convert the classical vector potential (equation 7.1) into the quantum operator, one reaches

$$\hat{\mathbf{A}}(\mathbf{r}, t) = \sum_{\mathbf{k}} \sum_{\lambda=1,2} \mathbf{e}_{\mathbf{k},\lambda} \hat{A}_{\mathbf{k},\lambda}(\mathbf{r}, t), \quad (7.17)$$

where

$$\hat{A}_{\mathbf{k},\lambda}(\mathbf{r}, t) = \sqrt{\frac{\hbar}{2\varepsilon_0 V \omega_k}} \left(\hat{a}_{\mathbf{k},\lambda}(t) e^{-i\omega_k t + i\mathbf{k}\cdot\mathbf{r}} + \hat{a}_{\mathbf{k},\lambda}^\dagger(t) e^{i\omega_k t - i\mathbf{k}\cdot\mathbf{r}} \right). \quad (7.18)$$

Similarly, with equation 7.16, we can turn the classical electric and magnetic fields (equations 7.6 and 7.7) into quantum operators. For the electric field,

$$\hat{\mathbf{E}}(\mathbf{r}, t) = \sum_{\mathbf{k}} \sum_{\lambda=1,2} \mathbf{e}_{\mathbf{k},\lambda} \hat{E}_{\mathbf{k},\lambda}(\mathbf{r}, t), \quad (7.19)$$

in which

$$\hat{E}_{\mathbf{k},\lambda}(\mathbf{r}, t) = i\omega_k \sqrt{\frac{\hbar}{2\varepsilon_0 V \omega_k}} \left[\hat{a}_{\mathbf{k},\lambda} e^{-i\omega_k t + i\mathbf{k}\cdot\mathbf{r}} - \hat{a}_{\mathbf{k},\lambda}^\dagger e^{i\omega_k t - i\mathbf{k}\cdot\mathbf{r}} \right]. \quad (7.20)$$

For convenience, we can split $\hat{\mathbf{E}} = \hat{\mathbf{E}}^+ + \hat{\mathbf{E}}^-$ to reach

$$\left. \begin{aligned} \hat{\mathbf{E}}^+(\mathbf{r}, t) &= \sum_{\mathbf{k}} \sum_{\lambda=1,2} \mathbf{e}_{\mathbf{k},\lambda} i \sqrt{\frac{\hbar\omega_{\mathbf{k}}}{2\varepsilon_0 V}} \hat{a}_{\mathbf{k},\lambda} e^{-i\omega_{\mathbf{k}}t + i\mathbf{k}\cdot\mathbf{r}}, \\ \hat{\mathbf{E}}^-(\mathbf{r}, t) &= - \sum_{\mathbf{k}} \sum_{\lambda=1,2} \mathbf{e}_{\mathbf{k},\lambda} i \sqrt{\frac{\hbar\omega_{\mathbf{k}}}{2\varepsilon_0 V}} \hat{a}_{\mathbf{k},\lambda}^\dagger e^{i\omega_{\mathbf{k}}t - i\mathbf{k}\cdot\mathbf{r}}, \end{aligned} \right\} \quad (7.21)$$

in which the operators $\hat{\mathbf{E}}^+$ and $\hat{\mathbf{E}}^-$ are complex conjugates and are responsible for destroying (absorbing) or creating (emitting) one photon in the cavity, respectively.

B - The decay rate and the partial local density of states

In this section, Fermi's golden rule is used to properly quantify the transition rate from these different eigenstates under the weak-perturbation frame [45]. According to Fermi's Golden Rule, the transition rate is

$$\gamma = \frac{2\pi}{\hbar^2} \sum_f \left| \langle f | \hat{H}_{int} | i \rangle \right|^2 \delta(\omega_i - \omega_f). \quad (7.22)$$

As discussed, spontaneous decay has a term independently of $n_{\mathbf{k},\lambda}$ so its transition rate probability γ_{sp} can be written as

$$\gamma_{sp} = \frac{2\pi}{\hbar^2} \sum_{\mathbf{k}} \sum_{\lambda} g_{\mathbf{k},\lambda}^2 \delta(\omega_{\mathbf{k}} - \omega_0), \quad (7.23)$$

and, using the definition of $g_{\mathbf{k},\lambda}$ (equation 1.76),

$$\gamma_{sp} = \frac{\pi\omega_{\mathbf{k}} |\boldsymbol{\mu}_{1,2}|^2}{\hbar\varepsilon_0} \frac{1}{V} \sum_{\mathbf{k}} \sum_{\lambda} \mathbf{n}_{\mu} \cdot |\mathbf{e}_{\mathbf{k},\lambda}|^2 \mathbf{n}_{\mu} \delta(\omega_{\mathbf{k}} - \omega_0), \quad (7.24)$$

where \mathbf{n}_{μ} is a unit vector taken in the direction of the dipole momentum. The right term of this equation is called a projection in $\boldsymbol{\mu}$ direction of the local density of electromagnetic states (EMLDOS- μ). This can be written as

$$\rho_{e,\boldsymbol{\mu}}(\mathbf{r}, \omega_0) = \frac{1}{V} \sum_{\mathbf{k}} \sum_{\lambda} \mathbf{n}_{\mu} \cdot |\mathbf{e}_{\mathbf{k},\lambda}|^2 \mathbf{n}_{\mu} \delta(\omega_{\mathbf{k}} - \omega_0). \quad (7.25)$$

Hence, the spontaneous decay time can be re-written as

$$\gamma_{sp} = \frac{\pi\omega_{\mathbf{k}} |\boldsymbol{\mu}_{1,2}|^2}{\hbar\varepsilon_0} \rho_{e,\boldsymbol{\mu}}(\mathbf{r}, \omega_0). \quad (7.26)$$

To trace the correspondence with the classical result, the EMLDOS must be defined in terms of Green's function. The first step is to write the Green's dyadic function as we have done for the vector potential (equation 7.1), electric and magnetic fields (equation 7.6)

$$\vec{\mathbf{G}}(\mathbf{r}, \mathbf{r}', \omega) = \sum_{\mathbf{k}} \sum_{\lambda} \mathbf{e}_{\mathbf{k},\lambda} G_{\mathbf{k},\lambda}, \quad (7.27)$$

in which $G_{\mathbf{k},\lambda}$ are yet to be determined. As the Green's function must satisfy the Helmholtz equation (1.31) we can substitute them to reach

$$\sum_{\mathbf{k}} \sum_{\lambda} G_{\mathbf{k},\lambda} \left[\nabla \times \nabla \times \mathbf{e}_{\mathbf{k},\lambda} - \frac{\omega^2}{c^2} \mathbf{e}_{\mathbf{k},\lambda} \right] = \vec{\mathbf{I}} \delta(\mathbf{r} - \mathbf{r}'), \quad (7.28)$$

and the terms inside brackets are components of the electric field, which must satisfy

$$\left[\nabla \times \nabla \times \mathbf{e}_{\mathbf{k},\lambda} - \frac{\omega_k^2}{c^2} \mathbf{e}_{\mathbf{k},\lambda} \right] = 0, \quad (7.29)$$

which leads to

$$\sum_{\mathbf{k}} \sum_{\lambda} G_{\mathbf{k},\lambda} \left[\frac{\omega_k^2}{c^2} - \frac{\omega^2}{c^2} \right] \mathbf{e}_{\mathbf{k},\lambda} = \vec{\mathbf{I}} \delta(\mathbf{r} - \mathbf{r}'), \quad (7.30)$$

and, if both sides are multiplied by $\mathbf{e}_{\mathbf{k},\lambda}$, the orthonormality property can be used to remove both summations and reach

$$G_{\mathbf{k}',\lambda'} \frac{\omega_k'^2 - \omega^2}{c^2} = \mathbf{e}_{\mathbf{k}',\lambda'}, \quad (7.31)$$

and putting this value back into 7.27:

$$\vec{\mathbf{G}}(\mathbf{r}, \mathbf{r}', \omega) = \sum_{\mathbf{k}} \sum_{\lambda} c^2 \frac{|\mathbf{e}_{\mathbf{k},\lambda}|^2}{\omega_k^2 - \omega}. \quad (7.32)$$

To proceed, a well-known mathematical identity in physics must be used [24, 321]. It states

$$\lim_{\eta \rightarrow 0} \Im \left\{ \frac{1}{\omega_k^2 - (\omega + i\eta)^2} \right\} = \frac{\pi}{2\omega_k} [\delta(\omega - \omega_k) - \delta(\omega + \omega_k)], \quad (7.33)$$

and by multiplying by $|\mathbf{e}_{\mathbf{k},\lambda}|^2$ in the identity and sum all over possible modes (in \mathbf{k} and in λ),

$$\Im \left\{ \lim_{\eta \rightarrow 0} \sum_{\mathbf{k}} \sum_{\lambda} \frac{|\mathbf{e}_{\mathbf{k},\lambda}|^2}{\omega_k^2 - (\omega + i\eta)^2} \right\} = \sum_{\mathbf{k}} \sum_{\lambda} \frac{\pi}{2\omega_k} |\mathbf{e}_{\mathbf{k},\lambda}|^2 \delta(\omega - \omega_k). \quad (7.34)$$

From the equation above, ω_k can be removed from the double sum because delta function will nonetheless restrict values to $\omega = \omega_k$. Negative frequency terms have also been dropped. Using equation 7.32, one can reach

$$\Im \{ \vec{\mathbf{G}}(\mathbf{r}, \mathbf{r}', \omega) \} = \frac{\pi c^2}{2\omega} \sum_{\mathbf{k}} \sum_{\lambda} |\mathbf{e}_{\mathbf{k},\lambda}|^2 \delta(\omega - \omega_k), \quad (7.35)$$

and thus finally rewrite the EMLDOS using equations 7.25 and 7.32 such that

$$\rho_{e,\mu}(\mathbf{r}, \omega) = \frac{2\omega}{\pi c^2 V} \left[\mathbf{n}_\mu \cdot \Im\{\vec{\mathbf{G}}(\mathbf{r}, \mathbf{r}', \omega)\} \mathbf{n}_\mu \right]. \quad (7.36)$$

In Cartesian coordinates, we can display the entire density of states instead of its projection in a given axis by summing up in the canonical basis (\mathbf{n}_x , \mathbf{n}_y and \mathbf{n}_z) such that

$$\rho_e(\mathbf{r}, \omega) = \sum_{\mathbf{u}=\mathbf{n}_x, \mathbf{n}_y, \mathbf{n}_z} \frac{2\omega}{\pi c^2 V} \left[\mathbf{u} \cdot \Im\{\vec{\mathbf{G}}(\mathbf{r}, \mathbf{r}', \omega)\} \mathbf{u} \right], \quad (7.37)$$

and by trivial tensorial operations, the full local density of states expression can be reached

$$\rho_e(\mathbf{r}, \omega) = \frac{2\omega}{\pi c^2 V} \left[\Im \left\{ Tr \left[\vec{\mathbf{G}}(\mathbf{r}, \mathbf{r}', \omega) \right] \right\} \right]. \quad (7.38)$$

This section has introduced, by using the quantum formalism, the EMLDOS, intimately linked to the spontaneous decay. By returning to the classical electromagnetic field, in which the Green's tensor was previously defined, it was shown that the EMLDOS is also related to the projection of the imaginary part of the Green's tensor along the net dipole direction. As shall be seen, electron energy-loss can be qualitatively associated with the classical dipole power loss and, thus, with the imaginary Green's tensor and the ELMDOS. Cathodoluminescence, on the other hand, measures the energy transferred to the far-field, and so is better related to the Poynting vector. Cathodoluminescence can also be linked to the QED formalism of spontaneous decay, as an electron can excite atomic states and light emission can happen even in the absence of external fields. Electron energy-gain, a less usual electron spectroscopic technique, also can be explained by the light-matter interaction Hamiltonian developed in the QED frame.

C - Pictures of the microscopes

Figure 7.1 displays two photographs of the microscopes used in this work. The instrumental developments of EEGS were done in the Vacuum Generators model HB 501 (VG) machine, which was dedicated to this project. The TPX3 was also developed in this microscope, and as soon as the live data treatment was successfully implemented, the detector went to a second VG microscope at our facility, which has an overall improved performance due to its liquid-nitrogen-cooled sample stage. Most of the measurements shown in this work were performed in ChromaTEM, our recently-acquired state-of-the-art electron microscope, containing an aberration-corrector up to the fifth order and an electron monochromator. The EEGS technique was successfully transferred to ChromaTEM, while TPX3 has not yet been used in this machine primarily due to the detector saturation issue. Other relevant details of the microscopes can be found in the discussion in the main text of this thesis.

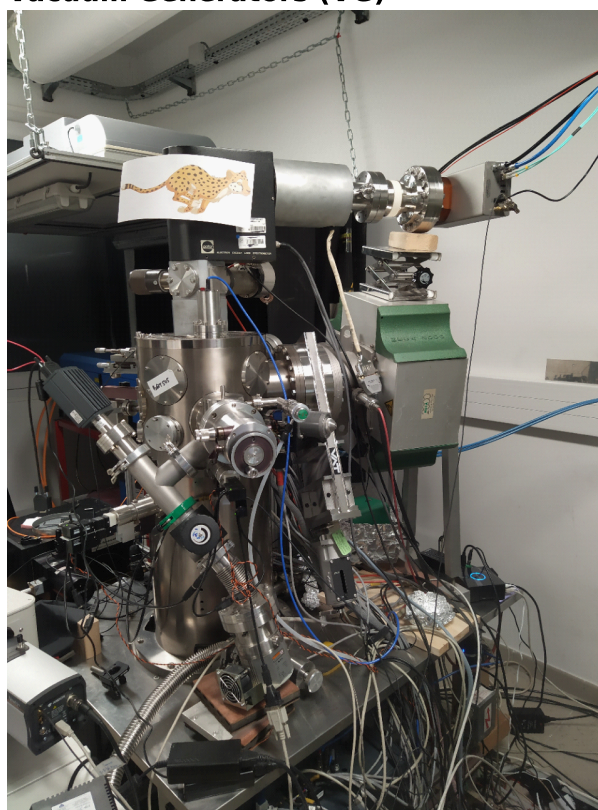
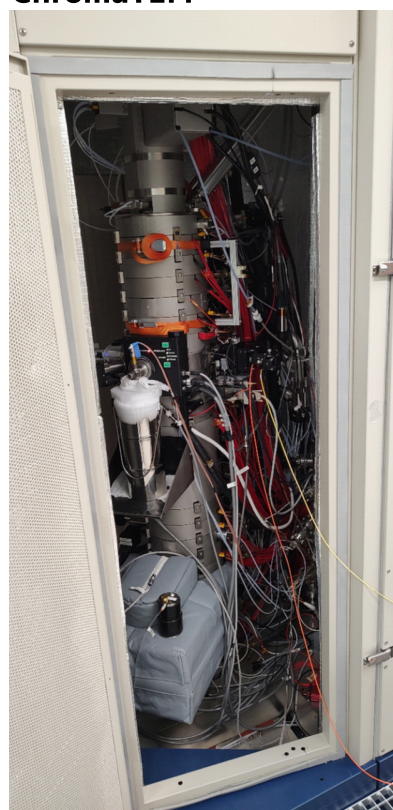
Vacuum Generators (VG)**ChromaTEM**

Figure 7.1: The microscopes used in this work. The instrumental developments were done in VG, while most of the presented measurements were done in ChromaTEM.

7.2 EEGS in monochromated continuous electron gun

A - User interface of the developed instruments

Figure 7.2 shows the user interface (UI) of NionSwift and a few of the Python3-based developed instruments during this thesis. The EELS spectrometer (1) has three windows, named “Focus”, “Dispersion” and “VSM”, in which all the available optical elements can be adjusted or wobbled. The EELS detector (2) settings can be adjusted between different modes. A common base class allows to use the same developed UI for the several available different detectors, by simply inheriting the class and defining the required methods. To perform CL experiments, an optical spectrometer must be controlled (3), and, similar to the EELS detector, the same UI is used for the several available light spectrometers. The scan channels are displayed in the center of the image. The windows called “ADF” and “BF” (4) actually displays the same image, apart from a Gaussian blur, which is a simulated data used for development, and they are both 2D data. Hyperspectral images were also developed in the scan channels (5), in which the “Pick Region” square allows to have the associated spectra, also simulated in the present case. Scan channels

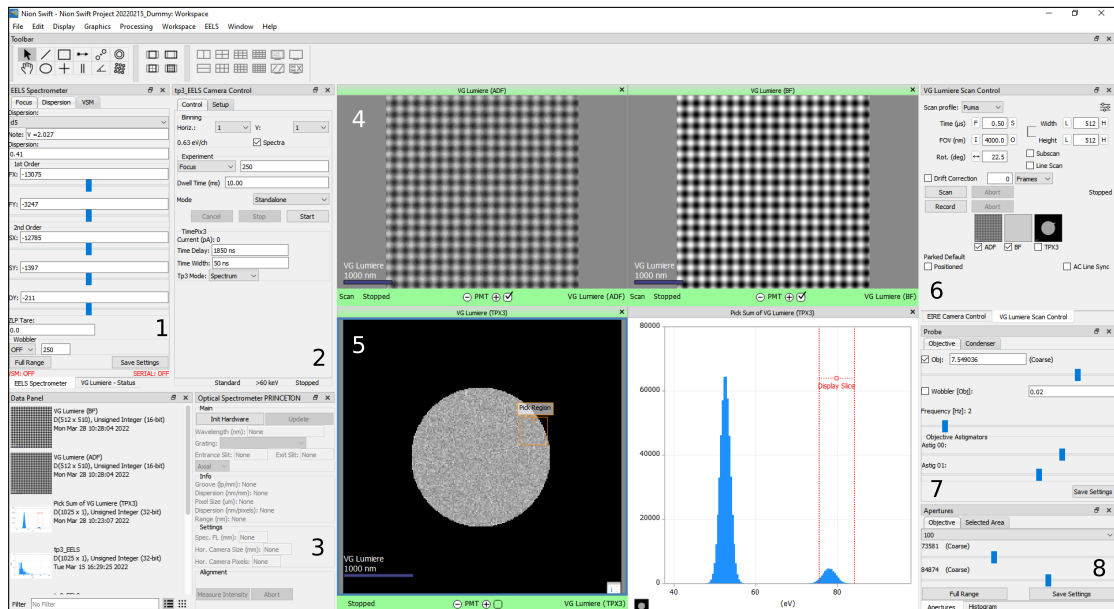


Figure 7.2: The user interface of the Nionswift software with the multiple developed instruments, including the EELS spectrometer (1), the EELS detector control, the optical spectrometer (3) for CL experiments, the scan channels, either 2D (4) or 3D datasets (5), which can be controlled by a standard interface (6), the electron lenses (7) and the apertures (8). Some instruments are not shown, specially the sample stage and the multiple the vacuum gauges values.

are controlled by a standard UI palette (6), in which the pixel dwell time, the field of view, the spatial sampling, the rotation, *etc.* can be set. The available channels are shown at the bottom and can be activated by their related check box. The magnetic lenses are also controlled (7), both for the objective and the condenser system, and including a wobbling system and an astigmatism control. Finally, the control of the available apertures is also developed (8). Some instruments are not shown, for the sake of clarity of Figure 7.2, most notable the sample stage and the multiple vacuum gauge controls in different sections of the microscope.

B - User interface and functioning of the EEGS experiments

Figure 7.3 shows how EEGS experiments can be performed in any microscope running Nionswift (considering the appropriate hardware, i.e. the fast blanker, is present). A stand-alone station was developed in Python3 to control the required instruments, i.e. the optical elements and the power meters (1), the laser (2), and the laser power supply (4). The available methods for these instruments

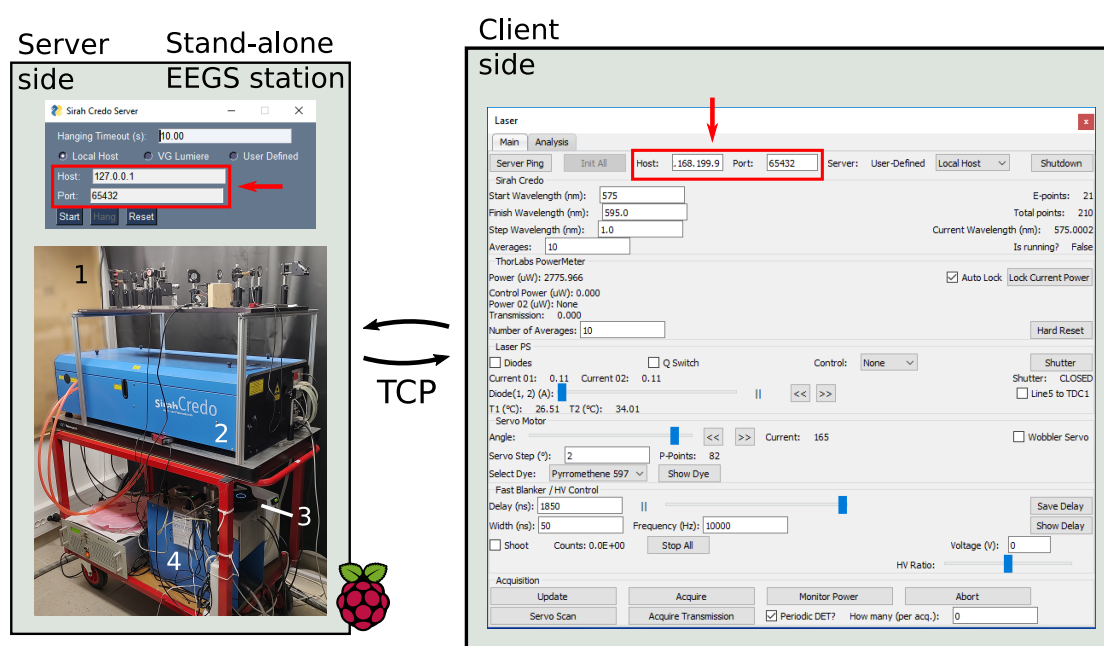


Figure 7.3: The stand-alone EEGS station developed. In the station, the optical table (1), the laser (2), a Raspberry Pi (3), and the power supplies and pumps (4) are together in the same mobile cart. The laser, the optical components and the power meters are controlled via USB, which is directly connected to the Raspberry Pi. A TCP socket server is opened in the Raspberry Pi, which allows to control the instruments by connecting a TCP socket client in the Nionswift computer running the microscope. In this configuration, only a TCP connection between the Raspberry Pi and the microscope computer is required, which can be achieved through a local network without physically connecting both ends.

can be wrapped in a TCP socket system, meaning a byte-based communication protocol can be developed to call the desired function. The instruments in the stand-alone station are connected to a Raspberry Pi (3), which also opens a TCP socket server in a custom-made UI box, as indicated by the red box and arrow at the server-side of Figure 7.3. If a client is connected (same host and port as the server, defined in the red box and arrow at the client side in Figure 7.3), a synchronous communication is capable of remotely control the instruments in the EEGS station. As an example, to set the laser wavelength to 580.001 nm, the TCP message must initiate with a specific header, which is the name of the function, followed by `<0x00000000>`, and then followed by the desired wavelength containing exactly 16 bytes, with exactly 8 bytes after the comma. The message continues with another `<0x00000000>` and by the name of the instrument, which is b'LASER' in this case. The server decodes the message, runs the desired method and replies when it is done, in a synchronously fashion.

The point of this station is to exempt the user from concern with the multiple instruments related to the performance of EEGS experiments. These do not need to access the properties of the microscope and thus can be isolated for better management. In this picture, the laser can be placed far away from the microscope and its control computer, as the only required connection is a TCP socket, which could be done using a local network.

7.3 Optical microcavities & electron beams

A - FDTD-simulated cube mode hybridization on a flat SiO₂ substrate

For the cube-SiO₂ substrate system, the finite-difference time-domain (FDTD)-simulated loss probability was obtained using a 1.25 nm mesh size with electric dipoles evenly spaced by ~ 8 nm. The SiO₂ substrate was 500 nm thick and the silver nanocube had 100 nm in side length. Figure 7.4a shows the results for the obtained spectra for the probe at the top edge (opposite from the interface Ag - SiO₂) and top corner positions for 200 keV and 100 keV electrons, in which the loss probability changes by less than a relative factor of two (compared to the factor of 100 for the bare resonator). In Figure 7.4b, the simulated and the experimental results are compared. The simulated modes are redshifted with respect to the experimental results in all observed modes (except for the distal face), presumably due to variations in the effective index of refraction between experiment and simulations.

Although redshifted, all experimentally observed resonances were also observed in FDTD. To make a correspondence between them, the absolute value of the near electric field was obtained, as shown in Figure 3c. This correspondence can also be done by simulating a full spectral image by rastering the electron probe position in a square mesh containing the cube and part of the substrate. For this, the mesh size was increased to 2.50 nm while dipoles were evenly spaced by ~ 25 nm intervals to reduce the simulation time. The electron impact position grid was 150 nm wide in both the x-y plane (z being the electron propagation direction)

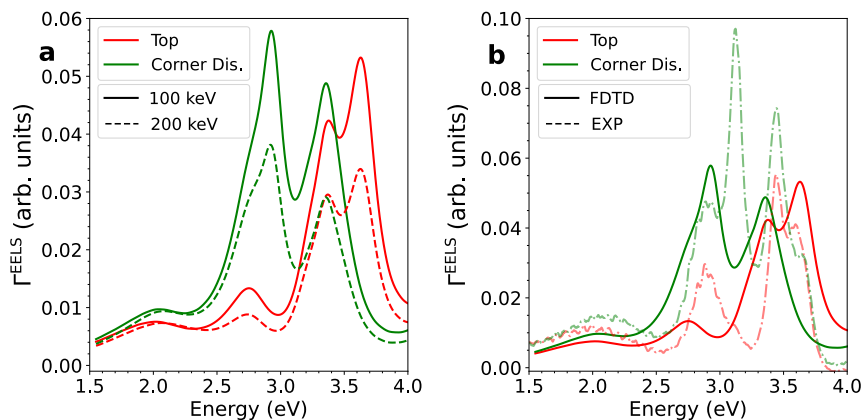


Figure 7.4: EELS probability comparison for different electron energies and between experiment and simulation. (a) FDTD simulated spectra for 200 keV and 100 keV electrons. (b) Comparison, for 100 keV electrons, between the experimental results and the simulations.

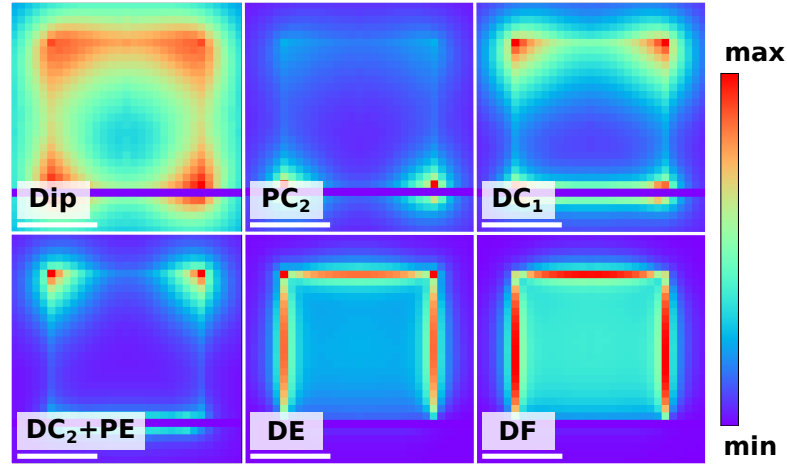


Figure 7.5: FDTD-simulated spectral maps for the cube-substrate system, including the dipolar (Dip), second proximal corner (PC_2), first distal corner (DC_1), second distal corner (DC_2), proximal edge (PE), distal edge (DE), and distal face (DF) modes. Scale bars are 50 nm.

and the impact distance step size was 5 nm. Only minor changes were found in the spectral maps with respect to each single loss spectrum at the corresponding probe positions despite the alleviated simulation conditions, thus indicating a good simulation convergence. Figure 7.5 shows the simulated spectral image under the above conditions for the resonances listed in the main text (Figure 3c), with a remarkable resemblance between them. Note that simulations have rendered the proximal edge mode (PE) as very faint and close to the second distal corner mode (DC_2), similarly to the experiment. Figure 7.5 for $DC_2 + PE$ clearly shows a proximal edge component, although much less strong than the distal corner.

Finally, note that a smaller order proximal order mode PC_1 has not been observed in EELS, despite being predicted in the FDTD simulations (Figure 3). This mode is known to be close to the global dipole and very diffuse, which makes it very challenging to detect experimentally [15]. It is also important to note that unequivocally characterizing the entire cube-substrate modes requires an extreme degree of electron beam monochromaticity. Experimentally, mode PC_2 is centered at 2.813 eV and mode DC_1 is centered at 2.898 eV. The 85 meV distance is smaller than the ~ 250 meV mode FWHM, and thus, mode overlap is expected in our spectral maps.

B - MNP polarizability

In the analytic model, the nanocube is described as a dipolar point scatterer of isotropic polarizability $\alpha(\omega)$ placed at the particle center. In order to estimate $\alpha(\omega)$, it was adopted the model of Fuchs and Sihvola [250, 322] for the quasistatic polarizability of the cube,

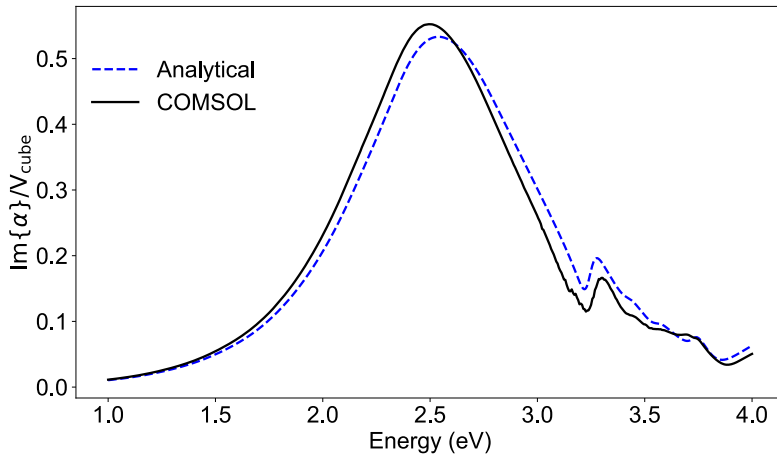


Figure 7.6: Comparison of the polarization obtained through COMSOL and the analytical form based on the quasistatic approximation with retardation corrections as described in the main text.

$$\alpha_{QS} = \frac{V}{4\pi} \sum_m \frac{C_m}{(\varepsilon/\varepsilon_h - 1)^{-1} + n_m}, \quad (7.39)$$

where V is the cube volume, ε is its dielectric function (taken from tabulated data [323] for silver), ε_h is the host permittivity (1 for vacuum in the present case), m is a mode index, and C_m and n_m are tabulated in Ref. [250]. The cube polarizability was obtained by using a finite-difference numerical method using the COMSOL multiphysics software. Comparison of the quasistatic polarizability and the numerical simulation reveals large discrepancies, which can be attributed to retardation effects. The latter can be incorporated in the analytical model through the relation [324]

$$\alpha = \frac{\alpha_{QS}}{1 - \frac{\alpha_{QS}}{V}M}, \quad (7.40)$$

where $M = (\frac{4\pi}{3})^{1/3}(kd)^2 + i\frac{2}{3}(kd)^3$, $k = \omega/c$, and d is the cube edge length. This prescription brings the model polarizability in close agreement with the numerical simulation, as shown in Figure 7.6. This analysis confirms the robustness of the polarizability here used for the analytical model of the MNP-sphere system, although it does not account for higher-order particle plasmons.

C - Additional results from the analytical model

It is shown in Figures 7.7 and 7.8 additional results obtained from the analytical model discussed in the main text for electrons moving with energies of 200 keV and 100 keV, respectively.

For 200 keV, Figure 7.7 shows that the coupling is also sensitive to the electron beam position, even in the sphere without a MNP, because the Mie resonances

under consideration become more evanescent outside the dielectric for higher orbital angular momentum. For 100 keV electrons (Figure 7.8), excitation of Mie resonances in the sphere without the MNP is negligible because of the mismatch between the electron velocity and the orbital group velocity of the whispering-gallery modes; however, the presence of a MNP acts as a mediator in the coupling to Mie modes, which leave sizable signatures in EELS for the hybrid system.

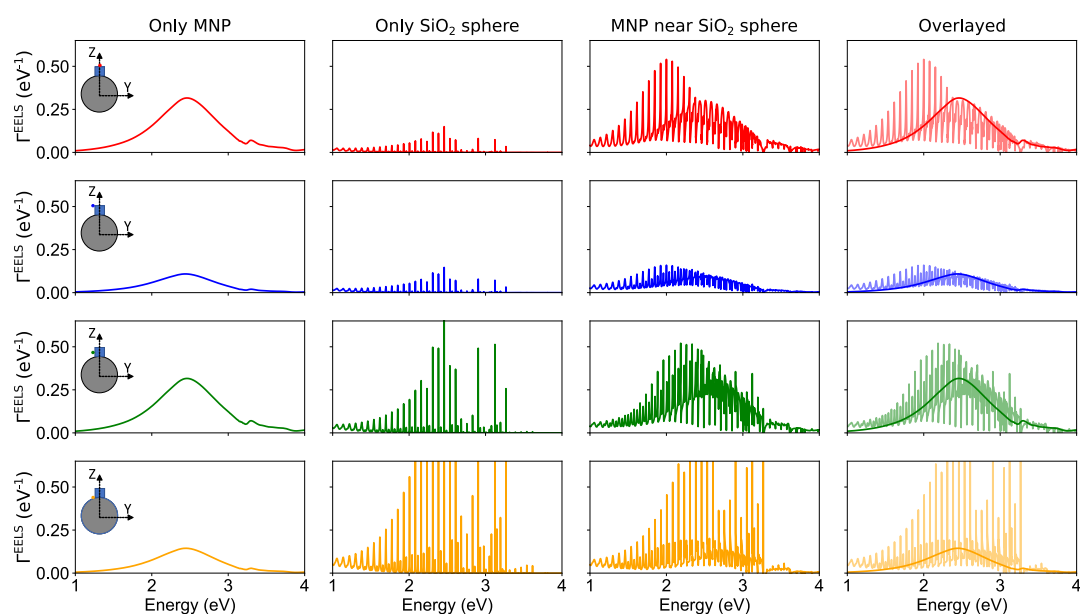


Figure 7.7: EELS probability calculated by assimilating the MNP to a dipolar scatterer and retaining the full multipolar response of the sphere. The spectra for the MNP alone (leftmost column), the sphere alone (second-left column), the hybrid MNP-sphere system (third column), as well as the overlay of only-sphere and MNP+sphere systems spectra (rightmost column) are compared for different positions of the electron beam (see insets in the left column) and an electron energy of 200 keV.

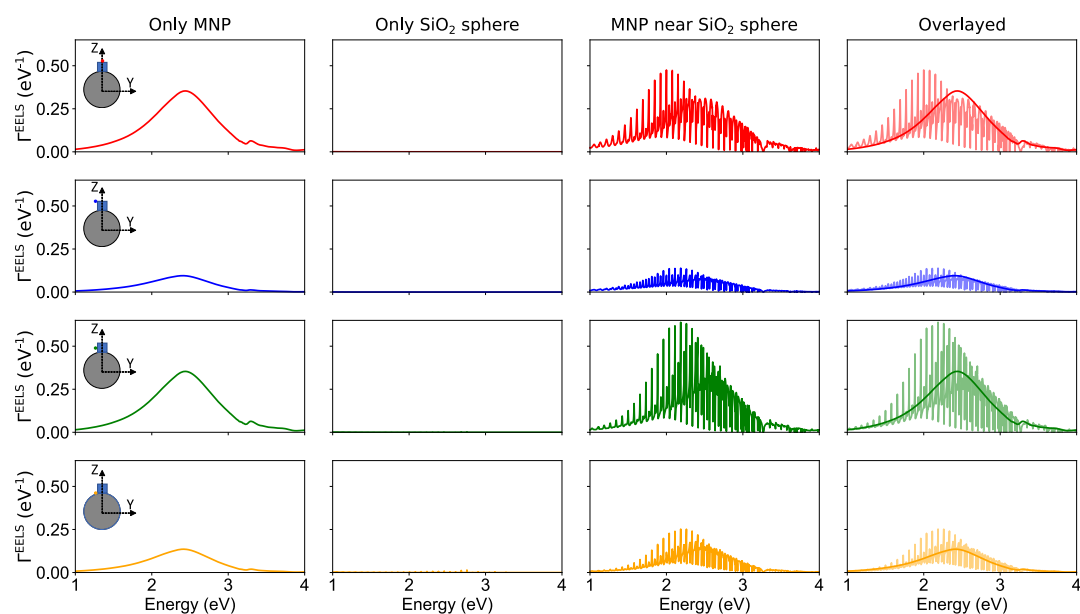


Figure 7.8: Same as Figure 7.7, but for 100 keV electrons.

7.4 Event-based EELS: developments & applications in the nanosecond scale

A - Hyperspectral reconstruction algorithm performance

To provide a better quantitative analysis of the developed live algorithm, some performance curves have been produced using simulated hyperspectral data. The simulation takes into account all the experimental variables, such as pixel dwell time (T_p), the sampling in the x_t and y_t positions, the number of acquired frames (F), the electron probe current (I , in electrons/s) and the flyback time (T_b). Unless otherwise stated, the standard values for the current, the flyback time, the pixel dwell time, the x and y spatial sampling are, respectively, 1 pA, 0, 1 μ s, 256 pixels, and 256 pixels.

The performance was analyzed using *perf* [288], a performance analyzing tool available from the Linux kernel. To not overcomplicate the benchmark statistics, only the *task-clock* event is shown here, which roughly translates into the human-perceivable time elapsed until the entirety of the data is processed. Additionally, *perf* was repeated between 50-100 times to obtain more meaningful results, in which error bars are the measurement standard deviation. The computer used to benchmark the data has a Intel Core i7-8665U running at 1.90 Ghz. The total acquisition time T_{total} , the number of electrons n_e , and the number of TDCs (one falling edge at the beginning of the scan row and one rising edge at the end of the scan row) n_{tdc} in each simulated data are, respectively

$$\left. \begin{aligned} T_{total} &= Fy_t(x_tT_p + T_b), \\ n_e &= T_{total}I, \\ n_{tdc} &= 2Fy. \end{aligned} \right\} \quad (7.41)$$

The total number of events is $n_e + n_{tdc} = T_{total} \times I + 2F \times y$. As there are only linear operations in both the electron and the TDC event packets, the processing time must scale, at worst, as $\mathcal{O}(n)$ for both the number of electrons and TDCs, where n is the number of processed events and \mathcal{O} is called the "Big O notation", usually used to describe the behavior of algorithms as a function of sampling size.

In the inset of Figure 7.9a, the processing time is plotted as a function of the input current, displaying a linear relationship, as expected. In the outer graph, the processing time is plotted as a function of the pixel dwell time (from 8 μ s to 62 ns), or, equivalently, the number of frames, given all the other parameters constant. The number of electrons is equal for all data points and the difference for smaller dwell times relative to bigger ones is the quantity of supplementary events, as more frames mean more scan rows. A linear dependence is only seen for a high rate of supplementary events, in which the number of TDCs starts to be comparable to the number of electron events (8% of the total number of events are TDCs for 62 ns pixel dwell time). Finally, note that, even for the 62 ns pixel

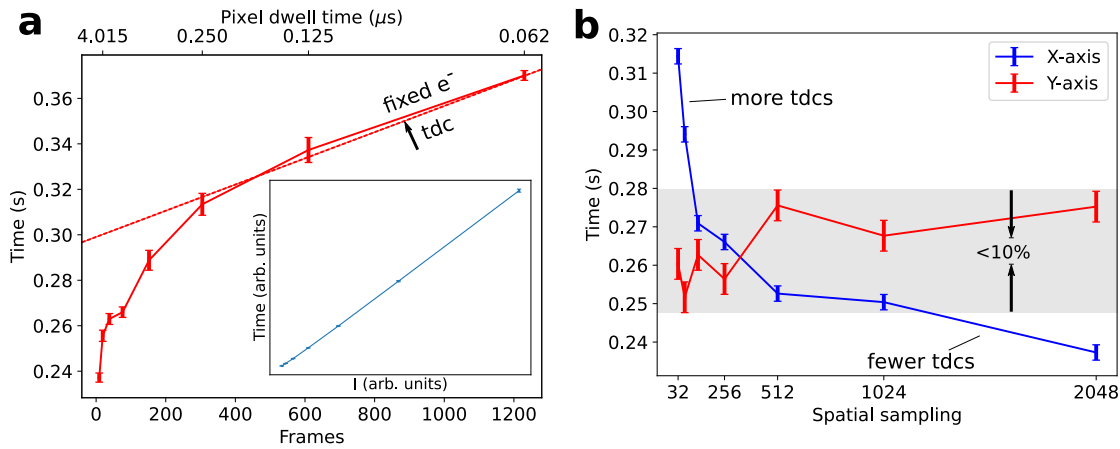


Figure 7.9: Algorithm performance for multiple acquisition parameters. Total acquisition time is fixed in 5 s and $T_b = 0$ for all cases. Spatial sampling, pixel dwell time, and current is 256 x 256, 1 μs and 1 pA unless said otherwise. (a) The processing time as a function of the number of frames by changing the pixel dwell time. In the inset, the processing time is shown as a function of the electron probe current, displaying a linear relationship. (b) Processing time as a function of the spatial sampling. For the blue (red) curve, Y (X) value is fixed at 256 bins, while the other dimension is varied.

dwel time data point, 5 s of acquired data, at 1 pA, can be processed as fast as ~ 0.36 s, which means currents up to ~ 14 pA could be theoretically processed live, albeit impossible to be verified due to the maximum throughput of TPX3 at ~ 5 pA. In Figure 7.9b, similar curves are obtained by independently varying x_t and the y_t sampling from 32 to 2048 pixels, while the other coordinate is kept fixed at 256. Interestingly, for a given current and total acquisition time, the processing time is smaller for higher sampling rates in the horizontal axis, which is simply explained by the reduced number of required scan rows (or TDCs). For the y axis, the processing time is approximately constant, or $\mathcal{O}(1)$, because the number of required supplementary events is constant as the increased number of lines is compensated by the reduced quantity of frames.

In general, these curves show that reducing pixel dwell time is not usually limiting, even for the small currents considered here. Besides, TPX3 provides a way of increasing the spatial sampling of hyperspectral images with no additional cost, although more computer memory (or storage disk space) is needed.

B - EELS spectra dependency on the total cluster ToT

For the same data studied in Figure 4.6, it was plotted the dependency of the summed time over threshold (ToT) on the detector hit position in the dispersive direction in Figure 7.10, intending to clarify the origin of the Poisson distribution after filtering data by the summed ToT. The histogram in Figure 7.10a clearly shows a central ToT value around ~ 139.12 ns (intense horizontal line), which

is associated with the 100 keV electrons for this particular used threshold. A Gaussian fit provides a fwhm of ~ 22.65 ns which is below the unit clock tick of 25 ns. The histogram of chip 1 alone provides a better contrast to see the high number of clusters with Σ ToT < 60 ns around the chip junctions (close to pixels 256 and 512). This region, additionally, is also known to have hot pixels with high counting rates even in the absence of the electron beam. In figure 7.10b it was plotted the accumulated EELS spectrum for the lower (blue) and upper (orange) side of the aforementioned histogram, which displays a disproportionate number of counts in the chip boundary, in the blue curve. Finally, it is shown in Figure 7.10c the relation between the summed ToT and the cluster size, which has its maximum around 139.12 ns for a cluster size of 4 electrons. Note also the high number of clusters with a unit cluster size (individual electrons) for lower ToTs, which can be caused by the physical boundary condition of on-chip junctions.

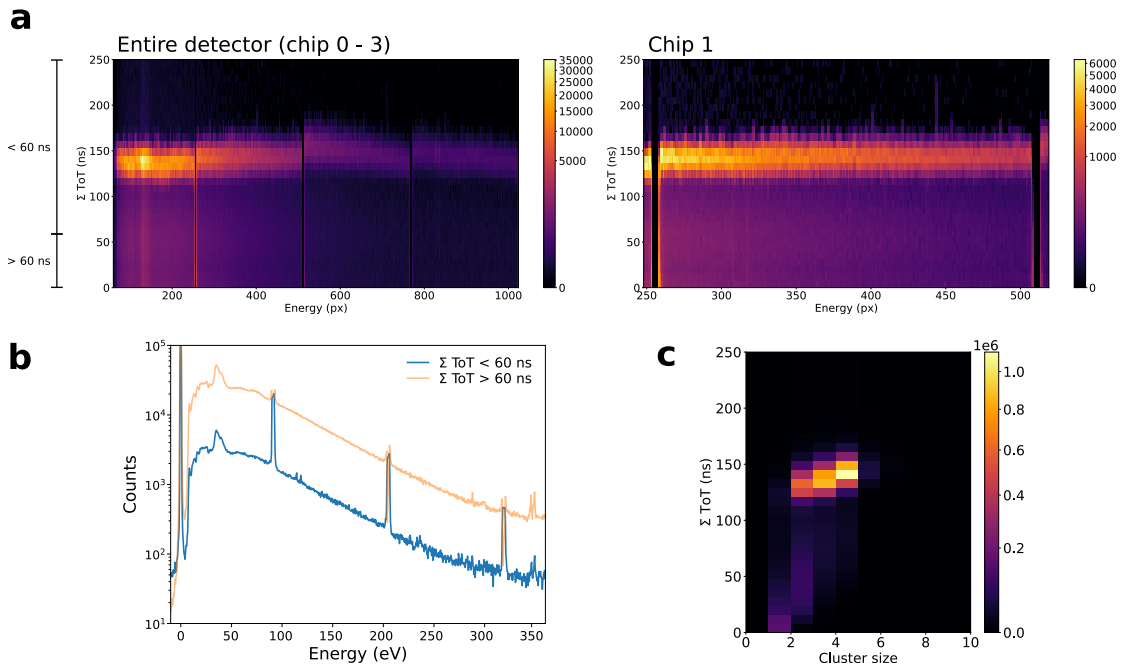


Figure 7.10: Relation of the summed ToT with the electron hits in the dispersive direction. (a) For the entire detector (chip 0 - 3) but excluding zero loss for better contrast, and for chip 1, in which the low sum ToT can be more easily identified within the chip borders. (b) The accumulated resultant spectra for the two regions identified as Σ ToT > 60 ns and < 60 ns. For the low ToT, the hit count between chips is orders of magnitude greater than neighbor pixels. (c) The relation between the summed ToT and the cluster size, displaying an average of 2.92 electrons/cluster.

C - Cluster-detection algorithm results for different parameters

As briefly discussed in the main text, cluster detection is performed by sorting the pixel hits by ToA and comparing them neighbor by neighbor: if the ToA increases by more than ΔToA or if the pixel spatial position increases by more than either $\Delta\alpha$ or $\Delta\beta$, a new cluster is formed. This procedure is performed for hits that are not yet within a cluster until convergence is achieved. Figure 7.11a shows the same plot as in main text (Figure 4.6) for different ΔToA values and for the uncorrected data set using $\Delta\alpha = \Delta\beta = 2$. As the pixel dead time is ~ 475 ns, there is no risk of same-pixel cluster identification as long as ΔToA is smaller than this value. The typical cluster formation interval, however, is smaller than 475 ns and one must be primarily careful not to underestimate ΔToA . This is undoubtedly the case for

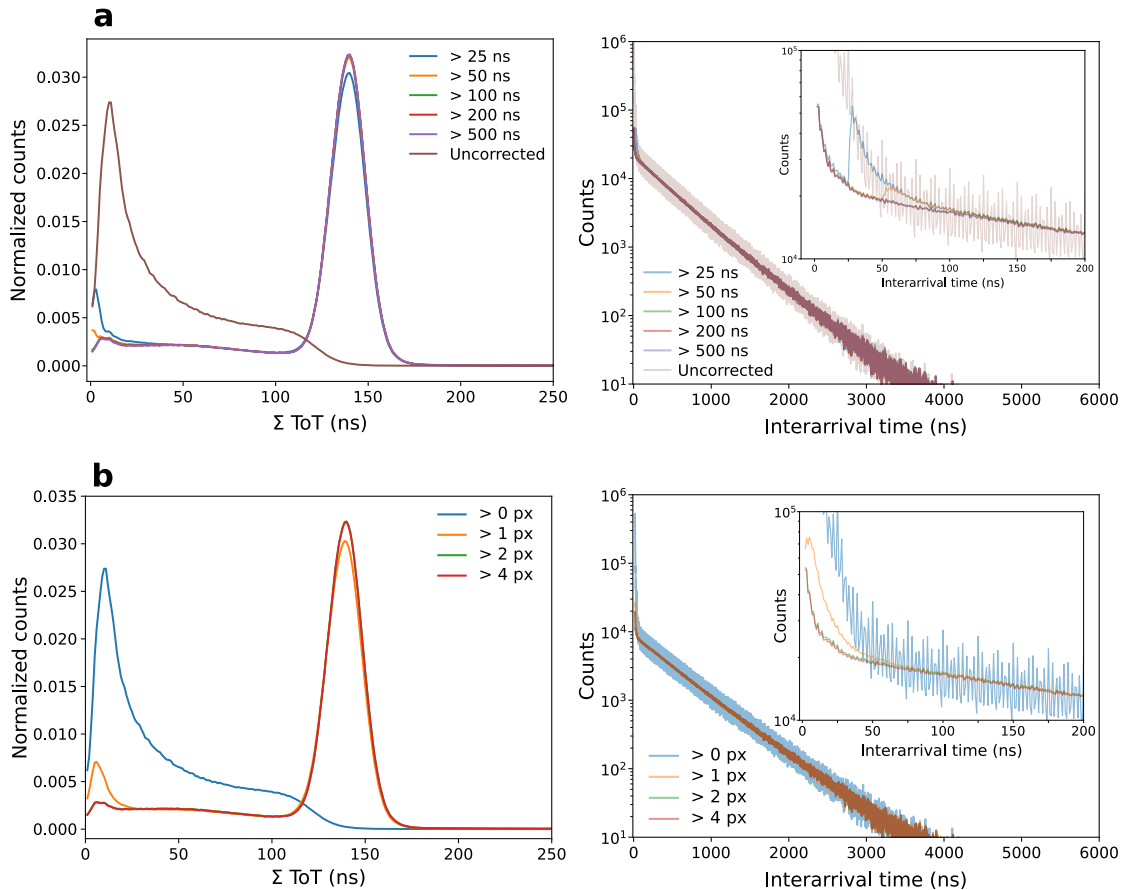


Figure 7.11: Results of the cluster-detection algorithm for different identification parameters. (a) Variation of Δtime of arrival (ToA) using $\Delta\alpha = \Delta\beta = 2$. Note how 25 ns and 50 ns underestimate cluster formation time. $\Delta\text{ToA} \geq 200$ ns is enough for the algorithm convergence. (b) Variations of $\Delta\alpha = \Delta\beta$ using $\Delta\text{ToA} = 200$ ns. Convergence is achieved for values ≥ 2 , meaning that there must have at least 3 pixels of distance (in each α and β independently) in order to produce a new cluster.

157.4. Event-based EELS: developments & applications in the nanosecond scale

25 ns, 50 ns, and, to a lesser extent, 100 ns. ΔToA of 200 ns and 500 ns provides almost identical data. In Figure 7.11b, $\Delta\alpha$ and $\Delta\beta$ was varied equally within the range $[0, 4]$ for $\Delta\text{ToA} = 200$ ns. For $\Delta\alpha = \Delta\beta = 0$, the result is identical to that for the uncorrected data, which is obvious considering any electron detected within $\Delta\text{ToA} = 200$ ns will be at a different pixel due to the pixel dead time. Data does converge for $\Delta\alpha = \Delta\beta \geq 2$.

Bibliography

1. Howie, A. Electrons and photons: exploiting the connection. *Inst. Phys. Conf. Electron Microscopy and Analysis Group Conf. EMAG99* **161**, 311 (1999).
2. Howie, A. Photon interactions for electron microscopy applications. *The European Physical Journal-Applied Physics* **54** (2011).
3. García de Abajo, F. J. & Kociak, M. Electron energy-gain spectroscopy. *New Journal of Physics* **10**, 073035 (2008).
4. Barwick, B., Flannigan, D. J. & Zewail, A. H. Photon-induced near-field electron microscopy. *Nature* **462**, 902–906 (2009).
5. Feist, A. *et al.* Quantum coherent optical phase modulation in an ultrafast transmission electron microscope. *Nature* **521**, 200–203 (2015).
6. Pomarico, E. *et al.* meV resolution in laser-assisted energy-filtered transmission electron microscopy. *ACS Photonics* **5**, 759–764 (2017).
7. Vanacore, G. M. *et al.* Attosecond coherent control of free-electron wave functions using semi-infinite light fields. *Nature Communications* **9**, 1–11 (2018).
8. Das, P. *et al.* Stimulated electron energy loss and gain in an electron microscope without a pulsed electron gun. *Ultramicroscopy* **203**, 44–51 (2019).
9. Auad, Y. *OrsayDev/NSLumiere: v5.24.5 release* version v5.24.5. Apr. 2022. <https://doi.org/10.5281/zenodo.6407648>.
10. Auad, Y. *OrsayDev/OrsayLaser: v6.1.0 release* version v6.1.0. Apr. 2022. <https://doi.org/10.5281/zenodo.6407642>.
11. Braginsky, V., Gorodetsky, M. & Ilchenko, V. Quality-factor and nonlinear properties of optical whispering-gallery modes. *Physics Letters A* **137**, 393–397 (1989).

12. Matsko, A. B. & Ilchenko, V. S. Optical resonators with whispering-gallery modes-part I: basics. *IEEE Journal of selected topics in quantum electronics* **12**, 3–14 (2006).
13. Kfir, O. *et al.* Controlling free electrons with optical whispering-gallery modes. *Nature* **582**, 46–49 (2020).
14. Hyun, J., Couillard, M., Rajendran, P., Liddell, C. & Muller, D. Measuring far-ultraviolet whispering gallery modes with high energy electrons. *Applied Physics Letters* **93**, 243106 (2008).
15. Nicoletti, O. *et al.* Three-dimensional imaging of localized surface plasmon resonances of metal nanoparticles. *Nature* **502**, 80–84 (2013).
16. Auad, Y. *et al.* Unveiling the coupling of single metallic nanoparticles to whispering-gallery microcavities. *Nano Letters* **22**, 319–327 (2022).
17. Vollmer, F. *et al.* Protein detection by optical shift of a resonant microcavity. *Applied Physics Letters* **80**, 4057–4059 (2002).
18. Weiss, D. *et al.* Splitting of high-Q Mie modes induced by light backscattering in silica microspheres. *Optics Letters* **20**, 1835–1837 (1995).
19. Auad, Y. *et al.* *TimeSTEM/Tp3_tools: Release v1.0.0* version v1.0.0. Mar. 2022. <https://doi.org/10.5281/zenodo.6346261>.
20. Auad, Y. *et al.* Event-based hyperspectral EELS: towards nanosecond temporal resolution. *Ultramicroscopy* **239**, 113539 (2022).
21. Hill, H. M. *et al.* Observation of excitonic Rydberg states in monolayer MoS₂ and WS₂ by photoluminescence excitation spectroscopy. *Nano Letters* **15**, 2992–2997 (2015).
22. Varkentina, N. *et al.* Cathodoluminescence excitation spectroscopy: nanoscale imaging of excitation pathways. *arXiv preprint arXiv:2202.12520* (2022).
23. Jackson, J. *Classical Electrodynamics* (Wiley, 1999).
24. Novotny, L. & Hecht, B. *Principles of Nano-Optics* (Cambridge Press, 2007).
25. Stratton, J. *Electromagnetic Theory* (McGraw-Hill, 1941).
26. Lorentz, L. On the identity of the vibrations of light with electrical currents. *Phil. Mag.* **34**, 287 (1867).
27. Faryad, M. & Lakhtakia, A. *Infinite-Space Dyadic Green Functions in Electromagnetism* (Morgan & Claypool Publishers, 2018).
28. Chen, H. C. *Theory of Electromagnetic Waves: A coordinate-Free Approach* (McGraw-Hill, 1983).
29. Tai, C. T. *Dyadic Green's Functions in Electromagnetic Theory* (New York: IEEE Press, 1993).

30. Carminati, R., Greffet, J.-J., Henkel, C. & Vigoureux, J.-M. Radiative and non-radiative decay of a single molecule close to a metallic nanoparticle. *Optics Communications* **261**, 368–375 (2006).
31. Novotny, L. Single molecule fluorescence in inhomogeneous environments. *Applied Physics Letters* **69**, 3806–3808 (1996).
32. Thomas, M., Greffet, J.-J., Carminati, R. & Arias-Gonzalez, J. Single-molecule spontaneous emission close to absorbing nanostructures. *Applied Physics Letters* **85**, 3863–3865 (2004).
33. Blanco, L. & De Abajo, F. G. Spontaneous light emission in complex nanostructures. *Physical Review B* **69**, 205414 (2004).
34. Drexhage, K. Influence of a dielectric interface on fluorescence decay time. *Journal of Luminescence* **1**, 693–701 (1970).
35. Anger, P., Bharadwaj, P. & Novotny, L. Enhancement and quenching of single-molecule fluorescence. *Physical Review Letters* **96**, 113002 (2006).
36. Purcell, E. M. in *Confined Electrons and Photons* 839–839 (Springer, 1995).
37. Goy, P., Raimond, J. M., Gross, M. & Haroche, S. Observation of Cavity-Enhanced Single-Atom Spontaneous Emission. *Physical Review Letters* **50**, 1903 (1983).
38. Kleppner, D. Inhibited Spontaneous Emission. *Physical Review Letters* **47**, 233 (1981).
39. Yablonovitch, E. Inhibited Spontaneous Emission in Solid-State Physics and Electronics. *Physical Review Letters* **58**, 2059 (1987).
40. John, S. Strong Localization of photons in certain disordered dielectric superlattice. *Physical Review Letters* **58**, 2486 (1987).
41. JJoannopoulos, J. D., Villeneuve, P. R. & Fan, S. Photonic Crystals: putting a new twist on light. *Nature* **386**, 143–149 (1997).
42. Cohen-Tannoudji, C., Dupont-Roc, J. & Grynberg, G. *Photons and Atoms: Introduction to Quantum Electrodynamics* (Wiley-Interscience, New York, 1989).
43. Craig, D. P. & Thirunamachandran, T. *Molecular Quantum Electrodynamics* (Academic Press, London, 1984).
44. Tokmakoff, A. *Quantum Mechanical Electric Dipole Hamiltonian* (Libre-Texts, 2020).
45. Sakurai, J. J. & Napolitano, J. *Modern Quantum Mechanics* (Pearson, 2010).
46. Loudon, R. *The Quantum Theory of Light* (Oxford University Press, 1983).
47. Cohen-Tannoudji, C., Diu, B. & Laloe, F. *Quantum Mechanics Vol. I* (Wiley, 1977).

48. Williams, D. B. & Carter, C. B. in *Transmission electron microscopy* (Springer, 1996).
49. Pennycook, S. J. & Nellist, P. D. *Scanning transmission electron microscopy: imaging and analysis* (Springer Science & Business Media, 2011).
50. Crewe, A. The physics of the high-resolution scanning microscope. *Reports on Progress in Physics* **43**, 621 (1980).
51. Pennycook, S. & Jesson, D. High-resolution Z-contrast imaging of crystals. *Ultramicroscopy* **37**, 14–38 (1991).
52. Xu, P., Loane, R. F. & Silcox, J. Energy-filtered convergent-beam electron diffraction in STEM. *Ultramicroscopy* **38**, 127–133 (1991).
53. Cowley, J. Applications of electron nanodiffraction. *Micron* **35**, 345–360 (2004).
54. Chu, M.-W., Liou, S., Chang, C.-P., Choa, F.-S. & Chen, C. Emergent chemical mapping at atomic-column resolution by energy-dispersive X-ray spectroscopy in an aberration-corrected electron microscope. *Physical Review Letters* **104**, 196101 (2010).
55. Slater, T. J. *et al.* STEM-EDX tomography of bimetallic nanoparticles: A methodological investigation. *Ultramicroscopy* **162**, 61–73 (2016).
56. Spence, J. C. & Zuo, J. *Electron microdiffraction* (Plenum, 1992).
57. Carter, C. B. & Williams, D. B. *Transmission electron microscopy: Diffraction, imaging, and spectrometry* (Springer, 2016).
58. Knauer, W. Boersch effect in electron-optical instruments. *Journal of Vacuum Science and Technology* **16**, 1676–1679 (1979).
59. Van Veen, A., Hagen, C., Barth, J. & Kruit, P. Reduced brightness of the ZrO/W Schottky electron emitter. *Journal of Vacuum Science & Technology B: Microelectronics and Nanometer Structures Processing, Measurement, and Phenomena* **19**, 2038–2044 (2001).
60. Maunders, C., Dwyer, C., Tiemeijer, P. & Etheridge, J. Practical methods for the measurement of spatial coherence—a comparative study. *Ultramicroscopy* **111**, 1437–1446 (2011).
61. Young, R. D. Theoretical total-energy distribution of field-emitted electrons. *Physical Review* **113**, 110 (1959).
62. De Heer, W. A., Chatelain, A. & Ugarte, D. A carbon nanotube field-emission electron source. *Science* **270**, 1179–1180 (1995).
63. Fransen, M., Van Rooy, T. L. & Kruit, P. Field emission energy distributions from individual multiwalled carbon nanotubes. *Applied Surface Science* **146**, 312–327 (1999).

64. Houdellier, F. *et al.* Development of TEM and SEM high brightness electron guns using cold-field emission from a carbon nanotip. *Ultramicroscopy* **151**, 107–115 (2015).
65. Zhang, H. *et al.* An ultrabright and monochromatic electron point source made of a LaB 6 nanowire. *Nature Nanotechnology* **11**, 273–279 (2016).
66. Zhang, H. *et al.* High-endurance micro-engineered LaB6 nanowire electron source for high-resolution electron microscopy. *Nature Nanotechnology*, 1–6 (2021).
67. Rose, H. & Wan, W. Aberration correction in electron microscopy. *Proceedings of the 2005 Particle Accelerator Conference*, 44–48 (2005).
68. Rose, H. H. Historical aspects of aberration correction. *Journal of Electron Microscopy* **58**, 77–85 (2009).
69. Hawkes, P. The correction of electron lens aberrations. *Ultramicroscopy* **156**, A1–A64 (2015).
70. Rose, H. Outline of a spherically corrected semiaplanatic medium-voltage transmission electron microscope. *Optik* **85**, 19–24 (1990).
71. Zach, J. & Haider, M. Aberration correction in a low voltage SEM by a multipole corrector. *Nuclear Instruments and Methods in Physics Research Section A: Accelerators, Spectrometers, Detectors and Associated Equipment* **363**, 316–325 (1995).
72. Krivanek, O., Dellby, N. & Lupini, A. Towards sub-Å electron beams. *Ultramicroscopy* **78**, 1–11 (1999).
73. Krivanek, O., Nellist, P., Dellby, N., Murfitt, M. & Szilagy, Z. Towards sub-0.5 Å electron beams. *Ultramicroscopy* **96**, 229–237 (2003).
74. Dellby, N. *et al.* Dedicated STEM for 200 to 40 keV operation. *The European Physical Journal-Applied Physics* **54** (2011).
75. Egerton, R. F. *Electron energy-loss spectroscopy in the electron microscope* (Springer Science & Business Media, 2011).
76. Wittry, D. An electron spectrometer for use with the transmission electron microscope. *Journal of Physics D: Applied Physics* **2**, 1757 (1969).
77. Tang, T. Correction of aberrations in a magnetic spectrometer by electric multipole lenses. *Ultramicroscopy* **7**, 305–309 (1982).
78. Castaing, R. Filtrage magnetique des vitesses en microscopie electronique. *Comptes Rendus de l'Académie des Sciences de Paris* **255**, 76–78 (1962).
79. Colliex, C. The “father” of microanalysis: Raymond Castaing, creator of a generation of scientific instruments, still in worldwide operation. *Comptes Rendus Physique* **20**, 746–755 (2019).

80. Schröder, B. & Geiger, J. Electron-spectrometric study of amorphous germanium and silicon in the two-phonon region. *Physical Review Letters* **28**, 301 (1972).
81. Krivanek, O. L. *et al.* Vibrational spectroscopy in the electron microscope. *Nature* **514**, 209–212 (2014).
82. Boersch, H., Geiger, J. & Stickel, W. Interaction of 25-keV electrons with lattice vibrations in LiF. Experimental evidence for surface modes of lattice vibration. *Physical Review Letters* **17**, 379 (1966).
83. Krivanek, O. L., Lovejoy, T. C., Dellby, N. & Carpenter, R. Monochromated STEM with a 30 meV-wide, atom-sized electron probe. *Microscopy* **62**, 3–21 (2013).
84. Krivanek, O. L. *et al.* Towards sub-10 meV energy resolution STEM-EELS. *Journal of Physics: Conference Series* **522**, 012023 (2014).
85. Krivanek, O. L. *et al.* High-energy-resolution monochromator for aberration-corrected scanning transmission electron microscopy/electron energy-loss spectroscopy. *Philosophical Transactions of the Royal Society A: Mathematical, Physical and Engineering Sciences* **367**, 3683–3697 (2009).
86. Ritchie, R. H. Plasma losses by fast electrons in thin films. *Physical Review* **106**, 874 (1957).
87. García De Abajo, F. Optical excitations in electron microscopy. *Reviews of Modern Physics* **82**, 209 (2010).
88. Kociak, M. & Stéphan, O. Mapping plasmons at the nanometer scale in an electron microscope. *Chemical Society Reviews* **43**, 3865–3883 (2014).
89. Losquin, A. & Kociak, M. Link between cathodoluminescence and electron energy loss spectroscopy and the radiative and full electromagnetic local density of states. *ACS Photonics* **2**, 1619–1627 (2015).
90. Losquin, A. *et al.* Unveiling Nanometer Scale Extinction and Scattering Phenomena through Combined Electron Energy Loss Spectroscopy and Cathodoluminescence Measurements. *Nano Letters* **15**, 1229–1237 (2015).
91. Yamamoto, N., Bhunia, S. & Watanabe, Y. Polarized cathodoluminescence study of InP nanowires by transmission electron microscopy. *Applied Physics Letters* **88**, 153106 (2006).
92. Zagonel, L. F. *et al.* Nanometer scale spectral imaging of quantum emitters in nanowires and its correlation to their atomically resolved structure. *Nano Letters* **11**, 568–573 (2011).
93. Bourrellier, R. *et al.* Bright UV single photon emission at point defects in h-BN. *Nano Letters* **16**, 4317–4321 (2016).

94. Zuloaga, J. & Nordlander, P. On the energy shift between near-field and far-field peak intensities in localized plasmon systems. *Nano Letters* **11**, 1280–1283 (2011).
95. Kats, M. A., Yu, N., Genevet, P., Gaburro, Z. & Capasso, F. Effect of radiation damping on the spectral response of plasmonic components. *Optics Express* **19**, 21748–21753 (2011).
96. Yamamoto, N., Spence, J. & Fathy, D. Cathodoluminescence and polarization studies from individual dislocations in diamond. *Philosophical Magazine B* **49**, 609–629 (1984).
97. Kociak, M. & Zagonel, L. Cathodoluminescence in the scanning transmission electron microscope. *Ultramicroscopy* **176**, 112–131 (2017).
98. Merano, M. *et al.* Probing carrier dynamics in nanostructures by picosecond cathodoluminescence. *Nature* **438**, 479–482 (2005).
99. Coenen, T., Vesseur, E. J. R., Polman, A. & Koenderink, A. F. Directional emission from plasmonic Yagi–Uda antennas probed by angle-resolved cathodoluminescence spectroscopy. *Nano Letters* **11**, 3779–3784 (2011).
100. Park, S. T., Lin, M. & Zewail, A. H. Photon-induced near-field electron microscopy (PINEM): theoretical and experimental. *New Journal of Physics* **12**, 123028 (2010).
101. García de Abajo, F. J., Asenjo-Garcia, A. & Kociak, M. Multiphoton absorption and emission by interaction of swift electrons with evanescent light fields. *Nano Letters* **10**, 1859–1863 (2010).
102. Asenjo-Garcia, A. & De Abajo, F. G. Plasmon electron energy-gain spectroscopy. *New Journal of Physics* **15**, 103021 (2013).
103. Jeanguillaume, C. & Colliex, C. Spectrum-image: the next step in EELS digital acquisition and processing. *Ultramicroscopy* **28**, 252–257 (1989).
104. Suenaga, K. *et al.* Element-selective single atom imaging. *Science* **290**, 2280–2282 (2000).
105. Tizei, L. & Kociak, M. Spatially resolved quantum nano-optics of single photons using an electron microscope. *Physical Review Letters* **110**, 153604 (2013).
106. Meuret, S. *et al.* Photon bunching in cathodoluminescence. *Physical Review Letters* **114**, 197401 (2015).
107. Attolight. *Mönch* Accessed on 18/02/2022. 2022. <https://attolight.com/monch/>.
108. Meyer, C. *et al.* Nion Swift: Open Source Image Processing Software for Instrument Control, Data Acquisition, Organization, Visualization, and Analysis Using Python. *Microscopy and Microanalysis* **25**, 122–123 (2019).

109. Hachtel, J. A. *et al.* Identification of site-specific isotopic labels by vibrational spectroscopy in the electron microscope. *Science* **363**, 525–528 (2019).
110. Hage, F., Radtke, G., Kepaptsoglou, D., Lazzeri, M. & Ramasse, Q. Single-atom vibrational spectroscopy in the scanning transmission electron microscope. *Science* **367**, 1124–1127 (2020).
111. Tizei, L. H. *et al.* Tailored nanoscale plasmon-enhanced vibrational electron spectroscopy. *Nano Letters* **20**, 2973–2979 (2020).
112. Mkhitarian, V. *et al.* Can Copper Nanostructures Sustain High-Quality Plasmons? *Nano Letters* **21**, 2444–2452 (2021).
113. Li, X. *et al.* Three-dimensional vectorial imaging of surface phonon polaritons. *Science* **371**, 1364–1367 (2021).
114. Bonnet, N. *et al.* Nanoscale modification of WS₂ trion emission by its local electromagnetic environment. *Nano Letters* **21**, 10178–10185 (2021).
115. De Abajo, F. G. & Howie, A. Retarded field calculation of electron energy loss in inhomogeneous dielectrics. *Physical Review B* **65**, 115418 (2002).
116. Myroshnychenko, V. *et al.* Modelling the optical response of gold nanoparticles. *Chemical Society Reviews* **37**, 1792–1805 (2008).
117. Geuquet, N. & Henrard, L. EELS and optical response of a noble metal nanoparticle in the frame of a discrete dipole approximation. *Ultramicroscopy* **110**, 1075–1080 (2010).
118. Bigelow, N. W., Vaschillo, A., Iberi, V., Camden, J. P. & Masiello, D. J. Characterization of the electron- and photon-driven plasmonic excitations of metal nanorods. *ACS Nano* **6**, 7497–7504 (2012).
119. Koh, A. L., Fernández-Domínguez, A. I., McComb, D. W., Maier, S. A. & Yang, J. K. High-resolution mapping of electron-beam-excited plasmon modes in lithographically defined gold nanostructures. *Nano Letters* **11**, 1323–1330 (2011).
120. Duan, H., Fernández-Domínguez, A. I., Bosman, M., Maier, S. A. & Yang, J. K. Nanoplasmonics: classical down to the nanometer scale. *Nano Letters* **12**, 1683–1689 (2012).
121. Hohenester, U. & Trügler, A. MNPBEM—A Matlab toolbox for the simulation of plasmonic nanoparticles. *Computer Physics Communications* **183**, 370–381 (2012).
122. Hohenester, U. Simulating electron energy loss spectroscopy with the MNPBEM toolbox. *Computer Physics Communications* **185**, 1177–1187 (2014).
123. Oskooi, A. F. *et al.* MEEP: A flexible free-software package for electromagnetic simulations by the FDTD method. *Computer Physics Communications* **181**, 687–702 (2010).

124. Inc., A. *Lumerical 2020 R2* version R2. 2020. <https://lumerical.com>.
125. Amelinckx, S., Van Dyck, D., Van Landuyt, J. & Van Tendeloo, G. Handbook of microscopy. *Practical Metallography* **34**, 12 (1997).
126. Mitsui, T., Yamamoto, N., Tadokoro, T. & Ohta, S.-i. Cathodoluminescence image of defects and luminescence centers in ZnS/GaAs (100). *Journal of Applied Physics* **80**, 6972–6979 (1996).
127. Boersch, H., Geiger, J., Imbusch, A. & Niedrig, N. High resolution investigation of the energy losses of 30 keV electrons in aluminum foils of various thicknesses. *Physics Letters* **22**, 146–147 (1966).
128. Schilling, J. & Raether, H. Energy gain of fast electrons interacting with surface plasmons. *Journal of Physics C: Solid State Physics* **6**, L358 (1973).
129. Idrobo, J. C. *et al.* Temperature measurement by a nanoscale electron probe using energy gain and loss spectroscopy. *Physical Review Letters* **120**, 095901 (2018).
130. Mizuno, K., Pae, J., Nozokido, T. & Furuya, K. Experimental evidence of the inverse Smith–Purcell effect. *Nature* **328**, 45–47 (1987).
131. Talebi, N. Schrödinger electrons interacting with optical gratings: quantum mechanical study of the inverse Smith–Purcell effect. *New Journal of Physics* **18**, 123006 (2016).
132. Wang, K. *et al.* Coherent interaction between free electrons and a photonic cavity. *Nature* **582**, 50–54 (2020).
133. Dahan, R. *et al.* Resonant phase-matching between a light wave and a free-electron wavefunction. *Nature Physics* **16**, 1123–1131 (2020).
134. Houdellier, F., Caruso, G. M., Weber, S., Kociak, M. & Arbouet, A. Development of a high brightness ultrafast transmission electron microscope based on a laser-driven cold field emission source. *Ultramicroscopy* **186**, 128–138 (2018).
135. Liu, C. *et al.* Continuous wave resonant photon stimulated electron energy-gain and electron energy-loss spectroscopy of individual plasmonic nanoparticles. *ACS Photonics* **6**, 2499–2508 (2019).
136. Collette, R., Garfinkel, D. A., Hu, Z., Masiello, D. J. & Rack, P. D. Near field excited state imaging via stimulated electron energy gain spectroscopy of localized surface plasmon resonances in plasmonic nanorod antennas. *Scientific Reports* **10**, 1–9 (2020).
137. Henke, J.-W. *et al.* Integrated photonics enables continuous-beam electron phase modulation. *Nature* **600**, 653–658 (2021).
138. Efimov, A. Spatial coherence at the output of multimode optical fibers. *Optics Express* **22**, 15577–15588 (2014).

139. Lomer, M., Rodriguez-Cobo, L., Madruga, F. & Lopez-Higuera, J. Interference of speckle patterns projected by multimode fibers. *Speckle 2015: VI International Conference on Speckle Metrology* **9660**, 96601S (2015).
140. Shabairou, N. *et al.* All-optical, an ultra-thin endoscopic photoacoustic sensor using multi-mode fiber. *Scientific Reports* **10**, 1–8 (2020).
141. Sorokin, P. P. & Lankard, J. Stimulated emission observed from an organic dye, chloro-aluminum phthalocyanine. *IBM Journal of Research and Development* **10**, 162–163 (1966).
142. Schäfer, F. P., Schmidt, W. & Volze, J. Organic dye solution laser. *Applied Physics Letters* **9**, 306–309 (1966).
143. Hänsch, T. W. Nobel lecture: passion for precision. *Reviews of Modern Physics* **78**, 1297 (2006).
144. Liechti, C. *PySerial* version 3.5. Accessed on 04/01/2022. 2020. <https://pypi.org/project/pyserial/>.
145. Zobelli, A. *et al.* Spatial and spectral dynamics in STEM hyperspectral imaging using random scan patterns. *Ultramicroscopy* **212**, 112912 (2020).
146. McClung, F. & Hellwarth, R. Giant optical pulsations from ruby. *Applied Optics* **1**, 103–105 (1962).
147. McClung, F. & Hellwarth, R. Characteristics of giant optical pulsations from ruby. *Proceedings of the IEEE* **51**, 46–53 (1963).
148. Maiman, T. Stimulated Optical Radiation in Ruby. *Nature* **187**, 493–494 (1960).
149. Geusic, J., Marcos, H. & Van Uitert, L. Laser oscillations in Nd-doped yttrium aluminum, yttrium gallium and gadolinium garnets. *Applied Physics Letters* **4**, 182–184 (1964).
150. Sorokin, P., Lankard, J., Hammond, E. C. & Moruzzi, V. L. Laser-pumped stimulated emission from organic dyes: Experimental studies and analytical comparisons. *IBM Journal of Research and Development* **11**, 130–148 (1967).
151. Hänsch, T. W. Repetitively pulsed tunable dye laser for high resolution spectroscopy. *Applied Optics* **11**, 895–898 (1972).
152. Littman, M. G. & Metcalf, H. J. Spectrally narrow pulsed dye laser without beam expander. *Applied Optics* **17**, 2224–2227 (1978).
153. Laser & Dyes, F. *Luxottica Exciton* Accessed on 31/01/2022. 2021. <https://exciton.luxottica.com/laser-dyes.html>.
154. UNO, A. *Servo* Accessed on 02/02/2022. 2022. <https://www.arduino.cc/reference/en/libraries/servo/>.

155. Thorlabs. *PM100USB - Power and Energy Meter Interface with USB Operation* Accessed on 02/02/2022. 2022. <https://www.thorlabs.com/thorproduct.cfm?partnumber=PM100USB>.
156. Thorlabs. *PIAK10 - Piezo Inertia Actuator, 10 mm Travel, 1/4"-80 Mounting Thread* Accessed on 02/02/2022. 2022. <https://www.thorlabs.com/thorproduct.cfm?partnumber=PIAK10>.
157. Thorlabs. *MAX313D/M - 3-Axis NanoMax Stage, Differential Drives, No Piezos, Metric* Accessed on 02/02/2022. 2022. <https://www.thorlabs.com/thorproduct.cfm?partnumber=MAX313D/M>.
158. Kociak, M., Tence, M., Blazit, J.-D. & Das, P. *Stimulated or non-equilibrium energy-loss and energy-gain spectroscopy device* US Patent App. 16/830,646. Oct. 2020.
159. Auad, Y. *A study of electronic and optical spectroscopies in a scanning tunneling microscope and in a scanning transmission electron microscope* (Unicamp, 2019).
160. Rocca, M., Moresco, F. & Valbusa, U. Temperature dependence of surface plasmons on Ag (001). *Physical Review B* **45**, 1399 (1992).
161. Yeshchenko, O., Bondarchuk, I., Gurin, V., Dmitruk, I. & Kotko, A. Temperature dependence of the surface plasmon resonance in gold nanoparticles. *Surface Science* **608**, 275–281 (2013).
162. Mecklenburg, M. *et al.* Nanoscale temperature mapping in operating micro-electronic devices. *Science* **347**, 629–632 (2015).
163. Stolen, R. & Ippen, E. Raman gain in glass optical waveguides. *Applied Physics Letters* **22**, 276–278 (1973).
164. Stolen, R. H., Lee, C. & Jain, R. Development of the stimulated Raman spectrum in single-mode silica fibers. *JOSA B* **1**, 652–657 (1984).
165. Stolen, R. H., Gordon, J. P., Tomlinson, W. & Haus, H. A. Raman response function of silica-core fibers. *JOSA B* **6**, 1159–1166 (1989).
166. Instruments, A. S. *CheeTah* Accessed on 04/02/2022. 2022. <https://www.amscins.com/products/em-cheetah/#tab-id-3>.
167. Weppelman, I., Moerland, R., Hoogenboom, J. & Kruit, P. Concept and design of a beam blanker with integrated photoconductive switch for ultrafast electron microscopy. *Ultramicroscopy* **184**, 8–17 (2018).
168. Zhang, L., Hoogenboom, J. P., Cook, B. & Kruit, P. Photoemission sources and beam blankers for ultrafast electron microscopy. *Structural Dynamics* **6**, 051501 (2019).
169. Lassise, A., Mutsaers, P. & Luiten, O. Compact, low power radio frequency cavity for femtosecond electron microscopy. *Review of Scientific Instruments* **83**, 043705 (2012).

170. Verhoeven, W., Van Rens, J., Kieft, E., Mutsaers, P. & Luiten, O. High quality ultrafast transmission electron microscopy using resonant microwave cavities. *Ultramicroscopy* **188**, 85–89 (2018).
171. Link, S. & El-Sayed, M. A. Shape and size dependence of radiative, non-radiative and photothermal properties of gold nanocrystals. *International Reviews in Physical Chemistry* **19**, 409–453 (2000).
172. Tian, Z.-Q., Ren, B. & Wu, D.-Y. Surface-enhanced Raman scattering: from noble to transition metals and from rough surfaces to ordered nanostructures. *The Journal of Physical Chemistry B* **106**, 9463–9483 (2002).
173. Sun, Y. & Xia, Y. Gold and silver nanoparticles: a class of chromophores with colors tunable in the range from 400 to 750 nm. *Analyst* **128**, 686–691 (2003).
174. Liz-Marzán, L. M. Nanometals: formation and color. *Colloidal Synthesis of Plasmonic Nanometals*, 26–31 (2004).
175. Vahala, K. J. Optical microcavities. *Nature* **424**, 839–846 (2003).
176. Vernooy, D., Furusawa, A., Georgiades, N. P., Ilchenko, V. & Kimble, H. Cavity QED with high-Q whispering gallery modes. *Physical Review A* **57**, R2293 (1998).
177. Wiederhecker, G. S., Chen, L., Gondarenko, A. & Lipson, M. Controlling photonic structures using optical forces. *Nature* **462**, 633–636 (2009).
178. Kippenberg, T., Rokhsari, H., Carmon, T., Scherer, A. & Vahala, K. Analysis of radiation-pressure induced mechanical oscillation of an optical microcavity. *Physical Review Letters* **95**, 033901 (2005).
179. Chow, E., Grot, A., Mirkarimi, L., Sigalas, M. & Girolami, G. Ultracompact biochemical sensor built with two-dimensional photonic crystal microcavity. *Optics Letters* **29**, 1093–1095 (2004).
180. Zhu, J. *et al.* On-chip single nanoparticle detection and sizing by mode splitting in an ultrahigh-Q microresonator. *Nature Photonics* **4**, 46–49 (2010).
181. Zheng, Y. *et al.* Sensing and lasing applications of whispering gallery mode microresonators. *Opto-Electronic Advances* **1**, 180015–1 (2018).
182. Liang, W. *et al.* Fabry-Perot interference in a nanotube electron waveguide. *Nature* **411**, 665–669 (2001).
183. Hernández, G. *Fabry-perot interferometers* (Cambridge University Press, 1988).
184. McCall, S., Levi, A., Slusher, R., Pearton, S. & Logan, R. Whispering-gallery mode microdisk lasers. *Applied Physics Letters* **60**, 289–291 (1992).
185. Armani, D., Kippenberg, T., Spillane, S. & Vahala, K. Ultra-high-Q toroid microcavity on a chip. *Nature* **421**, 925–928 (2003).

186. Djordjev, K., Choi, S.-J., Choi, S.-J. & Dapkus, R. Microdisk tunable resonant filters and switches. *IEEE Photonics Technology Letters* **14**, 828–830 (2002).
187. Richtmyer, R. Dielectric resonators. *Journal of Applied Physics* **10**, 391–398 (1939).
188. Garrett, C., Kaiser, W. & Bond, W. Stimulated emission into optical whispering modes of spheres. *Physical Review* **124**, 1807 (1961).
189. Ashkin, A. & Dziedzic, J. Observation of resonances in the radiation pressure on dielectric spheres. *Physical Review Letters* **38**, 1351 (1977).
190. Benner, R., Barber, P., Owen, J. & Chang, R. Observation of structure resonances in the fluorescence spectra from microspheres. *Physical Review Letters* **44**, 475 (1980).
191. Hill, S. C., Benner, R. E., Rushforth, C. K. & Conwell, P. R. Structural resonances observed in the fluorescence emission from small spheres on substrates. *Applied Optics* **23**, 1680–1683 (1984).
192. Tzeng, H.-M., Wall, K. F., Long, M. & Chang, R. Laser emission from individual droplets at wavelengths corresponding to morphology-dependent resonances. *Optics Letters* **9**, 499–501 (1984).
193. Lin, H.-B., Huston, A., Justus, B. & Campillo, A. J. Some characteristics of a droplet whispering-gallery-mode laser. *Optics Letters* **11**, 614–616 (1986).
194. Kimble, H. J. Strong interactions of single atoms and photons in cavity QED. *Physica Scripta* **1998**, 127 (1998).
195. Thompson, R., Rempe, G. & Kimble, H. Observation of normal-mode splitting for an atom in an optical cavity. *Physical Review Letters* **68**, 1132 (1992).
196. Gérard, J.-M. *et al.* Enhanced spontaneous emission by quantum boxes in a monolithic optical microcavity. *Physical Review Letters* **81**, 1110 (1998).
197. Bayer, M. *et al.* Inhibition and enhancement of the spontaneous emission of quantum dots in structured microresonators. *Physical Review Letters* **86**, 3168 (2001).
198. Gorodetsky, M. L., Savchenkov, A. A. & Ilchenko, V. S. Ultimate Q of optical microsphere resonators. *Optics Letters* **21**, 453–455 (1996).
199. Vernooy, D., Ilchenko, V. S., Mabuchi, H., Streed, E. & Kimble, H. High-Q measurements of fused-silica microspheres in the near infrared. *Optics Letters* **23**, 247–249 (1998).
200. Akahane, Y., Asano, T., Song, B.-S. & Noda, S. High-Q photonic nanocavity in a two-dimensional photonic crystal. *Nature* **425**, 944–947 (2003).

201. Mabuchi, H., Turchette, Q., Chapman, M. & Kimble, H. Real-time detection of individual atoms falling through a high-finesse optical cavity. *Optics Letters* **21**, 1393–1395 (1996).
202. García de Abajo, F. Relativistic energy loss and induced photon emission in the interaction of a dielectric sphere with an external electron beam. *Physical Review B* **59**, 3095 (1999).
203. Müller, N. *et al.* Broadband coupling of fast electrons to high-Q whispering-gallery mode resonators. *ACS Photonics* **8**, 1569–1575 (2021).
204. Nelayah, J. *et al.* Mapping surface plasmons on a single metallic nanoparticle. *Nature Physics* **3**, 348–353 (2007).
205. Rayleigh, L. CXII. The problem of the whispering gallery. *The London, Edinburgh, and Dublin Philosophical Magazine and Journal of Science* **20**, 1001–1004 (1910).
206. Treussart, F. *Etude expérimentale de l'effet laser dans des microsphères de silice dopées avec des ions neodyme* PhD thesis (Université Pierre et Marie Curie-Paris VI, 1997).
207. Righini, G. *et al.* Whispering gallery mode microresonators: fundamentals and applications. *La Rivista del Nuovo Cimento* **34**, 435–488 (2011).
208. Balac, S. & Féron, P. *Whispering gallery modes volume computation in optical micro-spheres* (Institut FOTON - UMR CNRS 6082, 2014).
209. Nussenzveig, H. M. *Diffraction effects in semiclassical scattering* (Cambridge University Press, 1992).
210. Mie, G. Beiträge zur Optik trüber Medien, speziell kolloidaler Metallösungen. *Annalen der physik* **330**, 377–445 (1908).
211. Hulst, H. Optics of Spherical Particles. *Recherches Astronomiques de l'Observatoire d'Utrecht* **11**, 1 (1946).
212. García De Abajo, F. Multiple scattering of radiation in clusters of dielectrics. *Physical Review B* **60**, 6086 (1999).
213. Knight, J. C., Cheung, G., Jacques, F. & Birks, T. Phase-matched excitation of whispering-gallery-mode resonances by a fiber taper. *Optics Letters* **22**, 1129–1131 (1997).
214. Cai, M., Painter, O. & Vahala, K. J. Observation of critical coupling in a fiber taper to a silica-microsphere whispering-gallery mode system. *Physical Review Letters* **85**, 74 (2000).
215. Miri, N. & Mohammadzadeh, M. Optical sensing using microspheres with different size and material. *IEEE Sensors Journal* **14**, 3593–3598 (2014).
216. Liu, C. *et al.* Enhanced energy storage in chaotic optical resonators. *Nature Photonics* **7**, 473–478 (2013).

217. Lacey, S. & Wang, H. Directional emission from whispering-gallery modes in deformed fused-silica microspheres. *Optics Letters* **26**, 1943–1945 (2001).
218. Kippenberg, T. J., Tchebotareva, A., Kalkman, J., Polman, A. & Vahala, K. J. Purcell-factor-enhanced scattering from Si nanocrystals in an optical microcavity. *Physical Review Letters* **103**, 027406 (2009).
219. Motsch, M., Zeppenfeld, M., Pinkse, P. W. & Rempe, G. Cavity-enhanced Rayleigh scattering. *New Journal of Physics* **12**, 063022 (2010).
220. Mazzei, A. *et al.* Controlled coupling of counterpropagating whispering-gallery modes by a single Rayleigh scatterer: a classical problem in a quantum optical light. *Physical Review Letters* **99**, 173603 (2007).
221. Zhi, Y., Valenta, J. & Meldrum, A. Structure of whispering gallery mode spectrum of microspheres coated with fluorescent silicon quantum dots. *JOSA B* **30**, 3079–3085 (2013).
222. Zhi, Y., Yu, X.-C., Gong, Q., Yang, L. & Xiao, Y.-F. Single nanoparticle detection using optical microcavities. *Advanced Materials* **29**, 1604920 (2017).
223. Vollmer, F., Arnold, S. & Keng, D. Single virus detection from the reactive shift of a whispering-gallery mode. *Proceedings of the National Academy of Sciences* **105**, 20701–20704 (2008).
224. Özdemir, Ş. K., Zhu, J., He, L. & Yang, L. Estimation of Purcell factor from mode-splitting spectra in an optical microcavity. *Physical Review A* **83**, 033817 (2011).
225. Shen, B.-Q. *et al.* Detection of single nanoparticles using the dissipative interaction in a high-Q microcavity. *Physical Review Applied* **5**, 024011 (2016).
226. Shao, L. *et al.* Detection of single nanoparticles and lentiviruses using microcavity resonance broadening. *Advanced Materials* **25**, 5616–5620 (2013).
227. Zhang, J. *et al.* Engineering the absorption and field enhancement properties of Au–TiO₂ nanohybrids via whispering gallery mode resonances for photocatalytic water splitting. *ACS Nano* **10**, 4496–4503 (2016).
228. Wang, P. *et al.* Single-band 2-nm-line-width plasmon resonance in a strongly coupled Au nanorod. *Nano Letters* **15**, 7581–7586 (2015).
229. Ai, Q. *et al.* Ultranarrow second-harmonic resonances in hybrid plasmon-fiber cavities. *Nano Letters* **18**, 5576–5582 (2018).
230. Gu, F., Zhang, L., Zhu, Y. & Zeng, H. Free-space coupling of nanoantennas and whispering-gallery microcavities with narrowed linewidth and enhanced sensitivity. *Laser & Photonics Reviews* **9**, 682–688 (2015).

231. Yamamoto, N., Araya, K. & de Abajo, F. G. Photon emission from silver particles induced by a high-energy electron beam. *Physical Review B* **64**, 205419 (2001).
232. Yablonovitch, E. & Gmitter, T. Photonic band structure: The face-centered-cubic case. *Physical Review Letters* **63**, 1950 (1989).
233. Yablonovitch, E., Gmitter, T. & Leung, K.-M. Photonic band structure: The face-centered-cubic case employing nonspherical atoms. *Physical Review Letters* **67**, 2295 (1991).
234. Joannopoulos, J. D., Johnson, S. G., Winn, J. N. & Meade, R. D. *Photonic Crystals* (Princeton University Press, 2011).
235. Kuramochi, E. *et al.* Ultrahigh-Q photonic crystal nanocavities realized by the local width modulation of a line defect. *Applied Physics Letters* **88**, 041112 (2006).
236. Painter, O. *et al.* Two-dimensional photonic band-gap defect mode laser. *Science* **284**, 1819–1821 (1999).
237. Noda, S., Chutinan, A. & Imada, M. Trapping and emission of photons by a single defect in a photonic bandgap structure. *Nature* **407**, 608–610 (2000).
238. Srinivasan, K. & Painter, O. Momentum space design of high-Q photonic crystal optical cavities. *Optics Express* **10**, 670–684 (2002).
239. Srinivasan, K. *et al.* Experimental demonstration of a high quality factor photonic crystal microcavity. *Applied Physics Letters* **83**, 1915–1917 (2003).
240. Happ, T. *et al.* Enhanced light emission of In x Ga 1- x As quantum dots in a two-dimensional photonic-crystal defect microcavity. *Physical Review B* **66**, 041303 (2002).
241. Akahane, Y., Mochizuki, M., Asano, T., Tanaka, Y. & Noda, S. Design of a channel drop filter by using a donor-type cavity with high-quality factor in a two-dimensional photonic crystal slab. *Applied Physics Letters* **82**, 1341–1343 (2003).
242. Bangs Laboratories, I. *Non-functionalized Silica* Accessed on 04/01/2022. <https://bangslabs.com>.
243. Cao, Y., Manjavacas, A., Large, N. & Nordlander, P. Electron energy-loss spectroscopy calculation in finite-difference time-domain package. *ACS Photonics* **2**, 369–375 (2015).
244. Sumlin, B. *PyMieScatt: Release v1.8.1* version 1.8.1. Accessed on 15/02/2022. 2020. <https://pymiescatt.readthedocs.io>.
245. Malitson, I. H. Interspecimen comparison of the refractive index of fused silica. *JOSA* **55**, 1205–1209 (1965).

246. Schunk, G. *et al.* Identifying modes of large whispering-gallery mode resonators from the spectrum and emission pattern. *Optics Express* **22**, 30795–30806 (2014).
247. Buck, J. & Kimble, H. Optimal sizes of dielectric microspheres for cavity QED with strong coupling. *Physical Review A* **67**, 033806 (2003).
248. Zheng, Y., Zhong, X., Li, Z. & Xia, Y. Successive, Seed-Mediated Growth for the Synthesis of Single-Crystal Gold Nanospheres with Uniform Diameters Controlled in the Range of 5–150 nm. *Particle & Particle Systems Characterization* **31**, 266–273 (2014).
249. Mayer, M. *et al.* Controlled living nanowire growth: precise control over the morphology and optical properties of AgAuAg bimetallic nanowires. *Nano Letters* **15**, 5427–5437 (2015).
250. Fuchs, R. Theory of the optical properties of ionic crystal cubes. *Physical Review B* **11**, 1732 (1975).
251. Langbein, D. Normal modes at small cubes and rectangular particles. *Journal of Physics A: Mathematical and General* **9**, 627 (1976).
252. Sherry, L. J. *et al.* Localized surface plasmon resonance spectroscopy of single silver nanocubes. *Nano Letters* **5**, 2034–2038 (2005).
253. Mazzucco, S. *et al.* Ultralocal modification of surface plasmons properties in silver nanocubes. *Nano Letters* **12**, 1288–1294 (2012).
254. Lourenço-Martins, H. & Kociak, M. Vibrational surface electron-energy-loss spectroscopy probes confined surface-phonon modes. *Physical Review X* **7**, 041059 (2017).
255. Zhang, S., Bao, K., Halas, N. J., Xu, H. & Nordlander, P. Substrate-induced Fano resonances of a plasmonic nanocube: a route to increased-sensitivity localized surface plasmon resonance sensors revealed. *Nano Letters* **11**, 1657–1663 (2011).
256. Hall, J. M. *et al.* Method for predicting whispering gallery mode spectra of spherical microresonators. *Optics Express* **23**, 9924–9937 (2015).
257. García de Abajo, F. Relativistic description of valence energy losses in the interaction of fast electrons with clusters of dielectrics: Multiple-scattering approach. *Physical Review B* **60**, 6103 (1999).
258. Han, Z., Checoury, X., Haret, L.-D. & Boucaud, P. High quality factor in a two-dimensional photonic crystal cavity on silicon-on-insulator. *Optics Letters* **36**, 1749–1751 (2011).
259. Han, Z. *et al.* Optimized design for 2×10^6 ultra-high Q silicon photonic crystal cavities. *Optics Communications* **283**, 4387–4391 (2010).
260. Pennycook, S. J. The impact of STEM aberration correction on materials science. *Ultramicroscopy* **180**, 22–33 (2017).

261. Stevens, A. *et al.* A sub-sampled approach to extremely low-dose STEM. *Applied Physics Letters* **112**, 043104 (2018).
262. Trampert, P. *et al.* How should a fixed budget of dwell time be spent in scanning electron microscopy to optimize image quality? *Ultramicroscopy* **191**, 11–17 (2018).
263. Li, X., Dyck, O., Kalinin, S. V. & Jesse, S. Compressed sensing of scanning transmission electron microscopy (STEM) with nonrectangular scans. *Microscopy and Microanalysis* **24**, 623–633 (2018).
264. Strauss, M., Naday, I., Sherman, I. & Zaluzec, N. CCD-based parallel detection system for electron energy-loss spectroscopy and imaging. *Ultramicroscopy* **22**, 117–123 (1987).
265. Faruqi, A., Henderson, R., Pryddetch, M., Allport, P. & Evans, A. Direct single electron detection with a CMOS detector for electron microscopy. *Nuclear Instruments and Methods in Physics Research Section A: Accelerators, Spectrometers, Detectors and Associated Equipment* **546**, 170–175 (2005).
266. Stoffle, N. *et al.* Timepix-based radiation environment monitor measurements aboard the International Space Station. *Nuclear Instruments and Methods in Physics Research Section A: Accelerators, Spectrometers, Detectors and Associated Equipment* **782**, 143–148 (2015).
267. Ponchut, C. *et al.* Photon-counting X-ray imaging at kilohertz frame rates. *Nuclear Instruments and Methods in Physics Research Section A: Accelerators, Spectrometers, Detectors and Associated Equipment* **576**, 109–112 (2007).
268. Pennicard, D. *et al.* The LAMBDA photon-counting pixel detector and high-Z sensor development. *Journal of Instrumentation* **9**, C12026 (2014).
269. Russo, P. *et al.* 18F-FDG positron autoradiography with a particle counting silicon pixel detector. *Physics in Medicine & Biology* **53**, 6227 (2008).
270. Jakubek, J. Energy-sensitive X-ray radiography and charge sharing effect in pixelated detector. *Nuclear Instruments and Methods in Physics Research Section A: Accelerators, Spectrometers, Detectors and Associated Equipment* **607**, 192–195 (2009).
271. Nederlof, I., van Genderen, E., Li, Y.-W. & Abrahams, J. P. A Medipix quantum area detector allows rotation electron diffraction data collection from submicrometre three-dimensional protein crystals. *Acta Crystallographica Section D: Biological Crystallography* **69**, 1223–1230 (2013).
272. Van Genderen, E. *et al.* Ab initio structure determination of nanocrystals of organic pharmaceutical compounds by electron diffraction at room temperature using a Timepix quantum area direct electron detector. *Acta Crystallographica Section A: Foundations and Advances* **72**, 236–242 (2016).

273. McMullan, G. *et al.* Electron imaging with Medipix2 hybrid pixel detector. *Ultramicroscopy* **107**, 401–413 (2007).
274. Van Gastel, R. *et al.* Medipix 2 detector applied to low energy electron microscopy. *Ultramicroscopy* **110**, 33–35 (2009).
275. Krajenak, M., McGrouther, D., Maneuski, D., O’Shea, V. & McVitie, S. Pixelated detectors and improved efficiency for magnetic imaging in STEM differential phase contrast. *Ultramicroscopy* **165**, 42–50 (2016).
276. Van Schayck, J. P. *et al.* Sub-pixel electron detection using a convolutional neural network. *Ultramicroscopy* **218**, 113091 (2020).
277. Hart, J. L. *et al.* Direct detection electron energy-loss spectroscopy: a method to push the limits of resolution and sensitivity. *Scientific Reports* **7**, 1–14 (2017).
278. Goodge, B. H., Baek, D. J. & Kourkoutis, L. F. Atomic-resolution elemental mapping at cryogenic temperatures enabled by direct electron detection. *arXiv preprint arXiv:2007.09747* (2020).
279. Ballabriga, R. *et al.* Medipix3: A 64 k pixel detector readout chip working in single photon counting mode with improved spectrometric performance. *Nuclear Instruments and Methods in Physics Research Section A: Accelerators, Spectrometers, Detectors and Associated Equipment* **633**, S15–S18 (2011).
280. Jannis, D. *et al.* Event driven 4D STEM acquisition with a Timepix3 detector: microsecond dwell time and faster scans for high precision and low dose applications. *Ultramicroscopy* **233**, 113423 (2022).
281. Llopart, X., Ballabriga, R., Campbell, M., Tlustos, L. & Wong, W. Timepix, a 65k programmable pixel readout chip for arrival time, energy and/or photon counting measurements. *Nuclear Instruments and Methods in Physics Research Section A: Accelerators, Spectrometers, Detectors and Associated Equipment* **581**, 485–494 (2007).
282. Ballabriga, R., Campbell, M. & Llopart, X. Asic developments for radiation imaging applications: The Medipix and Timepix family. *Nuclear Instruments and Methods in Physics Research Section A: Accelerators, Spectrometers, Detectors and Associated Equipment* **878**, 10–23 (2018).
283. Poikela, T. *et al.* Timepix3: a 65K channel hybrid pixel readout chip with simultaneous ToA/ToT and sparse readout. *Journal of Instrumentation* **9**, C05013 (2014).
284. Van Der Heijden, B. *et al.* SPIDR, a general-purpose readout system for pixel ASICs. *Journal of Instrumentation* **12**, C02040 (2017).
285. Visser, J. *et al.* SPIDR: a read-out system for Medipix3 & Timepix3. *Journal of Instrumentation* **10**, C12028 (2015).

286. Heijhoff, K. *et al.* Timing performance of the LHCb VELO Timepix3 telescope. *Journal of Instrumentation* **15**, P09035 (2020).
287. Matsakis, N. D. & Klock, F. S. The rust language. *ACM SIGAda Ada Letters* **34**, 103–104 (2014).
288. De Melo, A. C. The new linux'perf'tools. *Linux Kongress* **18**, 1–42 (2010).
289. Tencé, M. *et al.* Electron irradiation effects: a time-energy representation. *Emag-Micro* **98**, 311–314 (1989).
290. Walls, M. G. & Tencé, M. EELS study of beam-induced decomposition of calcite in the STEM. *Emag-Micro* **98**, 255–258 (1989).
291. Golla-Schindler, U., Benner, G., Orchowski, A. & Kaiser, U. In situ observation of electron beam-induced phase transformation of CaCO₃ to CaO via ELNES at low electron beam energies. *Microscopy and Microanalysis* **20**, 715–722 (2014).
292. De la Peña, F. *et al.* *hyperspy/hyperspy: Release v1.6.2* version v1.6.2. Apr. 2021. <https://doi.org/10.5281/zenodo.4683076>.
293. Arenal, R. *et al.* Extending the analysis of EELS spectrum-imaging data, from elemental to bond mapping in complex nanostructures. *Ultramicroscopy* **109**, 32–38 (2008).
294. De la Peña, F. *et al.* Mapping titanium and tin oxide phases using EELS: An application of independent component analysis. *Ultramicroscopy* **111**, 169–176 (2011).
295. Muller, D. A. Why changes in bond lengths and cohesion lead to core-level shifts in metals, and consequences for the spatial difference method. *Ultramicroscopy* **78**, 163–174 (1999).
296. Bergmann, B. *et al.* 3D track reconstruction capability of a silicon hybrid active pixel detector. *The European Physical Journal C* **77**, 1–9 (2017).
297. Pitters, F. *et al.* Time resolution studies of Timepix3 assemblies with thin silicon pixel sensors. *Journal of Instrumentation* **14**, P05022 (2019).
298. Tararan, A., Zobelli, A., Benito, A. M., Maser, W. K. & Stéphan, O. Revisiting graphene oxide chemistry via spatially-resolved electron energy loss spectroscopy. *Chemistry of Materials* **28**, 3741–3748 (2016).
299. Htoon, H., O'Connell, M., Doorn, S. & Klimov, V. Single carbon nanotubes probed by photoluminescence excitation spectroscopy: The role of phonon-assisted transitions. *Physical Review Letters* **94**, 127403 (2005).
300. Roquelet, C. *et al.* Quantum efficiency of energy transfer in noncovalent carbon nanotube/porphyrin compounds. *Applied Physics Letters* **97**, 141918 (2010).

301. Robert, C. *et al.* Optical spectroscopy of excited exciton states in MoS₂ monolayers in van der Waals heterostructures. *Physical Review Materials* **2**, 011001 (2018).
302. Polman, A., Kociak, M. & García de Abajo, F. J. Electron-beam spectroscopy for nanophotonics. *Nature materials* **18**, 1158–1171 (2019).
303. Kruit, P., Shuman, H. & Somlyo, A. Detection of X-rays and electron energy loss events in time coincidence. *Ultramicroscopy* **13**, 205–213 (1984).
304. Jannis, D., Müller-Caspary, K., Béché, A., Oelsner, A. & Verbeeck, J. Spectroscopic coincidence experiments in transmission electron microscopy. *Applied Physics Letters* **114**, 143101 (2019).
305. Jannis, D., Müller-Caspary, K., Béché, A. & Verbeeck, J. Coincidence detection of EELS and EDX spectral events in the electron microscope. *Applied Sciences* **11**, 9058 (2021).
306. Graham, R., Spence, J. & Alexander, H. Infrared Cathodoluminescence Studies from Dislocations in Silicon in tem, a Fourier Transform Spectrometer for Cl in Tem and Els/cl Coincidence Measurements of Lifetimes in Semiconductors. *MRS Online Proceedings Library (OPL)* **82** (1986).
307. De Abajo, F. G., Rivacoba, A., Zabala, N. & Yamamoto, N. Boundary effects in Cherenkov radiation. *Physical Review B* **69**, 155420 (2004).
308. De Abajo, F. G. *et al.* Cherenkov effect as a probe of photonic nanostructures. *Physical Review Letters* **91**, 143902 (2003).
309. Yamamoto, N., Sugiyama, H. & Toda, A. Cherenkov and transition radiation from thin plate crystals detected in the transmission electron microscope. *Proceedings of the Royal Society of London. Series A: Mathematical, Physical and Engineering Sciences* **452**, 2279–2301 (1996).
310. Yamamoto, N., Toda, A. & Axaya, K. Imaging of transition radiation from thin films on a silicon substrate using a light detection system combined with TEM. *Microscopy* **45**, 64–72 (1996).
311. Gómez-Medina, R., Yamamoto, N., Nakano, M. & De Abajo, F. G. Mapping plasmons in nanoantennas via cathodoluminescence. *New Journal of Physics* **10**, 105009 (2008).
312. Meuret, S. *et al.* Photon bunching reveals single-electron cathodoluminescence excitation efficiency in InGaN quantum wells. *Physical Review B* **96**, 035308 (2017).
313. Meuret, S. *et al.* Nanoscale relative emission efficiency mapping using cathodoluminescence g (2) imaging. *Nano Letters* **18**, 2288–2293 (2018).
314. Cassabois, G., Valvin, P. & Gil, B. Hexagonal boron nitride is an indirect bandgap semiconductor. *Nature Photonics* **10**, 262–266 (2016).

315. Feist, A. *et al.* Cavity-mediated electron-photon pairs. *arXiv preprint arXiv:2202.12821* (2022).
316. Beha, K., Batalov, A., Manson, N. B., Bratschitsch, R. & Leitenstorfer, A. Optimum photoluminescence excitation and recharging cycle of single nitrogen-vacancy centers in ultrapure diamond. *Physical Review Letters* **109**, 097404 (2012).
317. Zelewski, S. *et al.* Revealing the nature of photoluminescence emission in the metal-halide double perovskite Cs₂AgBiBr₆. *Journal of Materials Chemistry C* **7**, 8350–8356 (2019).
318. Campbell, M. *et al.* Towards a new generation of pixel detector readout chips. *Journal of Instrumentation* **11**, C01007 (2016).
319. Guzzinati, G. *et al.* Probing the symmetry of the potential of localized surface plasmon resonances with phase-shaped electron beams. *Nature Communications* **8**, 1–8 (2017).
320. Lourenço-Martins, H., Gérard, D. & Kociak, M. Optical polarization analogue in free electron beams. *Nature Physics* **17**, 598–603 (2021).
321. Arfken, G. & Weber, H. J. *Mathematical methods for physicists* (Elsevier, 2005).
322. Sihvola, A., Ylä-Oijala, P., Jarvenpää, S. & Avelin, J. Polarizabilities of platonic solids. *IEEE transactions on antennas and propagation* **52**, 2226–2233 (2004).
323. Johnson, P. B. & Christy, R.-W. Optical constants of the noble metals. *Physical Review B* **6**, 4370 (1972).
324. Yurkin, M. A. & Hoekstra, A. G. The discrete dipole approximation: an overview and recent developments. *Journal of Quantitative Spectroscopy and Radiative Transfer* **106**, 558–589 (2007).

List of publications

The list of publications during my Ph.D. is presented below, from the beginning to the time of writing (October/2019 - August/2022 or 2 years 10 months). Below each item, the author's contributions are described.

- Ricardo Javier Peña Román, **Yves Auad**, Lucas Grasso, Fernando Alvarez, Ingrid David Barcelos, Luiz Fernando Zagonel. “Tunneling-current-induced local excitonic luminescence in p-doped WSe₂ monolayers”. *Nanoscale* 12.25 (2020), pp. 13460–13470.
 - RJPR, FA, and LFZ designed the experiment. YA, RJPR, and LFZ developed the light collection device for the scanning tunneling microscope. RJPR and LG performed the experiments. IDB provided materials.
- Ismail Benabdallah, **Yves Auad**, Wilfried Sigle, Peter A. van Aken, Mathieu Kociak, Mohammed Benaissa. “Electronic properties of black phosphorus using monochromated low-loss EELS”. *Materials Science and Engineering: B* 265 (2021), p. 115002.
 - WS, PA, MK, and MB designed the experiment. IB, YA and MK performed the experiments.
- Sophie Meuret, Luiz Henrique Galvão Tizei, Florent Houdellier, S. Weber, **Yves Auad**, Marcel Tencé, H-C Chang, Mathieu Kociak, Arnaud Arbouet. “Time-resolved cathodoluminescence in an ultrafast transmission electron microscope”. *Applied Physics Letters* 119.6 (2021), p. 062106.
 - SM, LHGT, MK, AA designed the experiment. FH designed the microscope. SM and LHGT performed the experiments with support from SW, YA, and MT. HCC provided materials.
- **Yves Auad**, Michael Walls, Jean-Denis Blazit, Odile Stéphan, Luiz HG Tizei, Mathieu Kociak, Francisco De la Penã, Marcel Tencé. “Event-based

hyperspectral EELS: towards nanosecond temporal resolution". *Ultramicroscopy* 239, 113539 (2022).

– YA, OS, LHGT, MK, FDLP, and MT designed the experiment. YA, JDB, and MT developed the Timepix3 implementation for EELS. YA, FDLP, MW, LHGT, and MK analyzed the data.

- **Yves Auad**, Cyrille Hamon, Marcel Tencé, Hugo Lourenço-Martins, Vahagn Mkhitarian, Odile Stéphan, F Javier Garcia de Abajo, Luiz HG Tizei, Mathieu Kociak. "Unveiling the coupling of single metallic nanoparticles to whispering-gallery microcavities". *Nano letters* 22.1 (2022), pp. 319–327.

– YA, OS, FJGA, LHGT, and MK designed the experiment. YA, LHGT and MK performed the experiments with support from MT. YA, LHGT, and MK analyzed the data, with support from CH and HLM. YA performed the FDTD simulations. VM and FJGA performed the BEM simulation and the coupling theory. CH provided materials.

- Nadezda Varkentina*, **Yves Auad***, Steffi Y. Woo, Alberto Zobelli, Jean-Denis Blazit, Xiaoyan Li, Marcel Tencé, Kenji Watanabe, Takashi Taniguchi, Odile Stéphan, Mathieu Kociak, Luiz H.G. Tizei. "Cathodoluminescence excitation spectroscopy: nanoscale imaging of excitation pathways". arXiv preprint arXiv:2202.12520 (2022). *Under review*.

– LHGT, OS, LB, AZ, and MK designed the experiment. YA, MT, and JDB developed the Timepix3 implementation for EELS. NV, YA, SYW, and LHGT performed experiments with support from XL. NV, YA, and LHGT analyzed the data. KW and TT the provided materials.

* These authors have contributed equally.

- Ricardo Javier Peña Román, **Yves Auad**, Lucas Grasso, Lázaro Padilha, Fernando Alvarez, Ingrid David Barcelos, Mathieu Kociak, and Luiz Fernando Zagonel. "Design and implementation of a device based on an off-axis parabolic mirror to perform luminescence experiments in a Scanning Tunneling Microscope". *Review of Scientific Instruments* (2022). *Accepted*.

– LFZ, LP, FA, and MK designed the experiment. YA, RJPR, and LFZ developed the light collection device for the scanning tunneling microscope. RJPR and LG performed the experiments with support from YA. IDB provided materials.

Glossary

- ADF** Annular dark-field. 14, 21, 39–41, 50, 100, 108, 113, 114, 116–118, 136
- BF** Bright-field. 21, 39, 40, 50
- CCD** Charged-coupled device. 14, 21, 44, 51, 106, 107, 136, 186
- cFEG** Cold field-emission gun. 19, 42, 43, 51, 59, 71, 72, 78, 100, 105, 121, 128, 183
- ChromaTEM** A C_s -corrected microscope based on a Nion Hermes200 that operates between 30 keV and 200 keV. The electron monochromator (α type) is capable of reaching down to ~ 5 meV spectral resolution at the electron acceleration of 60 keV. 19, 20, 50, 51, 60, 66, 69–75, 79, 91, 100–102, 104, 105, 125, 127, 128, 135, 143, 144
- CL** Cathodoluminescence. 12, 13, 18–21, 39, 47, 48, 51, 52, 54, 55, 57, 58, 62, 66, 67, 69, 79, 83–85, 88, 89, 91–93, 96–100, 104, 122–129, 131, 133–135, 145, 186
- CLE** Cathodoluminescence excitation spectroscopy. 12, 14, 21, 22, 47, 122–124, 126–134, 136, 137, 186
- CMOS** Complementary metal–oxide–semiconductor. 14, 106, 107
- EEGS** Electron energy-gain spectroscopy, sometimes also referred as stimulated electron energy-gain spectroscopy (sEEGS). 12, 13, 18–21, 39, 48–50, 54, 55, 59, 62, 65–70, 72–74, 76, 78–80, 84, 85, 100, 101, 104, 105, 135–137, 143, 146, 147, 186

- EELS** Electron energy-loss spectroscopy. 12–14, 18–21, 23, 38–41, 44–48, 50–52, 54, 55, 57, 59–62, 66, 70–77, 79, 83–85, 88, 89, 91–100, 102–109, 111, 114–131, 133–136, 145, 148, 149, 151, 152, 155, 186
- EMLDOS** Local electromagnetic density of states. 33, 38, 46–48
- FDTD** Finite-difference time-domain. 52, 53, 91–95, 104, 148, 149
- HPD** Hybrid-pixel detector. 13, 21, 106, 107, 126
- MNP** Metallic nanoparticle. 13, 20, 81, 82, 85, 95, 96, 98, 99, 104, 135, 136, 150–152, 186
- PLE** Photoluminescence excitation spectroscopy. 14, 21, 22, 122–124, 126, 131, 133, 134
- PMT** Photomultiplier tube. 39, 44, 50, 122–124, 128, 129, 134
- PSF** Point spread function. 21, 51, 76, 106, 107, 118, 120
- STEM** Scanning transmission electron microscope. 12, 14, 18–20, 39–41, 43, 45, 48, 50, 61, 62, 71, 89, 100, 104, 107, 108, 123–125, 129, 133, 135, 186
- TDC** In electronics, a time-to-digital converter (TDC) is a device that provides a digital representation of the time an event has occurred. 21, 75–78, 111, 113, 121, 128, 133, 136, 153, 154, 186
- ToA** Time of arrival. 21, 80, 105, 108–111, 113, 116, 120, 127, 156, 157
- ToT** Time over threshold. 21, 108–111, 116, 117, 121, 127, 154, 155
- TPX3** Timepix3. 12–14, 21, 75–80, 105, 108–110, 115, 117, 120, 122, 124, 126, 128–130, 134, 136, 143, 154, 186
- VG** A microscope dedicated to instrumental developments that operates between 40 keV and 100 keV. It uses a cold field-emission gun (cFEG) and can reach a spectral resolution of ~ 300 meV. 21, 50, 51, 58, 66, 68, 69, 72, 76, 100, 101, 115, 143, 144
- WGMR** Whispering-gallery mode resonator. 12, 13, 20, 79, 81, 82, 84, 85, 88, 89, 93, 95, 96, 99, 100, 104, 135, 136, 186
- ZLP** Zero-loss peak. 12, 39, 40, 45, 48, 51, 54, 69–72, 76–78, 80, 102, 104, 107, 118, 120

Titre: Nouvelles spectroscopies nanosecondes et milliélectronvolts au microscope électronique et leurs applications à la nano-optique

Mots clés: microscope électronique en transmission à balayage; spectroscopie de gain d'énergie des électrons; spectroscopie de perte d'énergie des électrons; cathodoluminescence; timepix3; spectroscopie d'excitation de cathodoluminescence

Résumé:

Dans cette thèse, un ensemble d'interactions électron/matière/lumière ont été explorées dans un microscope électronique en transmission à balayage (STEM, *scanning transmission electron microscope*) combinant les spectroscopies électroniques traditionnelles, telles que la spectroscopie de perte d'énergie des électrons (EELS, *electron energy-loss spectroscopy*) et la cathodoluminescence (CL) avec de nouvelles techniques, telles que la spectroscopie de gain d'énergie des électrons (EEGS, *electron energy-gain spectroscopy*) et la spectroscopie d'excitation de cathodoluminescence (CLE, *cathodoluminescence excitation spectroscopy*), au développement desquelles ce travail a contribué. En particulier, la mesure des résonances à bande étroite d'un micro-résonateur à modes de galerie (WGMR, *whispering-gallery mode resonators*) optique ont motivé le développement de l'EEGS, une technique prometteuse qui pourrait combiner la résolution spectrale des sources laser avec la résolution spatiale des microscopes électroniques modernes. En outre, l'échelle de temps des résonances souhaitées, de l'ordre de la nanoseconde, a déclenché le développement de l'instrumentation de déflecteurs et de détecteurs rapides à résolution temporelle, tels que la Timepix3 (TPX3). Les WGMRs ont été étudiés seuls ou couplés à une nanoparticule métallique (MNP, *metallic nanoparticle*) en utilisant

les trois principales techniques mentionnées ci-dessus, c'est-à-dire l'EELS, la CL et l'EEGS. Plus de 80 modes de galerie ont pu être identifiés simultanément dans le résonateur seul, tandis qu'un faible couplage a été observé dans le système couplé dans les modes plasmoniques d'ordre inférieur du MNP. En plus, la nature « event-based » du TPX3 a permis le développement d'une reconstruction d'image hyperspectrale qui peut être exécutée en étant uniquement limitée par l'unité de balayage au lieu de la limitation du temps de lecture des détecteurs à frame, comme c'est le cas pour les CCDs (*charge-coupled devices*). Ainsi, la décomposition de la calcite (CaCO_3) a été utilisée pour explorer les potentiels de résolution temporelle de ces détecteurs. Enfin, la présence de *time-to-digital converters* (TDCs) dans la TPX3 a également déclenché le développement de la CLE car les électrons et les événements photons peuvent être codés avec la même horloge de référence et ainsi associé l'électron à une émission photon. La CLE a été utilisé pour étudier les interactions électrons-photons en phase, telles que le rayonnement de transition et les plasmons de surface localisés, et les interactions sans relation de phase, telles que l'absorption proche de le band gap et d'un plasmon de volume. Une nanosphère d'or à coquille de silice et un flocon de h -BN ont été utilisés comme échantillons.

Title: Novel nanosecond and millielectronvolt spectroscopies in the electron microscope and their applications to nano-optics

Keywords: scanning transmission electron microscope; electron energy-gain spectroscopy; electron energy-loss spectroscopy; cathodoluminescence; timepix3; cathodoluminescence excitation spectroscopy

Abstract:

In this thesis, a myriad of electron/matter/light interactions have been explored in a scanning transmission electron microscope (STEM) combining traditional electron spectroscopies, such as electron energy-loss spectroscopy (EELS) and cathodoluminescence (CL) with novel techniques, such as electron energy-gain spectroscopy (EEGS) and cathodoluminescence excitation spectroscopy (CLE), in which this work has contributed to developing. In particular, the narrow-band resonances of an optical whispering-gallery mode resonator (WGMR) have motivated the development of EEGS, a promising technique that could combine the spectral resolution of laser sources with the spatial resolution of modern electron microscopes. Besides, the time-scale of the desired resonances, in the nanosecond range, has triggered instrumentation developments of time-resolved fast deflectors and detectors, such as Timepix3 (TPX3). WGMRs were studied either bare or coupled to a metallic nanoparticle (MNP) by using all the three main techniques aforementioned, i.e. EELS, CL, and EEGS. More than 80

gallery modes could be simultaneously identified in the bare resonator, while weak coupling was observed in the coupled system in the lower-order plasmonic modes of the MNP. Additionally, the event-based nature of TPX3 allowed the development of a hyperspectral image reconstruction that can be performed limited by the scanning unit instead of the long-lasting limitation of the readout time of frame-based detectors, such as in charged-coupled devices (CCDs). With this, the decomposition of calcite (CaCO_3) was used to explore the time-resolved potentials of such detectors. Finally, the presence of time-to-digital converters (TDCs) in the TPX3 also triggered the development of CLE because electrons and photon events can be timestamped with the same reference clock and thus relate to the electron associated with a photon emission. CLE was used to study phase-locked electron-photon interactions, such as in transition radiation and localized surface plasmons, and non-phase-locked interactions, such as near-band edge and bulk plasmon absorption. For such, a silica-shelled gold nanosphere and a h -BN flake were used as samples.